Unified computational frameworks bridging low to high frequency simulations : fast and high fidelity modelling from brain to radio-frequency scenarios

Adrien Merlini

UNIVERSITE BRETAGNE LOIRE / MATHSTIC

IMT Atlantique
Bretagne-Pays de la Loire
École Mines-Télécom

THESE DE DOCTORAT DE

L'ÉCOLE NATIONALE SUPERIEURE MINES-TELECOM ATLANTIQUE
BRETAGNE PAYS DE LA LOIRE - IMT ATLANTIQUE
COMUE UNIVERSITE BRETAGNE LOIRE

ECOLE DOCTORALE N° 601
Mathématiques et Sciences et Technologies de l'Information et de la Communication
Spécialité : *Génie Electrique*

Par

Adrien MERLINI

Unified Computational Frameworks Bridging Low to High Frequency Simulations

Fast and High Fidelity Modelling from Brain to Radio-Frequency Scenarios

Thèse présentée et soutenue à Brest, le 2019/01/31
Unité de recherche : LabSTIC, Pôle MoM
Thèse N° : 2019IMTA0130

Rapporteurs avant soutenance :

Hélène Roussel	Professeure, Sorbonne Université
Roberto D. Graglia	Professeur, Politecnico di Torino

Composition du Jury :

Président :	Joe Wiart	Professeur de la chaire C2M, Télécom ParisTech
Rapporteurs :	Hélène Roussel	Professeure, Sorbonne Université
	Roberto D. Graglia	Professeur, Politecnico di Torino
Examinateurs :	Daniel Bourreau	Enseignant-Chercheur, IMT Atlantique
	Kristof Cools	Assistant Professor, Delft University of Technology
	Édouard Demaldent	Ingénieur Chercheur, LIST/CEA
Directeur de thèse :	Francesco P. Andriulli	Professeur, Politecnico di Torino

École Nationale Supérieure Mines-Télécom Atlantique Bretagne-Pays de la Loire
École doctorale MathSTIC – № 601

PhD Thesis
№ 2019IMTA0130

Unified Computational Frameworks Bridging Low to High Frequency Simulations

Fast and High Fidelity Modelling from Brain to Radio-Frequency Scenarios

Adrien Merlini

Département Micro-Ondes — LabSTIC, MOM-PIM

Thèse soutenue à Brest le 31 janvier 2019

Président :	Joe Wiart, Professeur de la Chaire C2M, Télécom ParisTech
Rapporteurs :	Hélène Roussel, Professeure, Sorbonne Université
	Roberto D. Graglia, Professeur, Politecnico di Torino
Examinateurs :	Daniel Bourreau, Enseignant-Chercheur, IMT Atlantique
	Kristof Cools, Assistant Professor, Delft University of Technology
	Édouard Demaldent, Ingénieur Chercheur, LIST-CEA
Directeur :	Francesco P. Andriulli, Professeur, Politecnico di Torino

IMT Atlantique
Bretagne-Pays de la Loire
École Mines-Télécom

Abstract

In computational electromagnetics, boundary integral equations are the scheme of choice for solving extremely large forward electromagnetic problems due to their high efficiency. However, two of the most used of these formulations, the electric and combined field integral equations (EFIE and CFIE), suffer from stability issues at low frequency and dense discretization, limiting their applicability at both ends of the spectrum. This thesis focusses on remedying these issues to obtain full-wave solvers stable from low to high frequencies, capable of handling scenarios ranging from electromagnetic compatibility to radar applications. The solutions presented include (i) extending the quasi-Helmholtz (qH) projectors to higher order modeling thus combining stability with high order convergence rates; (ii) leveraging on the qH projectors to numerically stabilize the magnetic field integral equation and obtain a highly accurate and provably resonance-free Calderón-augmented CFIE immune to both of the aforementioned problems; and (iii) introducing a new low frequency and dense discretization stable wire EFIE based on projectors and linear B-splines. In addition, a research axis focussed on enhancing Brain Computer Interface (BCIs) with high resolution electromagnetic modeling of the brain has been opened; a particular attention is dedicated to the inverse problem of electromagnetics and the associated integral equation-based forward problem. The first results of this new line of investigations include the development of one of the first peer-reviewed, freely available framework for end-to-end simulation of BCI experiments.

Résumé

Dans le domaine de l'électromagnétisme computationnel, les équations intégrales de frontière sont très largement utilisées pour résoudre certains des plus grands problèmes directs, grâce à leur grande efficacité. Cependant les équations intégrales du champ électrique et du champ combiné (EFIE et CFIE), deux des formulations les plus employées, souffrent d'instabilités à basse fréquence et à haute discrétisation, ce qui limite leur versatilité. Dans cette thèse différentes approches sont présentées pour obtenir des algorithmes applicables aussi bien à des problèmes de compatibilité électromagnétique qu'à des applications radar. Les solutions présentées incluent (i) l'extension des projecteurs dit quasi-Helmholtz (qH) aux modélisations d'ordre supérieur ; (ii) l'utilisation de ces projecteurs pour stabiliser l'équation intégrale du champ magnétique et former une CFIE extrêmement précise, augmentée par des techniques de type Calderón, qui ne souffre de problèmes ni à basse fréquence ni à haute discrétisation et qui n'est pas sujette aux résonances artificielles ; (iii) le développement d'une EFIE filaire, basée sur des B-splines linéaires et les projecteurs qH, stable aux deux extrémités du spectre. Ces travaux ont été suivis de l'ouverture d'un nouvel axe de recherche visant l'amélioration des techniques de résolution des problèmes inverses en électromagnétique, avec pour objectif principal l'augmentation des performances des interfaces cerveau machine (BCIs). Les premiers résultats obtenus incluent le développement de l'un des premiers systèmes libres de simulation de bout en bout de session de BCI ayant été publié après revue par les pairs.

Contents

Acknowledgment

Before diving into the technical parts of this dissertation I would like to thank the persons who have been instrumental to its completion. First of all I would like to thank my family for their support and Giulia Sacco for being there and handling the many side effects of this writing. In the CERL, I would like to express my gratitude to Francesco Andriulli for his advising, to Axelle Pillan and John Erick Ortiz Guzman for helping take the edge off the sometimes frustrating research, to Lyes Rahmouni and Rajendra Mitharwal for their wisdom, to Alexandre Dély for the very productive discussions about nothing, to Jussi Lindgren for sharing its machine learning expertise, Simon Adrian for his LaTeX-fu and to all the younger members recently arrived: Clément Henry, Maxime Monin, Tiffany Chhim, François Néron and Davide Consoli. Finally, I would like to thank Serge Guelton for pushing me both in professional and sportive contexts.

Brest, France

Adrien Merlini
May 1, 2019

Résumé Long

Dans le domaine de l'électromagnétisme computationnel, les équations intégrales de frontière sont très largement utilisées pour résoudre certains des plus grands problèmes directs, grâce à leur grande efficacité. Cependant ces équations souffrent de diverses instabilités, en particulier à haute et à basse fréquences qui restreignent leurs domaines d'applicabilités. Les travaux présentés dans cette thèse s'articulent autour de la stabilisation de plusieurs équations intégrales largement utilisées, aussi bien dans les milieux académiques que dans l'industrie, grâce à des analyses spectrales détaillées permettant dans un premier temps de caractériser les instabilités et dans un second temps de concevoir des familles de préconditionneurs adaptés aux différents problèmes ainsi identifiés. Ces différents aspects sont présentés de façon synthétique dans le Chapitre 1.

Dans le Chapitre 2 certaines des équations intégrales principales de l'électromagnétisme sont dérivées à partir des équations de Maxwell

$$\nabla \times \boldsymbol{e} = -\boldsymbol{m} - \mathrm{j}\omega\mu\boldsymbol{h}\,, \tag{0.1a}$$
$$\nabla \times \boldsymbol{h} = \boldsymbol{j} + \mathrm{j}\omega\epsilon\boldsymbol{e}\,, \tag{0.1b}$$
$$\nabla \cdot \boldsymbol{d} = \rho_e\,, \tag{0.1c}$$
$$\nabla \cdot \boldsymbol{b} = \rho_m\,. \tag{0.1d}$$

En haute fréquence ces équations sont l'équation intégrale du champ électrique (EFIE) et l'équation intégrale du champ magnétique (MFIE)

$$\left[\mathrm{j}k^+\eta^+\left(\mathcal{T}\boldsymbol{j}_\Gamma^+\right)(\boldsymbol{r}) + \left(\mathcal{K}\boldsymbol{m}_\Gamma^+\right)(\boldsymbol{r})\right]_{\tan} + \frac{1}{2}\hat{\boldsymbol{n}}\times\boldsymbol{m}_\Gamma^+(\boldsymbol{r}) = \left[\boldsymbol{e}^i(\boldsymbol{r})\right]_{\tan}, \qquad \boldsymbol{r}\in\Gamma\,, \tag{0.2}$$
$$\left[\frac{\mathrm{j}k^+}{\eta^+}\left(\mathcal{T}\boldsymbol{m}_\Gamma^+\right)(\boldsymbol{r}) - \left(\mathcal{K}\boldsymbol{j}_\Gamma^+\right)(\boldsymbol{r})\right]_{\tan} - \frac{1}{2}\hat{\boldsymbol{n}}\times\boldsymbol{j}_\Gamma^+(\boldsymbol{r}) = \left[\boldsymbol{h}^i(\boldsymbol{r})\right]_{\tan}, \qquad \boldsymbol{r}\in\Gamma\,, \tag{0.3}$$

qui seront le sujet de nombreux développements tout au long de cette thèse. Puisque le dernier chapitre de cette thèse se concentre sur le développement de nouvelles interfaces cerveau-machine (sICMs), l'une des formations intégrales les plus utilisées pour la modélisation électromagnétique du cerveau est aussi introduite dans ce

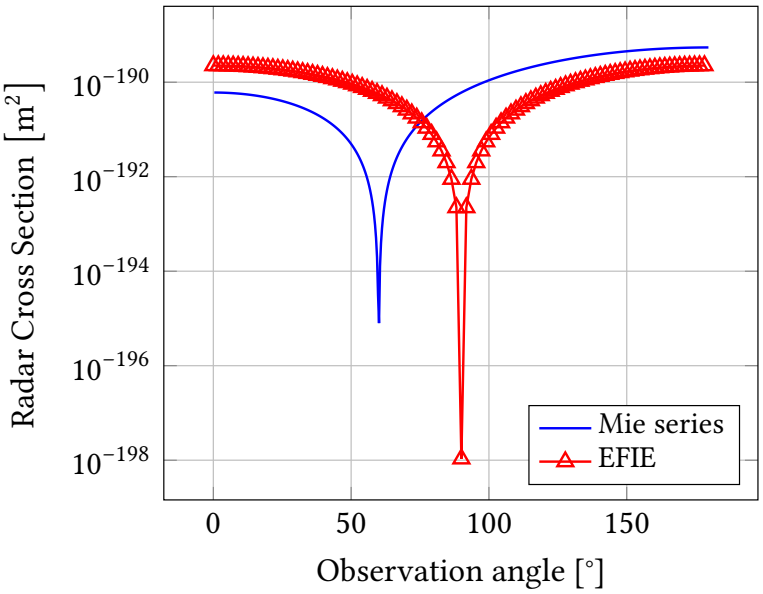

FIGURE 0.1. : Illustration de la dégradation de la solution de l'EFIE en basses fréquences, obtenue en simulant un sphère de rayon 1 m à $1 \cdot 10^{-40}$ Hz. Les séries de Mie représentent la solution analytique exacte.

premier chapitre à partir de équations de Maxwell en régime quasi-statique

$$\nabla \times \boldsymbol{e} = -\mu \frac{\partial \boldsymbol{h}}{\partial t}\,, \tag{0.4}$$

$$\nabla \times \boldsymbol{h} = \epsilon \frac{\partial \boldsymbol{e}}{\partial t} + \boldsymbol{j}\,, \tag{0.5}$$

$$\nabla \cdot \boldsymbol{d} = \rho_e\,, \tag{0.6}$$

$$\nabla \cdot \boldsymbol{b} = \boldsymbol{0}\,. \tag{0.7}$$

Dans le Chapitre 3 une nouvelle approche est présentée pour stabiliser l'EFIE à basse fréquence lorsqu'une modélisation d'ordre supérieur est employée. L'EFIE souffre en effet de problèmes de conditionnement et de précision à basse fréquence (*low frequency breakdown*), qui la rendent difficilement utilisable dans ce régime (Figures 0.1 et 0.2). Ces problèmes ont récemment été résolus de façon efficaces par l'utilisation de projecteurs dit quasi-Helmholtz (qH). Ces projecteurs qui permettent de décomposer l'espace des fonctions de base en un sous-espace solénoïdal et un sous-espace non solénoïdal ne sont cependant pas directement applicables aux problèmes dont la géométrie est discrétisée à l'aide d'éléments d'ordre supérieur ou courbés (Figure 0.3). Les modélisations d'ordre supérieur ont de nombreux avantages

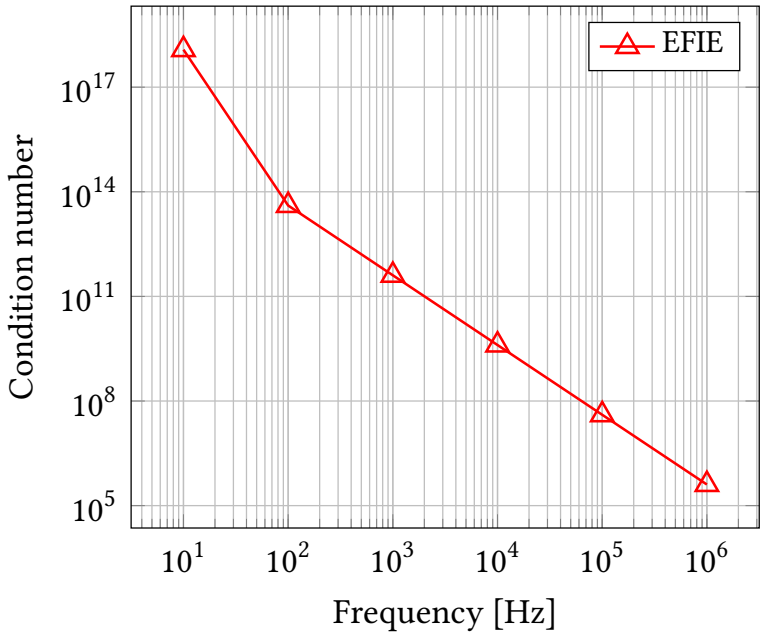

FIGURE 0.2. : Évolution du conditionnement des matrices d'impédance de l'EFIE à différentes fréquences pour une sphère de rayon 1 m.

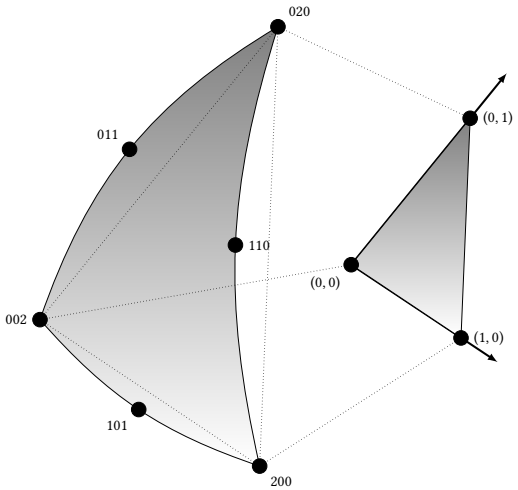

FIGURE 0.3. : Illustration d'un élément triangulaire quadratique.

en terme de nombre d'inconnues et de vitesse de convergence de la solution et sont donc nécessaires au développement de simulateurs haute performance. Pour étendre les projecteurs à ce type d'équation il est nécessaire de les redéfinir à partir de la matrice $\boldsymbol{\Sigma}$ discrétisant l'opérateur gradient

$$\left[\boldsymbol{\Sigma}^{\mathrm{T}}\right]_{ij} = \left\langle \sigma_i(\boldsymbol{r}), \nabla \cdot \boldsymbol{f}_j^p(\boldsymbol{r}) \right\rangle, \tag{0.8}$$

et les deux projecteurs (non-solénoïdal et solénoïdal) sont

$$\boldsymbol{P}_{\boldsymbol{\Sigma}} = \boldsymbol{\Sigma}\left(\boldsymbol{\Sigma}^{\mathrm{T}}\boldsymbol{G}_{\sigma,\sigma}^{-1}\boldsymbol{\Sigma}\right)^{+}\boldsymbol{\Sigma}^{\mathrm{T}}, \tag{0.9}$$

$$\boldsymbol{P}_{\boldsymbol{\Lambda}} = \mathbf{I} - \boldsymbol{P}_{\boldsymbol{\Sigma}}. \tag{0.10}$$

Une technique de calcul rapide de la pseudo-inverse nécessaire au calcul de $\boldsymbol{P}_{\boldsymbol{\Sigma}}$ est toujours en cours d'étude pour atteindre une résolution en complexité linéaire. En effet, la complexité linéaire de calcul des projecteurs obtenue pour les discrétisations traditionnelles ne peut pas être obtenue de la même façon car la matrice $\boldsymbol{\Sigma}^{\mathrm{T}}\boldsymbol{\Sigma}$ ne se comporte plus comme une matrice de Laplace.

Dans le Chapitre 4 la version filaire de l'EFIE

$$-\mathrm{j}k\eta_0\left[\int_l \hat{\boldsymbol{l}}(\boldsymbol{r})\cdot\hat{\boldsymbol{l}}(\boldsymbol{r}')\,i(\boldsymbol{r}')K_{\mathrm{ex}}(\boldsymbol{r}-\boldsymbol{r}')\,\mathrm{d}l' + \frac{1}{k^2}\hat{\boldsymbol{l}}(\boldsymbol{r})\cdot\nabla\int_l \nabla'\cdot\left(\hat{\boldsymbol{l}}(\boldsymbol{r}')\,i(\boldsymbol{r}')\right)K(\boldsymbol{r}-\boldsymbol{r}')\,\mathrm{d}l'\right] = -\hat{\boldsymbol{l}}(\boldsymbol{r})\cdot\boldsymbol{e}^i, \tag{0.11}$$

est étudiée en profondeur en pour être stabilisée aussi bien en basse fréquence qu'en discrétisation. En particulier une analyse spectrale détaillée est obtenue pour les deux noyaux de l'équation $K = K_{\mathrm{ex}}$ et $K = K_{\mathrm{red}}$, ce qui permet d'obtenir directement le spectre de l'opérateur intégral du champ électrique (EFIO) dans le cas d'un dipôle infiniment long. Cette analyse a mis en évidence l'existence de deux régimes différents des EFIEs filaires qui sont la conséquence de la forte influence du diamètre du fil les propriétés de l'opérateur. Ces deux régimes, observables pour les deux noyaux, donnent donc naissance à quatre comportements spectraux devant être analysés indépendamment. Les expressions analytiques des spectres sont ensuite utilisées pour choisir une famille de préconditionneurs hiérarchiques adaptés (Figure 0.4) et capables de compenser les instabilités en haute discrétisation dans les cas où cela est possible. Le préconditionneur hiérarchique est ensuite couplé avec une extension des projecteurs qH aux structures filaires ce qui permet une stabilisation complète de l'équation sur une large bande de fréquence. L'équation ainsi obtenue

$$\boldsymbol{D}\boldsymbol{H}^{\mathrm{T}}\boldsymbol{M}\boldsymbol{Z}\boldsymbol{M}\boldsymbol{H}\boldsymbol{D}\boldsymbol{y} = \boldsymbol{D}\boldsymbol{H}^{\mathrm{T}}\boldsymbol{M}\boldsymbol{v}, \tag{0.12}$$

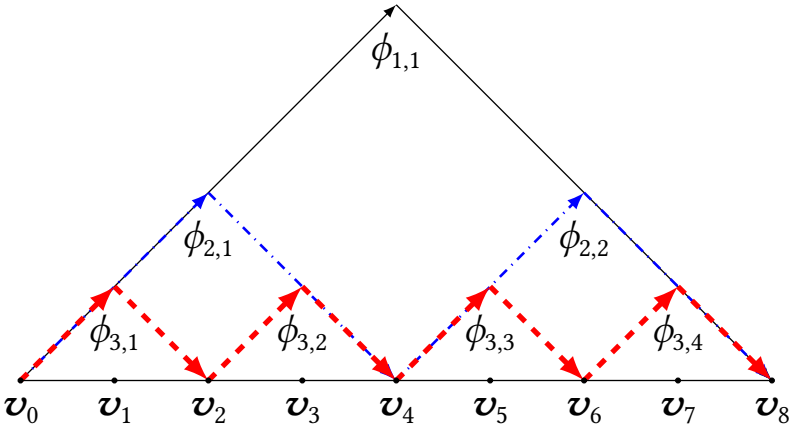

FIGURE 0.4. : Exemple d'ondelettes construites sur un segment filaire.

est capable d'opérer aussi bien en haute qu'en basse fréquences.

Dans le Chapitre 5 la MFIE est elle aussi stabilisée en basse fréquence et en haute discrétisation en utilisant des projecteurs qH et les identités de Calderón, respectivement. Combiner cette nouvelle MFIE avec une nouvelle EFIE récemment introduite permet d'obtenir une équation stable en basse et haute fréquences qui est aussi insensible aux résonances non physiques dont les équations souffrent lorsqu'elles sont séparées. La nouvelle MFIE

$$\left(\frac{\mathcal{I}}{2} - \mathcal{K}_{-\mathrm{j}k}\right)\left(\frac{\mathcal{I}}{2} + \mathcal{K}_k\right)(j) = \left(\frac{\mathcal{I}}{2} - \mathcal{K}_{-\mathrm{j}k}\right)\left(\hat{\boldsymbol{n}}_r \times \boldsymbol{h}^i\right). \tag{0.13}$$

peut correctement représenter le noyau statique de l'opérateur magnétique sur les structures à connexité multiple et ne souffre pas de perte de précision en basse fréquence (Figure 0.5). Cette nouvelle équation peut ensuite être combinée avec une EFIE régularisée pour former la nouvelle équation intégrale du champ combiné (CFIE)

$$\left(\eta^2\left(\frac{\mathcal{I}}{2} - \mathcal{K}_{-\mathrm{j}k}\right)\left(\frac{\mathcal{I}}{2} + \mathcal{K}_k\right)(k) + \mathcal{T}_{-\mathrm{j}k}\mathcal{T}_k\right)(j) = \left(\frac{\mathcal{I}}{2} - \mathcal{K}_{-\mathrm{j}k}\right)\left(\hat{\boldsymbol{n}} \times \boldsymbol{h}^i\right) + \mathcal{T}_{-\mathrm{j}k}\left(\hat{\boldsymbol{n}} \times \boldsymbol{e}^i\right), \tag{0.14}$$

dont il peut être prouvé qu'elle n'est pas sujette aux résonances non physiques (Figure 0.6). Les différentes propriétés de ces nouvelles équations sont illustrées au travers de nombreux exemples numériques.

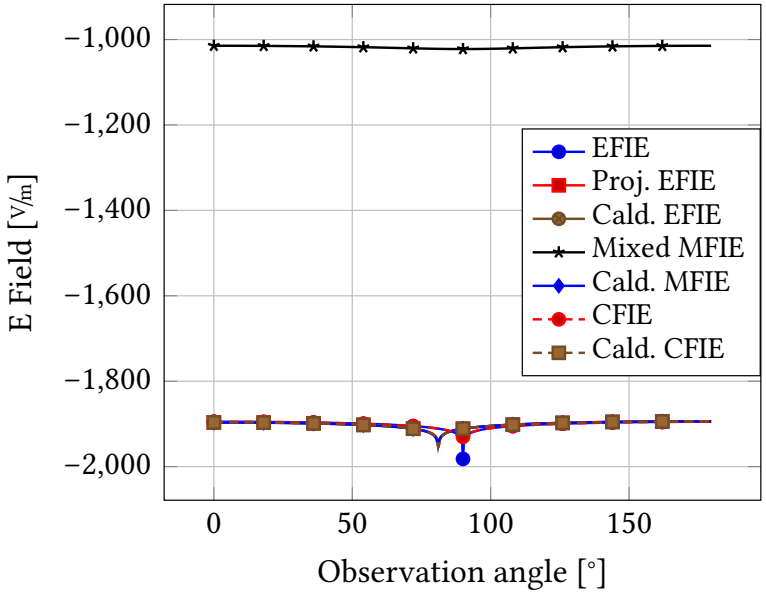

FIGURE 0.5. : Comparaison des champs rayonnés par différentes formulations à $1 \cdot 10^{-40}$ Hz.

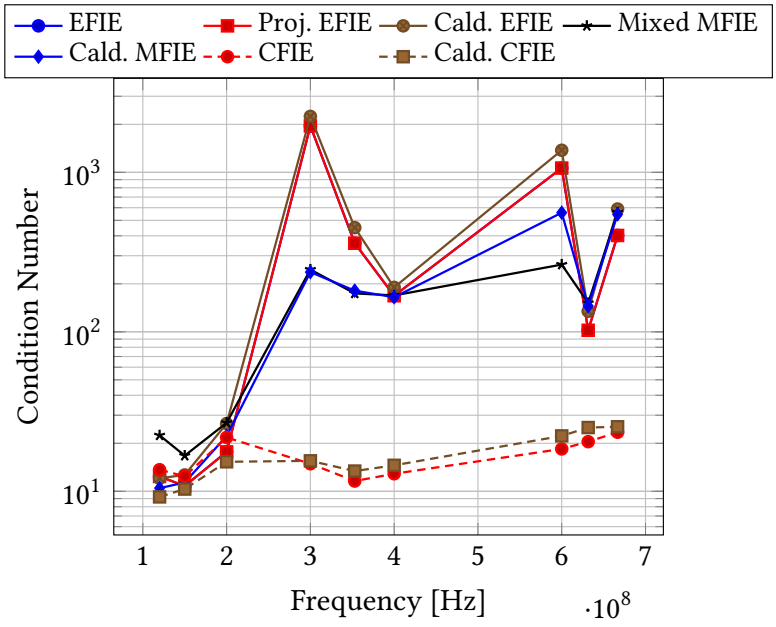

FIGURE 0.6. : Illustration de la résilience de la nouvelle CFIE aux résonances.

FIGURE 0.7. : Illustration d'un *pipeline* d'ICM augmenté par imagerie cérébrale.

Dans le Chapitre 6 une nouvelle approche permettant d'améliorer considérablement la précision des ICMs en utilisant des techniques d'imagerie cérébrale à haute résolution est présentée (Figure 0.7). Cette approche est permise par le développement du premier logiciel libre de simulation de données ICM, qui permet d'obtenir un cadre de test robuste des nouveaux algorithmes proposés. En particulier l'utilisation de données ICM simulées permet de se passer dans un premier temps de la génération d'un jeu de données issus de sujets humains. Un autre avantage crucial de cette approche est qu'elle permet de contrôler complètement le signal observé, ce qui permet de comprendre en profondeur les avantages et les points faibles de chacune des techniques employées. Ce travail sera dans un future proche l'élément fondateur d'un axe de recherche sur le développement de nouveaux types d'ICM capables d'exploiter au maximum les données issues de l'imagerie cérébrale haute résolution.

Ce manuscrit se termine dans le Chapitre 7 sur une réflexion du travail accompli durant cette thèse et propose de futurs axes de recherche dans leurs continuation.

Chapter 1

Introduction

Thanks to their numerous advantages, boundary integral formulations are widely used for solving predictive electromagnetic forward problems. In particular, they yield reduced-size interaction matrices because only the surfaces of the scatterer are discretized, as opposed to the full volume discretization of differential methods (e.g. the finite element method (FEM)). In addition, these techniques offer a generally high precision due to their resilience to numerical dispersion. Among the numerous integral formulations that have been proposed in the literature the electric field integral equation (EFIE) has seen widespread usage in applications ranging from electromagnetic compatibility to radio-frequency simulations thanks to its versatility. It suffers, however, from issues reducing its stability at both ends of the spectrum. At low frequency it becomes extremely ill-conditioned and its solutions undergo numerical cancellations. At high frequency, when the density of the discretization increases, its conditioning grows quadratically. The conditioning breakdowns are problematic because they reduce the performance of iterative solvers and thus jeopardize the linear in complexity resolution that can be attained with fast algorithms such as the Multilevel Fast Multipole Method (MLFMM). Another source of ill-conditioning of the electric equation are the artificial resonances which cause it to become periodically ill-conditioned. This last problem is usually addressed by linearly combining the EFIE with the magnetic field integral equation (MFIE) in order to form the resonance free combined field integral equation (CFIE). However, while the magnetic equation does not suffer from dense discretization issues, it exhibits its own numerical instabilities at low frequency in addition to being applicable only to closed structures. In this thesis, after reviewing the relevant electromagnetic (EM) background in Chapter 2, solutions to some of the aforementioned issues are introduced (or pre-existing solutions extended) to stabilize these equations and obtain solvers capable of reliably handling a wide range of scenarios.

The low frequency issues plaguing the EFIE have recently been addressed by introducing the quasi-Helmholtz (qH) projectors that allow for a computationally efficient loop star decomposition and hence can be used to cure to the root cause

of the so-called low frequency breakdown. In Chapter 3 the qH projectors are extended to higher order modeling. Because higher order techniques enable better discretization of the geometry and introduce electrically large basis function, they offer significantly higher convergence rates than standard modeling. Extending the projectors to this family of schemes will open up the development of extremely stable, accurate and fast solvers.

The simulation of wire-like structures (or structures made of a combination of wires and surfaces) is often performed using the wire EFIE which takes advantage of the fact that, if the radius of the wires is small enough with regards to the wavelength, it is possible to modelize the structure with one dimensional basis functions, thus considerably reducing the dimensionality of the problem. The efficiency of this reduced problem is however compromised by both low frequency and dense discretization breakdowns. The underlying causes of this low frequency breakdown are similar to these of the surface EFIE hence a cure based on a one-dimensional extension of the qH projectors is presented in Chapter 4, along with a refinement regularization. Differently from the surface formulation, however, the dense discretization breakdown is not addressed with Calderón-like techniques but with wavelet preconditioning (b-spline wavelets). The careful combination of these techniques yields a stable formulation that is proved to be immune from both breakdowns in a canonical case, through a detailed spectral analysis of the wire electric field integral operators (sEFIOs).

Thanks to its resilience to artificial resonances, the CFIE is a staple formulation in the integral equation community. However, while the low and high frequency limitations of the surface EFIE have been recently addressed, the low frequency issues of the MFIE are still salient and adversely impact the precision of the combined equation. Even though the numerical instabilities of the magnetic equation are radically different than these of the EFIE, they can be addressed by using the qH projectors on a newly introduced, symmetrized magnetic equation. Once stabilized, this new equation is combined, in Chapter 5, with the corresponding EFIE in order to form a new and highly stable combined field equation that is proved to be immune to spurious resonances.

Finally, a line of investigations dedicated to the enhancement of Brain Computer Interfaces (sBCIs) through high precision anatomical modeling based on integral equations has been opened. It focusses mainly on the challenges of the inverse problem in EM and, in particular, on improving the reconstruction of the brain activity from the electroencephalogram (EEG) signals. Despite still being in its early stages, this work, detailed in Chapter 6, has already produced one of the first peer-reviewed framework for fully simulated BCI experiments which is expected to help improve the pace of innovation in this field by reducing the cost in both

time and finances induced by human experiments.

This dissertation closes in Chapter 7 with a reflection on the work achieved and more importantly on how these contributions can be extended in the future.

Chapter 2

Background on Electromagnetic Scattering

Maxwell's equations are the four fundamental equations governing the behaviour of electromagnetic waves and hence will serve as the starting point of this dissertation. In this chapter the formulations and operators that will be used throughout this thesis are derived starting from these relations. The background material presented in the following sections includes considerations for both high – non-zero – frequency and statics and on the solutions of the corresponding Helmholtz's and Poisson's equations.

Maxwell's and Helmholtz's equations are recalled in Sections 2.a and 2.b and used to derive relations for the fields generated by free current distributions in Section 2.c. These expressions are then extended to the case of scattering by perfectly electrically conducting (PEC) objects in Section 2.e using the EM boundary condition introduced in Section 2.d. Techniques for numerical solution of the newly introduced EM problems are then presented in Sections 2.f and 2.g. Finally, the EEG forward problem is introduced in Section 2.i using the static formulation of Maxwell's equations introduced in Section 2.h.

Because this thesis focuses on time-harmonic fields, the time-dependency $e^{j\omega t}$ will be omitted throughout its developments.

a) Maxwell's Equations

In a homogeneous dielectric region of space the equations governing the behaviour of the electric field $\boldsymbol{e}$ and of the magnetic field $\boldsymbol{h}$ are, in the frequency domain,

$$\nabla \times \boldsymbol{e} = -\boldsymbol{m} - j\omega\mu\boldsymbol{h}\,, \tag{2.1a}$$

$$\nabla \times \boldsymbol{h} = \boldsymbol{j} + j\omega\epsilon\boldsymbol{e}\,, \tag{2.1b}$$

$$\nabla \cdot \boldsymbol{d} = \rho_e\,, \tag{2.1c}$$

$$\nabla \cdot \boldsymbol{b} = \rho_m\,, \tag{2.1d}$$

where ω is the angular frequency, $\boldsymbol{d} = \epsilon \boldsymbol{e}$, $\boldsymbol{b} = \mu \boldsymbol{h}$, $\boldsymbol{j}$ and $\boldsymbol{m}$ are electric and magnetic current densities, and ρ_e and ρ_m are electric and magnetic charge densities; $\boldsymbol{m}$ and ρ_m are not physical quantities and are introduced for simplifying further developments.

b) Helmholtz's Equation

To solve general scattering problems the solution of the inhomogeneous scalar Helmholtz equation is required. Given a wavenumber k and a function $f : \mathbb{R}^3 \mapsto \mathbb{C}$ with compact support, the equation can be written

$$\nabla^2 A(\boldsymbol{r}) + k^2 A(\boldsymbol{r}) = -f(\boldsymbol{r}), \quad \boldsymbol{r} \in \mathbb{R}^3. \tag{2.2}$$

Unicity of its solution requires a physically meaningful boundary condition to be enforced. In the case of electromagnetic fields this boundary condition is the Sommerfeld radiation condition, which states that the energy radiated by the solution must disperse at infinity, i.e. if A is a solution of eq. (2.2), then

$$\lim_{\|\boldsymbol{r}\| \to \infty} \|\boldsymbol{r}\| \left(\frac{\partial}{\partial \|\boldsymbol{r}\|} + \mathrm{j}k \right) A(\boldsymbol{r}) = 0, \tag{2.3}$$

uniformly in all directions $\hat{\boldsymbol{r}} = \boldsymbol{r}/\|\boldsymbol{r}\|$.

Under the Sommerfeld radiation condition, the solution of eq. (2.2) is the convolution of the right hand side (RHS) with the 3-dimensional free-space Green's function G

$$\big(G * f\big)(\boldsymbol{r}) = \int_{\mathbb{R}^3} G(\boldsymbol{r} - \boldsymbol{r}') f(\boldsymbol{r}') \mathrm{d}\boldsymbol{r}', \tag{2.4}$$

and the Green's function is the solution of the inhomogeneous scalar Helmholtz equation with the Dirac delta function as RHS

$$\nabla^2 G(\boldsymbol{r}) + k^2 G(\boldsymbol{r}) = -\delta(\boldsymbol{r}), \quad \boldsymbol{r} \in \mathbb{R}^3, \tag{2.5}$$

which in $\mathbb{R}^3$ is

$$G(\boldsymbol{r}) = \frac{\mathrm{e}^{-\mathrm{j}k\|\boldsymbol{r}\|}}{4\pi\|\boldsymbol{r}\|}, \quad \boldsymbol{r} \in \mathbb{R}^3. \tag{2.6}$$

c) Fields Currents Distributions

Maxwell's equations can be used to model electromagnetic fields generated by current distributions living in free space. In this section the expressions of these fields are presented using two different approaches. This canonical case will serve as foundation for scattering problems introduced later on.

α) Expression of the Fields

The expression of the electric field $\boldsymbol{e}$ as a function of the electric and magnetic currents can be obtained by applying the curl operator to eq. (2.1a) before substituting eq. (2.1b) into the resulting equation, yielding

$$\nabla \times \nabla \times \boldsymbol{e} - k^2 \boldsymbol{e} = -\nabla \times \boldsymbol{m} - \mathrm{j}\omega\mu \boldsymbol{j}\,, \tag{2.7}$$

with $k = \omega\sqrt{\mu\epsilon}$. Leveraging on the vector identity

$$\nabla \times \nabla \times \boldsymbol{A} = \nabla(\nabla \cdot \boldsymbol{A}) - \nabla^2 \boldsymbol{A}\,, \tag{2.8}$$

and using eq. (2.1c), eq. (2.7) can be re-written as

$$\nabla^2 \boldsymbol{e} + k^2 \boldsymbol{e} = \nabla \times \boldsymbol{m} + \mathrm{j}\omega\mu \boldsymbol{j} + \frac{\nabla \rho_e}{\epsilon}\,. \tag{2.9}$$

An expression for $\nabla \cdot \boldsymbol{e}$ is derived by applying the divergence operator to eq. (2.1b) and noting that $\nabla \cdot (\nabla \times \boldsymbol{A}) = \boldsymbol{0}$,

$$\nabla^2 \boldsymbol{e} + k^2 \boldsymbol{e} = \nabla \times \boldsymbol{m} + \mathrm{j}\omega\mu \boldsymbol{j} - \frac{1}{\mathrm{j}\omega\epsilon}\nabla\big(\nabla \cdot \boldsymbol{j}\big)\,. \tag{2.10}$$

Equation (2.10) is actually an Helmholtz's equation with the electric field, which must satisfy the Sommerfeld boundary condition, as unknown. Therefore an expression for $\boldsymbol{e}$ can be immediately derived using the results from Section 2.b,

$$\boldsymbol{e}(\boldsymbol{r}) = -\mathrm{j}\omega\mu \int_{\mathbb{R}^3} G\big(\boldsymbol{r} - \boldsymbol{r}'\big)\left[1 + \frac{1}{k^2}\nabla'\nabla'\cdot\right]\boldsymbol{j}\big(\boldsymbol{r}'\big)\mathrm{d}\boldsymbol{r}' - \int_{\mathbb{R}^3} G\big(\boldsymbol{r} - \boldsymbol{r}'\big)\nabla' \times \boldsymbol{m}\big(\boldsymbol{r}'\big)\mathrm{d}\boldsymbol{r}'\,. \tag{2.11}$$

This equation can be used to obtain an expression of the electric field generated by arbitrary electric and magnetic current densities anywhere in space. A similar approach will deliver the magnetic counterpart of eq. (2.11)

$$\boldsymbol{h}(\boldsymbol{r}) = -\mathrm{j}\omega\epsilon \int_{\mathbb{R}^3} G\big(\boldsymbol{r} - \boldsymbol{r}'\big)\left[1 + \frac{1}{k^2}\nabla'\nabla'\cdot\right]\boldsymbol{m}\big(\boldsymbol{r}'\big)\mathrm{d}\boldsymbol{r}' + \int_{\mathbb{R}^3} G\big(\boldsymbol{r} - \boldsymbol{r}'\big)\nabla' \times \boldsymbol{j}\big(\boldsymbol{r}'\big)\mathrm{d}\boldsymbol{r}'\,. \tag{2.12}$$

β) Potentials

Another method to derive the expression of the electric field relies on the explicit definition of a vector and scalar potentials. Even though this approach yields

results equivalent to these of the previous section, the potentials are useful for some theoretical considerations. Their definitions will be recalled without going through their whole derivations.

In the absence of magnetic charges $\nabla \cdot \boldsymbol{B} = \boldsymbol{0}$ which implies that there exists a magnetic vector potential $\boldsymbol{A}$ such that

$$\boldsymbol{h} = \frac{1}{\mu} \nabla \times \boldsymbol{A} \,. \tag{2.13}$$

Using Maxwell's equations an electric scalar potential Φ_e

$$\boldsymbol{e} = -\mathrm{j}\omega \boldsymbol{A} - \nabla \Phi_e \,. \tag{2.14}$$

can also be constructed. Considering that only curl of $\boldsymbol{A}$ has been fixed so far, its divergence can be freely chosen. The usual choice is the so-called Lorentz gauge

$$\nabla \cdot \boldsymbol{A} = -\mathrm{j}\omega\mu\epsilon\Phi_e \,, \tag{2.15}$$

which effectively cancels out one of the potentials. After simple derivations $\boldsymbol{A}$ can be shown to be solution of the inhomogeneous vector Helmholtz equation

$$\nabla^2 \boldsymbol{A} + k^2 \boldsymbol{A} = -\mu \boldsymbol{j} \,, \tag{2.16}$$

thus it can be expressed as

$$\boldsymbol{A}(\boldsymbol{r}) = \mu \int_{\mathbb{R}^3} \boldsymbol{j}\big(\boldsymbol{r}'\big) G\big(\boldsymbol{r} - \boldsymbol{r}'\big) \mathrm{d}\boldsymbol{r}' \,, \tag{2.17}$$

and, finally,

$$\boldsymbol{e}(\boldsymbol{r}) = -\mathrm{j}\omega \left[1 + \frac{1}{k^2} \nabla\nabla\cdot \right] \boldsymbol{A}(\boldsymbol{r}) \,. \tag{2.18}$$

Similar considerations in the presence of magnetic charges will yield the expressions for the electric vector potential $\boldsymbol{F}$ and the magnetic scalar potential Φ_m

$$\boldsymbol{F}(\boldsymbol{r}) = \epsilon \int_{\mathbb{R}^3} \boldsymbol{m}(\boldsymbol{r}') G\big(\boldsymbol{r} - \boldsymbol{r}'\big) \mathrm{d}\boldsymbol{r}' \,, \tag{2.19}$$

$$\Phi_m = -\frac{1}{\mathrm{j}\omega\mu\epsilon} \nabla \cdot \boldsymbol{F} \,, \tag{2.20}$$

which can be used to express the magnetic field as

$$\boldsymbol{h}(\boldsymbol{r}) = -\mathrm{j}\omega [1 + \frac{1}{k^2} \nabla\nabla\cdot] \boldsymbol{F}(\boldsymbol{r}) \,. \tag{2.21}$$

Finally, the fields generated by arbitrary electromagnetic current distributions can be obtained by superposition, i.e. by summing the contributions of the electric and magnetic densities

$$\boldsymbol{e}(\boldsymbol{r}) = -\mathrm{j}\omega\left[1 + \frac{1}{k^2}\nabla\nabla\cdot\right]\boldsymbol{A}(\boldsymbol{r}) - \frac{1}{\epsilon}\nabla\times\boldsymbol{F}(\boldsymbol{r})\,, \tag{2.22}$$

$$\boldsymbol{h}(\boldsymbol{r}) = -\mathrm{j}\omega\left[1 + \frac{1}{k^2}\nabla\nabla\cdot\right]\boldsymbol{F}(\boldsymbol{r}) + \frac{1}{\mu}\nabla\times\boldsymbol{A}(\boldsymbol{r})\,. \tag{2.23}$$

The careful reader will have noticed that 2.22 and 2.11 are different since the differential operators do not act on the same variables. Their equivalence can be demonstrated through simple but cumbersome derivations that can be found in [Jin15].

γ) Far Field Approximation

While the previous expressions are valid anywhere in space, it is sufficient for numerous applications to study the behaviour of the electromagnetic fields far from the sources. In this case the distance between the sources and the observation point can be approximated as $\|\boldsymbol{r} - \boldsymbol{r}'\| \approx \|\boldsymbol{r}\|$, when the term is used as an amplitude scaling; when it is used as a phase term – i.e. in the exponential of the Green's function – the more subtle approximation

$$\|\boldsymbol{r} - \boldsymbol{r}'\| \approx \|\boldsymbol{r}\| - \hat{\boldsymbol{r}}\cdot\boldsymbol{r}'\,, \tag{2.24}$$

should be used. This last approximation is derived by expanding $\|\boldsymbol{r} - \boldsymbol{r}'\|$ into its inner product definition and neglecting $\boldsymbol{r}'\cdot\boldsymbol{r}'$ with regards to $\boldsymbol{r}\cdot\boldsymbol{r}$. Furthermore, the derivatives in eqs. (2.22) and (2.23) contribute terms negligible in front of $\|\boldsymbol{r} - \boldsymbol{r}'\|^{-1}$, thus

$$\boldsymbol{e}(\boldsymbol{r}) \approx -\mathrm{j}\omega\boldsymbol{A}(\boldsymbol{r}) - \frac{1}{\epsilon}\nabla\times\boldsymbol{F}(\boldsymbol{r})\,, \tag{2.25}$$

$$\boldsymbol{h}(\boldsymbol{r}) \approx -\mathrm{j}\omega\boldsymbol{F}(\boldsymbol{r}) + \frac{1}{\mu}\nabla\times\boldsymbol{A}(\boldsymbol{r})\,. \tag{2.26}$$

After introducing the notations

$$\boldsymbol{N}(\boldsymbol{r}) = \int_{\mathbb{R}^3}\boldsymbol{j}\left(\boldsymbol{r}'\right)\mathrm{e}^{\mathrm{j}k\boldsymbol{r}'\cdot\hat{\boldsymbol{r}}}\mathrm{d}\boldsymbol{r}'\,, \tag{2.27}$$

$$\boldsymbol{L}(\boldsymbol{r}) = \int_{\mathbb{R}^3}\boldsymbol{m}\left(\boldsymbol{r}'\right)\mathrm{e}^{\mathrm{j}k\boldsymbol{r}'\cdot\hat{\boldsymbol{r}}}\mathrm{d}\boldsymbol{r}'\,, \tag{2.28}$$

the potentials can be written in the far field region

$$\boldsymbol{A}(\boldsymbol{r}) \approx \frac{\mu}{4\pi\|\boldsymbol{r}\|}\mathrm{e}^{-\mathrm{j}k\|\boldsymbol{r}\|}\boldsymbol{N}(\boldsymbol{r})\,, \tag{2.29}$$

$$\boldsymbol{F}(\boldsymbol{r}) \approx \frac{\epsilon}{4\pi\|\boldsymbol{r}\|}\mathrm{e}^{-\mathrm{j}k\|\boldsymbol{r}\|}\boldsymbol{L}(\boldsymbol{r})\,, \tag{2.30}$$

because

$$\frac{\mathrm{e}^{-\mathrm{j}k\|\boldsymbol{r}-\boldsymbol{r}'\|}}{4\pi\|\boldsymbol{r}-\boldsymbol{r}'\|} \approx \frac{\mathrm{e}^{-\mathrm{j}k\|\boldsymbol{r}\|}}{4\pi\|\boldsymbol{r}\|}\mathrm{e}^{\mathrm{j}k\boldsymbol{r}'\cdot\hat{\boldsymbol{r}}}\,. \tag{2.31}$$

Before obtaining the final expressions, it should be demonstrated that the radial components of the potentials are negligible with regards to the azimuthal and polar components. This can be demonstrated by properties of the integration in spherical coordinates, but for the sake of brevity this will not be detailed here; details can be found in [Bal12]. Finally, the complete expressions of the far fields, after all simplifications have been carried out, are

$$\boldsymbol{e}(\boldsymbol{r}) \approx -\frac{\mathrm{j}k}{4\pi\|\boldsymbol{r}\|}\mathrm{e}^{-\mathrm{j}k\|\boldsymbol{r}\|}\left[\hat{\boldsymbol{\theta}}\big(\boldsymbol{L}_{\phi}(\boldsymbol{r}) + \eta\boldsymbol{N}_{\theta}(\boldsymbol{r})\big) - \hat{\boldsymbol{\phi}}\big(\boldsymbol{L}_{\theta}(\boldsymbol{r}) - \eta\boldsymbol{N}_{\phi}(\boldsymbol{r})\big)\right], \tag{2.32}$$

$$\boldsymbol{h}(\boldsymbol{r}) \approx -\frac{\mathrm{j}k}{4\pi\eta\|\boldsymbol{r}\|}\mathrm{e}^{-\mathrm{j}k\|\boldsymbol{r}\|}\left[\hat{\boldsymbol{\theta}}\big(\boldsymbol{L}_{\theta}(\boldsymbol{r}) - \eta\boldsymbol{N}_{\phi}(\boldsymbol{r})\big) + \hat{\boldsymbol{\phi}}\big(\boldsymbol{L}_{\phi}(\boldsymbol{r}) + \eta\boldsymbol{N}_{\theta}(\boldsymbol{r})\big)\right]. \tag{2.33}$$

δ) Radar Cross-Section

When studying radiation patterns the radar cross-section (RCS) is often preferred to the raw far fields. The RCS σ of a scatterer is defined as

$$\sigma(\boldsymbol{r}) = \lim_{\|\boldsymbol{r}\|\to\infty} 4\pi\|\boldsymbol{r}\|^2 \frac{\|\boldsymbol{e}^s(\boldsymbol{r})\|^2}{\|\boldsymbol{e}^i(\boldsymbol{r})\|^2}\,, \tag{2.34}$$

where $\boldsymbol{e}^s$ is the far field scattered by the object and $\boldsymbol{e}^i$ is the incident field. Note that the RCS only depends on the angle of observation of the object and not on the distance.

d) Boundary Conditions

To solve problems of scattering by arbitrary objects it is necessary to establish the behaviours of the electromagnetic fields at their boundaries. In a region of space Ω

with a smooth boundary Γ characterized by its outgoing unit surface normal vector $\hat{\boldsymbol{n}}$, the fields must satisfy the following properties near Γ

$$\hat{\boldsymbol{n}} \times \left(\boldsymbol{e}^{+} - \boldsymbol{e}^{-}\right) = -\boldsymbol{m}_{\Gamma}\,, \tag{2.35a}$$
$$\hat{\boldsymbol{n}} \times \left(\boldsymbol{h}^{+} - \boldsymbol{h}^{-}\right) = \boldsymbol{j}_{\Gamma}\,, \tag{2.35b}$$
$$\hat{\boldsymbol{n}} \cdot \left(\boldsymbol{d}^{+} - \boldsymbol{d}^{-}\right) = \rho_{e,\Gamma}\,, \tag{2.35c}$$
$$\hat{\boldsymbol{n}} \cdot \left(\boldsymbol{b}^{+} - \boldsymbol{b}^{-}\right) = \rho_{m,\Gamma}\,, \tag{2.35d}$$

where the $\pm$ superscript indicates quantities at the inner and outer boundaries and the $_{\Gamma}$ subscript indicates surface quantities. More formally,

$$\{\boldsymbol{e}, \boldsymbol{h}\}^{+}(\boldsymbol{r}) = \lim_{\boldsymbol{r} \to \boldsymbol{r}'} \{\boldsymbol{e}, \boldsymbol{h}\}(\boldsymbol{r})\,, \quad \boldsymbol{r} \in \mathbb{R}^3 \setminus \Omega\,, \tag{2.36}$$
$$\{\boldsymbol{e}, \boldsymbol{h}\}^{-}(\boldsymbol{r}) = \lim_{\boldsymbol{r} \to \boldsymbol{r}'} \{\boldsymbol{e}, \boldsymbol{h}\}(\boldsymbol{r})\,, \quad \boldsymbol{r} \in \Omega\,. \tag{2.37}$$

A case of particular interest for the developments of this thesis is that of PEC objects, for which the boundary conditions simplify as

$$\hat{\boldsymbol{n}} \times \left(\boldsymbol{e}^{+} - \boldsymbol{e}^{-}\right) = \boldsymbol{0}\,, \tag{2.38a}$$
$$\hat{\boldsymbol{n}} \times \left(\boldsymbol{h}^{+} - \boldsymbol{h}^{-}\right) = \boldsymbol{j}_{\Gamma}\,, \tag{2.38b}$$
$$\hat{\boldsymbol{n}} \cdot \left(\boldsymbol{d}^{+} - \boldsymbol{d}^{-}\right) = \rho_{e,\Gamma}\,, \tag{2.38c}$$
$$\hat{\boldsymbol{n}} \cdot \left(\boldsymbol{b}^{+} - \boldsymbol{b}^{-}\right) = 0\,. \tag{2.38d}$$

e) Equivalence Principle

Another crucial element for solving scattering problems involving arbitrarily shaped objects is the equivalence principle which states that any distribution of electromagnetic sources enclosed within a surface Γ radiating fields $(\boldsymbol{e},\ \boldsymbol{h})$ can be replaced by surface current densities $\left(\boldsymbol{j}_{\Gamma}, \boldsymbol{m}_{\Gamma}\right)$ on Γ that will radiate the same fields outside of the surface. If current densities are properly chosen, the fields inside Γ can be replaced by any fields $\left(\boldsymbol{e}',\ \boldsymbol{h}'\right)$ satisfying Maxwell's equations without perturbing the outside fields. The choice of current densities is imposed by the boundary conditions eq. (2.35) and are

$$\boldsymbol{j}_{\Gamma} = \hat{\boldsymbol{n}} \times \left(\boldsymbol{h} - \boldsymbol{h}'\right)\,, \tag{2.39}$$
$$\boldsymbol{m}_{\Gamma} = -\hat{\boldsymbol{n}} \times \left(\boldsymbol{e} - \boldsymbol{e}'\right)\,, \tag{2.40}$$

where $\hat{\boldsymbol{n}}$ is the outgoing normal unit vector of Γ. Since these current densities create a field identical to the original one on the outer surface, the uniqueness theorem dictates that the fields outside of Γ are indeed $(\boldsymbol{e},\ \boldsymbol{h})$.

In particular, since the fields inside the surface can be arbitrarily chosen, it is possible to set them to $\left(\boldsymbol{e}',\ \boldsymbol{h}'\right) = (\boldsymbol{0},\ \boldsymbol{0})$, so that the material enclosed by the surface can be set arbitrarily with no influence on the fields. This is particularly useful since the presence of the object was preventing usage of the relations in eqs. (2.11), (2.12), (2.22) and (2.23).

Before trying to obtain expressions for the total fields in the domain, some additional notations should be introduced. First, the distinction is made between the total fields that would be present in the absence of the scatterer and the fields created by the equivalent surface current densities on the boundary of the scatterer. The former are the incident fields $\left(\boldsymbol{e}^i, \boldsymbol{h}^i\right)$ and the later are the scattered fields $(\boldsymbol{e}^s, \boldsymbol{h}^s)$. It is clear that, because of superposition, $(\boldsymbol{e}, \boldsymbol{h}) = \left(\boldsymbol{e}^i, \boldsymbol{h}^i\right) + (\boldsymbol{e}^s, \boldsymbol{h}^s)$. To simplify the upcoming expressions the following operator notations are introduced for the electric and magnetic fields

$$(\mathcal{T}X)(\boldsymbol{r}) = (\mathcal{T}_s X)(\boldsymbol{r}) + \frac{1}{k^2}(\mathcal{T}_h X)(\boldsymbol{r}), \tag{2.41}$$

$$(\mathcal{T}_s X)(\boldsymbol{r}) = \oiint_{\Gamma} X\left(\boldsymbol{r}'\right) \frac{\mathrm{e}^{-\mathrm{j}k\|\boldsymbol{r}-\boldsymbol{r}'\|}}{4\pi\|\boldsymbol{r}-\boldsymbol{r}'\|}\mathrm{d}\boldsymbol{r}', \tag{2.42}$$

$$(\mathcal{T}_h X)(\boldsymbol{r}) = \nabla \oiint_{\Gamma} \nabla' \cdot X\left(\boldsymbol{r}'\right) \frac{\mathrm{e}^{-\mathrm{j}k\|\boldsymbol{r}-\boldsymbol{r}'\|}}{4\pi\|\boldsymbol{r}-\boldsymbol{r}'\|}\mathrm{d}\boldsymbol{r}', \tag{2.43}$$

$$(\mathcal{K}X)(\boldsymbol{r}) = \oiint_{\Gamma} \frac{\mathrm{e}^{-\mathrm{j}k\|\boldsymbol{r}-\boldsymbol{r}'\|}}{4\pi\|\boldsymbol{r}-\boldsymbol{r}'\|} \times \nabla' X\left(\boldsymbol{r}'\right)\mathrm{d}\boldsymbol{r}'. \tag{2.44}$$

Using the new notations in combination with the equivalence principle yields, in the exterior region,

$$\boldsymbol{m}_{\Gamma}^{+} = -\hat{\boldsymbol{n}} \times \boldsymbol{e} = -\hat{\boldsymbol{n}} \times \left(\boldsymbol{e}^i + \boldsymbol{e}^s\right), \tag{2.45}$$

$$\boldsymbol{j}_{\Gamma}^{+} = \hat{\boldsymbol{n}} \times \boldsymbol{h} = \hat{\boldsymbol{n}} \times \left(\boldsymbol{h}^i + \boldsymbol{h}^s\right). \tag{2.46}$$

These expressions are then combined with eqs. (2.11) and (2.12)

$$\boldsymbol{m}_{\Gamma}^{+}(\boldsymbol{r}) + \hat{\boldsymbol{n}} \times \left(-\mathrm{j}k^{+}\eta^{+}\left(\mathcal{T}\boldsymbol{j}_{\Gamma}^{+}\right)(\boldsymbol{r}) - \left(\mathcal{K}\boldsymbol{m}_{\Gamma}^{+}\right)(\boldsymbol{r})\right) = -\hat{\boldsymbol{n}} \times \boldsymbol{e}^i(\boldsymbol{r}), \tag{2.47}$$

$$\boldsymbol{j}_{\Gamma}^{+}(\boldsymbol{r}) - \hat{\boldsymbol{n}} \times \left(-\frac{\mathrm{j}k^{+}}{\eta^{+}}\left(\mathcal{T}\boldsymbol{m}_{\Gamma}^{+}\right)(\boldsymbol{r}) + \left(\mathcal{K}\boldsymbol{j}_{\Gamma}^{+}\right)(\boldsymbol{r})\right) = \hat{\boldsymbol{n}} \times \boldsymbol{h}^i(\boldsymbol{r}). \tag{2.48}$$

Equations (2.47) and (2.48) are however not valid on Γ itself because $\mathcal{K}$ has a non-zero Cauchy principal value when $\boldsymbol{r} \longrightarrow \boldsymbol{r}'$. This singularity requires a non-trivial treatment that can be found in [Jin15] or in most electromagnetic books; once it has been addressed the previous expressions become, on a closed and smooth surface,

$$\frac{1}{2}\boldsymbol{m}_\Gamma^+(\boldsymbol{r}) + \hat{\boldsymbol{n}} \times \left(-\mathrm{j}k^+\eta^+\left(\mathcal{T}\boldsymbol{j}_\Gamma^+\right)(\boldsymbol{r}) - \left(\mathcal{K}\boldsymbol{m}_\Gamma^+\right)(\boldsymbol{r})\right) = -\hat{\boldsymbol{n}} \times \boldsymbol{e}^i(\boldsymbol{r}), \quad \boldsymbol{r} \in \Gamma, \tag{2.49}$$

$$\frac{1}{2}\boldsymbol{j}_\Gamma^+(\boldsymbol{r}) - \hat{\boldsymbol{n}} \times \left(-\frac{\mathrm{j}k^+}{\eta^+}\left(\mathcal{T}\boldsymbol{m}_\Gamma^+\right)(\boldsymbol{r}) + \left(\mathcal{K}\boldsymbol{j}_\Gamma^+\right)(\boldsymbol{r})\right) = \hat{\boldsymbol{n}} \times \boldsymbol{h}^i(\boldsymbol{r}), \quad \boldsymbol{r} \in \Gamma, \tag{2.50}$$

if the surface is not infinitely thin.

The current densities on the interior boundary can be derived via similar considerations, with the difference that the incident fields are $\boldsymbol{0}$,

$$\frac{1}{2}\boldsymbol{m}_\Gamma^-(\boldsymbol{r}) - \hat{\boldsymbol{n}} \times \left(-\mathrm{j}k^-\eta^-\left(\mathcal{T}\boldsymbol{j}_\Gamma^-\right)(\boldsymbol{r}) - \left(\mathcal{K}\boldsymbol{m}_\Gamma^-\right)(\boldsymbol{r})\right) = \boldsymbol{0}, \quad \boldsymbol{r} \in \Gamma, \tag{2.51}$$

$$\frac{1}{2}\boldsymbol{j}_\Gamma^-(\boldsymbol{r}) + \hat{\boldsymbol{n}} \times \left(-\frac{\mathrm{j}k^-}{\eta^-}\left(\mathcal{T}\boldsymbol{m}_\Gamma^-\right)(\boldsymbol{r}) + \left(\mathcal{K}\boldsymbol{j}_\Gamma^-\right)(\boldsymbol{r})\right) = \boldsymbol{0}. \quad \boldsymbol{r} \in \Gamma. \tag{2.52}$$

In addition, Equations (2.49) to (2.52) can be reformulated in terms of tangential components on Γ by using the vector identity

$$\hat{\boldsymbol{n}} \times \hat{\boldsymbol{n}} \times \boldsymbol{X} = -[\boldsymbol{X}]_{\tan} \tag{2.53}$$

yielding,

$$\left[\mathrm{j}k^+\eta^+\left(\mathcal{T}\boldsymbol{j}_\Gamma^+\right)(\boldsymbol{r}) + \left(\mathcal{K}\boldsymbol{m}_\Gamma^+\right)(\boldsymbol{r})\right]_{\tan} + \frac{1}{2}\hat{\boldsymbol{n}} \times \boldsymbol{m}_\Gamma^+(\boldsymbol{r}) = \left[\boldsymbol{e}^i(\boldsymbol{r})\right]_{\tan}, \quad \boldsymbol{r} \in \Gamma, \tag{2.54}$$

$$\left[\frac{\mathrm{j}k^+}{\eta^+}\left(\mathcal{T}\boldsymbol{m}_\Gamma^+\right)(\boldsymbol{r}) - \left(\mathcal{K}\boldsymbol{j}_\Gamma^+\right)(\boldsymbol{r})\right]_{\tan} - \frac{1}{2}\hat{\boldsymbol{n}} \times \boldsymbol{j}_\Gamma^+(\boldsymbol{r}) = \left[\boldsymbol{h}^i(\boldsymbol{r})\right]_{\tan}, \quad \boldsymbol{r} \in \Gamma, \tag{2.55}$$

$$\left[\mathrm{j}k^-\eta^-\left(\mathcal{T}\boldsymbol{j}_\Gamma^-\right)(\boldsymbol{r}) + \left(\mathcal{K}\boldsymbol{m}_\Gamma^-\right)(\boldsymbol{r})\right]_{\tan} - \frac{1}{2}\hat{\boldsymbol{n}} \times \boldsymbol{m}_\Gamma^-(\boldsymbol{r}) = \boldsymbol{0}, \quad \boldsymbol{r} \in \Gamma, \tag{2.56}$$

$$\left[\frac{\mathrm{j}k^-}{\eta^-}\left(\mathcal{T}\boldsymbol{m}_\Gamma^-\right)(\boldsymbol{r}) - \left(\mathcal{K}\boldsymbol{j}_\Gamma^-\right)(\boldsymbol{r})\right]_{\tan} + \frac{1}{2}\hat{\boldsymbol{n}} \times \boldsymbol{j}_\Gamma^-(\boldsymbol{r}) = \boldsymbol{0}, \quad \boldsymbol{r} \in \Gamma. \tag{2.57}$$

Equations (2.54) to (2.57) can be used to determine the surface current densities when coupled with the proper boundary conditions, which can in turn be used to compute the total fields anywhere in space using eqs. (2.11) and (2.12). Equations (2.54) and (2.55) are respectively the EFIE and MFIE. These equations both suffer from the existence of non-physical resonances in their solutions, a problem that is traditionally alleviated by linearly combining them to form the CFIE

$$\alpha\mathrm{EFIE} + \eta(1-\alpha)\hat{\boldsymbol{n}} \times \mathrm{MFIE}, \tag{2.58}$$

where $\alpha \in]0\,,1[$ (0 and 1 are excluded because they degenerate to the original, resonating equations).

A case of particular interest is that of a PEC scatterer, in which case the above equations simplify because $\boldsymbol{m}_\Gamma = \mathbf{0}$.

f) Discretization

The different formulations derived so far can only yield analytic solutions for some simple, canonical cases (e.g. spheres). While these closed-form results will be useful for verifying the correctness of several schemes presented in this thesis, they are of little practical use for real case scattering scenarios. To characterize and predict the behaviour of electromagnetic fields when non-trivial structures are involved, numerical schemes must be employed.

The first step in the conception of a numerical method is the discretization of the problem. In this thesis only Petrov-Galerkin schemes are studied because they offer, under certain conditions [SS11], a guaranteed convergence to the exact solution. If applied to surface integral equations, these schemes form the boundary element methods (sBEMs) or methods of moments (sMoMs). In these approaches the unknown is first expanded with basis functions living in the correct space and capable of representing the properties of the unknown; the resulting set of equations is then tested with functions living in the dual of the range of the operator. The functions are defined on a small subset of elements of the tessellated scatter (in this thesis the tessellation is always made of tringles). Other approaches include Nyström [Ged03] or collocation methods.

The EFIE is commonly discretized with Rao-Wilton-Glisson (RWG) functions [RWG82], which live in $H^{-1/2}(\mathrm{div})$ – the correct functional space for the current density – and have a well defined divergence, i.e. they do not give rise to unphysical charges. An RWG function is defined on a pair of triangles $\left(c_n^+\,, c_n^+\right)$, sharing an inner edge $\boldsymbol{e}_n$ connecting vertices $\boldsymbol{v}_n^+$ and $\boldsymbol{v}_n^-$, as

$$\boldsymbol{f}_n(\boldsymbol{r}) = \begin{cases} \dfrac{\boldsymbol{r} - \boldsymbol{r}_n^+}{2A_{c_n^+}} & \text{for } \boldsymbol{r} \in c_n^+\,, \\ \dfrac{\boldsymbol{r}_n^- - \boldsymbol{r}}{2A_{c_n^-}} & \text{for } \boldsymbol{r} \in c_n^-\,, \\ \mathbf{0} & \text{otherwise,} \end{cases} \tag{2.59}$$

where the vertices $\boldsymbol{r}_n^+$ and $\boldsymbol{r}_n^-$ are the vertices of c_n^+ and c_n^- that do not belong to $\boldsymbol{e}_n$ and $A_{c_n^+}$ and $A_{c_n^-}$ are the respective areas of the cells (Figure 2.1). This definition does not

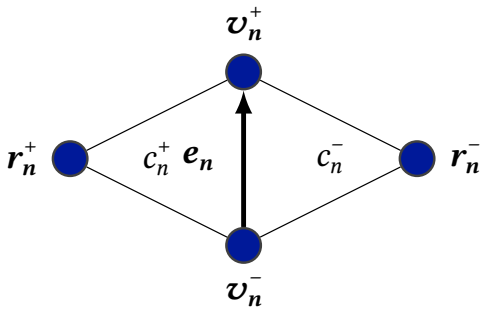

Fig. 2.1.: Illustration of an RWG basis function defined on the inner edge $\boldsymbol{e}_n$ between vertices $\boldsymbol{v}_n^+$ and $\boldsymbol{v}_n^-$, and connecting the cells c_n^+ and c_n^-, which are the two triangles attached to the defining edge and completed by the vertices $\boldsymbol{r}_n^+$ and $\boldsymbol{r}_n^-$, respectively.

include any normalization by the edge-length $\|\boldsymbol{e}_n\|$, which is used in some instances in the literature. The current is approximately expanded as a linear combination of N RWG basis functions $\{f_m\}$,

$$\boldsymbol{j}(\boldsymbol{r}) \approx \sum_{m=1}^{N} [\boldsymbol{j}]_m \boldsymbol{f}_m(\boldsymbol{r}), \tag{2.60}$$

where $[\boldsymbol{j}]_m = \langle f_m, \boldsymbol{j} \rangle$ and $\langle \boldsymbol{a}, \boldsymbol{b} \rangle = \iint \boldsymbol{a}(\boldsymbol{r}) \cdot \boldsymbol{b}(\boldsymbol{r}) \mathrm{d}\boldsymbol{r}$ denotes the duality product. In the case of a PEC scatterer Γ the EFIE is approximated as

$$\big(\mathcal{T}_s \boldsymbol{j}\big)(\boldsymbol{r}) \approx \sum_{m=1}^{N} [\boldsymbol{j}]_m \hat{\boldsymbol{n}} \times \iint_{\Gamma} \boldsymbol{f}_m(\boldsymbol{r}) \frac{\mathrm{e}^{-\mathrm{j}k\|\boldsymbol{r}-\boldsymbol{r}'\|}}{4\pi\|\boldsymbol{r}-\boldsymbol{r}'\|} \mathrm{d}\boldsymbol{r}', \tag{2.61}$$

$$\big(\mathcal{T}_h \boldsymbol{j}\big)(\boldsymbol{r}) \approx \sum_{m=1}^{N} [\boldsymbol{j}]_m \hat{\boldsymbol{n}} \times \nabla \iint_{\Gamma} \nabla' \cdot \boldsymbol{f}_n(\boldsymbol{r}) \frac{\mathrm{e}^{-\mathrm{j}k\|\boldsymbol{r}-\boldsymbol{r}'\|}}{4\pi\|\boldsymbol{r}-\boldsymbol{r}'\|} \mathrm{d}\boldsymbol{r}', \tag{2.62}$$

$$\big(\mathcal{T}_h \boldsymbol{j}\big)(\boldsymbol{r}) \approx \sum_{m=1}^{N} [\boldsymbol{j}]_m \left(-\mathrm{j}k\eta \big(\mathcal{T}_s \boldsymbol{f}_m\big)(\boldsymbol{r}) + \frac{\eta}{\mathrm{j}k} \big(\mathcal{T}_h \boldsymbol{f}_m\big)(\boldsymbol{r}) \right). \tag{2.63}$$

These equations are then tested with the functions $\{\hat{\boldsymbol{n}} \times \boldsymbol{f}_n\}$ in the dual of the range of the operators, giving rise to the matrix system

$$\boldsymbol{T}\boldsymbol{j} = -\mathrm{j}k\eta \boldsymbol{T}_s \boldsymbol{j} + \frac{\eta}{\mathrm{j}k} \boldsymbol{T}_h \boldsymbol{j} = \boldsymbol{v}_e, \tag{2.64}$$

where

$$[\boldsymbol{T}_s]_{mn} = \left\langle \hat{\boldsymbol{n}} \times \boldsymbol{f}_m \,, \mathcal{T}_s \boldsymbol{f}_n \right\rangle , \tag{2.65}$$

$$[\boldsymbol{T}_h]_{mn} = \left\langle \hat{\boldsymbol{n}} \times \boldsymbol{f}_m \,, \mathcal{T}_h \boldsymbol{f}_n \right\rangle , \tag{2.66}$$

$$[\boldsymbol{v}_e]_m = -\left\langle \hat{\boldsymbol{n}} \times \boldsymbol{f}_m \,, \boldsymbol{e}^i \right\rangle , \tag{2.67}$$

$$\boldsymbol{T} = -\mathrm{j}k\eta \boldsymbol{T}_s + \frac{\eta}{\mathrm{j}k} \boldsymbol{T}_h \,. \tag{2.68}$$

The system then be solved for $\boldsymbol{j}$ in order to obtain the coefficients of the current in the interpolatory basis. The radiated field is obtained by radiating this current using eqs. (2.11) and (2.12).

The MFIE can be discretized in a very similar fashion. However particular care should be given to the testing basis functions. This equation has traditionally been tested with standard RWG basis functions, but this discretization yields inaccurate results [Coo+11]. A new, conforming, discretization has been introduced more recently [Coo+11] in which rotated Buffa-Christiansen (BC) basis functions $\left\{ \tilde{\boldsymbol{f}}_m \right\}$, which live in the dual of the operator, are used for the testing. A formal definition of the BC functions can be found in [BC07]. The discretized MFIE is

$$\left(\frac{\boldsymbol{G}_{\tilde{f},f}}{2} + \boldsymbol{K} \right) \boldsymbol{j} = \boldsymbol{v}_h \,, \tag{2.69}$$

where

$$[\boldsymbol{G}]_{mn} = \left\langle \hat{\boldsymbol{n}} \times \tilde{\boldsymbol{f}}_m \,, \mathcal{I} \boldsymbol{f}_n \right\rangle , \tag{2.70}$$

$$[\boldsymbol{K}]_{mn} = \left\langle \hat{\boldsymbol{n}} \times \tilde{\boldsymbol{f}}_m \,, \mathcal{K} \boldsymbol{f}_n \right\rangle , \tag{2.71}$$

$$[\boldsymbol{v}_h]_m = \left\langle \hat{\boldsymbol{n}} \times \tilde{\boldsymbol{f}}_m \,, \boldsymbol{h}^i \right\rangle . \tag{2.72}$$

g) Iterative Methods and Conditioning

α) Iterative Methods

Because of its cubic complexity, direct resolution of linear problems is seldom applicable in any practical case. In electromagnetics, the linear problem

$$\boldsymbol{M}\boldsymbol{x} = \boldsymbol{b} \,, \tag{2.73}$$

is usually solved using iterative methods that have a more tractable, quadratic, complexity. As their name indicates, iterative methods attempt to approximate the

solution of the problem by iteratively minimizing a cost function. Every step usually involves matrix vector products which explains their complexity. This quadratic cost, however, only holds if the number of iterations required for converging to a predetermined error is somehow bounded (with regards to the number of unknowns). For instance the generalized minimal residual method (GMRES) method attempts to minimize the residual distance

$$\epsilon_n = \|\boldsymbol{M}\boldsymbol{x}_n - \boldsymbol{b}\|, \quad \boldsymbol{x}_n \in K_n, \tag{2.74}$$

where

$$K_n = \text{span}\left\{\boldsymbol{b}, \boldsymbol{M}\boldsymbol{b}, \dots, \boldsymbol{M}^{n-1}\boldsymbol{b}\right\}. \tag{2.75}$$

is the n-th Krylov subspace of the system. In the case of a symmetric positive definite (s.p.d) matrix, GMRES exhibits a convergence rate that is related to the conditioning of $\boldsymbol{M}$ (see Section 2.g.β)

$$\epsilon_n \leq \left(\frac{\text{cond}(\boldsymbol{M})^2 - 1}{\text{cond}(\boldsymbol{M})^2}\right)^{n/2} \epsilon_0 . \tag{2.76}$$

This results also implies that, if the condition number of $\boldsymbol{M}$ is constant with regards to the number of unknowns, then a solution of the problem can be obtained in quadratic complexity. In addition, if a fast matrix-vector product can be obtained, for instance using fast methods such as the MLFMM, the problem is effectively linearised.

β) Condition Number

The condition number of an invertible matrix $\boldsymbol{M}$ is defined as

$$\text{cond}(\boldsymbol{M}) = \|\boldsymbol{M}\|\|\boldsymbol{M}^{-1}\|. \tag{2.77}$$

In computational disciplines the conditioning plays a critical role because it affects the convergence rate of the iterative solvers and hence the complexity of solving the problem. And, as importantly, the condition number characterizes the numerical stability of the problem. Assuming that an error $\boldsymbol{e}$ is made in the estimation of $\boldsymbol{b}$ in eq. (2.73) – either purely numerical or experimental – then

$$\boldsymbol{x} = \boldsymbol{M}^{-1}\boldsymbol{b} + \boldsymbol{M}^{-1}\boldsymbol{e}, \tag{2.78}$$

and the relative error made on the solution is

$$\delta_{\boldsymbol{b},\boldsymbol{e}} = \frac{\|\boldsymbol{M}^{-1}\boldsymbol{e}\|}{\|\boldsymbol{M}^{-1}\boldsymbol{b}\|} \cdot \frac{\|\boldsymbol{b}\|}{\|\boldsymbol{e}\|}. \tag{2.79}$$

An upper bound δ on $\delta_{\boldsymbol{b},\boldsymbol{e}}$ can be found by considering the worst case scenario

$$\delta = \max_{\boldsymbol{b},\boldsymbol{e}} \delta_{\boldsymbol{b},\boldsymbol{e}} = \max_{\boldsymbol{e}} \frac{\|\boldsymbol{M}^{-1}\boldsymbol{e}\|}{\|\boldsymbol{e}\|} \cdot \max_{\boldsymbol{x}} \frac{\|\boldsymbol{M}\boldsymbol{x}\|}{\|\boldsymbol{x}\|} \tag{2.80}$$

and thus

$$\delta = \|\boldsymbol{M}\|\|\boldsymbol{M}^{-1}\| . \tag{2.81}$$

In conclusion, in order for the system to be resilient to numerical errors (e.g. floating point calculation round off) or even measurement noise, it must be well conditioned. Most of this thesis is dedicated to the pre-conditioning of EM problems to reduce their complexity and stabilize their numerical accuracy.

h) Maxwell's Equations in Statics

At low frequencies, when time derivatives can be neglected, Maxwell's equations decouple and new derivations are required. To detail some key passages of these new derivations, Maxwell's equations are re-stated with an explicit time dependency. One such – non-symmetrized – form is

$$\nabla \times \boldsymbol{e} = -\mu \frac{\partial \boldsymbol{h}}{\partial t} , \tag{2.82}$$

$$\nabla \times \boldsymbol{h} = \epsilon \frac{\partial \boldsymbol{e}}{\partial t} + \boldsymbol{j} , \tag{2.83}$$

$$\nabla \cdot \boldsymbol{d} = \rho_e , \tag{2.84}$$

$$\nabla \cdot \boldsymbol{b} = \boldsymbol{0} , \tag{2.85}$$

which, when the derivatives are negligible, implies the existence of a scalar potential V such that $\boldsymbol{e} = -\nabla V$. This result, in light of Ohm's law

$$\boldsymbol{j} = \sigma \boldsymbol{e} + \boldsymbol{j}_0 , \tag{2.86}$$

where σ is the conductivity of the medium and $\boldsymbol{j}_0$ is a constant initial contribution, implies, after few passages, that

$$\nabla \cdot (\sigma \nabla V) = \nabla \cdot \boldsymbol{j}_0 . \tag{2.87}$$

which is Poisson's equation. Because eq. (2.87) does not admit a unique solution, additional boundary conditions must be provided. To specify these conditions the trace operator that associates a function u defined on a compact domain Ω, with its generalized boundary function on $\partial\Omega$ is introduced

$$\gamma_0^{\pm} u = u_{|\Gamma^{\pm}} . \tag{2.88}$$

Similarly, the co-normal derivative is defined as

$$\gamma_1^{\pm} u = \hat{\boldsymbol{n}} \cdot \gamma_0^{\pm} \sigma^{\pm} \nabla u \,. \tag{2.89}$$

In the cases relevant to this thesis, the boundary conditions are

$$\gamma_0^{+} V = \gamma_0^{-} V \,, \tag{2.90}$$
$$\gamma_1^{+} V = \gamma_1^{-} V \,, \tag{2.91}$$

where $\hat{\boldsymbol{n}}$ is the outgoing normal of Γ. In physical terms, eq. (2.90) imposes continuity of the potential at the boundary, while eq. (2.91) imposes continuity of the normal component of the current. Finally, any solution should fulfil the Sommerfeld radiation conditions.

The solution of the Poisson's problem

$$-\nabla \cdot (\sigma \nabla V) = \delta_0 \tag{2.92}$$

in a homogeneous domain of unit conductivity is the static three dimensional Green's function

$$G_s(\boldsymbol{r}) = \frac{1}{4\pi \|\boldsymbol{r}\|} \,. \tag{2.93}$$

Following the same reasoning as for Helmholtz's equation it can be shown that the solutions of the problem

$$-\Delta V = f \tag{2.94}$$

are $V = -f * G_s$. This solution will be of particular importance in the derivation of the EEG forward problem.

i) EEG Forward Problem

α) Modeling of the Neurons

Because the physiological electric phenomenons occurring inside the brain typically have a maximum frequency of 1 kHz, the quasi-static approximations of Maxwell's equations can be used for predictive modeling [BML01]. In addition, the source of the electrical activity in the brain are the neurons which, conveniently, can be modeled as current dipoles [dMvDS88]. In algebraic form, the current distribution generated by a neuron located at $\boldsymbol{r}_0$ and of moment $\boldsymbol{q}$ is

$$\boldsymbol{j}(\boldsymbol{r}) = \boldsymbol{q}\delta(\boldsymbol{r} - \boldsymbol{r}_0) \,, \tag{2.95}$$

where δ denotes the Dirac delta function. The RHS of the corresponding Poisson's problem is

$$\nabla \cdot \boldsymbol{j}(\boldsymbol{r}) = \boldsymbol{q}\nabla\delta(\boldsymbol{r} - \boldsymbol{r}_0)\,. \tag{2.96}$$

Finally, in a homogeneous domain of unit conductivity, the dipole generates the potential

$$v_d = \frac{\boldsymbol{q}\cdot(\boldsymbol{r} - \boldsymbol{r}_0)}{4\pi\|\boldsymbol{r} - \boldsymbol{r}_0\|^3}\,. \tag{2.97}$$

β) Nested Domains

The BEM formulations of the EEG forward problem are not capable of handling fully anisotropic volumes (unlike FEM formulations). As a consequence the head is often modeled as being composed of three nested layers of uniform conductivities[1] – typically brain, skull and scalp – and Poisson's equation is solved in this multi-domain context, which requires additional developments.

The head is first decomposed into N bounded, nested domains Ω_i with uniform conductivity σ_i; the domain $\Omega_{N+1} = \mathbb{R}^3 \setminus \bigcup_{i=1}^{N} \Omega_i$ contains no sources. Then, if f is the RHS of the problem in $\mathbb{R}^3$, it can be decomposed into a sum of functions f_{Ω_i}, such that

$$f_{\Omega_i}(\boldsymbol{r}) = \begin{cases} f(\boldsymbol{r}) & \text{if } \boldsymbol{r} \in \Omega_i \\ 0 & \text{if } \boldsymbol{r} \notin \Omega_i\,. \end{cases} \tag{2.98}$$

The solutions of the sub-problems that satisfy the Sommerfeld radiation condition are $v_{\Omega_i} = -f_{\Omega_i} * G_s$, $i = 1 \dots N$. These local solutions are combined into a single function

$$v_d = \sum_{i=1}^{N} v_{\Omega_i}\,, \tag{2.99}$$

harmonic in Ω_{N+1}, that satisfies Poisson's equation. In addition, the function and its normal derivatives are continuous across the different domain boundaries. Using the representation theorem and Green's identities [Kyb+05], it follows that

$$v_d(\boldsymbol{r}) = \frac{\sigma_j + \sigma_{j+1}}{2} V(\boldsymbol{r}) - \sum_{i=1}^{N} (\sigma_{i+1} - \sigma_i)\big(\mathcal{D}\gamma_{0,i}V\big)(\boldsymbol{r})\,, \quad \boldsymbol{r} \in \Gamma_j\,, \tag{2.100}$$

1 This assumption has been disproved for the white matter [Wol+06], however standard BEM formulations are not capable of handling this anisotropy yet. New formulations addressing this limitation are being developed [Rah+17].

where $\mathcal{D}$ relates double layer potentials to their values on the domains' boundaries

$$(\mathcal{D}u)(\boldsymbol{r}) = \int_{\partial\Omega} \gamma_1' G_s\big(\boldsymbol{r} - \boldsymbol{r}'\big)\, u\big(\boldsymbol{r}'\big)\mathrm{d}\boldsymbol{r}' \,. \tag{2.101}$$

Other formulations are available for obtaining the surface potentials, however eq. (2.100) is the most straightforward and popular [BML01].

γ) Discretization

To solve the double layer formulation, the scalp, skull and cortex surfaces are tessellated into N_t^k triangles and N_v^k vertices and the unknown potential V in eq. (2.100) is expanded with pyramid basis function

$$V_k(\boldsymbol{r}) \approx \sum_{j=1}^{N_v} x_j^k \Psi_j(\boldsymbol{r}) \,, \quad \boldsymbol{r} \in \Gamma_k \,, \tag{2.102}$$

where the pyramids are defined to have unit value on their defining vertex and to linearly go to zero over the triangles sharing this vertex. The equation is then tested using the pyramids as testing functions, yielding a system of equation that can be numerically solved

$$\begin{bmatrix} \boldsymbol{G}_1 + \boldsymbol{D}_{1,1} & \boldsymbol{D}_{1,2} & \boldsymbol{D}_{1,3} \\ \boldsymbol{D}_{2,1} & \boldsymbol{G}_2 + \boldsymbol{D}_{2,2} & \boldsymbol{D}_{2,3} \\ \boldsymbol{D}_{3,1} & \boldsymbol{D}_{3,2} & \boldsymbol{G}_3 + \boldsymbol{D}_{3,3} \end{bmatrix} \begin{bmatrix} \boldsymbol{v}_1 \\ \boldsymbol{v}_2 \\ \boldsymbol{v}_3 \end{bmatrix} = \begin{bmatrix} \boldsymbol{b}_1 \\ \boldsymbol{b}_2 \\ \boldsymbol{b}_3 \end{bmatrix}, \tag{2.103}$$

where

$$[G_k]_{ij} = \frac{\sigma_k + \sigma_{k+1}}{2} \left\langle \Psi_i^k, \Psi_j^k \right\rangle , \tag{2.104}$$

$$[D_{kl}]_{ij} = (\sigma_{l+1} - \sigma_l) \left\langle \Psi_i^k, \mathcal{D}_{kl} \Psi_j^l \right\rangle , \tag{2.105}$$

$$[b_k]_i = \left\langle \Psi_i^k, v_d \right\rangle , \tag{2.106}$$

$$[x_k]_i = x_i^k \,. \tag{2.107}$$

A number of elementary results of EM theory have been presented in this introductory chapter. Most of the developments presented here will not be recalled in the next chapters but references will be made to the present section when necessary.

Chapter 3

High Order Quasi-Helmholtz Projectors

Boundary integral equations are particularly efficient for solving problems of scattering by conducting and penetrable objects. These methods stand out in terms of performance because they only require the surface of the scatterer to be discretized, as opposed to the full volume discretization of differential methods. However number of these formulations exhibit numerical instabilities at low frequency, a phenomenon designated as the low frequency breakdown in the literature. This chapter is devoted to presenting a recently introduced strategy based on quasi-Helmholtz projectors to cure the low frequency breakdown of the EFIE and extending it to higher order modeling. Because they preserve the convergence properties of the original formulations and do not necessitate the recovery of cycles of the structure – unlike several other solutions to the low frequency breakdown – projector approaches are well-suited for solving large problems at low frequencies. Hence the high order extension of the technique will enable the development of highly accurate formulations exhibiting higher order convergence rates.

a) Introduction

While the EFIE has several advantages over other formulations, such as being able to handle open structures (unlike the MFIE or the CFIE) and yielding smaller matrices than FEM techniques while automatically satisfying the radiation conditions, it suffers from ill-conditioning at low frequency [ATV10]. In addition, the formulation also suffers from ill-conditioning at high refinement [ATV10] but this problem is not detailed in the present chapter. Both ill-conditionings prevent numerical solvers from yielding accurate solutions or even prevent them from converging altogether. In addition, the EFIE suffers at low frequency from numerical cancellations in its solution vector [Yun+03; CTH08; QC10; Bog+11a; Bog+11b]. These cancellations are due to the different scaling

of the solenoidal and non-solenoidal parts of the solution. Because the former scales with the frequency while the latter scales with its inverse, the solenoidal contribution is cancelled out by the non-solenoidal one when computed – and stored together – in finite precision. Even though it might appear negligible, this loss of current information results in a severe degradation of the accuracy of the electrical charge and becomes even more critical when computing the scattered field. Indeed, for certain types of excitation the preserved and the cancelled out parts of the solution physically contribute with the same strength [And+13b] to the field. This means that a crucial part of the final result will have been lost and replaced by numerical noise. This phenomenon together with the low-frequency ill-conditioning, are indifferently referred to as the low-frequency breakdown of the EFIE.

Because these limitations are intrinsic to the operator itself, they are also present when higher order modeling is employed. This is particularity deplorable since higher order schemes offer significant improvements over traditional – low order – ones in terms of efficiency and flexibility. Thanks to their numerous advantages high order schemes are commonly used in a wide array of computational schemes [Not08]. Two of their most significant improvements with regards to low order techniques are (i) their more accurate discretizations – in less elements – of general geometries enabled by curved geometrical elements; (ii) their higher convergence rates permitted by the usage of electrically large basis functions (of the order of the wavelength). Overall these high order techniques are generally faster than the traditional ones. In particular the surface EFIE has been extended to higher orders using a wide array of techniques [Che+01; Not+01; DN03], a thorough review of which can be found in [Not08]. A particularly popular approach is to use higher order divergence conforming interpolatory basis functions such as the Graglia-Wilton-Peterson (GWP) functions [GP97] which are the higher order counterpart of the standard RWG functions [RWG82]. Other contributions have proposed high order hierarchical bases [Kol99] that allow for adaptive p-refinement of the mesh, however they are not as widely employed because of the conditioning issues they provoke. To address this issue, orthogonal high order hierarchical bases have been proposed more recently [DN03]. The community has also proposed numerous techniques permitting the integration of the singularity of the Green's function in the case of an higher order EFIE [JTY06]. In addition to its high order-related advantages, the high order EFIE still benefits from the properties of its standard counterpart. In particular it can be accelerated though the application of the MLFMM [Don+01].

The previous diagnostic should make it clear that one way of addressing the low-frequency breakdown is to separate and re-scale – in frequency – the solenoidal

and non-solenoidal parts of the solution. This approach has traditionally been implemented via Loop-Star (LS) decompositions in both low [WG81a; Vec99; ZC00; LLB03; Eib04] and high order [WW04]. However, LS decompositions have two major limitations : (i) they require the detection of the global loops of the structure [WG81a] which is an expensive – quadratic – operation and (ii) they increase the dense discretization ill-conditioning of the EFIE impedance matrix [Eib04]. The second issue is a consequence of the ill-conditioning of the LS decomposition operators that behave as graph Laplacians [And12; Sha+09]. These two problems render the LS techniques impractical for the simulation of large structures. Other formulations, immune to the low frequency breakdown, and that do not require detection of global loops, have been proposed [QC08b].

In this chapter a recently introduced family of solutions that rely on quasi-Helmholʒ (qH) projectors [And+13b] to perform the LS decomposition is presented and extended to high order. Relying on projectors has the advantage of not degrading the conditioning of the matrices they decompose because they have flat spectrum. An even more remarkable property is that, because the solenoidal projector deduced from its non-solenoidal counterpart, global loops do not have to be detected. While this chapter focusses on the EFIE, high order projectors can be used to stabilize numerous formulations, some of which are studied in this thesis.

To set the notations, this chapter opens with a summary of some key concepts of high order modeling in Section 3.b. In Section 3.c the standard LS matrices are defined before being used in Section 3.d to fully characterise the low-frequency breakdown phenomenon and the shortcomings of its standard remedies. These developments motivate the introduction of the qH projectors in Section 3.e and of their detailed analysis in Section 3.f. Strong of this knowledge, the projectors are extended to higher order in Section 3.g. The performances of the new projectors are illustrated in Section 3.i before introducing implementations details required to reproduce our results and obtain an optimal accuracy when using the schemes introduced throughout the chapter are presented in Section 3.h. Finally, the discussion is closed in Section 3.j. Most of the developments and illustrations of the low frequency breakdown throughout this chapter have been performed with order $p = 0$ discretization for practical reasons, but they extend directly to higher order, as will be made clear in Section 3.g.

b) High Order Modeling

Geometrical high order modeling relies on high order elements, which are more flexible than their order $p = 0$ counterparts. Most of the standard BEM elements

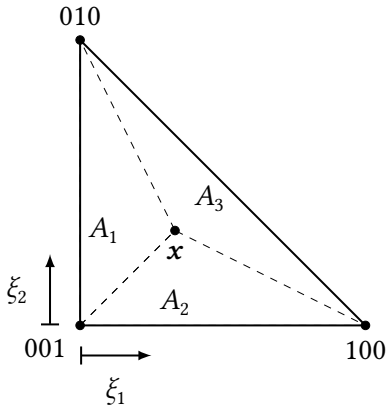

Fig. 3.1.: Illustration of the simplex coordinate system on the reference triangle. The ξ_i coordinates are defined as the ratio A_i/A where A is the area of the triangle, and A_i the area of the sub-triangles defined by $\boldsymbol{x}$.

(triangles and quadrilaterals for surface and tetrahedrons and hexahedrons for volume) have been extended to curvilinear geometries. In this section only curved triangles are considered, but details about other shapes can be found in [GP97; Pet05; GP15].

α) High Order Triangles

Curved triangles can be defined by leveraging on appropriate interpolation polynomials which are zero at all interpolation points but one. These points are usually provided by a mesher software and, for the simplicity of the discussion, are assumed to be uniformly distributed over the triangular elements. To clarify the discussion the interpolation points are designated via their simplex coordinates on the reference triangle. The simplex coordinates are defined as the ratios between the areas of the sub-triangles defined by the point under consideration and the complete triangle. For instance, in Figure 3.1, $\boldsymbol{x}$ is uniquely identified by its simplex coordinates

$$\left(\xi_1, \xi_2, \xi_3\right) = \left(\frac{A_1}{A}, \frac{A_2}{A}, \frac{A_3}{A}\right). \tag{3.1}$$

It is clear that these coordinates are not independent since $\xi_1 + \xi_2 + \xi_3 = 1$. In the case of a triangular element of order M the interpolation points are, in simplex

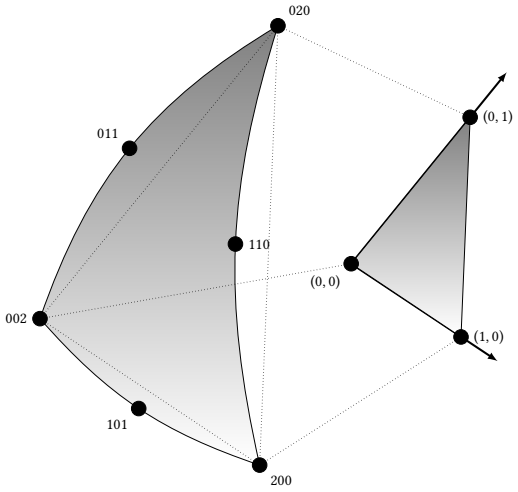

Fig. 3.2.: Illustration of a quadratic triangular element.

coordinates,

$$\left\{ \left(\frac{i}{M}, \frac{j}{M}, \frac{k}{M} \right) \,\middle|\, (i,j,k) \in [0,M]^3 \wedge i+j+k = M \right\}, \tag{3.2}$$

but for notation simplicity they are designated unequivocally with the triplet (i,j,k).

A common choice of interpolation polynomials for triangular elements are

$$S_{ijk}(\xi_1,\xi_2,\xi_3) = R_i^M\left(\xi_1\right) R_j^M\left(\xi_2\right) R_k^M\left(\xi_3\right), \tag{3.3}$$

where

$$R_m^M\left(\xi\right) = \begin{cases} \dfrac{1}{m!} \displaystyle\prod_{n=0}^{m-1} \left(M\xi - n\right) & \text{if } m > 0 \\ 1 & \text{if } m = 0\,. \end{cases} \tag{3.4}$$

are the Sylvester polynomials [SF96]. This family of polynomials is well suited to the problem at hand since the zeros of its members are equally spaced and each polynomial has unit value in a single point. In particular, the zeros of the polynomial $R_m^M\left(\xi\right)$ are $\xi \in \left\{ n/M \,:\, n \in [0, m-1] \right\}$ and it has unit value in $\xi = m/M$.

β) High Order Basis Functions

In order to ensure optimal flexibility and higher order convergence rates, the curvilinear elements introduced in the previous section must be coupled with

higher order basis function. A particularly convenient set of higher order functions are the so-called GWP [GP97] because they are, in part, constructed by multiplying the order $p = 0$ RWG functions with a shifted variation of the polynomials eq. (3.3) introduced for the curved elements. In addition, these functions are divergence conforming and are built to exhibit a representation complete to the same degree for both the basis function and its divergence. This prevents issues or inefficiencies when the functions are used to discretized an unknown quantity and its divergence, which occurs in the EFIE.

To facilitate the following developments the RWG functions are re-introduced in the same formalism as the higher order functions. Each triangle of the discretized geometry supports three RWG functions, that when mapped to the reference triangle, are expressed as

$$\boldsymbol{f}_1^0\left(\xi_1, \xi_2\right) = \left(\xi_1 - 1\right)\hat{\boldsymbol{\xi}}_1 + \xi_2\hat{\boldsymbol{\xi}}_2\,, \tag{3.5}$$

$$\boldsymbol{f}_2^0\left(\xi_1, \xi_2\right) = \left(\xi_2 - 1\right)\hat{\boldsymbol{\xi}}_2 + \xi_1\hat{\boldsymbol{\xi}}_1\,, \tag{3.6}$$

$$\boldsymbol{f}_3^0\left(\xi_1, \xi_2\right) = \left(\xi_1\hat{\boldsymbol{\xi}}_1 + \xi_2\hat{\boldsymbol{\xi}}_2\right). \tag{3.7}$$

The continuity of the normal component of the current across the edges of the defining triangle is imposed by coupling the functions with the corresponding functions on the adjacent triangles and weighted with the appropriate sign. The high order functions are then formed by multiplying the RWG functions with the shifted Sylvester polynomials

$$\tilde{R}_m^M\left(\xi\right) = \begin{cases} \dfrac{1}{(m-1)!}\displaystyle\prod_{n=1}^{m-1}\left(M\xi - n\right) & \text{if } m \in [2, M+1] \\ 1 & \text{if } m = 1\,, \end{cases} \tag{3.8}$$

which can be expressed from Sylvester polynomials (eq. (3.4)) as

$$\tilde{R}_m^M\left(\xi\right) = R_{m-1}^M\left(\xi - \frac{1}{M}\right). \tag{3.9}$$

The procedure described by [GP97] suggests to build one basis function per interpolation point located on an edge and two per point located within the cell. The general formula to build the functions defined on the edge $\xi_1 = 0$ is

$$\boldsymbol{f}_{ijk}\left(\xi_1, \xi_2\right) = \boldsymbol{f}_1^0\left(\xi_1, \xi_2\right) \cdot R_i^M(\xi_1)\tilde{R}_j^M(\xi_2)\tilde{R}_k^M(1 - \xi_1 - \xi_2)\,. \tag{3.10}$$

The functions interpolating on the other edges can be obtained by using the corresponding order $p = 0$ function and using shifted Sylvester polynomial of the appropriate simplex coordinate.

In the case of order $p = 1$ functions, six edge basis functions (two per edge) can be constructed. The shifted polynomial ensure that all basis functions have a non-zero normal component a single interpolation point. In this relatively simple case, the basis edge basis functions are

$$\boldsymbol{f}_{102}(\xi_1, \xi_2) = \boldsymbol{f}_2^0(\xi_1, \xi_2)\tilde{R}_2^3(1 - \xi_1 - \xi_2), \tag{3.11}$$
$$\boldsymbol{f}_{201}(\xi_1, \xi_2) = \boldsymbol{f}_2^0(\xi_1, \xi_2)\tilde{R}_2^3(\xi_1), \tag{3.12}$$
$$\boldsymbol{f}_{012}(\xi_1, \xi_2) = \boldsymbol{f}_1^0(\xi_1, \xi_2)\tilde{R}_2^3(1 - \xi_1 - \xi_2), \tag{3.13}$$
$$\boldsymbol{f}_{021}(\xi_1, \xi_2) = \boldsymbol{f}_1^0(\xi_1, \xi_2)\tilde{R}_2^3(\xi_2), \tag{3.14}$$
$$\boldsymbol{f}_{120}(\xi_1, \xi_2) = \boldsymbol{f}_3^0(\xi_1, \xi_2)\tilde{R}_2^3(\xi_2), \tag{3.15}$$
$$\boldsymbol{f}_{210}(\xi_1, \xi_2) = \boldsymbol{f}_3^0(\xi_1, \xi_2)\tilde{R}_2^3(\xi_1), \tag{3.16}$$

with $\tilde{R}_2^3(\xi) = 3\xi - 1$ and the three possible cell basis functions are

$$\boldsymbol{f}_{111}^1(\xi_1, \xi_2) = \boldsymbol{f}_1^0(\xi_1, \xi_2)R_1^3(\xi_1), \tag{3.17}$$
$$\boldsymbol{f}_{111}^2(\xi_1, \xi_2) = \boldsymbol{f}_2^0(\xi_1, \xi_2)R_1^3(\xi_2), \tag{3.18}$$
$$\boldsymbol{f}_{111}^3(\xi_1, \xi_2) = \boldsymbol{f}_3^0(\xi_1, \xi_2)R_1^3(1 - \xi_1 - \xi_2), \tag{3.19}$$

with $R_1^3(\xi) = 3\xi$. Because the three inner basis functions are linearly dependant one of them should be discarded; at higher orders one function is discarded at every inner interpolation point.

c) Loop Star Matrices

To compare the qH projectors to the standard LS technique, the LS matrices are introduced in this section. For the remainder of this chapter the EFIE eq. (2.54) is supposed to be discretized on the tessellation of a surface Γ composed of N_v vertices, N_e edges and N_f faces (which are the triangles of the mesh). The LS matrices decompose the space of standard RWG functions $\{\boldsymbol{f}_i\}$, $i \in [1, N_e]$, into a solenoidal subspace Λ, a non-solenoidal subspace Σ and a harmonic subspace H.

The solenoidal subspace Λ is composed of divergence-free functions (i.e. $\forall \boldsymbol{l} \in \Lambda, \nabla \cdot \boldsymbol{l} = \boldsymbol{0}$) which, since they discretize the unknown of the EFIE, represent current density functions. It has been demonstrated [WGK95] that solenoidal current density form closed path, which is the origin of the term *loop functions*. These considerations lead us to define Λ as the subspace of *local* – by opposition to global – loops. This space is generated by the N_v loop basis functions $\{\boldsymbol{\lambda}_j\}$, $j \in [1, N_v]$, respectively defined on each of the N_v vertices $\{\boldsymbol{v}_j\}$ of the mesh. These functions

are a linear combination of the p RWG basis functions defined on the p edges connected to $\boldsymbol{v}_j$ (p is the degree of $\boldsymbol{v}_j$). More formally

$$\boldsymbol{\Lambda}_j(\boldsymbol{r}) = \sum_{i=1}^{N_e} \left[\tilde{\boldsymbol{\Lambda}}\right]_{ij} \boldsymbol{f}_i(\boldsymbol{r}), \quad j \in [1, N_v], \tag{3.20}$$

where, for each loop function $\boldsymbol{\Lambda}_j$, the p non-zero elements of $\tilde{\boldsymbol{\Lambda}}$ are chosen so that $\nabla \cdot \boldsymbol{\Lambda}_j = \boldsymbol{0}$. The matrix $\tilde{\boldsymbol{\Lambda}} \in \mathbb{R}^{N_v, N_e}$ is a transformation matrix from the RWG space to Λ. Using the notations from Figure 5.1 the elements of the matrix are

$$\left[\tilde{\boldsymbol{\Lambda}}\right]_{ij} = \begin{cases} 1 & \text{if vertex } j \text{ is } \boldsymbol{v}_i^+, \\ -1 & \text{if vertex } j \text{ is } \boldsymbol{v}_i^-, \\ 0 & \text{otherwise.} \end{cases} \tag{3.21}$$

The non-solenoidal subspace Σ has several possible constructions, the choice detailed thereafter corresponds to the dual definition to that of the loops, and will be designated as Σ^S. This subspace is generated by a set of N_f basis functions $\left\{\boldsymbol{\Sigma}_j^S\right\}$, $j \in \left[1, N_f\right]$; each function $\boldsymbol{\Sigma}_j^S$ is defined on the corresponding cell c_j as a linear combination of all RWG functions that are partially defined on this cell. Using the notations of Figure 5.1 this means that $\boldsymbol{\Sigma}_j^S$ is a linear combination of the N_j basis functions for which $c^+ = c_j$ or $c^- = c_j$. From trivial geometrical considerations it is clear that, in the absence of junctions, $N_j \in [1, 3]$ and in particular, for closed structures $N_j = 3$. In matrix form

$$\boldsymbol{\Sigma}_j^S(\boldsymbol{r}) = \sum_{i=1}^{N_e} \left[\tilde{\boldsymbol{\Sigma}}^S\right]_{ij} \boldsymbol{f}_i(\boldsymbol{r}), \quad j \in \left[1, N_f\right], \tag{3.22}$$

where $\tilde{\boldsymbol{\Sigma}}^S \in \mathbb{R}^{N_f, N_e}$. For each function Σ_j^S the N_j corresponding non-zero elements are set to ± 1 and chosen so that all currents flow out of the cell. The matrix $\tilde{\boldsymbol{\Sigma}}^S$ is an RWG to stars mapping, and its entries are

$$\left[\tilde{\boldsymbol{\Sigma}}^S\right]_{ij} = \begin{cases} 1 & \text{if cell } j \text{ is } c_i^+, \\ -1 & \text{if cell } j \text{ is } c_i^-, \\ 0 & \text{otherwise.} \end{cases} \tag{3.23}$$

The harmonic subspace H is more challenging to construct because it is spanned by the divergence free functions defined on the global loops of Γ, that are computationally expensive to identify. If g is the genus (or number of handles) of the structure, the number of global loops is $2g$. In simple cases, such as spherical

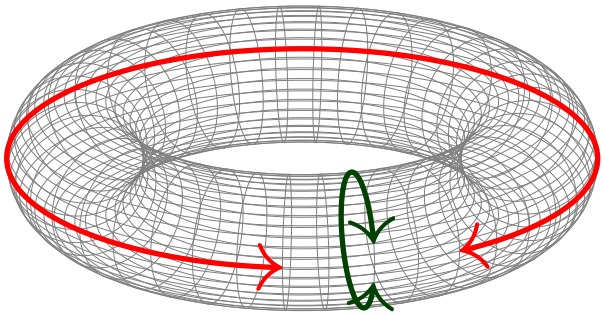

Fig. 3.3.: Illustration a toroidal structure and its associated global loops. The vertical – green – arrow indicates the poloidal direction while the horizontal – red – one indicates the toroidal direction.

geometries ($g = 0$) this space is empty because the structure is simply connected, i.e. it does not contain global loops. Tori are probably the simplest case of multiply connected surfaces ($g = 1$), and present two global loops corresponding to the toroidal and poloidal directions (Figure 3.3). Once the global loops have been identified[2], it is possible to construct a mapping matrix $\tilde{\boldsymbol{H}} \in \mathbb{R}^{2g,N_e}$ from RWGs to the harmonic subspace which contains the coefficients of the RWG functions composing the global loops as columns.

Before leveraging on the decomposition operators introduced thus far[3] to perform a LS decomposition, the linear dependency of the Loop and Star functions should be addressed. Euler-Poincaré [Wil83] formula provides a relationship between the number of faces f, vertices v, inner edges e, apertures a and handles h

$$f + v - e = 2 - 2h - a\,. \tag{3.24}$$

This formula, when compared to the dimensions of the different transformation matrices implies that, for each connected component of Γ, (i) one loop function must be removed if the component is closed and (ii) one star function must always be removed. To illustrate this relations consider a plate for which $h = 0$ and $a = 1$ then $e = f - 1 + v$, meaning that one star function (i.e. one column of $\tilde{\boldsymbol{\Sigma}}^S$) must be removed. In the case of a sphere ($h = 0$, $a = 0$, $e = f - 1 + v - 1$) one column should be removed from both $\tilde{\boldsymbol{\Sigma}}^S$ and $\tilde{\boldsymbol{\Lambda}}$. The linearly independant matrices $\boldsymbol{\Lambda}$ and $\boldsymbol{\Sigma}$ (corresponding respectively to $\tilde{\boldsymbol{\Lambda}}$ and $\tilde{\boldsymbol{\Sigma}}^S$) can be used to build the LS transformation

2 Global loops can be identified via specific graph-based search algorithm, or for small cases, via singular value decomposition (SVD).

3 The space $\Lambda \oplus H \oplus \Sigma^S$ is equal to the RWG space.

matrix $\boldsymbol{B}$ as

$$\boldsymbol{B} = [\boldsymbol{\Lambda}\ \boldsymbol{H}\ \boldsymbol{\Sigma}]\,, \tag{3.25}$$

where $\boldsymbol{H} = \tilde{\boldsymbol{H}}$ did not require any modifications.

Finally, $\boldsymbol{\Sigma}^{\mathrm{T}}$ corresponds to a discretization of the divergence operator on the RWG space. As a consequence $\boldsymbol{\Sigma}^{\mathrm{T}}\boldsymbol{\Lambda} = \boldsymbol{\Sigma}^{\mathrm{T}}\boldsymbol{H} = \boldsymbol{0}$ which means that the non-solenoidal subspace is orthogonal to the solenoidal and harmonic subspaces.

d) Low-Frequency Breakdown

This section focuses on the analysis of the low frequency breakdown itself and its root causes. The effects of the breakdown are first illustrated through numerical examples. The origin of its different effects are then analyzed before presenting the standard LS solution often used to address them.

α) Illustration of the Problem

In order to better describe the low frequency breakdown, its symptoms are demonstrated via numerical examples. Setting up these pathological cases will also serve to illustrate the effectiveness of the different schemes introduced to cure its underlying causes. To have an analytical solution as reference, the geometry in these examples is a PEC sphere for which the Mie series serve as closed-form solution.

First, the validity the setup is demonstrated by simulating the RCS of the sphere in a non-pathological case, at relatively high frequency. The results, illustrated in Figure 3.4, demonstrate a perfect match between the computed RCS and the Mie series. Next, the effects of the low frequency breakdown on the far field accuracy and on the conditioning of the system matrix are illustrated in Figures 3.5 and 3.6, respectively. The RCS was computed at $1 \cdot 10^{-40}$ Hz to confirm that the solutions proposed later on effectively address the low frequency breakdown at arbitrarily low frequency. However, the scattered field shows a visible mismatch with the Mie series as early as 1 MHz for a sphere of 1 m radius, and not only at extremely low frequencies.

It should be clear that, as is, the EFIE is not usable at low frequencies because (i) it yields the wrong solution and (ii) the conditioning of the impedance matrix will grow as k^{-2}, which reduces the convergence speed of iterative solvers, or prevent it altogether.

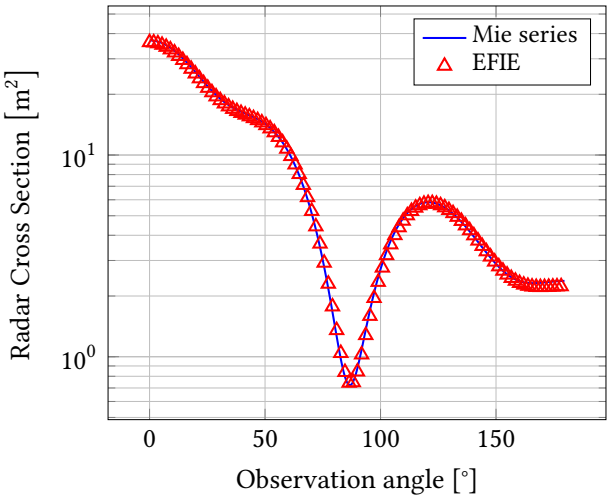

Fig. 3.4.: RCS of a PEC sphere of radius 1 m, excited by a plane wave oscillating at one wavelength per diameter. In this high frequency case the EFIE yields a result perfectly matching the Mie series.

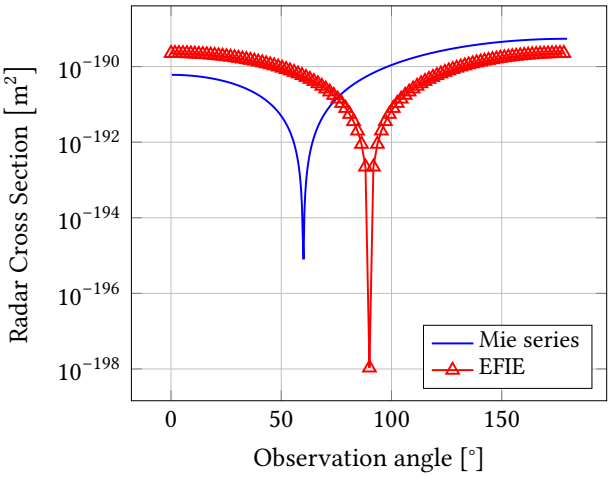

Fig. 3.5.: RCS of a PEC sphere of radius 1 m, excited by a plane wave oscillating at $1 \cdot 10^{-40}$ Hz. There is a clear mismatch between the Mie series and the EFIE solution caused by the low frequency breakdown of the formulation.

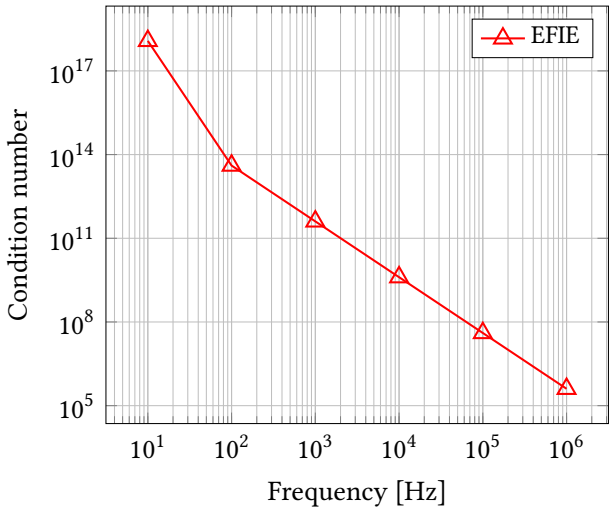

Fig. 3.6.: Evolution of the condition number of the EFIE matrices of a PEC sphere with unit radius at different frequencies. Because of numerical limitations in the computation of high condition numbers, very low frequency points are not displayed.

β) Analysis of the Low Frequency Breakdown

Now that the symptoms of the low frequency breakdown have been illustrated, its origins should be studied. The low frequency breakdown has two root causes: (i) the matrix blocks are ill-scaled as some blocks scale with the frequency while others scale with its inverse and (ii) numerical cancellations occur when the solution vector is stored in finite precision. To expose these two issues the solenoidal and non-solenoidal parts of the EFIE are separated and studied independently. This decomposition is achieved by applying the decomposition matrix $\boldsymbol{B}$ introduced in Equation (3.25) to the discretized EFIE eq. (2.64)

$$\boldsymbol{B}^{\mathrm{T}}\left(-\mathrm{j}k\eta\boldsymbol{T}_s + \frac{\eta}{-\mathrm{j}k}\boldsymbol{T}_h\right)\boldsymbol{B}\boldsymbol{y} = \boldsymbol{B}^{\mathrm{T}}\boldsymbol{v}_e\,, \tag{3.26}$$

where $\boldsymbol{j} = \boldsymbol{B}\boldsymbol{y}$. For notation simplicity the left-hand side of the equation is denoted $\boldsymbol{Z}_{\boldsymbol{\Lambda H \Sigma}}$; in block notation this term can be written

$$\boldsymbol{Z}_{\boldsymbol{\Lambda H \Sigma}} = -\eta\mathrm{j}k\begin{bmatrix} \boldsymbol{\Lambda}^{\mathrm{T}}\boldsymbol{Z}_s\boldsymbol{\Lambda} & \boldsymbol{\Lambda}^{\mathrm{T}}\boldsymbol{Z}_s\boldsymbol{H} & \boldsymbol{\Lambda}^{\mathrm{T}}\boldsymbol{Z}_s\boldsymbol{\Sigma} \\ \boldsymbol{H}^{\mathrm{T}}\boldsymbol{Z}_s\boldsymbol{\Lambda} & \boldsymbol{H}^{\mathrm{T}}\boldsymbol{Z}_s\boldsymbol{H} & \boldsymbol{H}^{\mathrm{T}}\boldsymbol{Z}_s\boldsymbol{\Sigma} \\ \boldsymbol{\Sigma}^{\mathrm{T}}\boldsymbol{Z}_s\boldsymbol{\Lambda} & \boldsymbol{\Sigma}^{\mathrm{T}}\boldsymbol{Z}_s\boldsymbol{H} & \boldsymbol{\Sigma}^{\mathrm{T}}\left(\boldsymbol{Z}_s + k^{-2}\boldsymbol{Z}_h\right)\boldsymbol{\Sigma} \end{bmatrix} \tag{3.27}$$

where the relations

$$\boldsymbol{Z}_h\boldsymbol{\Lambda} = \boldsymbol{0}\,,\ \boldsymbol{Z}_h\boldsymbol{H} = \boldsymbol{0}\,,\ \boldsymbol{\Lambda}^{\mathrm{T}}\boldsymbol{Z}_h = \boldsymbol{0}\,,\ \boldsymbol{H}^{\mathrm{T}}\boldsymbol{Z}_h = \boldsymbol{0}\,, \tag{3.28}$$

Tab. 3.1.: Frequency scaling of different kinds of excitations.

Type of excitation	$\boldsymbol{\Lambda}$	$\boldsymbol{H}$	$\boldsymbol{\Sigma}$
Plane wave	$\mathcal{O}(k)$	$\mathcal{O}(k)$	$\mathcal{O}(1)$
Capacitive voltage gap	0	0	$\mathcal{O}(1)$
Inductive voltage gap	$\mathcal{O}(1)$	$\mathcal{O}(1)$	$\mathcal{O}(1)$

have been used. The results in eq. (3.28) can be immediately deduced from the definition of the loops, i.e. $\forall \boldsymbol{l} \in \Lambda \oplus H\,, \nabla \cdot l = \mathbf{0}$, and the presence of the divergence operators in $\boldsymbol{\mathcal{T}}_h$. At low frequencies, the bottom-right block eq. (3.27) can be approximated as

$$\boldsymbol{\Sigma}^{\mathrm{T}}\left(\boldsymbol{Z}_s + k^{-2}\boldsymbol{Z}_h\right)\boldsymbol{\Sigma} \underset{k\longrightarrow 0}{\approx} k^{-2}\boldsymbol{\Sigma}^{\mathrm{T}}\boldsymbol{Z}_h\boldsymbol{\Sigma}\,, \tag{3.29}$$

which clearly demonstrates the incompatible scaling of the solenoidal and non-solenoidal parts of the matrix since all terms scale as k, while a single term scales as k^{-1}. The consequences of this ill-scaling are explored in the next sections.

3.d.β.1. Numerical Instability

The numerical instabilities degrading the solution of the EFIE can be brought into light by analysing the frequency scaling of the solution of eq. (3.26)

$$\boldsymbol{B}^{-1}\boldsymbol{j} = \boldsymbol{Z}_{\boldsymbol{\Lambda H \Sigma}}^{-1}\boldsymbol{B}^{\mathrm{T}}\boldsymbol{V}_e\,. \tag{3.30}$$

First, the frequency behaviour of $\boldsymbol{Z}_{\boldsymbol{\Lambda H \Sigma}}^{-1}$ is determined using well known results on the inverse of block matrix [HS81]

$$\boldsymbol{Z}_{\boldsymbol{\Lambda H \Sigma}}^{-1} = \begin{bmatrix} \mathcal{O}(1/k) & \mathcal{O}(1/k) & \mathcal{O}(k) \\ \mathcal{O}(1/k) & \mathcal{O}(1/k) & \mathcal{O}(k) \\ \mathcal{O}(k) & \mathcal{O}(k) & \mathcal{O}(k) \end{bmatrix}. \tag{3.31}$$

Then, given the scalings for different types of excitation recalled in Table 3.1 [QC10], specific analyses can be performed for each induced solution. The different excitation types present in the table are:

Plane-wave excitation corresponding to an impinging wave of the form $\boldsymbol{r} \mapsto e_0 \exp\left(-\mathrm{j}k\hat{\boldsymbol{k}}\cdot\boldsymbol{r}\right)\hat{\boldsymbol{u}}$ where e_0 is the amplitude of the wave, $\hat{\boldsymbol{k}}$ its direction of propagation and $\hat{\boldsymbol{u}}$ its polarization.

Capacitive voltage gap excitation corresponding to a delta gap that does not excite any of the global loops of the structure. A simple example of such an excitation is a delta gap on the conductive strip between the two parallel plates of a capacitor.

Inductive voltage gap excitation corresponding to a delta gap excitation that does excite a global loop of the structure. A simple example can be obtained by adding a second conductive strip to the capacitor used as example for the capacitive voltage gap.

In the case of a plane-wave excitation

$$\boldsymbol{B}^{-1}\boldsymbol{j} \underset{k\to 0}{=} \begin{bmatrix}\mathcal{O}(1) & \mathcal{O}(1) & \mathcal{O}(k)\end{bmatrix}^{\mathrm{T}}, \tag{3.32}$$

which implies that the current density scales as

$$\boldsymbol{j} \underset{k\to 0}{=} \mathcal{O}(1)\cdot\boldsymbol{\Lambda} + \mathcal{O}(1)\cdot\boldsymbol{H} + \mathcal{O}(k)\cdot\boldsymbol{\Sigma}\,. \tag{3.33}$$

It is then clear that at low frequencies and in finite precision the non-solenoidal contribution of the current will be erased. Thus the information about the charge $\nabla\cdot\boldsymbol{j}$ is lost since

$$\nabla\cdot\boldsymbol{j} = \boldsymbol{\Sigma}^{\mathrm{T}}\boldsymbol{j} = \mathcal{O}(k)\cdot\boldsymbol{\Sigma}^{\mathrm{T}}\boldsymbol{\Sigma}\,. \tag{3.34}$$

But even more severe problems arise when this current is used to compute the field scattered by Γ. Since the solenoidal and non-solenoidal parts of the current contribute equally to the far field, numerical noise will be amplified and corrupt the computations. This can be demonstrated by analyzing the solenoidal and non-solenoidal parts of the far field. First, following from eq. (2.32), the far field operator $\boldsymbol{\mathcal{F}}$ is introduced

$$\begin{aligned}\big(\boldsymbol{\mathcal{F}}\boldsymbol{j}\big)(\boldsymbol{r}) &= -\frac{\mathrm{j}k\eta}{4\pi\|\boldsymbol{r}\|}\mathrm{e}^{-\mathrm{j}k\|\boldsymbol{r}\|}\Big[\hat{\boldsymbol{\theta}}\boldsymbol{N}_{\theta}(\boldsymbol{r}) + \hat{\boldsymbol{\phi}}\boldsymbol{N}_{\phi}(\boldsymbol{r})\Big]\,,\\ &= -\frac{\mathrm{j}k\eta}{4\pi\|\boldsymbol{r}\|}\mathrm{e}^{-\mathrm{j}k\|\boldsymbol{r}\|}\Big(\hat{\boldsymbol{\theta}}\hat{\boldsymbol{\theta}} + \hat{\boldsymbol{\phi}}\hat{\boldsymbol{\phi}}\Big)\cdot\big(\boldsymbol{\mathcal{N}}\boldsymbol{j}\big)(\boldsymbol{r})\,.\end{aligned} \tag{3.35}$$

The solenoidal behaviour of this operator can be exposed by decomposing the exponential in $\boldsymbol{\mathcal{N}}$ as $\exp(x) = 1 + \exp(x) - 1$, yielding

$$\big(\boldsymbol{\mathcal{N}}\boldsymbol{j}\big)(\boldsymbol{r}) = \iint_{\Gamma}\boldsymbol{j}\big(\boldsymbol{r}'\big)\Big(\mathrm{e}^{\mathrm{j}k\boldsymbol{r}'\cdot\hat{\boldsymbol{r}}} - 1\Big)\mathrm{d}\boldsymbol{r}' + \iint_{\Gamma}\boldsymbol{j}\big(\boldsymbol{r}'\big)\mathrm{d}\boldsymbol{r}'\,. \tag{3.36}$$

While this procedure does not yield any insight for star functions, it is possible to simplify it when it is applied to divergence-free functions by noting that

$$\iint_l \boldsymbol{l}\left(\boldsymbol{r}'\right)\mathrm{d}\boldsymbol{r}' = \boldsymbol{0}\,, \quad \forall \boldsymbol{l} \in \Lambda \oplus H\,, \tag{3.37}$$

which derives from Green's theorem. This simplification, combined with a Taylor series expansion of $x \mapsto \exp(x) - 1$, provides the scaling of the solenoidal part of the far field

$$(\boldsymbol{\mathcal{N}}\boldsymbol{l})(\boldsymbol{r}) \underset{k\to 0}{=} \iint_l \boldsymbol{l}\left(\boldsymbol{r}'\right)\left(\mathrm{j}k\boldsymbol{r}'\cdot\hat{\boldsymbol{r}} + \mathcal{O}\left(k^2\right)\right)\mathrm{d}\boldsymbol{r}'\,, \quad \forall \boldsymbol{l} \in \Lambda \oplus H\,. \tag{3.38}$$

As a consequence, the discrete far field operator is equivalent to a multiplication by $k \cdot \left[\mathcal{O}(k)\ \mathcal{O}(k)\ \mathcal{O}(1)\right]$ and the scaling of the far field $\boldsymbol{e}_F$ induced by a plane wave is

$$k^{-1}\boldsymbol{e}_F \underset{k\to 0}{=} \begin{bmatrix}\mathcal{O}(k) & \mathcal{O}(k) & \mathcal{O}(1)\end{bmatrix} \cdot \boldsymbol{B}^{-1}\boldsymbol{j} \underset{k\to 0}{=} \mathcal{O}(k) + \mathcal{O}(k) + \mathcal{O}(k)\,. \tag{3.39}$$

In accordance with earlier statements, in the case of a plane wave excitation, the far field is composed in equal measures by the solenoidal and non-solenoidal current contributions, one of which was lost in the resolution process. Hence, the far field obtained through the standard EFIE can not be relied upon for this excitation. The situation is less dire for the voltage gap excitations: the capacitive voltage gap will not cause cancellations in the current and a physical cancellation will occur in the scattered field

$$\boldsymbol{j} \underset{k\to 0}{=} \mathcal{O}(k)\cdot\boldsymbol{\Lambda} + \mathcal{O}(k)\cdot\boldsymbol{H} + \mathcal{O}(k)\cdot\boldsymbol{\Sigma}\,, \tag{3.40}$$

$$k^{-1}\boldsymbol{e}_F \underset{k\to 0}{=} \mathcal{O}\left(k^2\right) + \mathcal{O}\left(k^2\right) + \mathcal{O}(k)\,; \tag{3.41}$$

the inductive gap is subject to numerical cancellation in its current but the lost term has a negligible contribution to the far field,

$$\boldsymbol{j} \underset{k\to 0}{=} \mathcal{O}(1/k)\cdot\boldsymbol{\Lambda} + \mathcal{O}(1/k)\cdot\boldsymbol{H} + \mathcal{O}(k)\cdot\boldsymbol{\Sigma}\,, \tag{3.42}$$

$$k^{-1}\boldsymbol{e}_F \underset{k\to 0}{=} \mathcal{O}(1) + \mathcal{O}(1) + \mathcal{O}(k)\,. \tag{3.43}$$

In these last two cases no numerical noise is amplified by the scattering operation and, as a consequence, the far field patterns should remain accurate at low frequencies. However the inductive voltage gap exhibits a loss of charge information and all the excitations are still subject to the ill-conditioning of the impedance matrix that will degrade the precision of numerical current solutions, even if they are not subject to cancellations *per se*.

3.d.β.2. Low-Frequency Ill Conditioning

To demonstrate the existence of the low frequency ill-conditioning of the EFIE, another matrix is shown to be well-conditioned and the conditioning of the original matrix is deduced from this result.

Consider the matrix $\boldsymbol{Z}_{\boldsymbol{LR}}$ defined by left and right multiplying $\boldsymbol{Z}_{\boldsymbol{\Lambda H \Sigma}}$ by two diagonal matrices

$$\boldsymbol{Z}_{\boldsymbol{LR}} = \boldsymbol{L}\boldsymbol{Z}_{\boldsymbol{\Lambda H \Sigma}}\boldsymbol{R} \underset{k\to 0}{=} \boldsymbol{L}\begin{bmatrix} \boldsymbol{\Lambda}^{\mathrm{T}}\boldsymbol{Z}_s\boldsymbol{\Lambda} & \boldsymbol{\Lambda}^{\mathrm{T}}\boldsymbol{Z}_s\boldsymbol{H} & -\mathrm{j}k\boldsymbol{\Lambda}^{\mathrm{T}}\boldsymbol{Z}_s\boldsymbol{\Sigma} \\ \boldsymbol{H}^{\mathrm{T}}\boldsymbol{Z}_s\boldsymbol{\Lambda} & \boldsymbol{H}^{\mathrm{T}}\boldsymbol{Z}_s\boldsymbol{H} & -\mathrm{j}k\boldsymbol{H}^{\mathrm{T}}\boldsymbol{Z}_s\boldsymbol{\Sigma} \\ -\mathrm{j}k\boldsymbol{\Sigma}^{\mathrm{T}}\boldsymbol{Z}_s\boldsymbol{\Lambda} & -\mathrm{j}k\boldsymbol{\Sigma}^{\mathrm{T}}\boldsymbol{Z}_s\boldsymbol{H} & \boldsymbol{\Sigma}^{\mathrm{T}}\boldsymbol{Z}_h\boldsymbol{\Sigma} \end{bmatrix}\boldsymbol{R}\,, \tag{3.44}$$

where $\boldsymbol{L} = \mathrm{diag}\big(-1/\mathrm{j}k,\, -1/\mathrm{j}k,\, 1\big)$ and $\boldsymbol{R} = \mathrm{diag}\big(1,\, 1,\, -\mathrm{j}k\big)$, and its low frequency limit

$$\boldsymbol{Z}^{\boldsymbol{0}}_{\boldsymbol{LR}} = \lim_{k\to 0}\boldsymbol{Z}_{\boldsymbol{LR}} = \boldsymbol{L}\begin{bmatrix} \boldsymbol{\Lambda}^{\mathrm{T}}\boldsymbol{Z}_s\boldsymbol{\Lambda} & \boldsymbol{\Lambda}^{\mathrm{T}}\boldsymbol{Z}_s\boldsymbol{H} & \boldsymbol{0} \\ \boldsymbol{H}^{\mathrm{T}}\boldsymbol{Z}_s\boldsymbol{\Lambda} & \boldsymbol{H}^{\mathrm{T}}\boldsymbol{Z}_s\boldsymbol{H} & \boldsymbol{0} \\ \boldsymbol{0} & \boldsymbol{0} & \boldsymbol{\Sigma}^{\mathrm{T}}\boldsymbol{Z}_h\boldsymbol{\Sigma} \end{bmatrix}\boldsymbol{R}\,. \tag{3.45}$$

Because $\boldsymbol{Z}^{\boldsymbol{0}}_{\boldsymbol{LR}}$ is frequency independent, it is clear that $\boldsymbol{Z}_{\boldsymbol{LR}}$ is immune from the low frequency conditioning breakdown

$$\lim_{k\to 0}\mathrm{cond}\,\boldsymbol{Z}_{\boldsymbol{LR}} = \mathrm{cond}\,\boldsymbol{Z}^{\boldsymbol{0}}_{\boldsymbol{LR}} \in \mathbb{R}\,. \tag{3.46}$$

Using properties of the condition number of products yields

$$\mathrm{cond}\,\boldsymbol{Z}_{\boldsymbol{\Lambda H \Sigma}} \leq \mathrm{cond}\,\boldsymbol{Z}_{\boldsymbol{LR}}\,\mathrm{cond}\,\boldsymbol{L}^{-1}\,\mathrm{cond}\,\boldsymbol{R}^{-1}\,. \tag{3.47}$$

In addition, because $\mathrm{cond}\big(\boldsymbol{A}^{\mathrm{T}}\boldsymbol{A}\big) = \mathrm{cond}\big(\boldsymbol{A}\boldsymbol{A}^{\mathrm{T}}\big)$ for all square matrices, and after re-writing $\boldsymbol{Z}_{\boldsymbol{LR}}$ as

$$\boldsymbol{Z}_{\boldsymbol{LR}} = \boldsymbol{D}\boldsymbol{Z}_{\boldsymbol{\Lambda H \Sigma}}\boldsymbol{D}\,, \tag{3.48}$$

where $\boldsymbol{D} = \mathrm{diag}\Big(\sqrt{\mathrm{j}/k},\, \sqrt{\mathrm{j}/k},\, \sqrt{k/\mathrm{j}}\Big)$, a few manipulations provide the equality

$$\mathrm{cond}\big(\boldsymbol{D}\boldsymbol{Z}^{-1/2}_{\boldsymbol{\Lambda H \Sigma}}\boldsymbol{Z}_{\boldsymbol{\Lambda H \Sigma}}\boldsymbol{Z}^{-1/2}_{\boldsymbol{\Lambda H \Sigma}}\boldsymbol{D}\big) \leq \mathrm{cond}\,\boldsymbol{Z}_{\boldsymbol{\Lambda H \Sigma}}\,\mathrm{cond}\,\boldsymbol{Z}_{\boldsymbol{LR}}\,. \tag{3.49}$$

The condition number of $\boldsymbol{Z}_{\boldsymbol{\Lambda H \Sigma}}$ is then bounded by both inequalities

$$\frac{1}{\gamma k^2} \leq \mathrm{cond}\,\boldsymbol{Z}_{\boldsymbol{\Lambda H \Sigma}} \leq \frac{\gamma}{k^2}\,, \tag{3.50}$$

where $\gamma = \mathrm{cond}\,\boldsymbol{Z}_{\boldsymbol{LR}}$, which immediately implies that

$$\mathrm{cond}\,\boldsymbol{Z}_{\boldsymbol{\Lambda H \Sigma}} \underset{k\to 0}{=} \mathcal{O}\big(k^{-2}\big)\,, \tag{3.51}$$

thereby demonstrating the existence of a low frequency ill-conditioning of the EFIE matrix, that grows with k^{-2}.

γ) Traditional Loop-Star Decomposition

One of the traditional techniques used to remedy the issues exposed in the previous sections is the Loop-Star (LS) decomposition. Despite its effectiveness this approach suffers from two crucial shortcomings: (i) it requires explicit detection of the global loops and (ii) it further degrades the EFIE conditioning behaviour with increasingly denser discretization. In this section the LS procedure is detailed to illustrate its shortcomings.

Given that the developments of the previous sections were actually already involving a LS decomposition, different passages of the required developments have already been detailed. The key motivation behind the LS technique is to re-scale the $\boldsymbol{Z}_{\Lambda H \Sigma}$ decomposition with $\boldsymbol{L}$ and $\boldsymbol{R}$, in order to obtain a numerically stable intermediate solution and a well-conditioned system matrix. The Loop-Star electric field integral equation (LS-EFIE) then reads

$$\boldsymbol{L}\boldsymbol{B}^{\mathrm{T}}\left(-\mathrm{j}k\boldsymbol{Z}_s - \frac{1}{\mathrm{j}k}\boldsymbol{Z}_h\right)\boldsymbol{B}\boldsymbol{R}\boldsymbol{y}_{\boldsymbol{LS}} = \boldsymbol{L}\boldsymbol{B}^{\mathrm{T}}\boldsymbol{v}_e\,, \tag{3.52}$$

where $\boldsymbol{j} = \boldsymbol{B}\boldsymbol{R}\boldsymbol{y}_{\boldsymbol{LS}}$. Previous developments immediately demonstrate the stability of the conditioning of this formulation, however its numerical stability is still to be demonstrated. Adapting eq. (3.30) and the related developments to the new formulation immediately yields

$$\boldsymbol{R}^{-1}\boldsymbol{B}^{-1}\boldsymbol{j} = \left(\boldsymbol{R}^{-1}\boldsymbol{Z}_{\Lambda H \Sigma}\boldsymbol{L}^{-1}\right)\boldsymbol{L}\boldsymbol{B}^{\mathrm{T}}\boldsymbol{v}_e\,, \tag{3.53}$$

and the current scaling for a plane-wave excitation are

$$\boldsymbol{y}_{\boldsymbol{LS}} = \boldsymbol{R}^{-1}\boldsymbol{B}^{-1}\boldsymbol{j} \underset{k\longrightarrow 0}{=} \begin{bmatrix}\mathcal{O}(1) & \mathcal{O}(1) & \mathcal{O}(1)\end{bmatrix}^{\mathrm{T}}. \tag{3.54}$$

The intermediate solution $\boldsymbol{y}_{\boldsymbol{LS}}$ is clearly immune from low frequency numerical cancellations and can be stored in finite precision. The loop and star components should then be radiated independently and $\boldsymbol{j}$ should never be explicitly computed, or numerical cancellations would occur.

To demonstrate the effectiveness of the scheme the same simulations as in Figures 3.5 and 3.6 have been performed with the LS formulation (Figures 3.7 and 3.8). It is clear from these results that the low frequency breakdown is cured. However, the LS matrices suffer from ill-conditioning for dense discretizations (Figure 3.9a). This, in turn, means that the decomposed formulation exhibits a worse refinement behaviour than the standard one (Figure 3.9b). These last results are in accordance with the fact that $\boldsymbol{\Lambda}$ is a graph-Laplacian and hence behaves as an operator of order two [And12].

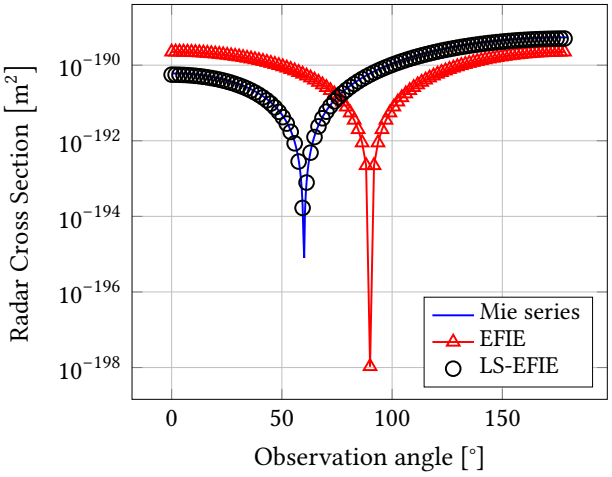

Fig. 3.7.: RCS of a PEC sphere of radius 1 m, excited by a plane wave oscillating at $1 \cdot 10^{-40}$ Hz. There is a clear mismatch between the Mie series and the EFIE solution caused by the low frequency breakdown of the formulation. On the other hand the LS-EFIE matches perfectly the Mie series.

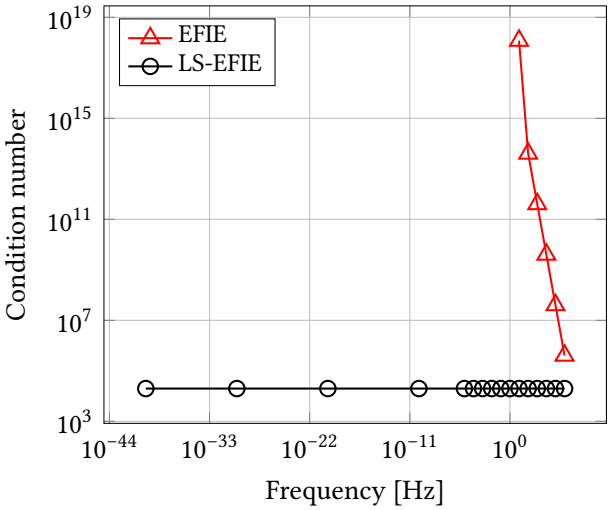

Fig. 3.8.: Evolution of the condition number of the LS-EFIE and EFIE impedance matrices for a PEC sphere with unit radius at different frequencies. The condition number of the LS-EFIE remains constant until $1 \cdot 10^{-40}$ Hz. Because of numerical limitations in the computation of high condition numbers, very low frequency points are not displayed.

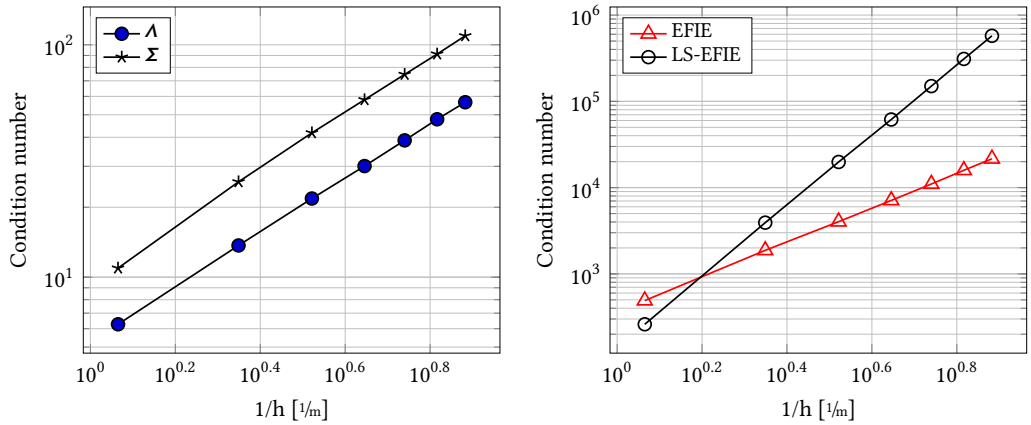

(a) *(b)*

Fig. 3.9.: Evolution of the conditioning of the LS matrices (a) and of the LS-EFIE and EFIE matrices with increasing refinement (b). The matrices correspond to a PEC sphere with radius 1 m at different levels of refinement.

e) The Quasi-Helmholtz Projectors

To solve the low frequency breakdown without the limitations of the LS decomposition, qH projectors have been recently introduced. They have the advantage of curing both aspects of the low frequency breakdown without (i) requiring detection of the global loops and (ii) degrading the dense discretization behaviour of the EFIE, as projectors have a flat spectrum.

The qH projectors do not require the detection of global loops because only the non-solenoidal projector

$$\boldsymbol{P}_{\boldsymbol{\Sigma}} = \boldsymbol{\Sigma}\left(\boldsymbol{\Sigma}^{\mathrm{T}}\boldsymbol{\Sigma}\right)^{+}\boldsymbol{\Sigma}^{\mathrm{T}}, \quad \boldsymbol{P}_{\boldsymbol{\Sigma}} \in \mathbb{R}^{N_e \times N_e}, \tag{3.55}$$

where $^{+}$ denotes the Moore-Penrose pseudo-inverse, is explicitly computed. The solenoidal projector

$$\boldsymbol{P}_{\boldsymbol{\Lambda H}} = \mathbf{I} - \boldsymbol{P}_{\boldsymbol{\Sigma}} \tag{3.56}$$

is computed as its remainder. In the case of simply connected geometries ($H = \emptyset$), the solenoidal projector can be computed directly

$$\boldsymbol{P}_{\boldsymbol{\Lambda H}} = \boldsymbol{P}_{\boldsymbol{\Lambda}} = \boldsymbol{\Lambda}\left(\boldsymbol{\Lambda}^{\mathrm{T}}\boldsymbol{\Lambda}\right)^{+}\boldsymbol{\Lambda}^{\mathrm{T}}, \tag{3.57}$$

but this is generally unnecessary.

It should be noted that the projectors are symmetric and, because they are complementary (by construction), they can decompose any RWG coefficient vector $\boldsymbol{j}$ into its solenoidal and non-solenoidal parts

$$\boldsymbol{j} = \boldsymbol{P}_{\Lambda H}\boldsymbol{j} + \boldsymbol{P}_{\boldsymbol{\Sigma}}\boldsymbol{j}\,. \tag{3.58}$$

Another key practical consideration, is that, relying on an explicit pseudo-inversion is computationally too expensive and would render the overall scheme at least as unpractical as the global loop detection of the standard LS approach. Alternatively the projectors can be computed in linear time with a fast matrix vector product based on multigrid techniques. Given that the $\boldsymbol{\Sigma}^{\mathrm{T}}\boldsymbol{\Sigma}$ matrix can be regularized with $\mathbf{1}_{\boldsymbol{\Sigma}}$

$$\left(\boldsymbol{\Sigma}^{\mathrm{T}}\boldsymbol{\Sigma} + \frac{1}{N_f}\mathbf{1}_{\boldsymbol{\Sigma}}\mathbf{1}_{\boldsymbol{\Sigma}}^{\mathrm{T}}\right)^{+} = \left(\boldsymbol{\Sigma}^{\mathrm{T}}\boldsymbol{\Sigma} + \frac{1}{N_f}\mathbf{1}_{\boldsymbol{\Sigma}}\mathbf{1}_{\boldsymbol{\Sigma}}^{\mathrm{T}}\right)^{-1}, \tag{3.59}$$

$$= \left(\boldsymbol{\Sigma}^{\mathrm{T}}\boldsymbol{\Sigma}\right)^{+} + \frac{1}{N_f}\mathbf{1}_{\boldsymbol{\Sigma}}\mathbf{1}_{\boldsymbol{\Sigma}}^{\mathrm{T}}, \tag{3.60}$$

and because $\mathbf{1}_{\boldsymbol{\Sigma}}$ is in the null-space of $\boldsymbol{\Sigma}$, it can be proven that

$$\boldsymbol{P}_{\boldsymbol{\Sigma}} = \boldsymbol{\Sigma}\left(\boldsymbol{\Sigma}^{\mathrm{T}}\boldsymbol{\Sigma} + \frac{1}{N_f}\mathbf{1}_{\boldsymbol{\Sigma}}\mathbf{1}_{\boldsymbol{\Sigma}}^{\mathrm{T}}\right)^{-1}\boldsymbol{\Sigma}^{\mathrm{T}}\,. \tag{3.61}$$

The inner term of the RHS is spectrally equivalent to a graph-Laplacian [And12], which means that it is possible to perform fast matrix-vector products with its inverse thanks to multigrid preconditioning [LB12; NN12].

f) Solution of the Low-Frequency Breakdown for the EFIE

Because of the drawbacks of the standard LS technique presented in Section 3.d.γ, other methods should be investigated. A more satisfactory solution can be derived from the qH projector introduced in Section 3.e.

α) Leveraging the Quasi-Helmholtz Projectors

Similarly to the LS decomposition, the qH projector techniques separates and independently re-scales the solenoidal and non-solenoidal parts of the EFIE matrix.

Dually to the decomposition and rescaling matrices $\boldsymbol{L}\boldsymbol{B}^{\mathrm{T}}$ and $\boldsymbol{B}\boldsymbol{R}$, the matrices

$$\boldsymbol{M} = -\frac{1}{\mathrm{j}k}\boldsymbol{P}_{\Lambda H} + \boldsymbol{P}_{\Sigma}\,, \tag{3.62}$$

$$\boldsymbol{N} = \boldsymbol{P}_{\Lambda H} - \mathrm{j}k\boldsymbol{P}_{\Sigma} \tag{3.63}$$

are used to build the quasi-Helmholtz projected electric field integral equation (qH-EFIE)

$$\boldsymbol{M}\left(-\mathrm{j}k\boldsymbol{Z}_s + \frac{1}{-\mathrm{j}k}\boldsymbol{Z}_h\right)\boldsymbol{N}\boldsymbol{y}_{qH} = \boldsymbol{M}^{\mathrm{T}}\boldsymbol{v}_e\,, \tag{3.64}$$

where $\boldsymbol{j} = \boldsymbol{N}\boldsymbol{y}_{qH}$. To verify that the matrix does not have a low frequency ill-conditioning, consider the expansion of the system matrix

$$\begin{aligned}\boldsymbol{M}\left(-\mathrm{j}k\boldsymbol{Z}_s + \frac{1}{\mathrm{j}k}\boldsymbol{Z}_h\right)\boldsymbol{N} &= (\boldsymbol{P}_{\Lambda H}\boldsymbol{Z}_s\boldsymbol{P}_{\Lambda H} + \boldsymbol{Z}_h) - (\boldsymbol{P}_{\Lambda H}\boldsymbol{Z}_s\boldsymbol{P}_{\Sigma} + \boldsymbol{P}_{\Sigma}\boldsymbol{Z}_s\boldsymbol{P}_{\Lambda H})\mathrm{j}k \\ &\quad - (\boldsymbol{P}_{\Sigma}\boldsymbol{Z}_s\boldsymbol{P}_{\Sigma})k^2 \\ &= (\boldsymbol{P}_{\Lambda H}\boldsymbol{Z}_s\boldsymbol{P}_{\Lambda H} + \boldsymbol{Z}_h) + \mathcal{O}(k)\,,\end{aligned} \tag{3.65}$$

where the relation

$$\boldsymbol{P}_{\Lambda H}\boldsymbol{Z}_h = \boldsymbol{Z}_h\boldsymbol{P}_{\Lambda H} = \boldsymbol{0}\,, \tag{3.66}$$

has been used and derives from the matrix relations $\boldsymbol{\Lambda}\boldsymbol{Z}_h = \boldsymbol{0}$ and

$$\boldsymbol{P}_{\Sigma}\boldsymbol{Z}_h = \boldsymbol{Z}_h\boldsymbol{P}_{\Sigma} = \boldsymbol{Z}_h\,, \tag{3.67}$$

which can be demonstrated by writing

$$\boldsymbol{Z}_h = (\boldsymbol{P}_{\Lambda H} + \boldsymbol{P}_{\Sigma})\boldsymbol{Z}_h = \boldsymbol{P}_{\Lambda H}\boldsymbol{Z}_h + \boldsymbol{P}_{\Sigma}\boldsymbol{Z}_h = \boldsymbol{0} + \boldsymbol{P}_{\Sigma}\boldsymbol{Z}_h\,. \tag{3.68}$$

Given that the expansion of the qH-EFIE is composed of a frequency independent term and an $\mathcal{O}(k)$ remainder

$$\lim_{k\to 0} \operatorname{cond} \boldsymbol{M}\boldsymbol{Z}\boldsymbol{N} = \operatorname{cond} \boldsymbol{P}_{\Lambda H}\boldsymbol{Z}_s\boldsymbol{P}_{\Lambda H} + \boldsymbol{Z}_h\,, \tag{3.69}$$

thus, the qH formulation is clearly immune from any low frequency conditioning breakdown. The stability of this conditioning is illustrated in Figure 3.11.

Finally, the numerical stability of the qH scheme can be verified by using the scaling obtained for the physical solution in eq. (3.33) to deduce the scaling of the intermediate solution $\boldsymbol{y}_{qH}$. Given that

$$\boldsymbol{j}^{\Lambda H} = \boldsymbol{P}_{\Lambda H}\boldsymbol{N}\boldsymbol{y}_{qH} = \boldsymbol{P}_{\Lambda H}\boldsymbol{y}_{qH} \underset{k\to 0}{=} \mathcal{O}(1)\,, \tag{3.70}$$

$$\boldsymbol{j}^{\Sigma} = \boldsymbol{P}_{\Sigma}\boldsymbol{N}\boldsymbol{y}_{qH} = -\mathrm{j}k\boldsymbol{P}_{\Sigma}\boldsymbol{y}_{qH} \underset{k\to 0}{=} \mathcal{O}(k)\,, \tag{3.71}$$

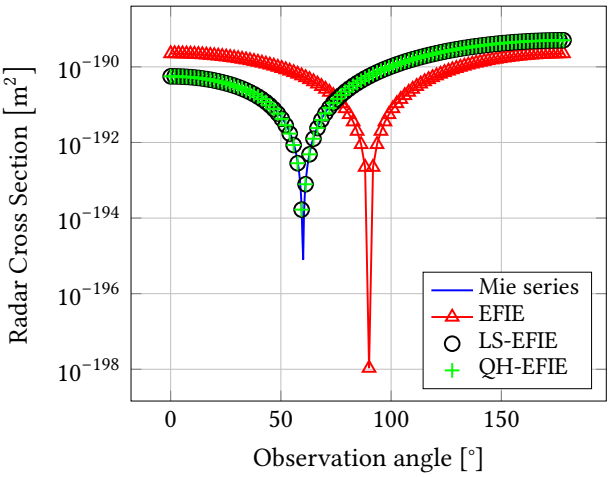

Fig. 3.10.: RCS of a PEC sphere of radius 1 m, excited by a plane wave oscillating at $1 \cdot 10^{-40}$ Hz. There is a clear mismatch between the Mie series and the EFIE solution, because of the low frequency breakdown of the formulation, while the LS-EFIE and qH-EFIE match perfectly with the Mie series.

and that the projectors have no frequency scaling, the solenoidal and non-solenoidal parts of the intermediary solution both have an $\mathcal{O}(1)$ low frequency behaviour. Hence, $\boldsymbol{y}_{qH}$ is numerically stable at low frequency. Numerical results confirm the stability and the accuracy of the far field obtained using this technique (Figure 3.10). Overall, qH projectors completely cure the low frequency breakdown while (i) not requiring the detection of global loops, allowing the overall scheme to be near-linear in complexity, and (ii) preserving the original conditioning of the EFIE matrix (Figure 3.11).

g) High Order Projectors

The objective of this chapter if to combine the overall stability of the projector schemes with the many computational improvements permitted by higher order modelling. Because the projectors are derived from $\boldsymbol{\Sigma}$, it is crucial to extend this matrix to higher order. However, even though $\boldsymbol{\Sigma}$ was efficiently built out of connectivity information, this definition does not generalize to higher orders. However, because $\boldsymbol{\Sigma}^{\mathrm{T}}$ is a discretization of the divergence operator it is possible to extend it to GWP functions. To discretize the operator, a set of scalar testing functions capable of representing any polynomial of degree p over each triangle of the dis-

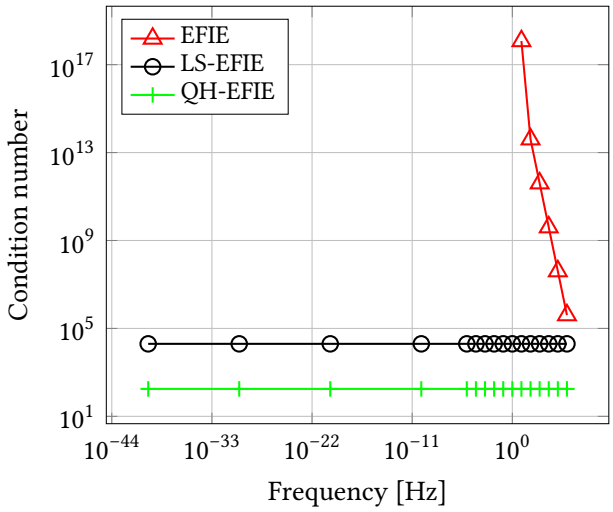

Fig. 3.11.: Evolution of the condition number of the qH-EFIE, LS-EFIE and EFIE matrices generated on a PEC sphere with radius 1 m at different frequencies. Because of numerical limitations in the computation of high condition numbers, very low frequency points are not displayed.

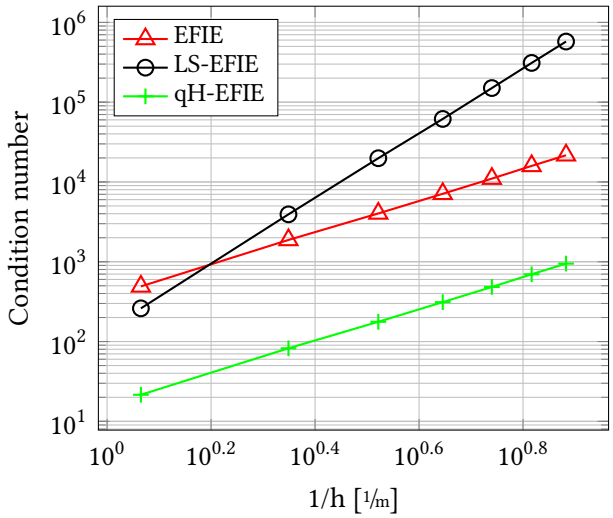

Fig. 3.12.: Evolution of the conditioning of the conditioning of the qH-EFIE, LS-EFIE and EFIE matrices with increasing refinement. The matrices correspond to a PEC sphere with radius 1 m at different levels of refinement.

cretized geometry must be constructed[4], because the divergence of GWP functions is complete to order p. Let $\{\sigma_i\}$ be one such set and $\left\{f_j^p\right\}$ be the set of vector GWP functions of order p, then

$$\left[\boldsymbol{\Sigma}^{\mathrm{T}}\right]_{ij} = \left\langle \sigma_i(\boldsymbol{r}), \nabla \cdot \boldsymbol{f}_j^p(\boldsymbol{r}) \right\rangle . \tag{3.72}$$

While this matrix has been used for extending loop star decompositions techniques to higher order [WW04], it would suffer from the same limitations as its order $p = 0$ counterparts (see Chapter 3). Instead, the divergence matrix is used to build quasi-Helmholtz projectors extending the technique prescribed in Section 3.e for RWG functions, i.e.

$$\boldsymbol{P}_{\boldsymbol{\Sigma}} = \boldsymbol{\Sigma}\left(\boldsymbol{\Sigma}^{\mathrm{T}}\boldsymbol{G}_{\sigma,\sigma}^{-1}\boldsymbol{\Sigma}\right)^{+}\boldsymbol{\Sigma}^{\mathrm{T}} , \tag{3.73}$$

$$\boldsymbol{P}_{\boldsymbol{\Lambda}} = \mathbf{I} - \boldsymbol{P}_{\boldsymbol{\Sigma}} , \tag{3.74}$$

where $\mathbf{I}$ is the identity and the terms of the Gram matrix $G_{\sigma,\sigma}$ are

$$\left[\boldsymbol{G}_{\sigma,\sigma}\right]_{ij} = \left\langle \sigma_i(\boldsymbol{r}) , \sigma_j(\boldsymbol{r}) \right\rangle . \tag{3.75}$$

Even though explicit construction of the GWP to local loops mapping $\boldsymbol{\Lambda}$ is out of the scope of this work, it is interesting to study the effect of higher order modeling on the taxonomy loop functions. While in order $p = 0$ modeling the loops are built around the vertices of the mesh (Figure 3.13a) [Vec99], additional loops appear at order $p = 1$ and $p = 2$. Starting from order $p = 1$ it is possible to construct loop functions associated to the edges of the mesh (in the same way that RWG are defined on the inner edges of the mesh), by linearly combining – after adjusting their scalings and orientations – the two GWP functions crossing the edge and the six functions defined within the two adjacent triangle cells (Figure 3.13b). The order $p = 2$ sees the appearance of a new family of functions that are defined within single cells as a linear combination of their inner functions (Figure 3.13c). The existence of these new families of functions further underlines the usefulness of the projectors that do not require their burdensome explicit computation unlike higher order loop star techniques [WW04] – in addition to not requiring the detection of the global loops of the structure. A detailed computation of the number of higher order loops is provided in [WW04] and will not be recalled here.

While the higher order qH projectors will effectively address the low frequency limitations of the EFIO, they involve the computation of a pseudo-inverse. Because

4 For instance, for order $p = 0$ the functions are the constant functions over each triangle (one per triangle) while for $p = 1$ a possible set of functions are the three pyramids defined on every edge of every triangle.

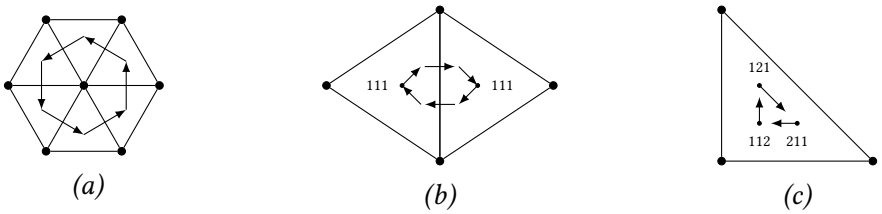

Fig. 3.13.: Different families of loop functions encountered in high order modeling. Figure 3.13a loop formed by the order $p = 0$ functions; Figure 3.13b loop formed by the vertex and inner order $p = 1$ functions over two adjacent cells; Figure 3.13c loop formed by linear combinations of the inner order $p = 2$ functions of a single cell.

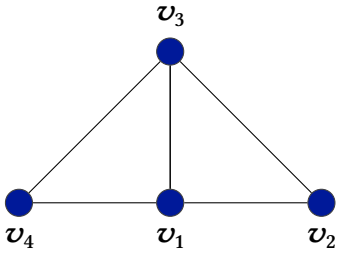

Fig. 3.14.: Simple structure composed of two symmetric triangles.

this operation is above linear complexity, it prevents usage of the projectors with fast schemes, such as the MLFMM and reduce their practical applicability. For order $p = 0$ the product $\boldsymbol{\Sigma}^{\mathrm{T}}\boldsymbol{\Sigma}$ is a graph Laplacian making it possible to evaluate the matrix vector product

$$\left(\boldsymbol{\Sigma}^{\mathrm{T}}\boldsymbol{\Sigma}\right)^{+}\boldsymbol{x}\,, \quad \boldsymbol{x} \in \mathbb{R}^{N_e}\,, \tag{3.76}$$

in near-linear complexity by leveraging multigrid techniques (see Section 3.e). However this approach is not directly generalizable to arbitrary order functions, since for order $p > 0$ the $\boldsymbol{\Sigma}^{\mathrm{T}}\boldsymbol{\Sigma}$ is no longer a graph Laplacian.

A consequent amount of time has already been dedicated to finding new techniques for performing near-linear evaluation of the generalized projectors, however results have not been conclusive yet. Several approaches have been investigated, the most promising of which is that the underlying graph Laplacian nature of the $\boldsymbol{\Sigma}^{\mathrm{T}}\boldsymbol{\Sigma}$ term could be recovered by decomposing it as Kronecker product of the order $p = 0$ Laplacian with a local, higher order, connectivity matrix.

To illustrate this approach, the elementary case of a structure composed of two triangles (Figure 3.14) is considered. It is clear that this structure will exhibit:

at order p = 0 one RWG function and two patch functions (one on each triangle);

at order p = 1 six GWP functions (two on the edge ($\boldsymbol{v}_1$, $\boldsymbol{v}_3$) and two on each triangle) and six pyramid functions (three on each triangle).

The block structure of the order $p = 1$ divergence matrix is straightforward to deduce from these consideration

$$\boldsymbol{\Sigma}_1 = \begin{bmatrix} \boldsymbol{A} & \boldsymbol{B} \\ \boldsymbol{C} & \boldsymbol{0} \\ \boldsymbol{0} & \boldsymbol{D} \end{bmatrix} \tag{3.77}$$

where $\boldsymbol{A}$ and $\boldsymbol{B}$ correspond to the contributions of the two edge GWP functions respectively tested from the pyramids of each triangle and $\boldsymbol{C}$ and $\boldsymbol{D}$ are the contributions of the inner GWP functions tested on the triangle on which they are defined. From this expression, it is possible to deduce the structure of $\boldsymbol{\Sigma}_1^{\mathrm{T}}\boldsymbol{\Sigma}_1$ as a block product

$$\boldsymbol{\Sigma}_1^{\mathrm{T}}\boldsymbol{\Sigma}_1 = \begin{bmatrix} \boldsymbol{A}^{\mathrm{T}}\boldsymbol{A} + \boldsymbol{C}^{\mathrm{T}}\boldsymbol{C} & \boldsymbol{A}^{\mathrm{T}}\boldsymbol{B} \\ \boldsymbol{B}^{\mathrm{T}}\boldsymbol{A} & \boldsymbol{B}^{\mathrm{T}}\boldsymbol{B} + \boldsymbol{D}^{\mathrm{T}}\boldsymbol{D} \end{bmatrix}. \tag{3.78}$$

In addition, given the appropriate normalization of the functions involved, $\boldsymbol{B} = -\boldsymbol{A}$ and $\boldsymbol{D} = \boldsymbol{C}$ and thus eq. (3.78) becomes

$$\boldsymbol{\Sigma}_1^{\mathrm{T}}\boldsymbol{\Sigma}_1 = \begin{bmatrix} \boldsymbol{A}^{\mathrm{T}}\boldsymbol{A} + \boldsymbol{C}^{\mathrm{T}}\boldsymbol{C} & -\boldsymbol{A}^{\mathrm{T}}\boldsymbol{A} \\ -\boldsymbol{A}^{\mathrm{T}}\boldsymbol{A} & \boldsymbol{A}^{\mathrm{T}}\boldsymbol{A} + \boldsymbol{C}^{\mathrm{T}}\boldsymbol{C} \end{bmatrix}. \tag{3.79}$$

In this extremely simple case this matrix form is generated by the order $p = 0$ connectivity information in the form of $\boldsymbol{\Sigma}_0^{\mathrm{T}}\boldsymbol{\Sigma}_0$ and higher order contributions $\boldsymbol{A}^{\mathrm{T}}\boldsymbol{A}$ and $\boldsymbol{C}^{\mathrm{T}}\boldsymbol{C}$

$$\begin{aligned} \boldsymbol{\Sigma}_1^{\mathrm{T}}\boldsymbol{\Sigma}_1 &= \begin{bmatrix} \boldsymbol{A}^{\mathrm{T}}\boldsymbol{A} & -\boldsymbol{A}^{\mathrm{T}}\boldsymbol{A} \\ -\boldsymbol{A}^{\mathrm{T}}\boldsymbol{A} & \boldsymbol{A}^{\mathrm{T}}\boldsymbol{A} \end{bmatrix} + \begin{bmatrix} \boldsymbol{C}^{\mathrm{T}}\boldsymbol{C} & \boldsymbol{0} \\ \boldsymbol{0} & \boldsymbol{C}^{\mathrm{T}}\boldsymbol{C} \end{bmatrix} \\ &= \boldsymbol{\Sigma}_0^{\mathrm{T}}\boldsymbol{\Sigma}_0 \otimes \boldsymbol{A}^{\mathrm{T}}\boldsymbol{A} + \mathbf{I} \otimes \boldsymbol{C}^{\mathrm{T}}\boldsymbol{C}\,, \end{aligned} \tag{3.80}$$

where $\otimes$ denotes the Kronecker product. The structure of $\boldsymbol{\Sigma}_1^{\mathrm{T}}\boldsymbol{\Sigma}$ and $\boldsymbol{\Sigma}_0^{\mathrm{T}}\boldsymbol{\Sigma}_0 \otimes \boldsymbol{A}^{\mathrm{T}}\boldsymbol{A}$ are illustrated in Figure 3.15 along with their relative difference, which underlines the effect of the high order perturbation $\boldsymbol{C}^{\mathrm{T}}\boldsymbol{C}$. The decomposition in Kronecker products is particularly promising thanks to the well know result about the pseudo-inverse of a Kronecker product

$$(\boldsymbol{M} \otimes \boldsymbol{N})^{+} = \boldsymbol{M}^{+} \otimes \boldsymbol{N}^{+}\,, \tag{3.81}$$

which could be used as a way to invert the order $p = 1$ product by inverting the small high order perturbations and leveraging on multigrid techniques for inverting

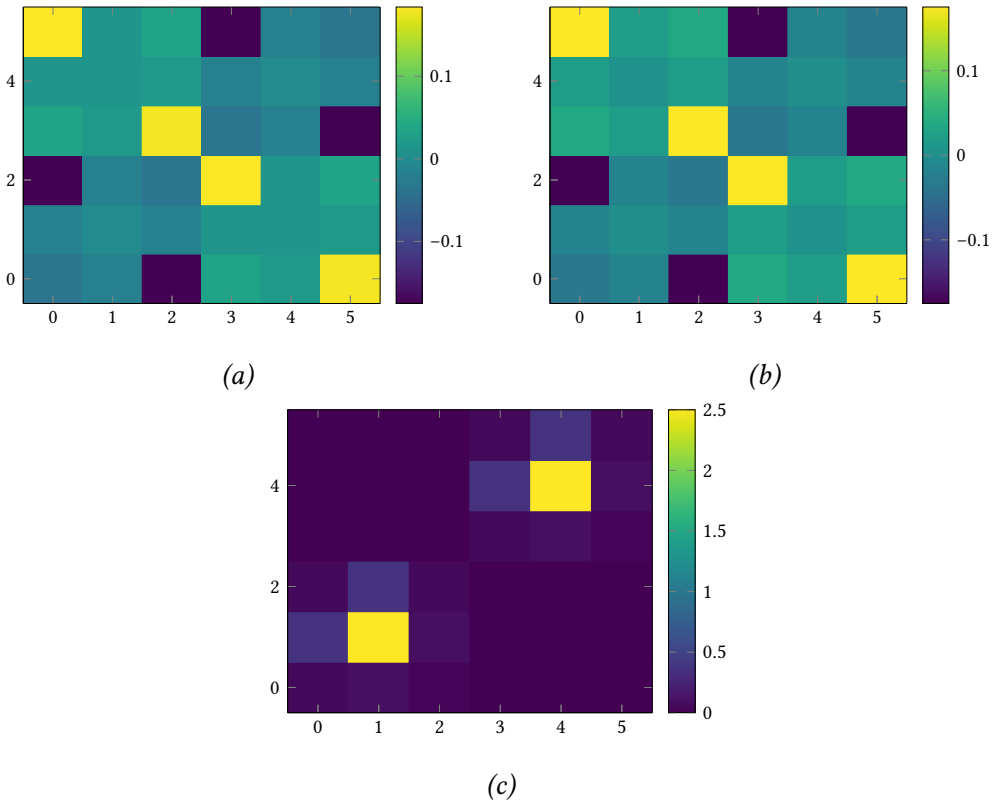

(a) *(b)*

(c)

Fig. 3.15.: Illustration of the matrices computed on a structure composed of two symmetric triangles (Figure 3.14) : order $p = 1$ product $\boldsymbol{\Sigma}_1^{\mathrm{T}}\boldsymbol{\Sigma}_1$ (Figure 3.15a), tentative reconstruction of the $\boldsymbol{\Sigma}_1^{\mathrm{T}}\boldsymbol{\Sigma}_1$ as $\boldsymbol{\Sigma}_0^{\mathrm{T}}\boldsymbol{\Sigma}_0 \otimes \boldsymbol{A}^{\mathrm{T}}\boldsymbol{A}$ (Figure 3.15b) and relative error between the order $\boldsymbol{\Sigma}_1^{T}\boldsymbol{\Sigma}_1$ and the corresponding Kronecker product (Figure 3.15c) which underlines the non-negligible effect of $\boldsymbol{C}^{\mathrm{T}}\boldsymbol{C}$.

the order $p = 0$ contribution. Several issues are preventing direct use of this approach: (i) a way to handle the $\mathbf{I} \otimes \boldsymbol{C}^{\mathrm{T}}\boldsymbol{C}$ perturbation has not been found yet; (ii) the structure of eq. (3.79) seems to globally hold for more complex structures, but the ordering of the functions and their normalizations make its recovery more challenging, especially for closed structures. In conclusion the Kronecker technique only seems applicable to very simple geometries but a more thorough study needs to be performed before discarding it. As of this writing these investigations are underway. Other approaches based on iterative solutions exploiting the nullspaces of the perturbations matrices are also being considered but are at very early stages of investigation and thus will not be detailed here.

h) Implementation Details

The numerical results presented so-far have relied on implementation details that have not been presented in the previous sections but are necessary for attaining optimal stability of the schemes.

The computation of the plane-wave RHS at low frequencies requires particular handling of the exponential term. The general expression of this excitation is

$$[\boldsymbol{v}_e]_i = e_0 \iint_{f_i} \mathrm{e}^{-\mathrm{j}k\hat{\boldsymbol{k}}\cdot\boldsymbol{r}'} \boldsymbol{f}_i(\boldsymbol{r}') \cdot \hat{\boldsymbol{u}} \mathrm{d}\boldsymbol{r}' \,, \tag{3.82}$$

which should be decomposed into solenoidal and non-solenoidal contributions using the qH projectors

$$\boldsymbol{v}_{\boldsymbol{\Sigma}} = \boldsymbol{P}_{\boldsymbol{\Sigma}}\boldsymbol{v}_e \,, \tag{3.83}$$

$$\boldsymbol{v}_{\Lambda H} = -\frac{1}{ik}\boldsymbol{P}_{\Lambda H}\boldsymbol{v}_e \,. \tag{3.84}$$

Following the reasoning behind eq. (3.38), the exponential in the solenoidal term of the RHS should be computed using $x \mapsto \big(\exp(x) - 1\big) + 1$, where the second term is null. This relation must be explicitly enforced because the RHS will scale as $\mathcal{O}(k)$ for solenoidal functions, and, at low frequencies, this contribution will be hidden by the 0-th order term of the Taylor series expansion of the exponential. Additionally, $x \mapsto \big(\exp(x) - 1\big)$ can not be computed naively as a subtraction, to avoid further numerical cancellations, specialized implementations must be employed. In most scientific computing libraries such implementations are available under the name `expm1`. All these considerations lead to the following expression of the solenoidal RHS

$$[\boldsymbol{P}_{\Lambda H}\boldsymbol{V}_{\boldsymbol{E}}]_i = e_0 \iint_{l_i} \mathtt{expm1}\Big(-\mathrm{j}k\hat{\boldsymbol{k}} \cdot \boldsymbol{r}'\Big) \boldsymbol{l}_i(\boldsymbol{r}') \cdot \hat{\boldsymbol{u}} \mathrm{d}\boldsymbol{r}' \,, \tag{3.85}$$

and the solenoidal contribution remains unchanged.

The far field is computed in a similar way. According to eq. (3.35) the far field scattered by a solenoidal current is

$$(\mathcal{F}\boldsymbol{l}_i)(\boldsymbol{r}) = -\frac{\mathrm{j}k\eta}{4\pi\|\boldsymbol{r}\|}\mathrm{e}^{-\mathrm{j}k\|\boldsymbol{r}\|}\left(\hat{\boldsymbol{\theta}}\hat{\boldsymbol{\theta}} + \hat{\boldsymbol{\phi}}\hat{\boldsymbol{\phi}}\right)\cdot\iint_{l_i}\boldsymbol{l}_i(\boldsymbol{r}')\mathrm{e}^{\mathrm{j}k\hat{\boldsymbol{r}}\cdot\boldsymbol{r}'}\mathrm{d}\boldsymbol{r}'\,, \tag{3.86}$$

which, for the same reasons as for the plane-wave excitation, should be computed as

$$(\mathcal{F}\boldsymbol{l}_i)(\boldsymbol{r}) = -\frac{\mathrm{j}k\eta}{4\pi\|\boldsymbol{r}\|}\mathrm{e}^{-\mathrm{j}k\|\boldsymbol{r}\|}\left(\hat{\boldsymbol{\theta}}\hat{\boldsymbol{\theta}} + \hat{\boldsymbol{\phi}}\hat{\boldsymbol{\phi}}\right)\cdot\iint_{l_i}\boldsymbol{l}_i(\boldsymbol{r}')\,\mathtt{expm1}\left(\mathrm{j}k\hat{\boldsymbol{r}}\cdot\boldsymbol{r}'\right)\mathrm{d}\boldsymbol{r}'\,. \tag{3.87}$$

The computation of the impedance matrix the qH-EFIE also requires some special care. Because of limitations of finite precision arithmetic, it is necessary to explicitly cancel out the terms listed in eq. (3.66) in the development of $\boldsymbol{MZN}$, hence the impedance matrix should only be computed as detailed in eq. (3.65). This requirement can be explained by considering that in finite precision the problematic terms are not exactly null:

$$\|\boldsymbol{P}_{\Lambda H}\boldsymbol{Z}_h\boldsymbol{P}_{\Lambda H}\| = \epsilon_{\mathrm{MACH}}\,, \tag{3.88}$$

where ϵ_{MACH} is typically around $1\cdot10^{-16}$, meaning that, because of their frequency scaling they will be artificially amplified

$$\|\frac{1}{\mathrm{j}k}\boldsymbol{P}_{\Lambda H}\boldsymbol{Z}_h\boldsymbol{P}_{\Lambda H}\| = \frac{\epsilon_{\mathrm{MACH}}}{k}\,, \tag{3.89}$$

when the frequency is low enough. For instance, at a frequency of $1\cdot10^{-40}$ Hz the norm of the term becomes of the order of $1\cdot10^{31}$.

Finally, as explained in Section 3.e, the projectors can be computed in near-linear complexity thanks to multi-grid preconditioning [LB12; NN12]. This technique being outside the scope of the chapter the reader is referred to *pyamg* [OS18] and *AGMG* [Not] which are two well-established and freely available implementations of the technique.

i) Numerical Results

In this section, the different properties of the higher order qH formulation are illustrated through a series of numerical examples.

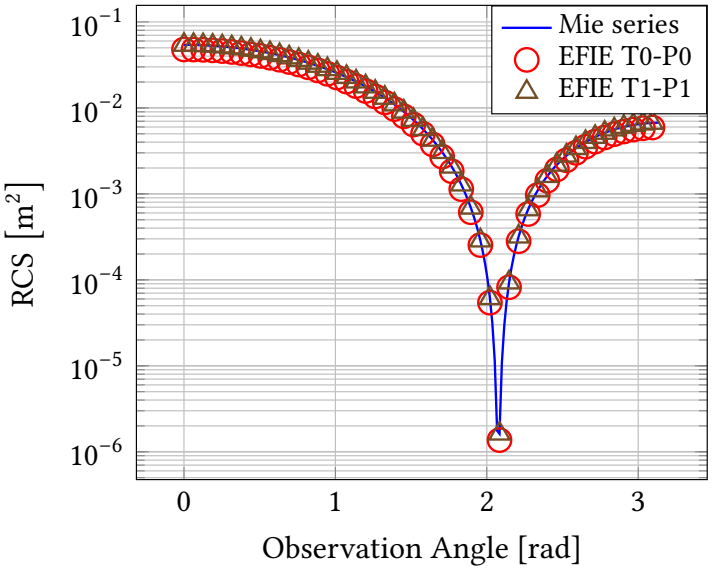

Fig. 3.16.: Far field scattered by a sphere of radius $\lambda/30$ – where λ is the wavelength of the impinging plane wave – using order $p = 0$ and $p = 1$ formulations. The Mie series are used as reference. Both formulations were computed with 75 element per wavelength but it is clear that the higher order formulation yields more accurate results for an equivalent discretization.

To verify the correctness of the order $p = 0$ and $p = 1$ qH projected formulations and of their implementations, the far field scattered by a sphere is verified against the Mie series at relatively low frequency (Figure 3.16). As expected both formulations converge to the analytical solution with the higher order formulation converging faster.

The low frequency stability of the conditioning of all formulations has been verified on both a sphere and a torus (Figures 3.17a and 3.17b, respectively) to control that global loops are appropriately handled by the new schemes. These results indicate that the projected formulations do not suffer from the low frequency ill-conditioning that their standard counterparts exhibit. In addition, the current cancellations introduced in Section 3.d.β.1 are also addressed by the qH schemes. The numerical stability of the currents computed with the new formulations has been studied at low frequency ($1 \cdot 10^{-10}$ Hz) by comparing the non-solenoidal and solenoidal parts of the solutions of order $p = 1$ of qH and non-qH formulations (Figures 3.18a and 3.18b). The results demonstrate that the non-solenoidal parts of the solutions are in agreement and have not been cancelled out in neither formulations. However, the solenoidal part of the standard EFIE has undergone

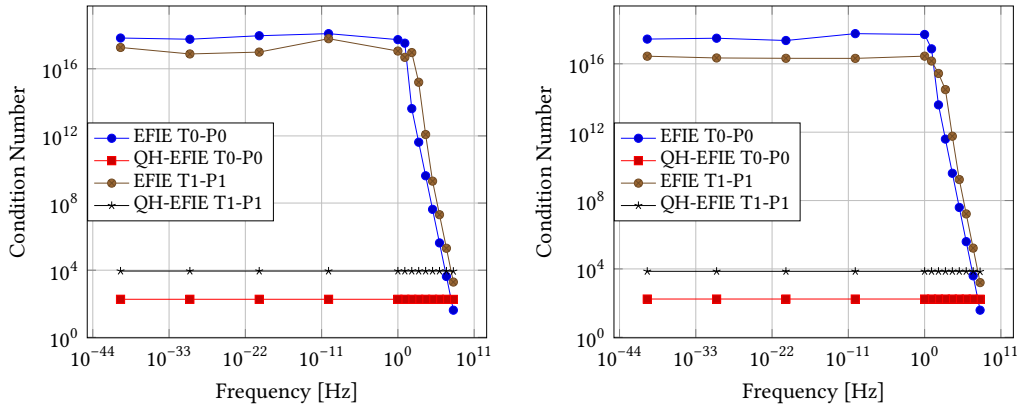

Fig. 3.17.: Evolution of the condition number of the order $p = 0$ and $p = 1$ formulations until extremely low frequencies, with and without qH projectors. The simulated structures are a sphere of radius 1 m discretized with a mesh parameter $h = 0.4$ m (Figure 3.17a) and a torus of large radius 1.3 m and small radius 1 m (Figure 3.17b). The flat condition number of the non-qH projected formulation is caused by numerical saturation in the computation of the condition numbers.

numerical cancellation and could not be recovered. These results are only presented for the case of the toroidal structure, but similar ones have been obtained for order $p = 0$ and $p = 1$ on both spherical and toroidal structures; the remaining results are not presented here for conciseness.

Finally, the dense discretization stability of the projectors has been verified on both a sphere and a torus by performing a refinement analysis of the condition number of the projected and non projected formulations (Figures 3.19a and 3.19b). Because the projectors have a flat spectrum, they are expected not to degrade further the dense discretization breakdown that intrinsically plagues the EFIO. Given that the projected and non-projected formulations exhibit a quadratic growth of their conditioning with increasing discretization, this property is verified.

j) Conclusion

In this chapter the low frequency breakdown of the EFIE and its causes have been introduced and analysed. This study was followed by a presentation of the traditional LS decomposition and its acting principle. However, because it is unpractical in complex scenarios a qH projectors based solution that alleviates all the limitations of the original scheme was introduced. The qH projectors have

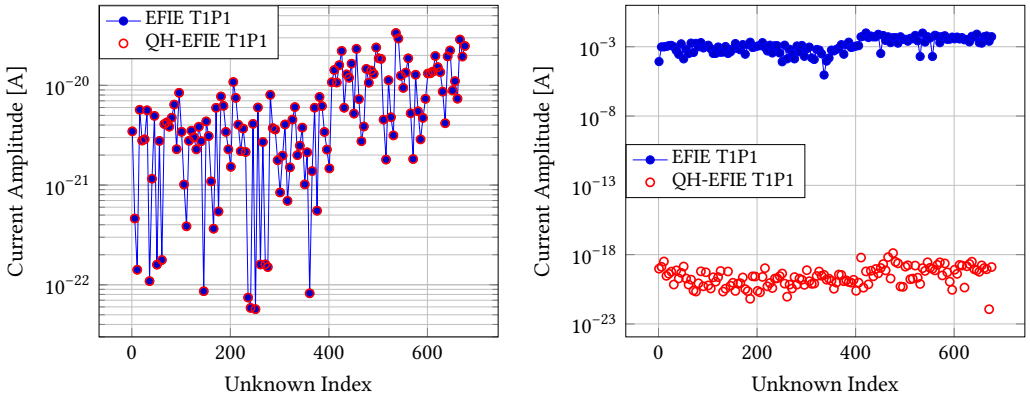

Fig. 3.18.: Illustration of cancellations occurring in the solenoidal part of the current (Figure 3.18b) of the non-qH EFIE of order $p = 1$. The non-solenoidal part of the current is fully preserved (Figure 3.18a). These currents have been obtained for a torus of large radius 1.3 m and small radius 1 m, discretized with elements of average edge length 0.4 m at $1 \cdot 10^{-10}$ Hz. Similar results can be obtained for order $p = 0$ and are omitted for conciseness.

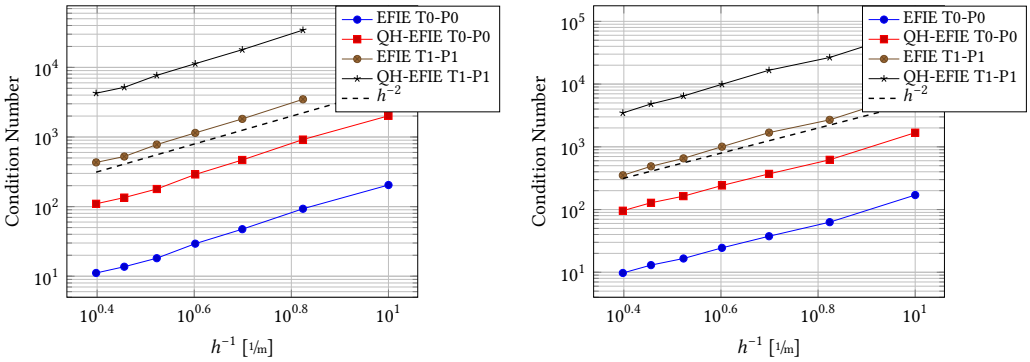

Fig. 3.19.: Dense discretization behaviour of the condition number of the order $p = 0$ and $p = 1$ EFIE formulation, with and without qH projectors. To verify the stability of the results with regards to global loops, all formulations were applied to a sphere of radius 1 meter (Figure 3.19a) and a torus of large radius 1.3 m and small radius 1.0 m (Figure 3.19b) simulated at $1 \cdot 10^7$ Hz.

then been extended to handle higher order discretization, in order to form highly efficient and accurate EFIE formulations. To allow the reader to reproduce the presented results, some of the most critical implementation details required for stability until arbitrarily low frequency were explained. Computational techniques required to compute the projectors in near-linear time have also been presented for order $p = 0$. The fast computation of the projectors for order $p > 0$ is still the topic of active investigations and is crucial for applying the projectors to the largest application scenarios.

In Chapter 4 the projectors will be extended to the case of wire-like structures discretized with 1-dimensional basis functions. Finally, in Chapter 5 they will be used to build a fully stabilized and extremely accurate CFIE formulation.

Chapter 4

Low Frequency and Refinement Regularization for the Thin-Wire EFIE

Thanks to its stability and efficiency, the wire Electric Field Integral Equation has been widely used to simulate scattering by wire-like structures. However, similarly to its surface counterpart, this formulation suffers from both a dense discretization and a low-frequency breakdown, which adversely impact its accuracy and solvability. In this chapter, new formulations, immune from both breakdowns, are introduced for the exact and reduced kernel formulations. These formulations rely on an extension to wire structures of the surface quasi-Helmholtz projectors, on a spectral analysis of both kernels in a canonical case and on a carefully chosen hierarchical preconditionner. The spectral analysis demonstrates the existence of two distinct simulation regimes, only one of which remains stable at high refinement. These new formulations have the strong benefit of not requiring the identification of global loops in the structure. Numerical results illustrate the regularization properties of our scheme.

a) Introduction

Thanks to its stability and computational efficiency, the thin-wire electric field integral equation (wire EFIE) has been widely used, in research and in commercial solvers, for simulating scattering problems by wire-like Perfect Electrical Conductors (PEC) structures. Provided that the simulated structures are thin enough not to have any radial current [WC06], the wire EFIE is more computationally efficient and stable than the traditional surface EFIE. This is why most solvers include hybrid wire-surface solvers [VW11].

Two different formulations of the wire EFIE, based on two different kernels, have been widely studied in the literature [WC06; CWR06; DDF01; MW06; FW01; BH07; WB76]. The so-called *exact* kernel has been proven to yield relatively well conditioned systems thanks to its logarithmic singularity [Pea75; WHW94; Ryn00], and is the one recommended [Ryn92; MW06] for accurate and stable simulations,

regardless of the Right Hand Side (RHS). However this kernel includes an azimuthal integral on the wire surface making it computationally expensive. This is why the *reduced* kernel, which assumes azimuthal invariance of the current density, has been introduced. However there has been a long discussion amongst the community regarding its solvability [Jon81; FPA08; Fik+11; PFM10; Fik01; BT07]. It turns out that the reduced kernel wire EFIE is ill-posed and only admits solutions for smooth enough RHS [FPA08]. Furthermore the stability of the solution it yields is also dependant on the wire radius of the simulated geometry [BT07]. Hence, extra caution should be used when dealing with the reduced kernel wire EFIE.

Despite its advantages, the wire EFIE shares some of the limitations of its surface counterpart. Most notably, it suffers from both a low-frequency breakdown [CC02] and a dense discretization breakdown [BT07]. When discretized via BEM, these issues will cause the EFIE to yield high condition number matrices. This, in turn, makes it difficult and expensive, or in extreme cases impossible, to solve the discretized system with iterative solvers. These two issues should be addressed in order for the wire EFIE to retain its advantages when simulating highly refined structures and/or structures at low frequency.

The low frequency breakdown is the consequence of an ill-scaling of the solenoidal and non-solenoidal parts of the EFIE operator. Not only does it cause the condition number of the EFIE matrix to increase drastically when the frequency goes down, it also causes numerical cancellations in the solution. The accuracy of the solution will then degrade until, at low enough frequency, resolution becomes impossible. The low frequency breakdown has traditionally been addressed via loop-star decomposition [VVW09], which is used to separate the solenoidal and non-solenoidal parts of the operator, in order to re-scale them appropriately. While effective, this solution requires the detection of global loops, which can make it inconvenient for complex structures. In order to address this limitation [And+13b] has recently introduced, for the surface EFIE, another technique which relies on projectors to perform the quasi-Helmholʒ decomposition and the re-scaling. These quasi-Helmholʒ projectors have the advantage of not requiring any loop detection, making them a good candidate for a scalable formulation.

Several contributions have focused on speeding up the resolution of the wire EFIE, in order to compensate the slowdown caused by the high-refinement breakdown. Many of these contributions [LL98; NGT97; GMS06; RBK15] have been using hierarchical basis functions in order to sparsify the BEM matrix. However this kind of techniques will degrade the solution, given that they rely on thresholding the elements of the impedance matrix. There have also been investigations on addressing the high-refinement breakdown directly. For instance [BT07] notices that, in a particular regime of the equation, a Laplacian preconditioner can cure

the high-refinement breakdown.

This chapter introduces, for both kernel, fully regularized wire EFIE formulations, immune from both breakdowns (in the amendable regime), that do not require the search for global loops. The low frequency regularization has been achieved by extending the quasi-Helmholtz projectors to wire structures. The high-refinement regularization relies on the usage of a carefully selected hierarchical preconditioner. The selection of the right hierarchical basis derives from a complete spectral analysis of the spectral behaviour of the exact and reduced kernel wire EFIE formulations. To the best of our knowledge no such formulation has yet been introduced.

This contribution is organized as follows. Background and notations are introduced in Section 4.b. In Section 4.c the spectral analysis of the exact and reduced kernel wire EFIE is developed. The extension of the quasi-Helmholtz projectors to wire structures is presented in Section 4.d and the fully regularized formulations are introduced in Section 4.f along with details related to their implementation in Section 4.g. Finally Section 4.h contains numerical results that illustrate the properties of the newly introduced formulations.

b) Thin-Wire EFIE Formulation

Let a PEC wire structure of length L, external surface S and radius a reside in a space of permittivity ϵ and permeability μ. Any incident electric field $\boldsymbol{e}^i$ impinging on the wire will induce a surface electric current density $\boldsymbol{j}$ radiating a scattered electric field $\boldsymbol{e}^s$. If a is small compared to the wavelength λ, the wire can be modeled by a curve l of length L, on which the current density $\boldsymbol{j}$ can be represented in terms of an unknown filamentary current $\boldsymbol{i}(\boldsymbol{r}) = 2\pi a \boldsymbol{j}(\boldsymbol{r})$, oriented along the wire axis, with no azimuthal variation [BW75]. In particular this means that the current can be expressed as $\boldsymbol{i}(\boldsymbol{r}) = i(\boldsymbol{r})\hat{\boldsymbol{l}}(\boldsymbol{r})$, where $\hat{\boldsymbol{l}}(\boldsymbol{r})$ is the unit tangent vector along the curve l. Under these assumptions the tangential part of the standard surface EFIE

$$-\mathrm{j}k\eta_0 \hat{\boldsymbol{l}}(\boldsymbol{r}) \cdot \left[\left(\mathcal{T}_s \boldsymbol{j}\right)(\boldsymbol{r}) + \frac{1}{k^2} \left(\mathcal{T}_h \boldsymbol{j}\right)(\boldsymbol{r}) \right] = -\hat{\boldsymbol{l}}(\boldsymbol{r}) \cdot \boldsymbol{e}^i \,, \tag{4.1}$$

where the singular and hyper-singular operators $\mathcal{T}_s$ and $\mathcal{T}_h$ are respectively defined as

$$\left(\mathcal{T}_s \boldsymbol{j}\right)(\boldsymbol{r}) = \iint_\Gamma \boldsymbol{j}(\boldsymbol{r}') \frac{\mathrm{e}^{-\mathrm{j}k\|\boldsymbol{r}-\boldsymbol{r}'\|}}{4\pi\|\boldsymbol{r}-\boldsymbol{r}'\|} \mathrm{d}\boldsymbol{r}' \tag{4.2}$$

and

$$\left(\mathcal{T}_h \boldsymbol{j}\right)(\boldsymbol{r}) = \nabla \iint_{\Gamma} \nabla' \cdot \boldsymbol{j}\left(\boldsymbol{r}'\right) \frac{\mathrm{e}^{-\mathrm{j}k\|\boldsymbol{r}-\boldsymbol{r}'\|}}{4\pi\|\boldsymbol{r}-\boldsymbol{r}'\|} \mathrm{d}\boldsymbol{r}' \,, \tag{4.3}$$

can be simplified as

$$-\mathrm{j}k\eta_0 \left[\int_l \hat{\boldsymbol{l}}(\boldsymbol{r}) \cdot \hat{\boldsymbol{l}}\left(\boldsymbol{r}'\right) i\left(\boldsymbol{r}'\right) K_{\mathrm{ex}}\left(\boldsymbol{r}-\boldsymbol{r}'\right) \mathrm{d}l' + \frac{1}{k^2} \hat{\boldsymbol{l}}(\boldsymbol{r}) \cdot \nabla \int_l \nabla' \cdot \left(\hat{\boldsymbol{l}}\left(\boldsymbol{r}'\right) i\left(\boldsymbol{r}'\right) \right) K_{\mathrm{ex}}\left(\boldsymbol{r}-\boldsymbol{r}'\right) \mathrm{d}l' \right] = -\hat{\boldsymbol{l}}(\boldsymbol{r}) \cdot \boldsymbol{e}^i \,, \tag{4.4}$$

where

$$K_{\mathrm{ex}}\left(\boldsymbol{r}-\boldsymbol{r}'\right) = \frac{1}{2\pi} \int_{-\pi}^{\pi} \frac{\mathrm{e}^{-\mathrm{j}k\|\boldsymbol{r}-\boldsymbol{r}'\|}}{4\pi\|\boldsymbol{r}-\boldsymbol{r}'\|} \mathrm{d}\theta' \tag{4.5}$$

is the exact kernel of the wire EFIE and θ indicates the azimuthal direction along the wire cross-sections. To allow for numerical resolution of the problem, the wire is discretized into N_s segments s_m of average length h. The current can then be approximated as a sum of N triangle basis functions $\{\Lambda_m\}$

$$i(\boldsymbol{r}) \approx \sum_{m=0}^{N} \alpha_m \Lambda_m(\boldsymbol{r}) \,. \tag{4.6}$$

The triangle functions are defined, for each pair of segments s_m^+ and s_m^- sharing a vertex $\boldsymbol{v}_m$ and which other vertex is respectively $\boldsymbol{v}^+$ and $\boldsymbol{v}^-$ (Figure 4.1), as

$$\Lambda(\boldsymbol{r}) = \begin{cases} \dfrac{\|\boldsymbol{r}-\boldsymbol{v}^+\|}{\|\boldsymbol{v}_m-\boldsymbol{v}^+\|} & \text{for } \boldsymbol{r} \in s_m^+ \\ 1 - \dfrac{\|\boldsymbol{r}-\boldsymbol{v}^-\|}{\|\boldsymbol{v}_m-\boldsymbol{v}^-\|} & \text{for } \boldsymbol{r} \in s_m^- \\ 0 & \text{otherwise;} \end{cases} \tag{4.7}$$

This discretization is combined with a Galerkin scheme, yielding the matrix system

$$\boldsymbol{Z}\boldsymbol{i} = \left(-\mathrm{j}k\eta_0 \boldsymbol{Z}_s - \frac{\eta_0}{\mathrm{j}k} \boldsymbol{Z}_h \right) \boldsymbol{i} = \boldsymbol{v}_e \,, \tag{4.8}$$

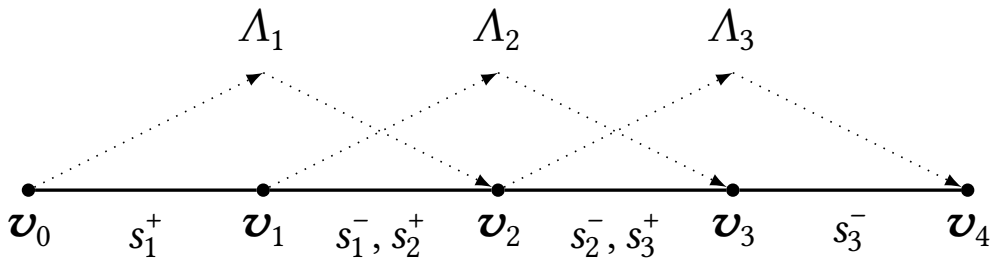

Fig. 4.1.: Illustration of hat basis functions, the dotted lines indicate the value of the function on the corresponding segments.

where

$$[\boldsymbol{Z}_s]_{mn} = \int_{\Lambda_m} \Lambda_m(\boldsymbol{r})\hat{\boldsymbol{l}}_m(\boldsymbol{r}) \cdot \int_{\Lambda_n} \Lambda_n(\boldsymbol{r}')\hat{\boldsymbol{l}}_n(\boldsymbol{r}')K_{\text{ex}}(\boldsymbol{r}-\boldsymbol{r}')\mathrm{d}\boldsymbol{r}'\mathrm{d}\boldsymbol{r}\,, \tag{4.9}$$

$$[\boldsymbol{Z}_h]_{mn} = \int_{\Lambda_m} \frac{\mathrm{d}\Lambda_m(\boldsymbol{r})}{\mathrm{d}l} \int_{\Lambda_n} \frac{\mathrm{d}\Lambda_m(\boldsymbol{r}')}{\mathrm{d}l'} K_{\text{ex}}(\boldsymbol{r}-\boldsymbol{r}')\mathrm{d}\boldsymbol{r}'\mathrm{d}\boldsymbol{r}\,, \tag{4.10}$$

$$[\boldsymbol{v}_e]_m = -\int_{\Lambda_m} \Lambda_m(\boldsymbol{r})\hat{\boldsymbol{l}}(\boldsymbol{r}) \cdot \boldsymbol{e}^i(\boldsymbol{r})\mathrm{d}\boldsymbol{r}\,, \tag{4.11}$$

$\boldsymbol{Z} = \left(-\mathrm{j}k\eta_0\boldsymbol{Z}_s - \eta_0/(\mathrm{j}k)\boldsymbol{Z}_h\right)$ and $[\boldsymbol{i}]_m = \alpha_m$.

Another widely used [Jin15] formulation for wire EFIE can be derived in a similar fashion, with the exception that testing of the equation is performed on the axis of the wire – and no longer on its surface – and the radius a is considered to be very small. The *reduced kernel* of this approximated formulation follows directly from K_{ex},

$$K_{\text{red}}(\boldsymbol{r}-\boldsymbol{r}') = \frac{\mathrm{e}^{-\mathrm{j}k\|\boldsymbol{r}-\boldsymbol{r}'\|}}{4\pi\|\boldsymbol{r}-\boldsymbol{r}'\|}\,. \tag{4.12}$$

c) Spectral Analysis

Several excellent works in literature have been analyzing the solvability of the reduced kernel EFIE concluding that it is questionable in general and that a naive use of this formulation may result in the well-known problem of numerical oscillations [Fik+11; PFM10; BT07; DDF01]. At the same time, the exact kernel EFIE has been traditionally considered to have a non critical spectrum. This section is propaedeutical to the next ones and it has the purpose to show that: i) the exact kernel EFIE still has a non-bounded condition number which, as a consequence, requires

regularization; ii) under certain discretization conditions, the ill-posedness of the reduced kernel EFIE can be treated by suitably tuned preconditioning. Regularization techniques for both cases will then be the subject of Section 4.e.

α) Spectrum of the Wire Equations

The required characterizations of the spectra of both exact and reduced kernels will be obtained on the infinite wire, effectively adapting to the case of interest the strategy in [FW01]. A generalization of the results to the finite wire case could be obtained, however, by leveraging on the strategies similar to those presented in [BvE12].

It is well known that for an infinite $\hat{z}$-oriented dipole of radius a the eigenvalues of the vector potential for the infinite wire are

$$\lambda^{\xi}_{\mathcal{T}_s,K} = \sqrt{2\pi}\mathfrak{F}[K]\big(\xi\big)\,, \tag{4.13}$$

where, for notation simplicity, K refers to either K_{ex} or K_{red} and where $\mathfrak{F}[K]$ denotes the Fourier transform of K. This result can be derived by first considering that

$$(\mathcal{T}_s i)(z) = \int_{-\infty}^{\infty} i(\boldsymbol{r}')K(\boldsymbol{r},\boldsymbol{r}')\mathrm{d}z = (i * K)(z)\,, \tag{4.14}$$

which after applying the Fourier transform and using the convolution theorem yields

$$\mathfrak{F}\big[(\mathcal{T}_s i)(z)\big]\big(\xi\big) = \sqrt{2\pi}\mathfrak{F}\big[i(z)\big]\big(\xi\big)\cdot\mathfrak{F}\big[K(z)\big]\big(\xi\big)\,. \tag{4.15}$$

Applying the ansatz $i(z) = \mathrm{e}^{\mathrm{j}nz}$ and noticing that $\mathfrak{F}\big[i(z)\big](\xi) = \sqrt{2\pi}\delta(n-2\pi\xi)$, the previous eq. (4.15) becomes

$$\mathfrak{F}\big[(\mathcal{T}_s i)(z)\big]\big(\xi\big) = \sqrt{2\pi}\mathfrak{F}\big[K(z)\big]\big(\xi\big)\cdot\sqrt{2\pi}\delta\big(n-2\pi\xi\big)\,, \tag{4.16}$$

$$\mathfrak{F}\big[(\mathcal{T}_s i)(z)\big]\big(\xi\big) = \mathfrak{F}\big[K(z)\big]\left(\frac{k}{2\pi}\right)\cdot\delta(\xi-\frac{n}{2\pi})\,, \tag{4.17}$$

and, using the inverse Fourier transform,

$$(\mathcal{T}_s i)(z) = \sqrt{2\pi}\mathfrak{F}\big[K(z)\big]\left(\frac{n}{2\pi}\right)\cdot\mathrm{e}^{\mathrm{j}nz} \tag{4.18}$$

hence the eigenvalues of $\mathcal{T}_s$ are

$$\lambda^{n}_{\mathcal{T}_s,K} = \sqrt{2\pi}\mathfrak{F}[K]\left(\frac{n}{2\pi}\right)\,. \tag{4.19}$$

For simplifying further the analysis it is sufficient to consider only the singular parts of the kernels since their dynamic remainder will only contribute a compact perturbation of the static spectrum. In addition, it is trivial to show that, in the case of an infinite z-oriented antenna,

$$\|\boldsymbol{r} - \boldsymbol{r}'\|^2 = 2a^2\Big(1 - \cos\big(\theta - \theta'\big)\Big) + \big(z - z'\big)^2 \tag{4.20}$$

and under the thin wire approximation

$$\|\boldsymbol{r} - \boldsymbol{r}'\|^2 = a^2 + z^2\,. \tag{4.21}$$

Using these considerations it is possible to establish the following asymptotic analytic expressions for the singular values of both kernels:

$$\lambda^{\xi}_{\boldsymbol{\mathcal{T}}_s,K_{\mathrm{ex}}} \sim (2\pi)^{-1} K_0\big(2\pi a\xi\big) I_0\big(2\pi a\xi\big)\,, \tag{4.22}$$

and

$$\lambda^{\xi}_{\boldsymbol{\mathcal{T}}_s,K_{\mathrm{red}}} \sim (2\pi)^{-1} K_0\big(2\pi a\xi\big)\,, \tag{4.23}$$

where I_0 and K_0 are the modified Bessel functions of the first and second kind. Here the spectral variable ξ will reside in the interval $\big[\xi_{\min}, \xi_{\max}\big]$ where $\xi_{\min}$ is strictly positive and corresponds to the least oscillating eigenvector (structure dependent) and $\xi_{\max}$ correspond to its most oscillating eigenvector (discretization dependent), i.e. $\xi_{\max} \propto (2h)^{-1}$.

β) Asymptotic Behaviors

Given the asymptotic behaviors of the spectra deduced from eqs. (4.22) and (4.23), the condition number of the exact and reduced kernel EFIEs can be studied in two regimes: (i) the coarse refinement regime in which $a \ll h$ and (ii) the high refinement regime in which $a \gg h$. The spectra of the kernels exhibit significantly different behaviours in these two regimes and require dedicated analyses to consistently address the dense discretization breakdown.

The behaviour of the eigenvalues of the exact kernel in case (i) ($a \ll h$), which in the spectral domain translates into $a\xi_{max} \ll 1$, can be obtained by performing a power series expansion of eq. (4.22) near zero

$$\lambda^{\xi}_{\boldsymbol{\mathcal{T}}_s,K_{\mathrm{ex}}} \underset{a\xi\ll 1}{\sim} -(2\pi)^{-1}\Big(\gamma + \log(\pi) + \log\big(a\xi\big)\Big) + \mathcal{O}\big(\xi^2\big)\,, \tag{4.24}$$

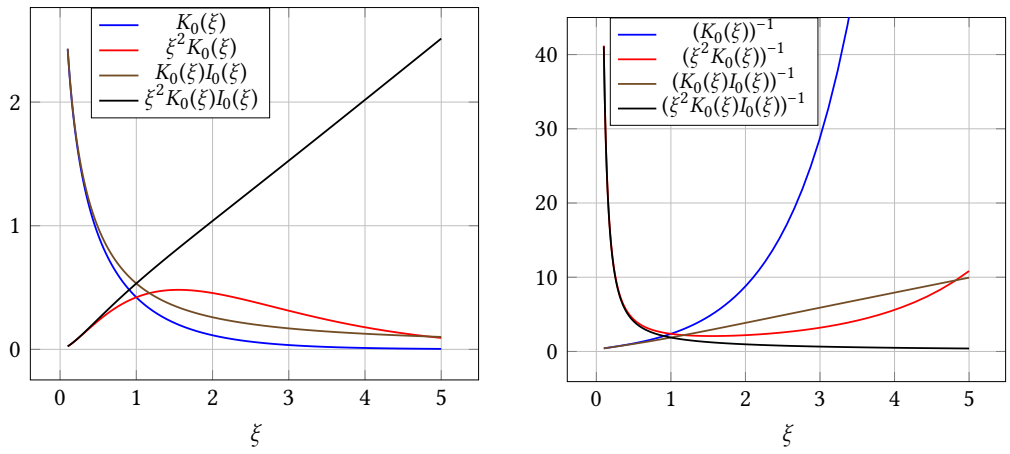

Fig. 4.2.: Illustration of the behavior of the various functions involved in the spectral analysis of the exact and reduce kernels (Figure 4.2a) and their inverses (Figure 4.2b).

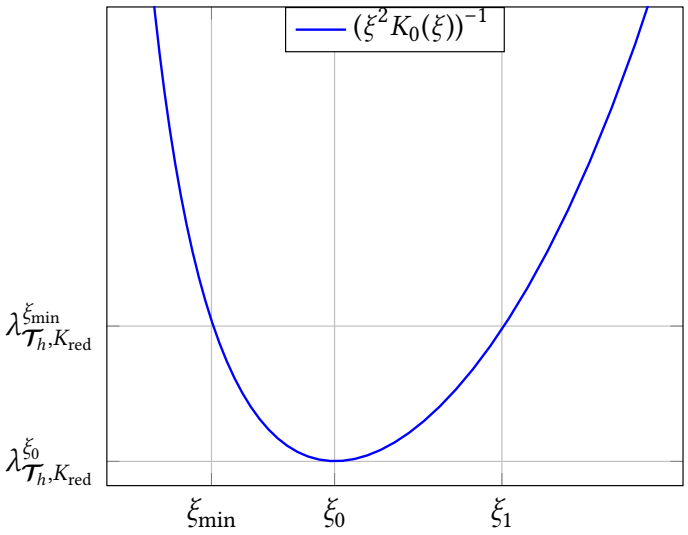

Fig. 4.3.: Illustration of the behaviour of the scalar potential of the reduced potential showing that the condition number will first increase $\xi \in \left[\xi_{\min}, \xi_0\right]$ because the minimum singular value decreases, remain constant for $\xi \in \left[\xi_0, \xi_1\right]$ and finally increase in $\xi > \xi_1$ because the maximum singular value increases while the minimum remains constant.

where γ is Euler's constant. From the power expansion of the vector potential, the behavior of the eigenvalues $\lambda^{\xi}_{\boldsymbol{\mathcal{T}}_h,K_{\text{ex}}}$ of scalar potential are obtained considering the net two derivative difference between vector and scalar potential operators

$$\lambda^{\xi}_{\boldsymbol{\mathcal{T}}_h,K_{\text{ex}}} \underset{a\xi\ll 1}{\sim} -\frac{1}{2\pi}\xi^2\Big(\gamma + \log(\pi) + \log\big(a\xi\big)\Big) + \mathcal{O}\big(\xi^4\big)\,. \tag{4.25}$$

The refinement behaviour of the spectrum of the exact kernel can be obtained by recalling that $\xi_{\max} = \alpha(2h)^{-1}$ (where α is an undetermined scaling factor) in eqs. (4.24) and (4.25)

$$\lambda^{\xi_{\min}}_{\boldsymbol{\mathcal{T}}_s,K_{\text{ex}}} \approx -(2\pi)^{-1}\Big(\gamma + \log(\pi) + \log\big(a\xi_{\min}\big)\Big)\,, \tag{4.26}$$

and

$$\lambda^{\xi_{\max}}_{\boldsymbol{\mathcal{T}}_s,K_{\text{ex}}} \approx -(2\pi)^{-1}\big(\gamma + \log(a\pi\alpha) - \log(2) - \log(h)\big)\,. \tag{4.27}$$

The study of case (ii) – $a\xi \gg 1$ – for the exact kernel requires an asymptotic analysis of eq. (4.22)

$$\lim_{h\to 0}\lambda^{\xi_{\min}}_{\boldsymbol{\mathcal{T}}_s,K_{\text{ex}}} = (2\pi)^{-1}K_0\big(2\pi a\xi_{\min}\big)I_0\big(2\pi a\xi_{\min}\big) = \mathcal{O}(1)\,, \tag{4.28}$$

and

$$\lim_{h\to 0}\lambda^{\xi_{\max}}_{\boldsymbol{\mathcal{T}}_s,K_{\text{ex}}} \propto \lim_{h\to 0} K_0\left(\frac{\pi a\alpha}{h}\right)I_0\left(\frac{\pi a\alpha}{h}\right) = \mathcal{O}(h)\,, \tag{4.29}$$

where for the latter the well known property

$$I_0(X)K_0(X) \underset{X\to+\infty}{=} \frac{1}{2X} + \mathcal{O}\left(\frac{1}{X^3}\right) \tag{4.30}$$

has been used [ON10]. Following the same reasoning as in the previous case yields for the scalar potential

$$\lim_{h\to 0}\lambda^{\xi_{\max}}_{\boldsymbol{\mathcal{T}}_h,K_{\text{ex}}} = \mathcal{O}\left(\frac{1}{h}\right)\,. \tag{4.31}$$

A similar analysis can be readily performed for the reduced kernel. The results for when case (i) is applied to equation eq. (4.23) are the same as for the exact kernel

$$\lambda^{\xi}_{\boldsymbol{\mathcal{T}}_s,K_{\text{red}}} \underset{a\xi\ll 1}{\sim} -(2\pi)^{-1}\Big(\gamma + \log(\pi) + \log\big(a\xi\big)\Big) + \mathcal{O}\big(\xi^2\big)\,, \tag{4.32}$$

and

$$\lambda^{\xi}_{\boldsymbol{\mathcal{T}}_h,K_{\text{red}}} \underset{a\xi\ll 1}{\sim} -(2\pi)^{-1}\xi^2\Big(\gamma + \log(\pi) + \log\big(a\xi\big)\Big) + \mathcal{O}\big(\xi^4\big)\,. \tag{4.33}$$

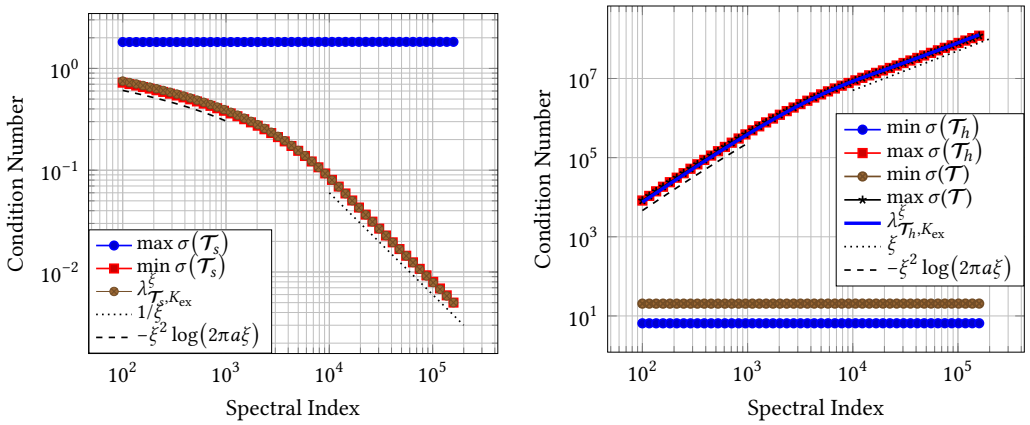

(a) *(b)*

Fig. 4.4.: Condition number of the exact kernel vector potential (Figure 4.4a), scalar potential and EFIO (Figure 4.4b) for an increasingly denser discretization of a loop of radius equal to one half of the wavelength of the impinging plane wave. The wire radius of the loop is $a = 1.6 \cdot 10^{-5}$ m.

Finally, in case (ii) the reduced kernel has the following behavior:

$$\lim_{h\to 0} \lambda^{\xi_{\min}}_{\mathcal{T}_s,K_{\text{red}}} = \frac{1}{\sqrt{2\pi}} K_0(2\pi a \xi_{\min}) = \mathcal{O}(1)\,, \tag{4.34}$$

and

$$\lim_{h\to 0} \lambda^{\xi_{\max}}_{\mathcal{T}_s,K_{\text{ex}}} = \lim_{h\to 0} \frac{1}{\sqrt{2\pi}} K_0\left(\pi\alpha\frac{a}{h}\right) = \mathcal{O}\left(\sqrt{\frac{h}{\pi\alpha a}}\mathrm{e}^{-\pi\alpha a/h}\right). \tag{4.35}$$

The spectral behavior of the two kernels on a loop of unitary radius is illustrated in Figures 4.4 and 4.5 and all numerical results are in agreement with the former analysis. A regression analysis of the coarse refinement logarithmic behaviour has been performed and is illustrated in *Figure* 4.6

d) Low Frequency Regularization

α) Quasi-Helmholtz Projectors

In order to address the low frequency breakdown of the wire EFIE the surface projectors presented in Section 3.e are extended to wire geometries. Because the low frequency breakdown of the wire EFIE has the same underlying causes as its

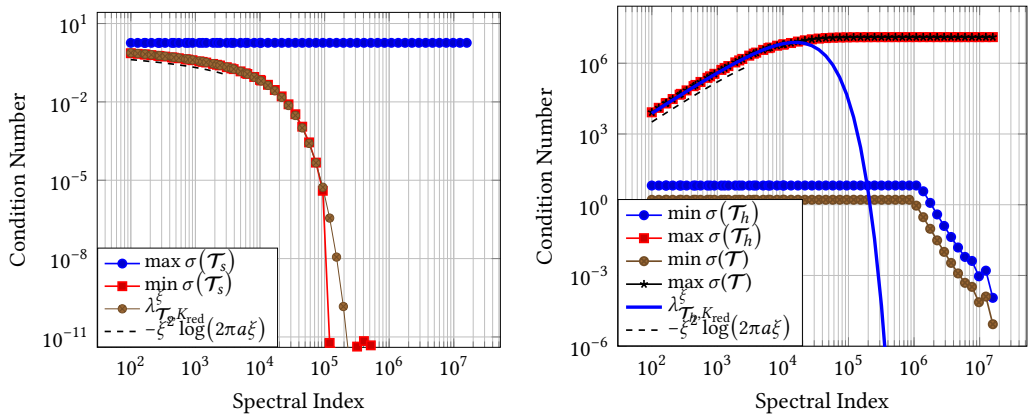

(a) *(b)*

Fig. 4.5.: Condition number of the reduced kernel vector potential (Figure 4.4a), scalar potential and EFIO (Figure 4.4b) for an increasingly denser discretization of a loop of radius equal to one half of the wavelength of the impinging plane wave. The wire radius of the loop is $a = 1.6 \cdot 10^{-5}$ m. The dip of the scalar potential's condition number is explained by the trends illustrated in Figure 4.3.

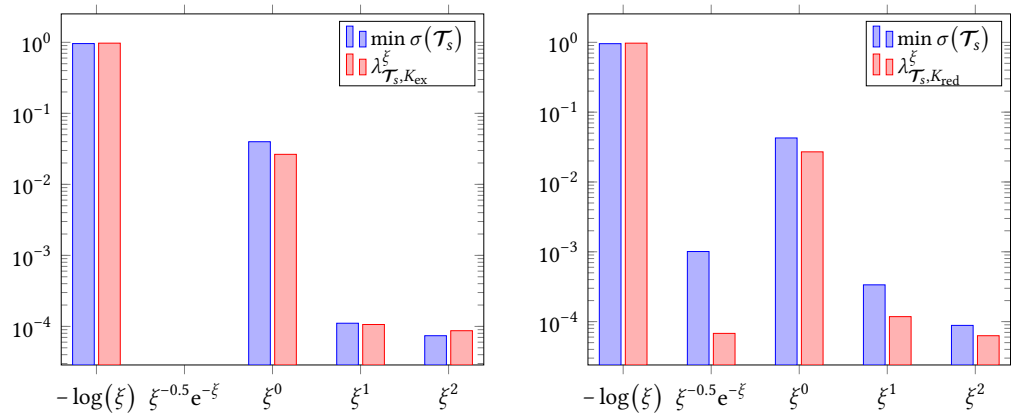

(a) *(b)*

Fig. 4.6.: Regression coefficients of the scalar potential of the exact (Figure 4.6a) and reduced kernel (Figure 4.6b), corresponding to the five points of coarsest refinement in Figures 4.4 and 4.5, respectively. These figures demonstrate that the numerical results exhibit the expected logarithmic behaviours predicted by theory. The curves of the analytical result for the infinite wire kernels are presented in the corresponding figures in order to serve as reference.

surface counterpart, projector based solutions will retain their efficiency and their edge over traditional techniques such as loop star decompositions. The extension of the projectors relies on the fact that the non-solenoidal decomposition matrix $\boldsymbol{\Sigma} \in \mathbb{R}^{N_v \times N_s}$ is actually a discretization of the gradient operator

$$[\boldsymbol{\Sigma}]_{mn} = \left\langle \boldsymbol{\Lambda}_m, P_n \right\rangle , \tag{4.36}$$

where $\left\{ P_j \right\}$ is the set composed of the constant function $x \longmapsto 1$ over each segments of the discretized geometry. This matrix can be computed only using connectivity information of the meshed geometry

$$[\boldsymbol{\Sigma}]_{ij} = \begin{cases} 1 & \text{if } s_n \text{ is } s_m^+ , \\ -1 & \text{if } s_n \text{ is } s_m^- , \\ 0 & \text{otherwise.} \end{cases} \tag{4.37}$$

The solenoidal projector $\boldsymbol{P}_{\boldsymbol{\Sigma}}$ can then be defined as

$$\boldsymbol{P}_{\boldsymbol{\Sigma}} = \boldsymbol{\Sigma} \left(\boldsymbol{\Sigma}^{\mathrm{T}} \boldsymbol{\Sigma} \right)^{+} \boldsymbol{\Sigma}^{\mathrm{T}} , \tag{4.38}$$

and the solenoidal projector $\boldsymbol{P}_{\boldsymbol{\Lambda H}}$ as its remainder

$$\boldsymbol{P}_{\boldsymbol{\Lambda H}} = \mathbf{I} - \boldsymbol{P}_{\boldsymbol{\Sigma}} . \tag{4.39}$$

The wire counterpart of the solenoidal decomposition matrix $\boldsymbol{\Lambda}$ can not be established in simple terms because the solenoidal functions are cycles of the mesh, and can not be built from purely local information. The overall solenoidal mapping could be built using cycle and/or global loop detection algorithms, however these techniques exhibit an above quadratic complexity [Pat69], hence it is more convenient and computationally efficient to use the definition proposed in eq. (4.39).

The quasi-Helmholtz projectors can be used to decompose any hat function expansion coefficient vector into its solenoidal and non-solenoidal components

$$\boldsymbol{i} = \boldsymbol{P}_{\boldsymbol{\Lambda H}} \boldsymbol{i} + \boldsymbol{P}_{\boldsymbol{\Sigma}} \boldsymbol{i} . \tag{4.40}$$

One crucial property of the projectors is that they can be computed with a near-linear cost through the algorithm detailed in Section 3.e, leveraging on multigrid preconditioner [NN12], making them a very efficient alternative to traditional techniques.

β) Leveraging Quasi-Helmholtz Projectors

The quasi-Helmholtz projectors can be used to define the quasi-Helmholtz decomposition operator

$$\boldsymbol{M} = \frac{1}{\sqrt{k}}\boldsymbol{P}_{\Lambda H} + \mathrm{j}\sqrt{k}\boldsymbol{P}_{\boldsymbol{\Sigma}}, \tag{4.41}$$

which has the property $\boldsymbol{M}^{\mathrm{T}} = \boldsymbol{M}$. The result of applying $\boldsymbol{M}$ to the wire EFIE matrix can be expanded as

$$\begin{aligned}\boldsymbol{M}^{\mathrm{T}}\boldsymbol{Z}\boldsymbol{M} &= -\mathrm{j}(\boldsymbol{P}_{\Lambda H}\boldsymbol{Z}_s\boldsymbol{P}_{\Lambda H} + \boldsymbol{P}_{\boldsymbol{\Sigma}}\boldsymbol{Z}_h\boldsymbol{P}_{\boldsymbol{\Sigma}}) + (\boldsymbol{P}_{\Lambda H}\boldsymbol{Z}_s\boldsymbol{P}_{\boldsymbol{\Sigma}} + \boldsymbol{P}_{\boldsymbol{\Sigma}}\boldsymbol{Z}_s\boldsymbol{P}_{\Lambda H})k \\ &\quad + (\boldsymbol{P}_{\boldsymbol{\Sigma}}\boldsymbol{Z}_s\boldsymbol{P}_{\boldsymbol{\Sigma}})\mathrm{j}k^2 \\ &= -\mathrm{j}(\boldsymbol{P}_{\Lambda H}\boldsymbol{Z}_s\boldsymbol{P}_{\Lambda H} + \boldsymbol{Z}_h) + \mathcal{O}(k)\end{aligned} \tag{4.42}$$

by recognizing that $\boldsymbol{P}_{\boldsymbol{\Sigma}}\boldsymbol{Z}_h\boldsymbol{P}_{\boldsymbol{\Sigma}} = \boldsymbol{Z}_h$ – which derives from the complementarity of the projctors $\boldsymbol{P}_{\Lambda H} + \boldsymbol{P}_{\boldsymbol{\Sigma}} = \mathbf{I}$ – and that $\boldsymbol{P}_{\Lambda H}\boldsymbol{Z}_h = \boldsymbol{Z}_h\boldsymbol{P}_{\Lambda H} = \mathbf{0}$. Since the loop and star main contributions do not scale in frequency, this formulation is immune from the low frequency breakdown. In particular, following the reasoning detailed in Section 3.e it can be shown that both the numerical cancellations and the condition number breakdown are addressed.

Even with the low frequency breakdown cured, this formulation still suffers from an ill-scaling between the vector and scalar potential. This ill-scaling can be compensated, to further reduce the condition number, by adding a scaling term

$$\delta = \sqrt{\frac{\|\boldsymbol{Z}_h\|}{\|\boldsymbol{Z}_s\|}} \tag{4.43}$$

to $\boldsymbol{M}$

$$\boldsymbol{M} = \sqrt{\frac{\delta}{k}}\boldsymbol{P}_{\Lambda H} + \mathrm{j}\sqrt{\frac{k}{\delta}}\boldsymbol{P}_{\boldsymbol{\Sigma}}\,. \tag{4.44}$$

Even though δ is defined using norms, it can be computed efficiently by using power methods.

e) Hierarchical Preconditioning

To stabilize the dense discretization breakdown of the wire EFIO, which is asymptotically spectrally equivalent to a Laplacian operator in its quadratic regime, a hierarchical preconditioner based on linear B-splines can be employed. In addition, this preconditioner can also regularize the operator in its linear regime.

For this chapter to be clearer, some key passages in the demonstration of the effectiveness of the hierarchical scheme will be recalled. For a more complete discussion on the topic, the reader can refer to [Dah03].

Let $\mathcal{H}$ be an Hilbert space equipped with a norm $\|\cdot\|_{\mathcal{H}}$ induced by the s.p.d operator $\mathcal{O}$, i.e.

$$\|v\|_{\mathcal{H}}^2 = \left\langle v, \mathcal{O}(v) \right\rangle, \quad \forall v \in \mathcal{H}, \tag{4.45}$$

which can be re-written in matrix form as

$$\|v\|_{\mathcal{H}}^2 = \boldsymbol{\alpha}_B^{\mathrm{T}} \boldsymbol{O} \boldsymbol{\alpha}_B, \tag{4.46}$$

where $[\boldsymbol{\alpha}_B]_i$ are the coefficients of v in an arbitrary basis $B = \{\boldsymbol{v}_i\}$, i.e.

$$\forall v \in \mathcal{H} \ \exists \boldsymbol{\alpha}_B \mid v = \sum_i [\alpha_B]_i v_i. \tag{4.47}$$

Given two function x and y, $x \asymp y$ denotes that $x \lesssim y$ and $y \lesssim x$, where $x \lesssim y$ if $\exists C > 0$ such that $x \leq Cy$. With this notation, assume the existence of a basis W of $\mathcal{H}$ that satisfies the condition

$$\|v\|_{\mathcal{H}}^2 \asymp \sum_i [\boldsymbol{\alpha}_W]_i^2 d_i^2, \tag{4.48}$$

or, in matrix form,

$$\|v\|_{\mathcal{H}}^2 \asymp \boldsymbol{\alpha}_W^{\mathrm{T}} \boldsymbol{D}^{\mathrm{T}} \boldsymbol{D} \boldsymbol{\alpha}_W, \tag{4.49}$$

where $\boldsymbol{D}$ is a diagonal matrix, then combining eqs. (4.46) and (4.49) yields

$$\boldsymbol{\alpha}_B^{\mathrm{T}} \boldsymbol{O} \boldsymbol{\alpha}_B \asymp \boldsymbol{\alpha}_W^{\mathrm{T}} \boldsymbol{D}^{\mathrm{T}} \boldsymbol{D} \boldsymbol{\alpha}_W. \tag{4.50}$$

Because the basis B is not defined, it is chosen to be composed of the same vectors as W but scaled, i.e. $\boldsymbol{\alpha}_B \longleftarrow \boldsymbol{D}\boldsymbol{\alpha}_W$; this choice yields

$$\boldsymbol{\alpha}_W^{\mathrm{T}} \boldsymbol{D}^{\mathrm{T}} \boldsymbol{O} \boldsymbol{D} \boldsymbol{\alpha}_W \asymp \boldsymbol{\alpha}_B^{\mathrm{T}} \boldsymbol{\alpha}_B, \tag{4.51}$$

which implies that $\boldsymbol{D}^{\mathrm{T}} \boldsymbol{O} \boldsymbol{D}$ is spectrally equivalent to an identity and hence is well-conditioned. This means that if a basis satisfying eq. (4.49) exists then combining a wavelet change of basis with a diagonal preconditioner will yield a well conditioned operator $\mathcal{O}$ [DK92].

It can be shown that the linear B-spline wavelets are a preconditioning basis for the Laplacian operator [CT99]. To define the functions generating this basis the segment $S = [0, 1]$ is partitioned at level j into 2^j segments $S_{j,k} = \left[x_{jk}, x_{j,k+1}\right]$ where

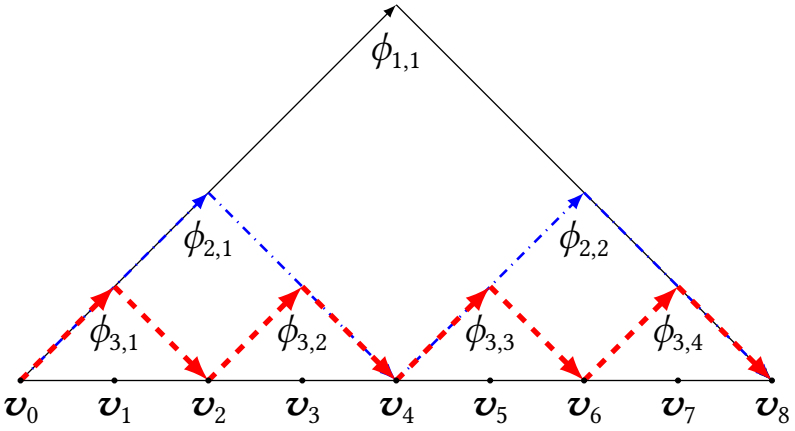

Fig. 4.7.: Example of wavelets constructed on a wire segment.

$x_{j,k} = k2^{-j}$ and $k = 0 \dots 2^j$. The B-splines wavelets are well suited to the problem at hand since they are scaled and translated hat function

$$\phi_{jk}(x) = \begin{cases} 2^j(x - x_{j,k-1}) & \text{if } x \in S_{j,k-1}\,, \\ 2^j(x_{j,k+1} - x) & \text{if } x \in S_{j,k}\,, \\ 0 & \text{otherwise.} \end{cases} \tag{4.52}$$

The hierarchical basis can then be built by complementing the set Φ_j of functions of previous levels with the functions defined on the new nodes of the current level

$$\Phi_{j+1} = \Phi_j \oplus \left\{ \phi_{j,2k+1} \middle/ k = 0, \dots, 2^j - 1 \right\}. \tag{4.53}$$

A construction of Φ_3 is illustrated in Figure 4.7. While this construction is given on straight wire with uniform discretization, it can be generalized to less trivial cases in a way in a natural way.

f) Preconditioned Equation

After regularizing the frequency behaviour of the wire EFIE, its condition number still increases with h^{-1} or h^{-2}, depending on the regime. These behaviours can be preconditioned using the hierarchical preconditioner

$$\boldsymbol{D}\boldsymbol{H}^{\mathrm{T}}\boldsymbol{Z}\boldsymbol{H}\boldsymbol{D}, \tag{4.54}$$

where $\boldsymbol{D}$ is a diagonal preconditioner and $\boldsymbol{H}$ is the matrix expressing the hierarchical B-pline functions as a linear combination of the triangle basis functions used to discretize $\boldsymbol{Z}$.

The fully regularized wire EFIE combines both the frequency and high refinement regularizations and yields the system

$$\boldsymbol{D}\boldsymbol{H}^{\mathrm{T}}\boldsymbol{M}\boldsymbol{Z}\boldsymbol{M}\boldsymbol{H}\boldsymbol{D}\boldsymbol{y} = \boldsymbol{D}\boldsymbol{H}^{\mathrm{T}}\boldsymbol{M}\boldsymbol{v}\,, \tag{4.55}$$

where $\boldsymbol{D}$ is a diagonal preconditioner and $\boldsymbol{i} = \boldsymbol{M}\boldsymbol{H}\boldsymbol{D}\boldsymbol{y}$. However, particular care should be taken when computing the δ scaling factor of the quasi-Helmholtz projectors. If eq. (4.43) was used directly δ would reintroduce a dependency on the refinement of the geometry, which would counterbalance the regularization effect of the hierarchical preconditioner. However, because the gap in singular values addressed by δ is caused by the geometry only the top level hierarchical functions can be extracted for the re-scaling, i.e.

$$\delta = \sqrt{\frac{\|\boldsymbol{H}_0^{\mathrm{T}}\boldsymbol{Z}_h\boldsymbol{H}_0\|}{\|\boldsymbol{H}_0^{\mathrm{T}}\boldsymbol{Z}_s\boldsymbol{H}_0\|}}, \tag{4.56}$$

where $\boldsymbol{H}_0$ is the part of $\boldsymbol{H}$ that only contains the coefficients for the top level (i.e. least refined) hierarchical functions. Since these functions still contain the structural informations but do not change with increasing refinement, this δ is constant with regards to h. This formulation is then well-conditioned and immune from both the low frequency and dense discretization breakdowns.

g) Implementation Details

This section will address some of the implementation details that need to taken into account for an effective implementation of the new schemes.

First, in order to avoid numerical instabilities in the computation of $\boldsymbol{M}\boldsymbol{Z}\boldsymbol{M}$, the matrix product has to be expanded as in eq. (4.42). This will allow explicit cancellation of the $\boldsymbol{P}_{\Lambda H}\boldsymbol{Z}_h$ and $\boldsymbol{Z}_h\boldsymbol{P}_{\Lambda H}$ terms, that may cause numerical instabilities.

Moreover, the RHS also requires careful treatment: after rewriting eq. (4.55) as

$$\boldsymbol{D}\boldsymbol{H}^{\mathrm{T}}\boldsymbol{M}\boldsymbol{Z}\boldsymbol{M}\boldsymbol{H}\boldsymbol{D}\boldsymbol{y} = \boldsymbol{v}_{\Lambda H} + \boldsymbol{v}_{\Sigma}\,, \tag{4.57}$$

where

$$\boldsymbol{v}_{\Lambda H} = \sqrt{\frac{\delta}{k}}\boldsymbol{D}\boldsymbol{H}^{\mathrm{T}}\boldsymbol{P}_{\Lambda H}\boldsymbol{v}\,, \tag{4.58}$$

$$\boldsymbol{v}_{\Sigma} = \mathrm{j}\sqrt{\frac{k}{\delta}}\boldsymbol{D}\boldsymbol{H}^{\mathrm{T}}\boldsymbol{P}_{\Sigma}\boldsymbol{v}\,, \tag{4.59}$$

numerical cancellations need to be accounted for in the computation of $\boldsymbol{v}_{\Lambda H}$. When $\boldsymbol{v}$ is induced by a plane-wave excitation of the form $\exp(-\mathrm{j}k\hat{\boldsymbol{k}}\cdot\boldsymbol{r})$, for example, it should be replaced by its extracted version $\boldsymbol{v}_{ext}$, generated by $\exp(-\mathrm{j}k\hat{\boldsymbol{k}}\cdot\boldsymbol{r})-1$ in eq. (4.58), as suggested by [Zha+02]. Dually, after solving this system the solution $\boldsymbol{i}$ should be retrieved as

$$\boldsymbol{i}_{\Lambda H} = \sqrt{\frac{\delta}{k}}\boldsymbol{P}_{\Lambda H}\boldsymbol{H}\boldsymbol{D}\boldsymbol{y}\,, \tag{4.60}$$

$$\boldsymbol{i}_{\Sigma} = \mathrm{j}\sqrt{\frac{k}{\delta}}\boldsymbol{P}_{\Sigma}\boldsymbol{H}\boldsymbol{D}\boldsymbol{y}\,, \tag{4.61}$$

$$\boldsymbol{i} = \boldsymbol{i}_{\Lambda H} + \boldsymbol{i}_{\Sigma}\,. \tag{4.62}$$

and the far field must be computed from the two components $\boldsymbol{i}_{\Sigma}$ and $\boldsymbol{i}_{\Lambda H}$ separately so that the extracted exponential $\exp(-\mathrm{j}k\hat{\boldsymbol{k}}\cdot\boldsymbol{r})-1$ can be used in the computation of the field scattered by the solenoidal current $\boldsymbol{i}_{\Lambda H}$.

Finally, the singularity extraction of the kernels of both EFIEs should be computed with high accuracy in order for the transformations from triangles to wavelet functions to remain correct.

h) Numerical Results

To verify the correctness, preconditioning properties and stability of the fully-regularized formulations eq. (4.55), both with the exact and reduced kernels, a series of numerical experiments have been performed.

First, the new regularized formulations were tested for correctness by simulating the field scattered by a dipole antenna of unit length and wire diameter of $1\cdot10^{-2}$ m. The simulation was performed at $3\cdot10^{7}$ Hz, with both the full and reduced wire EFIE kernels. The results, illustrated in Figure 4.8, are compared against the analytical expression of the field radiated by a small dipole and demonstrate the accuracy of the formulation, regardless of the kernel used.

To confirm the stability of the new formulations at low frequency, their conditioning has been studied until $1\cdot10^{-40}$ Hz. While not practical, this extremely low frequency serves to illustrate the continued robustness of the schemes. This study has been performed on a square loop of radius 1 m and on the complex structure illustrated in Figure 4.9 (Figures 4.10a and 4.10b, respectively). Both cases exhibit a stabilized conditioning until arbitrarily low frequencies. The high (but stable) conditioning of the tower structure is due to the scalar potential contribution (which has been verified to exhibit an intrinsically high condition number) becoming more

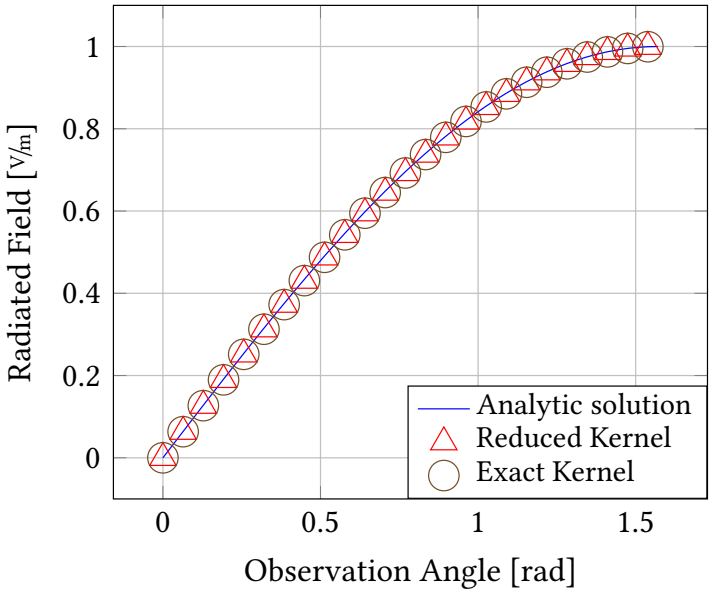

Fig. 4.8.: Field scattered by a 1 m dipole antenna at $3 \cdot 10^7$ Hz.

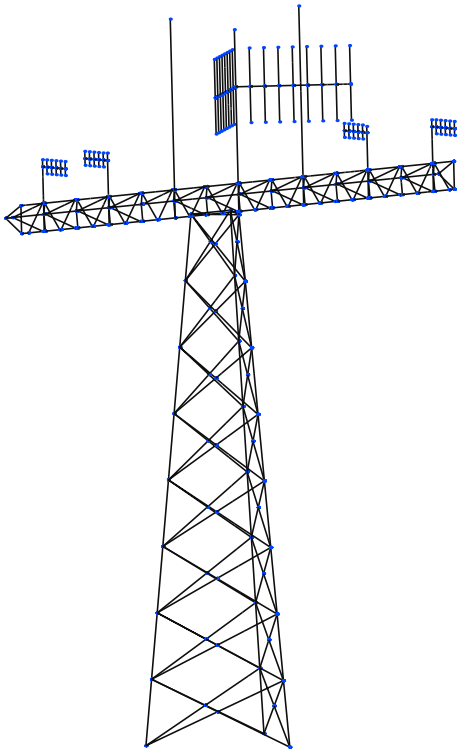

Fig. 4.9.: Wire-discretized antenna structure.

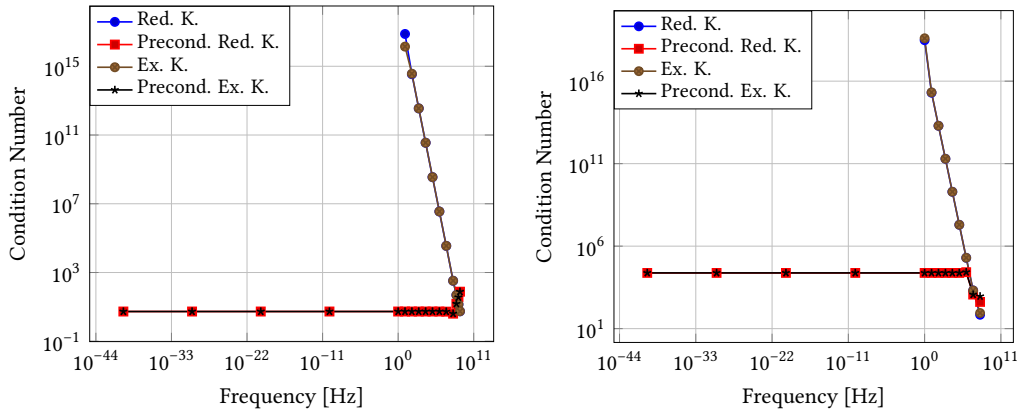

Fig. 4.10.: Frequency behaviour of the condition number of the standard EFIEs and the new formulations, computed on a square loop of 1 m side (Figure 4.10a) and on the structure illustrated in Figure 4.9 (Figure 4.10b) both with a wire radius $a = 1 \cdot 10^{-3}$ m.

important at low frequencies because it is no longer dampened by its k^{-1} scaling. In addition, the apparently stable conditioning at $1 \cdot 10^{16}$ of the standard formulations is due to numerical saturations in the computation of the condition number and should be disregarded. The numerical stability of the schemes have been verified on the square loop by computing the loop and star components of the solution vectors of the standard full kernel EFIE, the corresponding qH formulation and a loop star decomposed EFIE for reference (Figures 4.11a and 4.11b). The simulations clearly demonstrate that, while all formulations preserve the non-solenoidal parts of their solutions, only the decomposed ones yield accurate solenoidal parts. For more details in the causes of these cancellations see Chapter 3.

The high-refinement behaviour of the new formulations is illustrated in the dense discretization regime in Figure 4.12a. Given the compactness of the reduced kernel, the condition number of the corresponding formulation is not regularized. However, as expected, the exact kernel formulations exhibits a flat condition number with increasingly denser discretization. A similar study, illustrated in Figure 4.12b, has been performed for the coarse refinement regime. Both formulations are stabilized in this regime, up to logarithmic increase in the condition number. Similar results also hold for the complex structure illustrated in Figure 4.9 (Figures 4.13a and 4.13b).

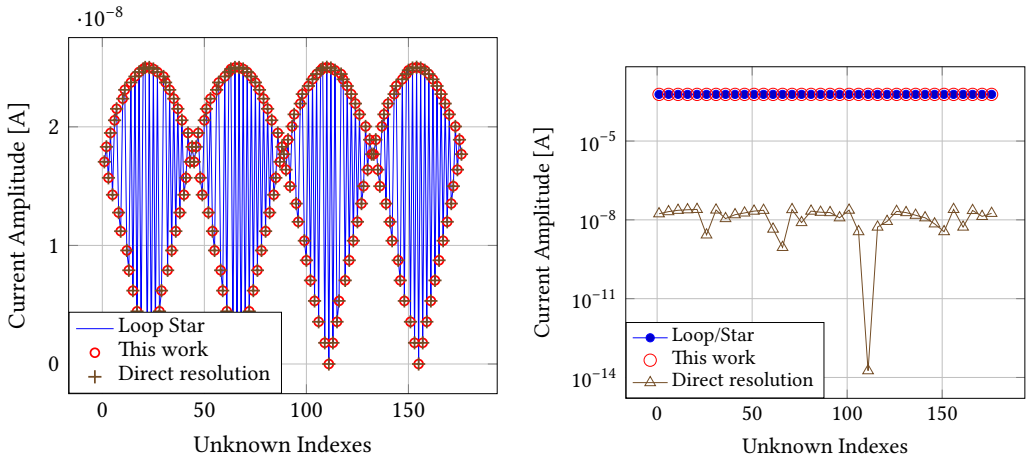

Fig. 4.11.: Non-solenoidal part (Figure 4.11a) and solenoidal part (Figure 4.11b) of the current on a square loop of 1 m radius induced by an impinging plane-wave at 500 Hz.

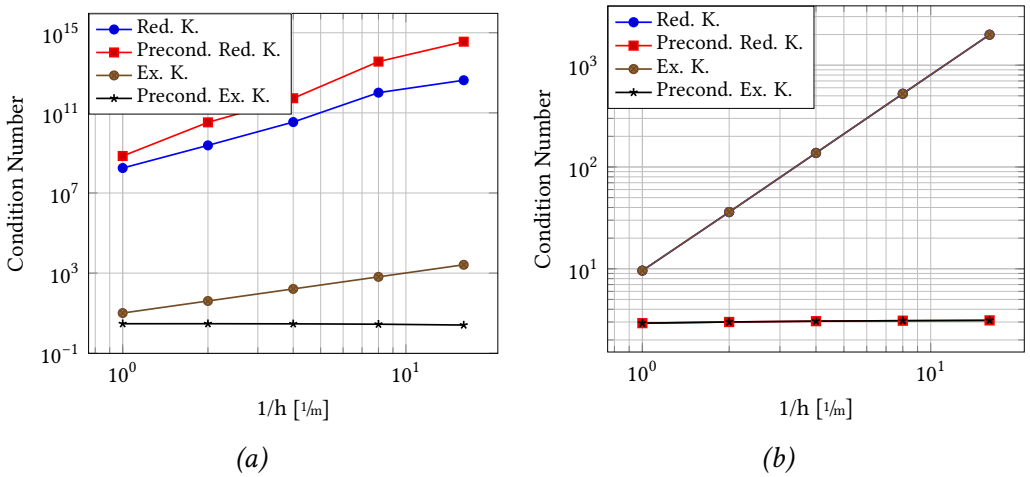

Fig. 4.12.: Spectral behaviour of the EFIEs on square loop of side 1 m at $6 \cdot 10^7$ Hz, in the dense refinement regime obtained with a wire radius $a = 0.159$ m (Figure 4.12a) and in the coarse refinement regime obtained with a wire radius $a = 1.59 \cdot 10^{-8}$ m (Figure 4.12b).

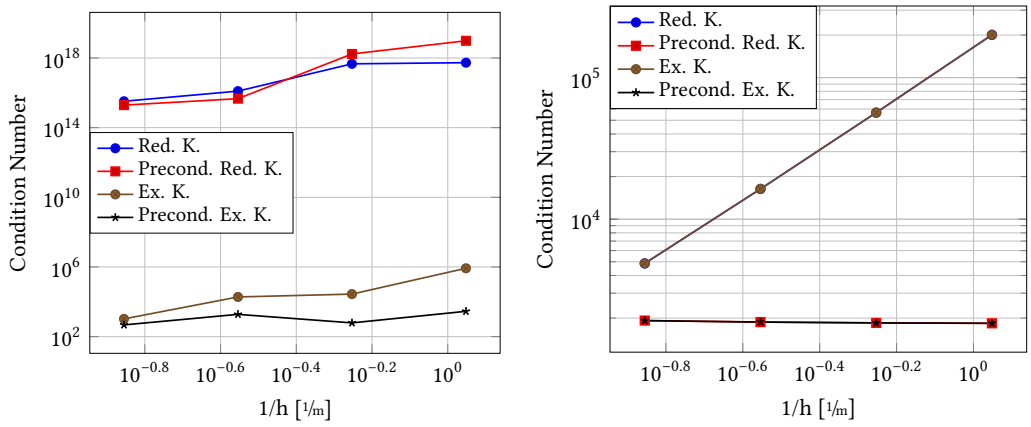

Fig. 4.13.: Spectral behaviour of the EFIEs on the structure illustrated in Figure 4.9 at $8.4 \cdot 10^6$ Hz, in the dense refinement regime obtained with a wire radius $a = 15.91$ m Figure 4.13a and in the coarse refinement regime obtained with a wire radius $a = 1.6 \cdot 10^{-6}$ m Figure 4.13b.

i) Conclusion

The new wire EFIE formulations presented in this work are immune from both the high-refinement and the low frequency breakdowns, and does not require the search for global loops. The hierarchical preconditioner have been chosen to match the spectral behaviour of both wire EFIE kernels under both of their regimes. Numerical results demonstrated the accuracy and regularization properties of our schemes in non-trivial cases.

Chapter 5

Magnetic and Combined Field Integral Equations Based on the Quasi-Helmholtz Projectors

Boundary integral equation methods for analyzing electromagnetic scattering phenomena typically suffer from several of the following problems: (i) ill-conditioning when the frequency is low; (ii) ill-conditioning when the discretization density is high; (iii) ill-conditioning when the structure contains global loops (which are computationally expensive to detect); (iv) incorrect solution at low frequencies due to current cancellations; (v) presence of spurious resonances. In this chapter[5], quasi-Helmholtz projectors are leveraged to obtain a MFIE formulation that is immune to drawbacks (i)-(iv). Moreover, when this new MFIE is combined with a regularized EFIE, a new quasi-Helmholtz projector CFIE is obtained that also is immune to (v). Numerical results corroborate the theory and show the practical impact of the newly proposed formulations.

a) Introduction

Time-harmonic scattering by PEC objects oftentimes is modeled using frequency domain boundary integral equations. Among them, electric and magnetic field integral equations (EFIE and MFIE) [Van07] are the most popular.

Although the EFIE is easily discretized using RWG basis functions [RWG82], it suffers from ill-conditioning when the frequency is low and/or the discretization density is high. The MFIE, on the other hand, remains well-conditioned in both regimes, provided that a mixed discretization scheme is employed [Coo+11]. In

5 This work is the result of a collaboration with Dr. Yves Beghein, Assistant Prof. Kristof Cools, Prof. Eric Michielssen and Prof. Francesco P. Andriulli. Part of this work has been performed before the start of this thesis and is recalled here for the completeness of the discussion. The present work has been submitted for publication in December, 2018 [Mer+18a].

practice, however, it is not feasible to obtain accurate results for the MFIE at extremely low frequencies without resorting to highly precise numerical quadrature methods. In addition to the above issues, both the EFIE and the MFIE suffer from current cancellations at low frequencies [Yun+03; QC10; QC08a].

The EFIE's conditioning and current cancellation problems can be overcome by using loop-star or loop-tree decompositions [WG81a; Vec99; ZC00; LLB03; Eib04]. For multiply connected geometries, this requires the detection of global loops, which is computationally expensive [WG81b]. These techniques also fail to address the dense discretization breakdown phenomena [ATV10; And+08] which causes the EFIE's condition number to grow quadratically with the mesh refinement parameter. Worse still, loop-star techniques for combatting the EFIE's low-frequency conditioning problems further degrade the equations dense discretization behavior [And12].

Several formulations have been introduced to address these low-frequency issues without the computational burden of global loop detection [QC08b; ZJ11]. These solutions, however, do not address the dense discretization ill-conditioning of the EFIE. Both issues can be concurrently tackled by leveraging hierarchical quasi-Helmholtz decompositions [VVP07; AVV08; Che+09; ATV10]. These decompositions also have been successfully coupled with other approaches such as Calderón preconditioning [CN02; Con+02; Ada04; Dar06; SL09; And+08; SJZ10] and Debye-inspired schemes [EG10]. The price to be paid for this dual stabilization is, once again, the need for global loop detection at very low frequencies. In addition, several of the aforementioned techniques fail to properly address low-frequency numerical cancellations occurring in the solution vector [Yun+03; CTH08; QC10; Bog+14]. Several of the above drawbacks have been successfully addressed by the promising scheme in [Vic+16]. Alternative remedies to current cancellations include perturbation methods [Yun+03; CTH08; Sun+13] and Calderón regularization combined with loop star decompositions [SL09; SJZ10]. Both families of solutions do, however, have shortcomings: the former is only applicable at low frequencies and exhibits the same spectral issues as the formulation it is applied to – high refinement breakdown for the EFIE or global loop detection for the MFIE and Calderón EFIE – while the latter also requires global loop detection and treatment of the high refinement instability of the loop-star decomposition. It should also be noted that some recent incarnations of augmented equations are immune to several of the above mentioned drawbacks, though they require the recovery of auxiliary quantities [Che+15; DG16].

Recently, an electric type equation based on quasi-Helmholtz projectors was proposed that is immune to all of the aforementioned issues [And+13b]. A similar regularization has also been applied to the time domain electric field integral

equation [BCA15a; BCA15b] and both the time domain and the frequency domain PMCHWT equations [Beg+15; BCA15c].

In this chapter, quasi-Helmholtz projectors are used to obtain a new MFIE that no longer requires interaction integrals to be computed using extremely accurate quadrature rules. Additionally, the solenoidal and nonsolenoidal current components are scaled such that low frequency cancellations are avoided. As a result, the formulation remains accurate down to extremely low frequencies. Scattering problems involving PEC objects can also be solved using the CFIE, which is a linear combination of the EFIE and the MFIE. This equation has the added benefit that it does not support spurious resonances [CS07]. In this chapter, the new regularization method for the MFIE is combined with that for the EFIE presented in [And+13b]. The resulting CFIE is not only low-frequency stable but also immune to spurious resonances. Preliminary results of this research have previously been presented as conference contributions [And+14; And+13a].

This chapter is organized as follows. To set notation, Section 5.b defines the standard EFIE and MFIE as well as their discretizations and related quasi-Helmholtz current decompositions. In Section 5.c, a quasi-Helmholtz decomposition is applied to a new symmetrized form of the MFIE. The resulting equation can be discretized accurately using standard numerical quadrature methods, and can be scaled in frequency such that no low frequency cancellations occur. In Section 5.d, this MFIE is combined with the regularized EFIE [And+13b] to obtain an extremely low frequency stable CFIE. Section 5.e discusses numerical results that corroborate the theory and conclusions are presented in Section 5.f.

b) Background and Notations

The EFIE and MFIE operators $\mathcal{T}_k$ and $\mathcal{K}_k$ are defined as

$$\left(\mathcal{T}_k \boldsymbol{j}\right)(\boldsymbol{r}) = \left(\mathcal{T}_{s,k} \boldsymbol{j}\right)(\boldsymbol{r}) + \left(\mathcal{T}_{h,k} \boldsymbol{j}\right)(\boldsymbol{r}), \tag{5.1}$$

$$\left(\mathcal{T}_{s,k} \boldsymbol{j}\right)(\boldsymbol{r}) = \mathrm{j}k\eta \hat{\boldsymbol{n}} \times \int_\Gamma \frac{e^{-\mathrm{j}kR}}{4\pi R} \boldsymbol{j}(\boldsymbol{r}') \mathrm{d}s', \tag{5.2}$$

$$\left(\mathcal{T}_{h,k} \boldsymbol{j}\right)(\boldsymbol{r}) = -\frac{\eta}{\mathrm{j}k} \hat{\boldsymbol{n}} \times \nabla \int_\Gamma \frac{e^{-\mathrm{j}kR}}{4\pi R} \nabla' \cdot \boldsymbol{j}(\boldsymbol{r}') \mathrm{d}s', \tag{5.3}$$

$$\left(\mathcal{K}_k \boldsymbol{j}\right)(\boldsymbol{r}) = -\hat{\boldsymbol{n}} \times p.v. \int_\Gamma \nabla \times \frac{e^{-\mathrm{j}kR}}{4\pi R} \boldsymbol{j}(\boldsymbol{r}') \mathrm{d}s', \tag{5.4}$$

where $R = \|\boldsymbol{r} - \boldsymbol{r}'\|$, Γ is the boundary of a closed domain $\Omega \subset \mathbb{R}^3$ and $\hat{\boldsymbol{n}}$ is its exterior normal vector. Furthermore, given the angular frequency ω, $k = \omega\sqrt{\mu\epsilon}$ and

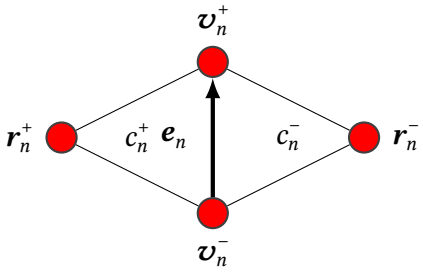

Fig. 5.1.: Notations used for the definition of an RWG basis function; $\boldsymbol{e}_n$ denotes the defining inner edge that links vertices $\boldsymbol{v}_n^+$ and $\boldsymbol{v}_n^-$ and c_n^+ and c_n^- the two triangles connected to this edge which are completed by the vertices $\boldsymbol{r}_n^+$ and $\boldsymbol{r}_n^-$, respectively.

$\eta = \sqrt{\mu/\epsilon}$; here ϵ and μ the permittivity and permeability of vacuum, respectively. If Ω is perfectly conducting, it supports an electric current $\boldsymbol{j}(\boldsymbol{r})$ satisfying both the EFIE

$$\left(\mathcal{T}_k \boldsymbol{j}\right)(\boldsymbol{r}) = \hat{\boldsymbol{n}} \times \boldsymbol{e}^i(\boldsymbol{r}) \tag{5.5}$$

and the MFIE

$$\left(\left(\frac{\mathcal{I}}{2} + \mathcal{K}_k\right)\boldsymbol{j}\right)(\boldsymbol{r}) = \hat{\boldsymbol{n}} \times \boldsymbol{h}^i(\boldsymbol{r}) \tag{5.6}$$

for all $\boldsymbol{r} \in \Gamma$; where $\boldsymbol{e}^i$ and $\boldsymbol{h}^i$ denote the impinging electric and magnetic fields, respectively. To numerically solve these equations via a Galerkin procedure, $\boldsymbol{j}(\boldsymbol{r})$ is expanded into RWG basis functions $\left\{\boldsymbol{f}_j(\boldsymbol{r})\right\}$ [RWG82] as

$$\boldsymbol{j}(\boldsymbol{r}) \approx \sum_{j=1}^{N_e} [\boldsymbol{j}]_j \boldsymbol{f}_j(\boldsymbol{r}), \tag{5.7}$$

where N_e is the number of edges of the mesh. Following [And+13b], the RWG functions are normalized such that the integrated flux through their defining edges equals one. Next, the EFIE (5.5) is tested with rotated RWG functions $\left\{\hat{\boldsymbol{n}} \times \boldsymbol{f}_i(\boldsymbol{r})\right\}$, while the MFIE (5.6) is tested with rotated BC functions [BC07] $\left\{\hat{\boldsymbol{n}} \times \boldsymbol{g}_i(\boldsymbol{r})\right\}$. The BC functions $\left\{\boldsymbol{g}_j\right\}$ are divergence-conforming functions defined on the barycentric refinement of the mesh. In addition, they are quasi curl-conforming in the sense that the mixed Gram matrix between curl-conforming rotated BC functions and RWG functions is well conditioned. For an explicit definition of these functions the reader is referred to [And+08; BC07]. Overall, the testing procedure results in the

following matrix equations:

$$\boldsymbol{T}\boldsymbol{j} = \boldsymbol{v}_e, \tag{5.8}$$

$$\left(\frac{\boldsymbol{G}^{\mathrm{T}}}{2} + \boldsymbol{K}_k\right)\boldsymbol{j} = \boldsymbol{v}_h, \tag{5.9}$$

where

$$[\boldsymbol{T}]_{ij} = \left(\hat{\boldsymbol{n}} \times \boldsymbol{f}_i, \mathcal{T}_k \boldsymbol{f}_j\right), \tag{5.10}$$

$$[\boldsymbol{T}_s]_{ij} = \left(\hat{\boldsymbol{n}} \times \boldsymbol{f}_i, \mathcal{T}_{s,k} \boldsymbol{f}_j\right), \tag{5.11}$$

$$[\boldsymbol{T}_h]_{ij} = \left(\hat{\boldsymbol{n}} \times \boldsymbol{f}_i, \mathcal{T}_{h,k} \boldsymbol{f}_j\right), \tag{5.12}$$

$$[\boldsymbol{K}_k]_{ij} = \left(\hat{\boldsymbol{n}} \times \boldsymbol{g}_i, \mathcal{K}_k \boldsymbol{f}_j\right), \tag{5.13}$$

$$[\boldsymbol{G}]_{ij} = \left(\boldsymbol{f}_i, \hat{\boldsymbol{n}} \times \boldsymbol{g}_j\right), \tag{5.14}$$

$$[\boldsymbol{v}_e]_i = \left(\hat{\boldsymbol{n}} \times \boldsymbol{f}_i, \hat{\boldsymbol{n}} \times \boldsymbol{e}^i\right), \tag{5.15}$$

$$[\boldsymbol{v}_h]_i = \left(\hat{\boldsymbol{n}} \times \boldsymbol{g}_i, \hat{\boldsymbol{n}} \times \boldsymbol{h}^i\right), \tag{5.16}$$

with $(\boldsymbol{a}, \boldsymbol{b}) = \int_\Gamma \boldsymbol{a}(\boldsymbol{r}) \cdot \boldsymbol{b}(\boldsymbol{r}) \mathrm{d}s$. In addition we denote by $\mathbb{T}$, $\mathbb{T}_s$ and $\mathbb{T}_h$ the BC-expanded and tested counterparts of the discretized operators $\boldsymbol{T}$, $\boldsymbol{T}_s$ and $\boldsymbol{T}_h$ computed with the complex wavenumber $-\mathrm{j}k$.

The solutions of (5.8) and (5.9) can be expressed as linear combinations of divergence free (loop and harmonic functions) and of non-divergence free (star functions) contributions via a quasi-Helmholtz decomposition

$$\boldsymbol{j} = \boldsymbol{\Lambda}\boldsymbol{l} + \boldsymbol{\Sigma}\boldsymbol{s} + \boldsymbol{H}\boldsymbol{h} \tag{5.17}$$

where the first two matrices $\boldsymbol{\Lambda} \in \mathbb{R}^{N_e \times N_v}$ and $\boldsymbol{\Sigma} \in \mathbb{R}^{N_e \times N_f}$ represent mappings from the RWG subspace to the local loop and star subspaces, respectively. Here, N_v and N_f are the number of vertices and facets of the mesh, respectively [WG81b; Coo+09b]. These two mappings can be defined using only the connectivity information of the discretized geometry as

$$\boldsymbol{\Lambda}_{ij} = \begin{cases} 1 & \text{if node } j \text{ equals } \boldsymbol{v}_i^+ \\ -1 & \text{if node } j \text{ equals } \boldsymbol{v}_i^- \\ 0 & \text{otherwise} \end{cases} \tag{5.18}$$

and

$$\boldsymbol{\Sigma}_{ij} = \begin{cases} 1 & \text{if the cell } j \text{ equals } c_i^+ \\ -1 & \text{if the cell } j \text{ equals } c_i^- \\ 0 & \text{otherwise}\,, \end{cases} \tag{5.19}$$

where vertices $\boldsymbol{v}_i^-$ and $\boldsymbol{v}_i^+$ define the oriented edge characterizing RWG function i, and c_i^- and c_i^+ denote the corresponding cells (Figure 5.1). The matrix $\boldsymbol{H}$ represents the mapping from the RWG space to the quasi-harmonic or *global loop* space composed of $2N_h$ functions, where N_h is the number of handles in the structure. For a complete description of this mapping and the associated harmonic functions, the reader is referred to [WG81b] and [Coo+09b].

A few properties of these matrices are recalled next to facilitate further developments. For the sake of simplicity we restrict ourselves to the case of a geometry with a single closed connected component. All derivations below can be extended to arbitrary geometries using the relations in [Wil83]. Given this assumption, $\boldsymbol{\Lambda}$ has a null-space spanned by the all-one vector $\mathbf{1}^{\boldsymbol{\Lambda}} \in \mathbb{R}^{N_v}$, i.e.

$$\boldsymbol{\Lambda}\mathbf{1}^{\boldsymbol{\Lambda}} = \mathbf{0}. \tag{5.20}$$

Similarly, linear dependency of the star functions cause $\boldsymbol{\Sigma}$ to exhibit a one-dimensional null space spanned by the all-one vector $\mathbf{1}^{\boldsymbol{\Sigma}} \in \mathbb{R}^{N_f}$, i.e.

$$\boldsymbol{\Sigma}\mathbf{1}^{\boldsymbol{\Sigma}} = \mathbf{0}. \tag{5.21}$$

Finally, it is trivial to show that the loop and star subspaces are orthogonal, i.e.

$$\boldsymbol{\Sigma}^{\mathrm{T}}\boldsymbol{\Lambda} = \mathbf{0}. \tag{5.22}$$

As $\boldsymbol{\Lambda}$ and $\boldsymbol{\Sigma}$ are ill-conditioned and because of the high computational cost of detecting global loops required to build $\boldsymbol{H}$, it is convenient to leverage the quasi-Helmholtz projectors introduced in [And+13b] to obtain a quasi-Helmholtz decomposition of the EFIE and MFIE operators. The projectors are defined as

$$\boldsymbol{P}^{\boldsymbol{\Sigma}} = \boldsymbol{\Sigma}\left(\boldsymbol{\Sigma}^{\mathrm{T}}\boldsymbol{\Sigma}\right)^{+}\boldsymbol{\Sigma}^{\mathrm{T}}\,, \tag{5.23}$$

$$\boldsymbol{P}^{\boldsymbol{\Lambda H}} = \mathrm{I} - \boldsymbol{P}^{\boldsymbol{\Sigma}}\,, \tag{5.24}$$

where $^+$ denotes the Moore-Penrose pseudo-inverse and I is the identity. Any RWG expansion coefficient vector can then be decomposed as

$$\boldsymbol{j} = \left(\boldsymbol{P}^{\boldsymbol{\Lambda H}}\boldsymbol{j}\right) + \left(\boldsymbol{P}^{\boldsymbol{\Sigma}}\boldsymbol{j}\right) \tag{5.25}$$

where $\boldsymbol{P}^{\boldsymbol{\Lambda H}}\boldsymbol{j}$ and $\boldsymbol{P}^{\boldsymbol{\Sigma}}\boldsymbol{j}$ contain the RWG expansions of the solenoidal (loop) and non-solenoidal (star) components of the current, respectively. These operators are self-adjoint and also can be used to decompose the RWG testing space. Similarly, the dual projectors $\mathbb{P}^{\boldsymbol{\Lambda}}$ and $\mathbb{P}^{\boldsymbol{\Sigma H}}$, defined as

$$\mathbb{P}^{\boldsymbol{\Lambda}} = \boldsymbol{\Lambda}\left(\boldsymbol{\Lambda}^{\mathrm{T}}\boldsymbol{\Lambda}\right)^{+}\boldsymbol{\Lambda}^{\mathrm{T}}, \tag{5.26}$$

$$\mathbb{P}^{\boldsymbol{\Sigma H}} = \mathrm{I} - \mathbb{P}^{\boldsymbol{\Lambda}}, \tag{5.27}$$

decompose any linear combination of BC (basis or testing) functions into a non-solenoidal and solenoidal part, respectively. It should be noted that construction of these projectors does not require the detection of global loops, and that $\left(\boldsymbol{\Sigma}^{\mathrm{T}}\boldsymbol{\Sigma}\right)^{+}$ can be efficiently computed using multigrid preconditioners [And+13b; NN12].

c) Regularizing the MFIE at Extremely Low Frequencies

α) Low Frequency Behaviour of the MFIE

The standard RWG discretization of the MFIE fails to provide accurate results at low frequencies due to the unphysical scaling of the loop and star (or tree) components of the current [Yun+03]. It was shown in [Coo+09a; Coo+11] that the mixed discretization of the MFIE (in which BC or CW functions [CW90] are used as testing functions) improves accuracy. In particular, the loop and star components of the current obtained from this formulation scale physically [Bog+14]. This result also holds true for multiply connected geometries [Bog+11a].

The mixed MFIE formulation still suffers from three problems. First, the physical scaling of the current can only be retrieved when interaction integrals are computed to high accuracy [Bog+14]. Second, the nonsolenoidal current component scales as $\mathcal{O}(\omega)$ whereas the solenoidal component is of $\mathcal{O}(1)$. As a result, at very low frequencies and when using finite precision, both components should be stored in different arrays to prevent the nonsolenoidal component from losing accuracy or even being cancelled out [Yun+03; CTH08; QC10; Bog+11b; Bog+11a]. Third, the static MFIE (at $\omega = 0$) has a null space when applied to multiply connected geometries. It follows that the discretized MFIE has N_h singular values that scale as $\mathcal{O}\left(\omega^2\right)$ [Coo+09b]. Any accurate discretization of the MFIE operator must preserve this null-space. Standard RWG discretizations of the MFIE operators are not capable of correctly modelling this null space [And+14]. The mixed MFIE, on the other hand, correctly models this null-space in infinite precision. However, after discretization, the null-space associated singular values will not be more accurate than the precision of the quadrature rule.

β) A Robust MFIE Formulation

To address the above described MFIE deficiencies we propose the following symmetrized MFIE:

$$\left(\frac{\mathcal{I}}{2} - \mathcal{K}_{-\mathrm{j}k}\right)\left(\frac{\mathcal{I}}{2} + \mathcal{K}_k\right)(\boldsymbol{j}) = \left(\frac{\mathcal{I}}{2} - \mathcal{K}_{-\mathrm{j}k}\right)\left(\hat{\boldsymbol{n}}_r \times \boldsymbol{h}^i\right). \tag{5.28}$$

This equation is the magnetic field counterpart of the (localized) Calderón preconditioned electric operator in [And+13b]. We propose to discretize (5.28) as

$$\begin{aligned} &\mathbb{M}^{\mathrm{T}}\left(\frac{\boldsymbol{G}^{\mathrm{T}}}{2} - \boldsymbol{K}_{-\mathrm{j}k}\right)\left(\boldsymbol{G}^{\mathrm{T}}\right)^{-1}\left(\frac{\boldsymbol{G}^{\mathrm{T}}}{2} + \boldsymbol{K}_k\right)\boldsymbol{M}\boldsymbol{i} \\ = \quad &\boldsymbol{O}\boldsymbol{i} = \mathbb{M}^{\mathrm{T}}\left(\frac{\boldsymbol{G}^{\mathrm{T}}}{2} - \boldsymbol{K}_{-\mathrm{j}k}\right)\left(\boldsymbol{G}^{\mathrm{T}}\right)^{-1}\boldsymbol{v}_h \end{aligned} \tag{5.29}$$

where

$$\boldsymbol{M} = \boldsymbol{P}^{\Lambda H}\frac{1}{\alpha} + \mathrm{j}\boldsymbol{P}^{\Sigma}\alpha\,, \tag{5.30}$$

$$\mathbb{M} = \mathbb{P}^{\Sigma H}\frac{1}{\alpha} + \mathrm{j}\mathbb{P}^{\Lambda}\alpha\,, \tag{5.31}$$

and $\boldsymbol{M}\boldsymbol{i} = \boldsymbol{j}$.

The coefficient α allows for re-scaling of the loop and star components of the solution $\boldsymbol{i}$ of (5.29) to prevent numerical cancellations. Because $\boldsymbol{P}^{\Sigma} + \boldsymbol{P}^{\Lambda H} = \mathbb{P}^{\Lambda} + \mathbb{P}^{\Sigma H} = \mathrm{I}$, operator $\boldsymbol{O}$ in (5.29) can be decomposed as

$$\begin{aligned} \boldsymbol{O} = (\mathbb{P}^{\Lambda} + \mathbb{P}^{\Sigma H})\boldsymbol{O}(\boldsymbol{P}^{\Sigma} + \boldsymbol{P}^{\Lambda H}) = \\ \mathbb{P}^{\Lambda}\boldsymbol{O}\boldsymbol{P}^{\Sigma} + \mathbb{P}^{\Lambda}\boldsymbol{O}\boldsymbol{P}^{\Lambda H} + \mathbb{P}^{\Sigma H}\boldsymbol{O}\boldsymbol{P}^{\Sigma} + \mathbb{P}^{\Sigma H}\boldsymbol{O}\boldsymbol{P}^{\Lambda H}, \end{aligned} \tag{5.32}$$

which allows for the study of the low-frequency behavior of each of the separate terms. Analysis of the frequency behavior of the first three terms is quite straightforward and yields

$$\mathbb{P}^{\Lambda}\boldsymbol{O}\boldsymbol{P}^{\Sigma} = \mathcal{O}\left(\alpha^2\right) \quad k \longrightarrow 0\,, \tag{5.33a}$$

$$\mathbb{P}^{\Lambda}\boldsymbol{O}\boldsymbol{P}^{\Lambda H} = \mathcal{O}(1) \quad k \longrightarrow 0\,, \tag{5.33b}$$

$$\mathbb{P}^{\Sigma H}\boldsymbol{O}\boldsymbol{P}^{\Sigma} = \mathcal{O}(1) \quad k \longrightarrow 0\,. \tag{5.33c}$$

Analysis of the last term in (5.32) requires special care. It is known that when decomposing $\boldsymbol{K}_k$ as

$$\boldsymbol{K}_k = \boldsymbol{K}_0 + \boldsymbol{K}_k'\,, \tag{5.34}$$

where $\boldsymbol{K}_0$ is the static limit of $\boldsymbol{K}_k$ and $\boldsymbol{K}'_k = \boldsymbol{K}_k - \boldsymbol{K}_0$ is the dynamic remainder, $\boldsymbol{K}'_k = \mathcal{O}\big(k^2\big)$ as $k \longrightarrow 0$ [Bog+11a]. When using this decomposition in (5.29), it can be verified that $\boldsymbol{K}_0$ satisfies

$$\mathbb{P}^{\boldsymbol{\Sigma H}}\left(\frac{\boldsymbol{G}^{\mathrm{T}}}{2} - \boldsymbol{K}_0\right)\big(\boldsymbol{G}^{\mathrm{T}}\big)^{-1}\left(\frac{\boldsymbol{G}^{\mathrm{T}}}{2} + \boldsymbol{K}_0\right)\boldsymbol{P}^{\boldsymbol{\Lambda H}} = \boldsymbol{0}\,. \tag{5.35}$$

The above equation holds the key to unlocking a frequency-stable MFIE and can be proven by introducing $\boldsymbol{P}^{\mathrm{Pol}}$, $\boldsymbol{P}^{\mathrm{Tor}}$, $\mathbb{P}^{\mathrm{Pol}}$, $\mathbb{P}^{\mathrm{Tor}}$ the orthogonal projectors into the right and left null-spaces of the internal and external MFIE operators, i.e.

$$\left(\frac{\boldsymbol{G}^{\mathrm{T}}}{2} + \boldsymbol{K}_0\right)\boldsymbol{P}^{\mathrm{Pol}} = \boldsymbol{0}\,, \tag{5.36}$$

$$\left(\frac{\boldsymbol{G}^{\mathrm{T}}}{2} - \boldsymbol{K}_0\right)\boldsymbol{P}^{\mathrm{Tor}} = \boldsymbol{0}\,, \tag{5.37}$$

$$\mathbb{P}^{\mathrm{Pol}}\left(\frac{\boldsymbol{G}^{\mathrm{T}}}{2} - \boldsymbol{K}_0\right) = \boldsymbol{0}\,, \tag{5.38}$$

$$\mathbb{P}^{\mathrm{Tor}}\left(\frac{\boldsymbol{G}^{\mathrm{T}}}{2} + \boldsymbol{K}_0\right) = \boldsymbol{0}\,. \tag{5.39}$$

Note that

$$\left(\frac{\boldsymbol{G}^{\mathrm{T}}}{2} + \boldsymbol{K}_0\right)\boldsymbol{P}^{\mathrm{Tor}} = \boldsymbol{G}^{\mathrm{T}}\boldsymbol{P}^{\mathrm{Tor}}\,, \tag{5.40}$$

$$\left(\frac{\boldsymbol{G}^{\mathrm{T}}}{2} - \boldsymbol{K}_0\right)\boldsymbol{P}^{\mathrm{Pol}} = \boldsymbol{G}^{\mathrm{T}}\boldsymbol{P}^{\mathrm{Pol}}\,, \tag{5.41}$$

$$\mathbb{P}^{\mathrm{Tor}}\left(\frac{\boldsymbol{G}^{\mathrm{T}}}{2} - \boldsymbol{K}_0\right) = \mathbb{P}^{\mathrm{Tor}}\boldsymbol{G}^{\mathrm{T}}\,, \tag{5.42}$$

$$\mathbb{P}^{\mathrm{Pol}}\left(\frac{\boldsymbol{G}^{\mathrm{T}}}{2} + \boldsymbol{K}_0\right) = \mathbb{P}^{\mathrm{Pol}}\boldsymbol{G}^{\mathrm{T}}\,. \tag{5.43}$$

We can then define

$$\mathbb{Q}^{\boldsymbol{\Lambda}} = \boldsymbol{P}^{\boldsymbol{\Lambda H}} - \boldsymbol{P}^{\mathrm{Pol}} - \boldsymbol{P}^{\mathrm{Tor}}\,, \tag{5.44}$$

which clearly satisfies

$$\mathbb{P}^{\boldsymbol{\Lambda}}\mathbb{Q}^{\boldsymbol{\Lambda}} = \mathbb{Q}^{\boldsymbol{\Lambda}}\,, \tag{5.45}$$

since the union of the right null spaces of the internal and external MFIE operators contains all the non-trivial cycles of the structure [Coo+09b]. Dually,

$$\boldsymbol{Q}^{\boldsymbol{\Sigma}} = \mathbb{P}^{\boldsymbol{\Sigma H}} - \mathbb{P}^{\mathrm{Pol}} - \mathbb{P}^{\mathrm{Tor}}, \tag{5.46}$$

satisfies

$$\boldsymbol{P}^{\boldsymbol{\Sigma}}\boldsymbol{Q}^{\boldsymbol{\Sigma}} = \boldsymbol{Q}^{\boldsymbol{\Sigma}}. \tag{5.47}$$

It follows that

$$\begin{aligned}
&\left(\frac{\boldsymbol{G}^{\mathrm{T}}}{2} - \boldsymbol{K}_0\right)\left(\boldsymbol{G}^{\mathrm{T}}\right)^{-1}\left(\frac{\boldsymbol{G}^{\mathrm{T}}}{2} + \boldsymbol{K}_0\right)\boldsymbol{P}^{\boldsymbol{\Lambda H}} \\
=&\left(\frac{\boldsymbol{G}^{\mathrm{T}}}{2} - \boldsymbol{K}_0\right)\left(\boldsymbol{G}^{\mathrm{T}}\right)^{-1}\left(\frac{\boldsymbol{G}^{\mathrm{T}}}{2} + \boldsymbol{K}_0\right)\left(\mathbb{Q}^{\boldsymbol{\Lambda}} + \boldsymbol{P}^{\mathrm{Pol}} + \boldsymbol{P}^{\mathrm{Tor}}\right) \\
=&\left(\frac{\boldsymbol{G}^{\mathrm{T}}}{2} - \boldsymbol{K}_0\right)\left(\boldsymbol{G}^{\mathrm{T}}\right)^{-1}\left(\frac{\boldsymbol{G}^{\mathrm{T}}}{2} + \boldsymbol{K}_0\right)\mathbb{Q}^{\boldsymbol{\Lambda}} \\
+&\left(\frac{\boldsymbol{G}^{\mathrm{T}}}{2} - \boldsymbol{K}_0\right)\left(\boldsymbol{G}^{\mathrm{T}}\right)^{-1}\left(\frac{\boldsymbol{G}^{\mathrm{T}}}{2} + \boldsymbol{K}_0\right)\boldsymbol{P}^{\mathrm{Tor}} \\
=&\left(\frac{\boldsymbol{G}^{\mathrm{T}}}{2} - \boldsymbol{K}_0\right)\left(\boldsymbol{G}^{\mathrm{T}}\right)^{-1}\left(\frac{\boldsymbol{G}^{\mathrm{T}}}{2} + \boldsymbol{K}_0\right)\mathbb{Q}^{\boldsymbol{\Lambda}} \\
+&\left(\frac{\boldsymbol{G}^{\mathrm{T}}}{2} - \boldsymbol{K}_0\right)\boldsymbol{P}^{\mathrm{Tor}} \\
=&\left(\frac{\boldsymbol{G}^{\mathrm{T}}}{2} - \boldsymbol{K}_0\right)\left(\boldsymbol{G}^{\mathrm{T}}\right)^{-1}\left(\frac{\boldsymbol{G}^{\mathrm{T}}}{2} + \boldsymbol{K}_0\right)\mathbb{Q}^{\boldsymbol{\Lambda}},
\end{aligned} \tag{5.48}$$

and similarly that

$$\begin{aligned}
&\mathbb{P}^{\boldsymbol{\Sigma H}}\left(\frac{\boldsymbol{G}^{\mathrm{T}}}{2} - \boldsymbol{K}_0\right)\left(\boldsymbol{G}^{\mathrm{T}}\right)^{-1}\left(\frac{\boldsymbol{G}^{\mathrm{T}}}{2} + \boldsymbol{K}_0\right) \\
=&\boldsymbol{Q}^{\boldsymbol{\Sigma}}\left(\frac{\boldsymbol{G}^{\mathrm{T}}}{2} - \boldsymbol{K}_0\right)\left(\boldsymbol{G}^{\mathrm{T}}\right)^{-1}\left(\frac{\boldsymbol{G}^{\mathrm{T}}}{2} + \boldsymbol{K}_0\right).
\end{aligned} \tag{5.49}$$

Combining the above equations it follows that

$$\mathbb{P}^{\Sigma H}\left(\frac{\boldsymbol{G}^{\mathrm{T}}}{2}-\boldsymbol{K}_0\right)\left(\boldsymbol{G}^{\mathrm{T}}\right)^{-1}\left(\frac{\boldsymbol{G}^{\mathrm{T}}}{2}+\boldsymbol{K}_0\right)\boldsymbol{P}^{\Lambda H} = \boldsymbol{Q}^{\Sigma}\left(\frac{\boldsymbol{G}^{\mathrm{T}}}{2}-\boldsymbol{K}_0\right)\left(\boldsymbol{G}^{\mathrm{T}}\right)^{-1}\left(\frac{\boldsymbol{G}^{\mathrm{T}}}{2}+\boldsymbol{K}_0\right)\mathbb{Q}^{\Lambda}. \quad (5.50)$$

In the above expression we now insert the identity matrices $\left(\boldsymbol{P}^{\Lambda H}+\boldsymbol{P}^{\Sigma}\right)$ and $\left(\mathbb{P}^{\Sigma H}+\mathbb{P}^{\Lambda}\right)$ obtaining

$$(5.50) = \boldsymbol{Q}^{\Sigma}\left(\frac{\boldsymbol{G}^{\mathrm{T}}}{2}-\boldsymbol{K}_0\right)\left(\boldsymbol{P}^{\Lambda H}+\boldsymbol{P}^{\Sigma}\right)\left(\boldsymbol{G}^{\mathrm{T}}\right)^{-1}\left(\mathbb{P}^{\Sigma H}+\mathbb{P}^{\Lambda}\right)\left(\frac{\boldsymbol{G}^{\mathrm{T}}}{2}+\boldsymbol{K}_0\right)\mathbb{Q}^{\Lambda}. \quad (5.51)$$

Given that

$$\boldsymbol{Q}^{\Sigma}\left(\frac{\boldsymbol{G}^{\mathrm{T}}}{2}-\boldsymbol{K}_0\right)\boldsymbol{P}^{\Lambda H} = \boldsymbol{Q}^{\Sigma}\boldsymbol{P}^{\Sigma}\left(\frac{\boldsymbol{G}^{\mathrm{T}}}{2}-\boldsymbol{K}_0\right)\boldsymbol{P}^{\Lambda H} = \boldsymbol{0} \quad (5.52)$$

and that

$$\mathbb{P}^{\Sigma H}\left(\frac{\boldsymbol{G}^{\mathrm{T}}}{2}+\boldsymbol{K}_0\right)\mathbb{Q}^{\Lambda} = \mathbb{P}^{\Sigma H}\left(\frac{\boldsymbol{G}^{\mathrm{T}}}{2}+\boldsymbol{K}_0\right)\mathbb{P}^{\Lambda}\mathbb{Q}^{\Lambda} = \boldsymbol{0} \quad (5.53)$$

and considering the property

$$\boldsymbol{P}^{\Sigma}\left(\boldsymbol{G}^{\mathrm{T}}\right)^{-1}\mathbb{P}^{\Lambda} = \boldsymbol{0}, \quad (5.54)$$

we obtain that

$$\begin{aligned}(5.50) =& \boldsymbol{P}^{\Sigma}\left(\frac{\boldsymbol{G}^{\mathrm{T}}}{2}-\boldsymbol{K}_0\right)\boldsymbol{P}^{\Sigma}\left(\boldsymbol{G}^{\mathrm{T}}\right)^{-1}\mathbb{P}^{\Lambda}\left(\frac{\boldsymbol{G}^{\mathrm{T}}}{2}+\boldsymbol{K}_0\right)\mathbb{P}^{\Lambda}\\ =& \boldsymbol{0}, \end{aligned} \quad (5.55)$$

which completes the proof.

The term $\mathbb{P}^{\Sigma H}\boldsymbol{O}\boldsymbol{P}^{\Lambda H}$ can now be studied. To this end, note that

$$\begin{aligned}\alpha^2\mathbb{P}^{\Sigma H}\boldsymbol{O}\boldsymbol{P}^{\Lambda H} = \;& \mathbb{P}^{\Sigma H}\left(\frac{\boldsymbol{G}^{\mathrm{T}}}{2}-\boldsymbol{K}_0\right)\left(\boldsymbol{G}^{\mathrm{T}}\right)^{-1}\left(\frac{\boldsymbol{G}^{\mathrm{T}}}{2}+\boldsymbol{K}_0\right)\boldsymbol{P}^{\Lambda H}\\ &+\mathbb{P}^{\Sigma H}\left(\frac{\boldsymbol{G}^{\mathrm{T}}}{2}-\boldsymbol{K}_0\right)\left(\boldsymbol{G}^{\mathrm{T}}\right)^{-1}\left(\boldsymbol{K}'_k\right)\boldsymbol{P}^{\Lambda H}\\ &-\mathbb{P}^{\Sigma H}\left(\boldsymbol{K}'_{-\mathrm{j}k}\right)\left(\boldsymbol{G}^{\mathrm{T}}\right)^{-1}\left(\frac{\boldsymbol{G}^{\mathrm{T}}}{2}+\boldsymbol{K}_0\right)\boldsymbol{P}^{\Lambda H}\\ &-\mathbb{P}^{\Sigma H}\left(\boldsymbol{K}'_{-\mathrm{j}k}\right)\left(\boldsymbol{G}^{\mathrm{T}}\right)^{-1}\left(\boldsymbol{K}'_k\right)\boldsymbol{P}^{\Lambda H}\\ =\;& 0+\mathcal{O}\left(k^2\right)+\mathcal{O}\left(k^2\right)-\mathcal{O}\left(k^4\right),\end{aligned} \tag{5.56}$$

which completes the low-frequency analysis of the overall operator

$$\begin{aligned}\boldsymbol{O} &= \mathbb{P}^{\Lambda}\boldsymbol{O}\boldsymbol{P}^{\Sigma}+\mathbb{P}^{\Lambda}\boldsymbol{O}\boldsymbol{P}^{\Lambda H}+\mathbb{P}^{\Sigma H}\boldsymbol{O}\boldsymbol{P}^{\Sigma}+\mathbb{P}^{\Sigma H}\boldsymbol{O}\boldsymbol{P}^{\Lambda H}\\ &= \mathcal{O}\left(\alpha^2\right)+\mathcal{O}(1)+\mathcal{O}(1)+\mathcal{O}\left(\frac{k^2}{\alpha^2}\right).\end{aligned} \tag{5.57}$$

To choose α, in addition to the conditioning constraint imposed by (5.57), we need to consider the physical scaling of the current, which for a plane wave excitation, is [QC10]

$$\boldsymbol{P}^{\Lambda H}\boldsymbol{j} = \mathcal{O}(1), \tag{5.58}$$

$$\boldsymbol{P}^{\Sigma}\boldsymbol{j} = \mathcal{O}(k). \tag{5.59}$$

These scaling laws reveal that for a standard formulation, a severe numerical cancellation is expected due to the fact that the non-solenoidal component of the current (which scales as $\mathcal{O}(k)$) will disappear when stored alongside the solenoidal component (which scales as $\mathcal{O}(1)$). Instead, for the regularized formulation proposed here, the equation is solved for $\boldsymbol{i} = \boldsymbol{M}^{-1}\boldsymbol{j}$, which scales as

$$\boldsymbol{P}^{\Lambda H}\boldsymbol{i} = \mathcal{O}(\alpha), \tag{5.60}$$

$$\boldsymbol{P}^{\Sigma}\boldsymbol{i} = \mathcal{O}(k/\alpha). \tag{5.61}$$

It is now evident that by setting $\alpha = \sqrt{k}$, the above scaling behaviors become

$$\boldsymbol{P}^{\Lambda H}\boldsymbol{i} = \mathcal{O}\left(\sqrt{k}\right), \tag{5.62}$$

$$\boldsymbol{P}^{\Sigma}\boldsymbol{i} = \mathcal{O}\left(\sqrt{k}\right), \tag{5.63}$$

eliminating the low frequency cancellation and, at the same time, stabilizing the matrix at low frequencies. The latter is seen upon inserting the new scalings into (5.57):

$$\begin{aligned} \boldsymbol{O} &= \mathcal{O}\left(\alpha^2\right) + \mathcal{O}(1) + \mathcal{O}(1) + \mathcal{O}\left(\frac{k^2}{\alpha^2}\right) \\ &= \mathcal{O}(k) + \mathcal{O}(1) + \mathcal{O}(1) + \mathcal{O}(k)\,. \end{aligned} \tag{5.64}$$

The deficiency of the MFIE in the static regime also is solved by the scheme proposed here. In fact, using (5.57) when $k = 0$ we obtain

$$\boldsymbol{O}\boldsymbol{P}^{\wedge H} = \mathbb{P}^{\wedge}\boldsymbol{O}\boldsymbol{P}^{\wedge H}\,, \tag{5.65}$$

which proves the existence of an exact matrix null-space in statics of dimension exactly equal to that of the harmonic subspace.

Summarizing, the proposed MFIE resolves the three main issues of prior standard and non-standard MFIE formulations and now can be linearly combined with EFIEs using projectors.

d) A New CFIE

The theoretical developments of the previous sections resulted in a magnetic field operator that can be stably discretized for arbitrarily low frequencies using standard integration rules. The electric counterpart of this operator was obtained in [And+13b]. We will now combine these two operators, first proving the resonance-free property of their continuous combination at high frequencies, and then showing their compatibility at arbitrarily low frequencies.

Standard Calderón CFIE equations use a localization strategy for the EFIE component to obtain a resonance-free equation [Ada04; Con+02]. Here, we follow the Yukawa-Calderón approach in [Con+02]. When the Yukawa-Calderón EFIE is linearly combined with the new magnetic operator defined in Section 5.c, the following symmetric Yukawa-Calderón CFIE is obtained:

$$\begin{aligned} \left(\eta^2\left(\frac{\mathcal{I}}{2} - \mathcal{K}_{-\mathrm{j}k}\right)\left(\frac{\mathcal{I}}{2} + \mathcal{K}_k\right)(k) + \mathcal{T}_{-\mathrm{j}k}\mathcal{T}_k\right)(j) = \\ \left(\frac{\mathcal{I}}{2} - \mathcal{K}_{-\mathrm{j}k}\right)\left(\hat{\boldsymbol{n}} \times \boldsymbol{h}^i\right) + \mathcal{T}_{-\mathrm{j}k}\left(\hat{\boldsymbol{n}} \times \boldsymbol{e}^i\right). \end{aligned} \tag{5.66}$$

To demonstrate that this equation represents a valid CalderónCFIE, i.e. is free from internal resonances, we prove that the operator

$$\left(\eta^2\left(\frac{\mathcal{I}}{2}-\mathcal{K}_{-\mathrm{j}k}\right)\left(\frac{\mathcal{I}}{2}+\mathcal{K}_{k}\right)(k)+\mathcal{T}_{-\mathrm{j}k}\mathcal{T}_{k}\right) \tag{5.67}$$

can be inverted for any k. Since the operator $\left(\frac{\mathcal{I}}{2}-\mathcal{K}\right)(-\mathrm{j}k)$ always admits an inverse, the invertibility of (5.67) is equivalent to the invertibility of

$$\left(\frac{\mathcal{I}}{2}+\mathcal{K}_{k}\right)+\left(\frac{\mathcal{I}}{2}-\mathcal{K}_{-\mathrm{j}k}\right)^{-1}\mathcal{T}_{-\mathrm{j}k}\mathcal{T}_{k}. \tag{5.68}$$

Given the anti-commutation property

$$\mathcal{T}^{-1}\mathcal{K}+\mathcal{K}\mathcal{T}^{-1}=0, \tag{5.69}$$

which follows directly from the second Calderón identity $\mathcal{T}^{-1}\mathcal{K}=\mathcal{T}^{-1}\mathcal{K}\mathcal{T}\mathcal{T}^{-1}=-\mathcal{T}^{-1}\mathcal{T}\mathcal{K}\mathcal{T}^{-1}=-\mathcal{K}\mathcal{T}^{-1}$, and defining

$$\mathcal{A}=\left(\frac{\mathcal{I}}{2}-\mathcal{K}_{-\mathrm{j}k}\right)^{-1}\mathcal{T}_{-\mathrm{j}k}, \tag{5.70}$$

it follows that

$$\begin{aligned}
\left(\hat{\boldsymbol{n}}\times\mathcal{A}\right)^{\mathrm{T}} &= \left(\hat{\boldsymbol{n}}\times\left(\frac{\mathcal{I}}{2}-\mathcal{K}_{-\mathrm{j}k}\right)^{-1}\mathcal{T}_{-\mathrm{j}k}\right)^{\mathrm{T}}\\
&= \left(\hat{\boldsymbol{n}}\times\left(\mathcal{T}_{-\mathrm{j}k}^{-1}\left(\frac{\mathcal{I}}{2}-\mathcal{K}_{-\mathrm{j}k}\right)\right)^{-1}\right)^{\mathrm{T}}\\
&= \left(\hat{\boldsymbol{n}}\times\left(\left(\frac{\mathcal{I}}{2}+\mathcal{K}_{-\mathrm{j}k}\right)\mathcal{T}_{-\mathrm{j}k}^{-1}\right)^{-1}\right)^{\mathrm{T}}\\
&= \left(\hat{\boldsymbol{n}}\times\mathcal{T}_{-\mathrm{j}k}\left(\frac{\mathcal{I}}{2}+\mathcal{K}_{-\mathrm{j}k}\right)^{-1}\right)^{\mathrm{T}}\\
&= \left(\left(\frac{\mathcal{I}}{2}+\mathcal{K}_{-\mathrm{j}k}\right)^{-1}\right)^{\mathrm{T}}\hat{\boldsymbol{n}}\times\mathcal{T}_{-\mathrm{j}k}\\
&= -\hat{\boldsymbol{n}}\times\left(\frac{\mathcal{I}}{2}-\mathcal{K}_{-\mathrm{j}k}\right)^{-1}\hat{\boldsymbol{n}}\times\hat{\boldsymbol{n}}\times\mathcal{T}_{-\mathrm{j}k}\\
&= \hat{\boldsymbol{n}}\times\left(\frac{\mathcal{I}}{2}-\mathcal{K}_{-\mathrm{j}k}\right)^{-1}\mathcal{T}_{-\mathrm{j}k}=\hat{\boldsymbol{n}}\times\mathcal{A}.
\end{aligned} \tag{5.71}$$

Given this result and the fact that

$$\hat{\boldsymbol{n}} \times \boldsymbol{\mathcal{A}} = \hat{\boldsymbol{n}} \times \left(\frac{\mathcal{I}}{2} - \mathcal{K}_{-\mathrm{j}k} \right)^{-1} \mathcal{T}_{-\mathrm{j}k} \tag{5.72}$$

is a real operator, the symmetry implies it being Hermitian, so that

$$\boldsymbol{x}^{\dagger} \left[\hat{\boldsymbol{n}} \times \left(\left(\frac{\mathcal{I}}{2} - \mathcal{K}_{-\mathrm{j}k} \right) (\mathrm{j}k) \right)^{-1} \mathcal{T}_{-\mathrm{j}k} \right] \boldsymbol{x} \tag{5.73}$$

is real and nonzero. By leveraging a straightforward extension of Theorem 3.1 in [Bru+09], it follows that

$$\left(\left(\frac{\mathcal{I}}{2} - \mathcal{K}_{-\mathrm{j}k} \right) \left(\frac{\mathcal{I}}{2} + \mathcal{K}_{k} \right) + \mathcal{T}_{-\mathrm{j}k} \mathcal{T}_{k} \right) \tag{5.74}$$

is always invertible. Otherwise said, the Yukawa-Calderón CFIE we propose is resonance free.

The discretization of the proposed Yukawa-Calderón CFIE follows directly from that of the new MFIE in Section 5.c and that of the EFIE in [And+13b]:

$$\begin{aligned} \eta^2 \mathbb{M}^{\mathrm{T}} \left(\frac{\boldsymbol{G}^{\mathrm{T}}}{2} - \boldsymbol{K}_{-\mathrm{j}k} \right) \left(\boldsymbol{G}^{\mathrm{T}} \right)^{-1} \left(\frac{\boldsymbol{G}^{\mathrm{T}}}{2} + \boldsymbol{K}_{k} \right) \boldsymbol{M}\boldsymbol{i} + \mathbb{M}^{\mathrm{T}} \mathbb{T}\mathbb{M} (\boldsymbol{G})^{-1} \boldsymbol{M}^{\mathrm{T}} \boldsymbol{T} \boldsymbol{M}\boldsymbol{i} \\ = \eta^2 \mathbb{M}^{\mathrm{T}} \left(\frac{\boldsymbol{G}^{\mathrm{T}}}{2} - \boldsymbol{K}_{-\mathrm{j}k} \right) \left(\boldsymbol{G}^{\mathrm{T}} \right)^{-1} \boldsymbol{v}_h + \mathbb{M}^{\mathrm{T}} \mathbb{T}\mathbb{M} (\boldsymbol{G})^{-1} \boldsymbol{M}^{\mathrm{T}} \boldsymbol{v}_e \,. \end{aligned} \tag{5.75}$$

Here $\alpha = 1$ and $\alpha = \sqrt{k}$ in the high and low frequency regime, respectively. We next study the latter more in detail.

Scaling in the latter regime follows from the results of the previous section:

$$\begin{aligned} & \eta^2 \mathbb{M}^{\mathrm{T}} \left(\frac{\boldsymbol{G}^{\mathrm{T}}}{2} - \boldsymbol{K}_{-\mathrm{j}k} \right) \left(\boldsymbol{G}^{\mathrm{T}} \right)^{-1} \left(\frac{\boldsymbol{G}^{\mathrm{T}}}{2} + \boldsymbol{K}_{k} \right) \boldsymbol{M}\boldsymbol{i} + \mathbb{M}^{\mathrm{T}} \mathbb{T}\mathbb{M} (\boldsymbol{G})^{-1} \boldsymbol{M}^{\mathrm{T}} \boldsymbol{T} \boldsymbol{M}\boldsymbol{i} \\ = & - \mathrm{j} \left(\mathbb{P}^{\Sigma H} \mathbb{T}_s \mathbb{P}^{\Sigma H} \right) \boldsymbol{G}^{-1} \boldsymbol{T}_h + \mathrm{j} \mathbb{T}_h \boldsymbol{G}^{-1} \left(\boldsymbol{P}^{\Lambda H} \boldsymbol{T}_s \boldsymbol{P}^{\Lambda H} \right) + \\ & \mathrm{j} \left(\mathbb{P}^{\Sigma H} \mathbb{T}_s \mathbb{P}^{\Sigma H} \right) \boldsymbol{G}^{-1} \left(\boldsymbol{P}^{\Lambda H} \boldsymbol{T}_s \boldsymbol{P}^{\Lambda H} \right) + \\ & \eta^2 \mathbb{P}^{\Sigma H} \left(\frac{\boldsymbol{G}^{\mathrm{T}}}{2} - \boldsymbol{K}_{0} \right) \left(\boldsymbol{G}^{\mathrm{T}} \right)^{-1} \left(\frac{\boldsymbol{G}^{\mathrm{T}}}{2} + \boldsymbol{K}_{0} \right) \mathrm{j} \boldsymbol{P}^{\Sigma} + \\ & \eta^2 \mathrm{j} \mathbb{P}^{\Lambda} \left(\frac{\boldsymbol{G}^{\mathrm{T}}}{2} - \boldsymbol{K}_{0} \right) \left(\boldsymbol{G}^{\mathrm{T}} \right)^{-1} \left(\frac{\boldsymbol{G}^{\mathrm{T}}}{2} + \boldsymbol{K}_{0} \right) \boldsymbol{P}^{\Lambda H} + \mathcal{O}(k) \\ = & \mathcal{O}(1) + \mathcal{O}(1) + \mathcal{O}(1) + \mathcal{O}(1) + \mathcal{O}(1) + \mathcal{O}(k) \,. \end{aligned} \tag{5.76}$$

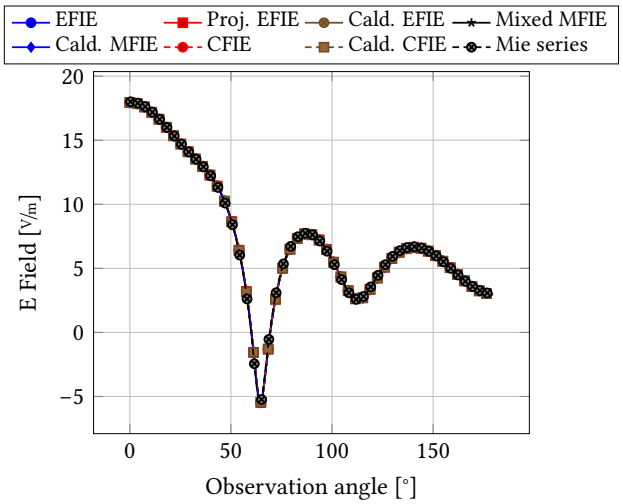

Fig. 5.2.: Comparison of the far field scattered by a PEC sphere of radius 1 m discretized with an average edge size of 0.15 m and excited by a plane wave oscillating at 200 MHz.

Combining this result with the corresponding right hand side scalings (5.62) and (5.63) proves the overall low-frequency stability of new CFIE.

e) Numerical Results

This section presents numerical results that validate the above properties of the proposed MFIE and CFIE.

The first set of tests involve a PEC sphere of radius 1 m. Figure 5.2 shows the scattered far field at $f = 200$ MHz obtained using the new MFIE and CFIE as well as other established formulations (standard EFIE, EFIE with projectors, Calderón EFIE with projectors, Mixed MFIE, CFIE). For this high frequency case all formulations deliver accurate results, thus validating our implementations. A first difference in performance between our new formulations and their standard counterparts is noted when lowering the frequency. Figure 5.3 shows data similar to Figure 5.2 but for $f = 1 \cdot 10^{-40}$ Hz. It is clear that accuracy breakdowns occur for the non-projected methods – the mixed MFIE, the EFIE, and the CFIE (for the latter two the lack of accuracy also is due to conditioning problems). On the other hand, all projected formulations, including the two new ones, deliver accurate results for arbitrarily low frequencies.

The low frequency stability of the new Calderón MFIE is further demonstrated

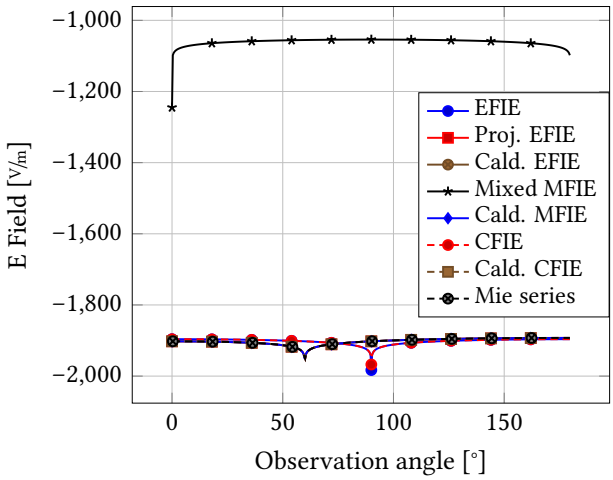

Fig. 5.3.: Comparison of the far field scattered by a PEC sphere of radius 1 m discretized with an average edge size of 0.15 m and excited by a plane wave oscillating at $1 \cdot 10^{-40}$ Hz.

in Figure 5.4, which illustrates the conditioning of the different operators for low frequencies. It is clear that the new MFIE remains as well-conditioned as its standard counterpart. The Calderón CFIE is also low-frequency stable, unlike the standard CFIE, which exhibits a severe ill-conditioning caused by its EFIE contribution.

Figure 5.5 shows that, despite its regularized low frequency behavior, the Calderón MFIE is prone to spurious resonances causing it to become periodically ill-conditioned. This issue is shared by all non combined formulations and can be overcome by combined field strategies. It is clear from the figure that both the new Calderón CFIE and its standard counterpart exhibit resonance-free behaviour.

The last key property to be illustrated is the refinement stability of the proposed formulations. This property was verified by studying the dependence of the condition number of the different formulations applied to a unit radius sphere with increasing discretization density (Figure 5.6). These results confirm that the second kind nature of our new formulations renders them immune to the high-refinement breakdown.

In summary, the above results show that the new Calderón MFIE yields correct results for arbitrarily low frequencies and is well conditioned for both low frequencies and dense discretization. Additionally, when combined with the projector Calderón EFIE the new Calderón CFIE, which is low frequency stable, immune to dense discretization breakdown, and free from non-physical resonances, is obtained.

To ensure that the properties illustrated so far still persist for multiply connected

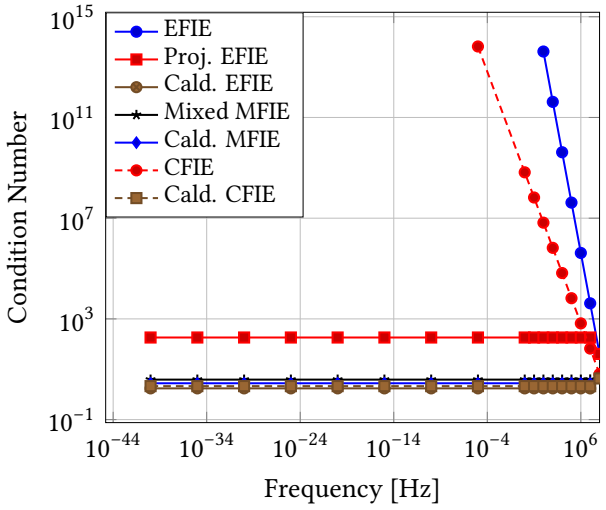

Fig. 5.4.: Low frequency behaviour of the conditioning of the different operators on a PEC sphere of radius 1 m. Because of numerical limitations in the computation of very high condition numbers ($> 1 \cdot 10^{16}$) some points have been left out.

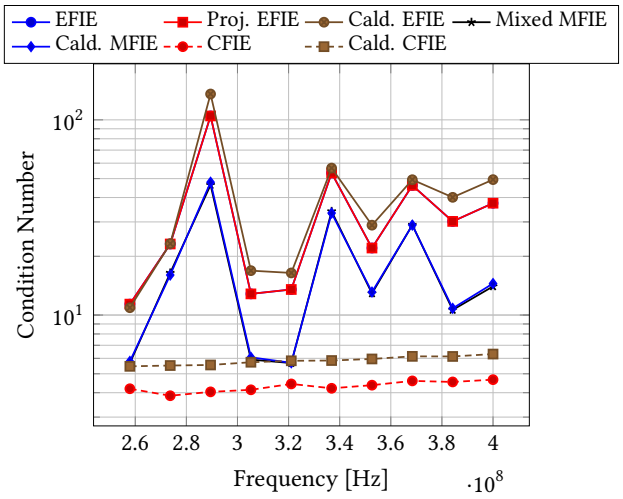

Fig. 5.5.: High frequency behaviour of the conditioning of the different operators on a PEC sphere of radius 1 m sphere illustrating the spurious resonances occurring in non-combined formulations. The average edge size of the discretized sphere has been kept at one-fifth of the wavelength for every simulation.

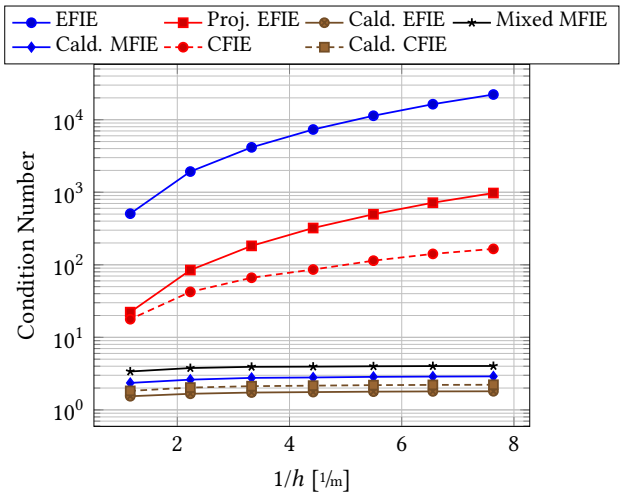

Fig. 5.6.: High-refinement behaviour of the conditioning of the different operators on a PEC sphere of radius 1 m. The non-resonant frequency has been kept constant for all simulations and corresponds to 5 unknowns per wavelength discretization for the least refined point.

structures, many of the previous analyses were repeated for a square torus. The correctness of the formulation has been verified by studying the far field scattered by the torus at high and very low frequencies, respectively (Figures 5.7 and 5.8). Since no analytic solution is readily available for the square torus, the solution of the Calderón EFIE was used as a reference and particular care was taken to avoid frequencies corresponding to an internal resonance. While the results are similar to those of the sphere, the reader should be aware that, because of its toroidal and poloidal null-spaces, the Calderón MFIE required the usage of a pseudo inversion to obtain current solutions at very low frequencies.

The low frequency stability of the Calderón MFIE and Calderón CFIE on the toroidal structure are demonstrated in Figure 5.9, while their resonance free behaviors are illustrated in Figure 5.10. Finally, the resilience of both formulations to dense discretization breakdown is illustrated in Figure 5.11, which presents the condition number of the integral operators with increasing discretization of the square torus.

One of the key advantages of the new Calderón MFIE scheme is that it does not require extremely accurate numerical integration rules because it allows explicit cancellation of near-zero terms that are challenging to obtain numerically. The slow convergence of the standard numerical integration schemes can be seen in Figure 5.12, in which the ratio of the norm of the term in (5.35) to the norm of the

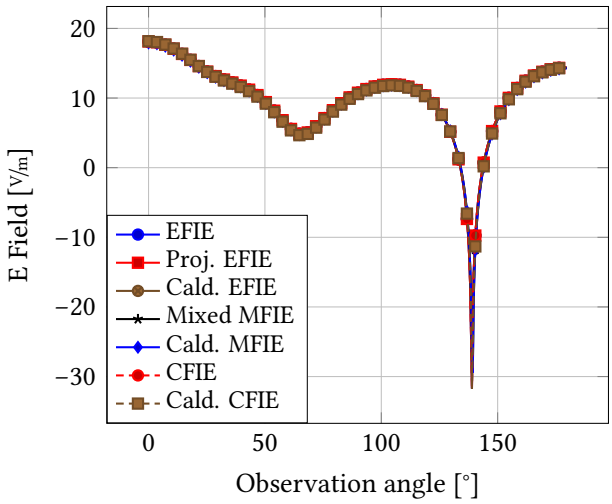

Fig. 5.7.: Comparison of the far field scattered by a PEC square torus with an inner radius of 0.5 m and a tube radius of 0.25 m, discretized with an average edge size of 0.15 m and excited by a plane wave oscillating at 200 MHz.

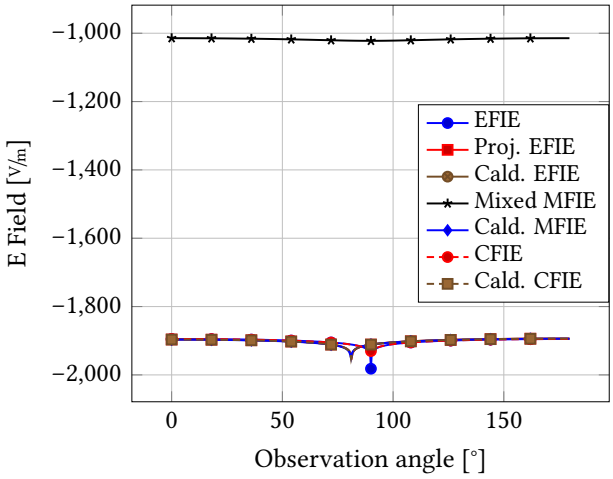

Fig. 5.8.: Comparison of the far field scattered by a PEC square torus with an inner radius of 0.5 m and a tube radius of 0.25 m, discretized with an average edge size of 0.15 m and excited by a plane wave oscillating at $1 \cdot 10^{-40}$ Hz.

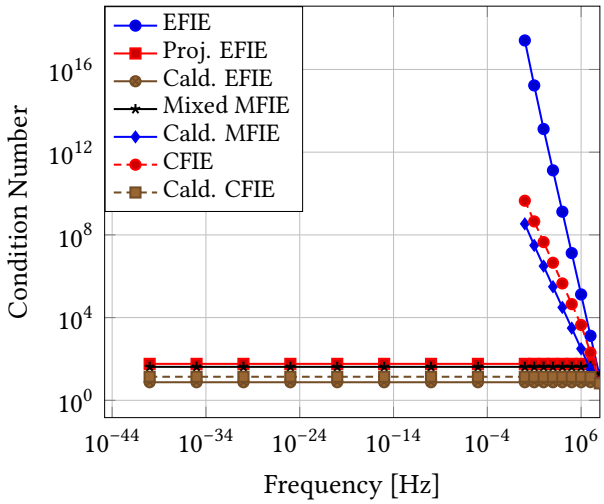

Fig. 5.9.: Low frequency behaviour of the conditioning of the different operators on a PEC square torus with an inner radius of 0.5 m, a tube radius of 0.25 m and meshed with an average edge length of 0.6 m. Because of numerical limitations in the computation of very high condition numbers ($> 1 \cdot 10^{16}$) some points have been left out.

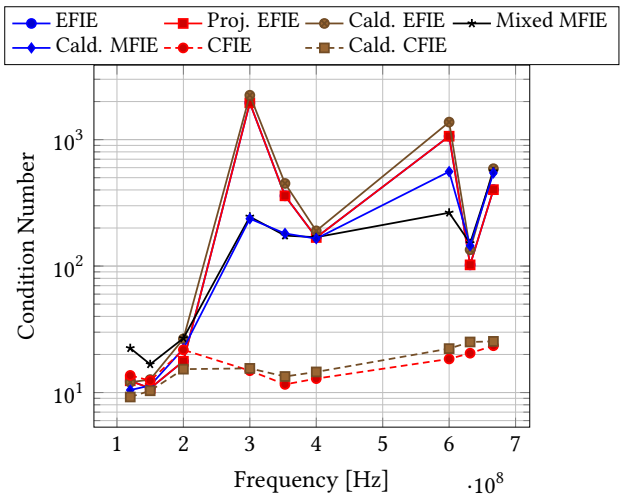

Fig. 5.10.: High frequency behaviour of the conditioning of the different operators on a PEC square torus of inner radius of 0.5 m and tube radius of 0.25 m, illustrating the resonances of non-combined formulations. The average edge size of the discretization has been kept at one-fifth of the wavelength for every simulation.

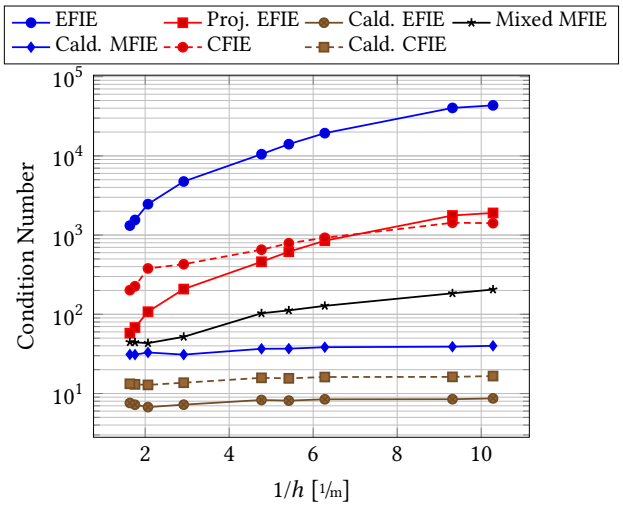

Fig. 5.11.: High-refinement behaviour of the conditioning of the different operators on a PEC square torus of inner radius of 0.5 m and tube radius of 0.25 m. The non-resonant frequency has been kept constant for all simulations and corresponds to a 5 unknowns per wavelength discretization for the least refined point.

full operator with increasing number of integration points is presented. While this ratio does decrease with the number of Gaussian quadrature points, it does so very slowly and remains far from a machine-precision zero value. The effect of these numerical inaccuracies is evident when comparing the singular value decompositions of the Mixed MFIE and of the new Calderón MFIE in Figure 5.13. It is clear that the null singular values corresponding to the toroidal and poloidal subspaces of the square torus immediately reach the machine precision zero in the case of the Calderón MFIE, while for the Mixed MFIE they will require an unreasonably complex integration rules to even remotely resemble a nullspace.

Finally, to demonstrate that our schemes can be readily applied to more complex problems we studied the low frequency conditioning of our operators (Figure 5.15) for the complex, multiply connected geometry in Figure 5.14.

f) Conclusion

This chapter presented a new symmetrized MFIE that can be stably and effectively discretized using quasi-Helmholtz projectors. When linearly combined with a quasi-Helmholtz projector-based Calderón EFIE, a new CFIE that is immune from all drawbacks that plague the majority of existing formulations is obtained. In fact,

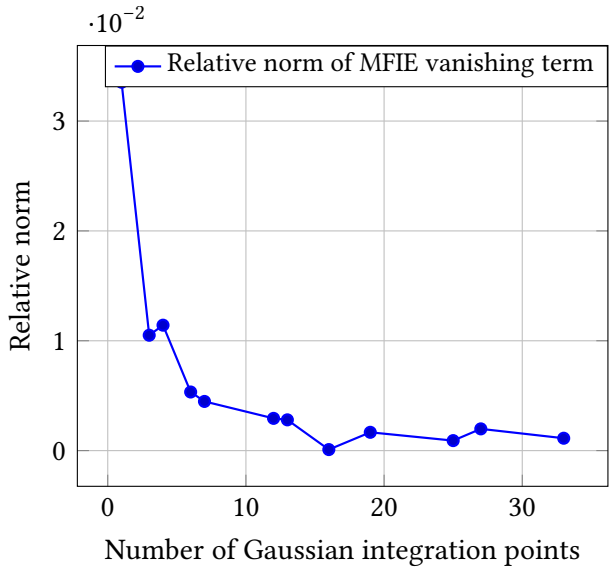

Fig. 5.12.: Decay of the relative (with regards to the full operator) norm of cancelled out term (5.35) of the Calderón CFIE as a function of the number of Gaussian integration points. These results correspond to a square torus of inner radius 0.5 m and tube radius 0.25 m simulated at $1 \cdot 10^{-10}$ Hz.

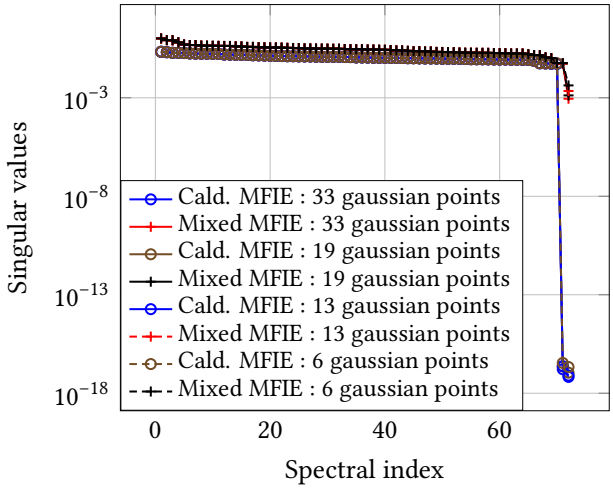

Fig. 5.13.: Accuracy of the toroidal and poloidal nullspaces obtained by the Calderón and Mixed MFIE as a function of the number of Gaussian integration points. The results correspond to a square torus of inner radius 0.5 m and tube radius 0.25 m simulated at $1 \cdot 10^{-10}$ Hz.

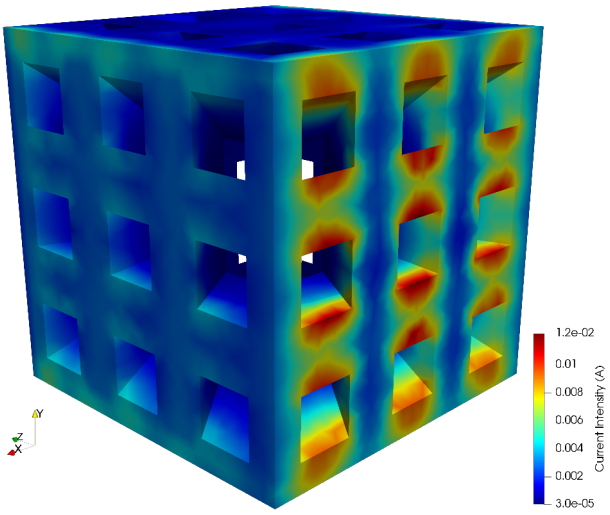

Fig. 5.14.: Complex multiply-connected geometry discretized with an average edge length of 0.35 m. The values represented on the geometry correspond to the intensity of the current induced on the PEC structure by a plane wave. The simulating frequency corresponds to 10 unknowns per wavelength.

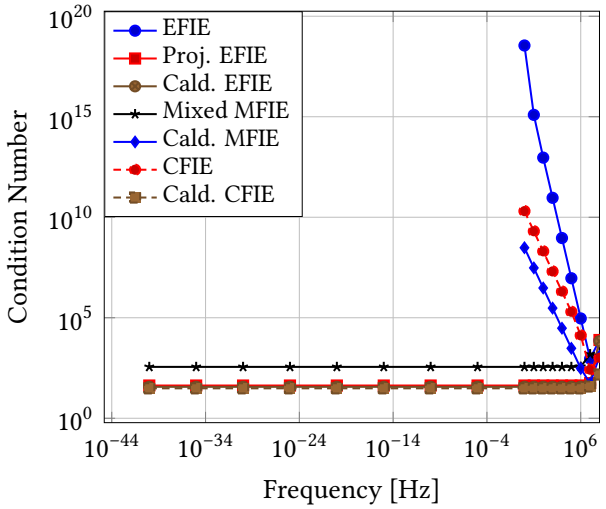

Fig. 5.15.: Low frequency behaviour of the conditioning of the different operators on the structure illustrated in Figure 5.14. Because of numerical limitations in the computation of very high condition numbers ($> 1 \cdot 10^{16}$) some points have been left out.

the proposed CFIE remains well-conditioned both at low frequencies and for high discretization densities, allows for an accurate solution at extremely low frequencies without requiring special numerical quadrature methods, does not require the detection of global loops when applied to multiply connected geometries, and is provably free from internal resonances. Numerical results confirm the theoretically predicted properties of the proposed equations.

Chapter 6

Impacting Brain Computer Interfaces with Computation Electromagnetics

Currently the most affordable and practical general purpose brain computer interfaces (BCIs) rely on electroencephalography (EEG) or magnetoencephalography which offer a high temporal resolution. However these techniques are severely limited in spatial resolution, especially compared to the very high level of details that can be obtained from magnetic resonance imaging. A widely explored approach to compensate this limitation is to integrate EEG source imaging (ESI) techniques into the process. These techniques are based on a model of the electromagnetic behaviour of the brain, often leveraging on BEM or FEM to reconstruct the brain activity from scalp measurements, and have shown promising results in challenging BCI applications. This chapter presents the first results of this thesis's work dedicated to enhancing the state of the art BCI via improvements to the integral equation models used for ESI. Early in this work, it became clear that the prohibitive cost of human experiments would make the research very challenging. In addition, because the human experiments are notoriously unreliable at small scales and because it is impossible to know what exactly happened in the head of the user, it was decided to use simulated BCI data. However, none of the few available works on the topic were matching the requirements to make strong statements about BCI performance. This state of facts motivated the development of a fully simulated BCI evaluation framework. While the simBCI framework is not a substitute for actual experiments, it makes it possible to study in details the impact of specific changes to the processing scheme and to gain insight into the interactions of the different components. A large amount of time has been devoted to the development of simBCI in order to make sure that it was able to produce realistic BCI signals while still being modular enough for allowing investigations. For this reason only very early results related to the improvement of the ESI-augmented BCI have been produced as of this writing. However the scientific contribution of simBCI itself has been recognized by its publication in a domain-specific journal. In this chapter the motivations behind simBCI are presented and the framework and its usage are descried. An experimental protocol is described that will be used in the near future to investigate

areas of improvements in integral equation based BCI.

a) Introduction

Brain computer interfaces are systems designed to translate the different brain states of its users into predetermined commands for the target system. Application scenarios for BCIs range from therapeutic where they can be used to command assistive technologies such as prostheses for amputees or spellers for patient suffering for locked-in syndrome [Bir06] to innovative interfaces for a wide variety of systems [ZK11; Coy+13]. Traditionally BCI systems are composed of an acquisition device, typically EEG or magnetoencephalogram (MEG), in charge of measuring part of the user's brain activity and of a processing pipeline that is trained to distinguish between the different mental states of the user and to translate them into the corresponding commands. In the case of non-invasive BCI, EEG remains the most widely used acquisition device thanks to its high temporal resolution, affordability and practicality. The signals it measures are, however, intrinsically difficult to work with because of their low signal-to-noise ratio (SNR) and low spatial resolution. These challenges have motivated the development of numerous and ever more advanced techniques to improve the accuracy of EEG-based BCIs; a thorough review of these techniques can be found in [Lot+07] and its updated version in [Lot+18].

Usage of EEG source imaging (ESI), often inherited from research in epilepsy, in BCI have seen a steady increase over the last few years [HVG18]. These techniques aim at reconstructing the current distribution inside the brain from the EEG scalp measurements. This reconstruction relies on an accurate anatomical modeling of the different components of the head (scalp, skull, cortical surface, white matter, etc.), which can be obtained from magnetic resonance imaging (MRI), to compute the mapping from current sources – modeling the neurons [dMvDS88] – within the brain to their effect on the electrodes. In the literature this problem is designated as the EEG forward problem (FP) and has been extensively studied [Hal+07]. FPs taking into account the complex anisotropy profiles of the brain are built using FEM [Wol+06] yielding large matrices, making the leadfield computationally expensive to compute. However, it is common to model the head as three concentric spheres with homogeneous conductivity profiles, in which case smaller systems can be obtained by leveraging BEMs [Hed+17]. Because this homogeneity approximation introduces non-negligible errors in the modelling, new BEM solvers capable of modeling the white matter anisotropy are being developed [OPC11; PRA16]. This

mapping is obtained for every dipoles on grid within the brain (or on the cortex) in order to form the leadfield matrix which maps the effects of all dipoles to the electrodes. In the context of ESI the reciprocal mapping needs to be obtained. However, given that research EEG headset are composed of, at most, 256 electrodes [Son+15] and that the number of reconstructed current sources is in the order of 10 000 [HVG18], the inverse problem is severely ill-posed and admits several solutions. Techniques based on regularization [Gre+08] and genetic algorithms [UHS98], among others, have been used to obtain reliable solutions to this inverse problem (IP).

This chapter focuses on identifying the impact of the accuracy of the integral equation-based ESI can have on the performance of BCI systems. In other words, this work tries to determine to what extent and under what conditions increasing the precision and complexity of the integral modeling of the forward problem leads to improvements in BCI performance. Early developments of this work have identified several issues with the traditional approach to BCI studies: (i) it is very costly and time consuming to train a large user base to perform statistically significant BCI experiments; (ii) using actual EEG recordings, even if acquired from freely available datasets, is unsatisfactory since it is not possible to know what actually happened in the brain of the user during the trial, and this lack of ground truth makes it almost impossible to draw insights or strong conclusions on the performance of BCI pipelines; (iii) in the case of ESI it is also complex to obtain and segment MRI models of every subject. These challenges have motivated the development of *simBCI*, the first – to the best of our knowledge – freely available full simulator for BCI generation and analysis of EEG recordings for BCI tasks and BCI processing pipelines. Other works have been published on simulated BCI but they are either based on modified actual EEG measurements [Lot11; CMT17] or not freely available [Tan+12]. The *simBCI* framework has been developed in collaboration with Dr. Jussi Lindgren and has been accepted for publication in a domain specific peer-reviewed journal [Lin+18b]. This tool enables new ways of approaching BCI development and numerous research axes are either under investigation or are to be in the near future. In order to take advantage of the new possibilities offered by *simBCI*, which allows for studies of very specific parameters of the pipelines (which is hardly possible with experimental approaches) an experimental protocol has been established and is being implemented. As a side effect this work has delivered the first (to the best of out knowledge) publicly available reimplementations of [Cin+08; EBH16; Tan+12].

The work on BCI of this thesis was part of the Seizing Advances in Bci from high Resolution Eeg imaging in runtime (SABRE) project financed by the CominLabs.

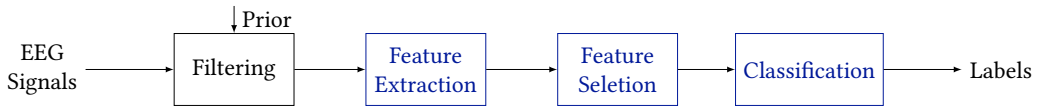

Fig. 6.1.: Illustration of a typical data-driven BCI pipeline. The blue color indicates components that need to be trained while the vertical arrow indicates that external information (prior) is provided to the system.

b) Traditional BCI Systems

Traditional BCI systems include a large number of components such as filters, classifiers, optimizers, etc. some of which need to be trained to learn the different features that characterize the mental states of interest (Figure 6.1). Because of the variabilities between tasks, patients and even sessions, the training should be performed for each patient at every session. During the training phase the system dictates the mental state its user should be in which allows the machine learning components to identify which features of the EEG signal are discriminant and which brain state or label, is also trained. The trained feature extractor and classifier are then used during the *online* phase to classify the unlabeled EEG signals and associate them to a specific command. Alternative schemes based on neural networks or Riemannian spaces have been introduced to unify the feature extraction and classification [Lot+18]. Others have attempted to use unsupervised learning approaches in order to do without the training phase altogether [Lot+18].

A simple example purely data-driven BCI pipeline can be obtained by using a common spatial pattern (CSP) as feature extractor and a linear discriminant analysis (LDA) as classifier [Lin+18b]. Despite its simplicity this pipeline as been shown, in *simBCI* to yield up to 80% accuracy given a long enough training and a favorable enough SNR.

c) Integral Equations-enhanced BCI

Enhancing BCI with integral equations and ESI has promising applications. One of the key advantages of this technique is physiological interpretability of the dipoles activity, which allows medical knowledge to be inserted in the problem to try to address its under-determination. This is in opposition with raw EEG signals that are reportedly less interpretable and potentially misleading in some instances. The spatial and anatomical informations provided by ESI make it possible, for instance, to only consider the signals coming from the region of interest (ROI) that

is known to be associated with the BCI task under consideration (e.g. the motor cortex in the case of motor imagery (MI) [Cin+08]). Such physical priors have the potential to reduce the under-determination of the inverse problem and to improve understanding of the merits of demerits of different BCI approaches, which is often not possible for purely data-driven approaches. In addition, because of the blurring effect caused by the forward problem, accurate ROI selection is less straightforward in the electrode space, contributions of one region of the brain is spread across several electrodes that are not necessarily the closest ones. Finally, the features in the dipole space have been shown to be more statistically significant [Cin+08], which indicates that data-driven approaches applied to the source space can be expected to be more robust than in the electrode space.

α) Forward Problem

The forward problem (FP) leverages on Maxwell's equations in the quasi-static regime (see Section 2.h) to compute the scalp potentials generated by a single dipole located in the brain. Under the approximation of a head composed of three homogeneous concentric volumes, integral equations are the scheme of choice to solve this problem: given the notations of Section 2.i, the $\mathcal{D}$ operator

$$(\mathcal{D}u)(\boldsymbol{r}) = \int_{\partial\Omega} \gamma_1' G_s\big(\boldsymbol{r} - \boldsymbol{r}'\big)\, u\big(\boldsymbol{r}'\big)\,\mathrm{d}\boldsymbol{r}' \tag{6.1}$$

is used to build the mapping from source space – neurons – to measurement space – electrodes – by repeatedly solving the forward problem

$$v_d(\boldsymbol{r}) = \frac{\sigma_j + \sigma_{j+1}}{2} V(\boldsymbol{r}) - \sum_{i=1}^{N} (\sigma_{i+1} - \sigma_i)\big(\mathcal{D}\gamma_{0,i} V\big)(\boldsymbol{r}), \quad \boldsymbol{r} \in \Gamma_j, \tag{6.2}$$

with different RHSs v_d, once for every dipolar source. The results of these inversions are then aggregated to form the *leadfield* matrix $\boldsymbol{G} \in \mathbb{R}^{N_e \times N_d}$ which maps the signal of the N_d dipolar sources in the brain $\boldsymbol{s}$ to the N_e electrodes on the scalp

$$\boldsymbol{v} = \boldsymbol{G}\boldsymbol{s}. \tag{6.3}$$

In the *distributed* approaches, which are the most popular in the literature, the dipoles are placed on a grid (either fully volumetric or restricted to the cortex), which results in a leadfield matrix composed of typically 10 000 columns and 256 rows. Alternatively, in the localized approaches, a few dipoles (typically less than ten) are placed in the brain, at arbitrary locations. These modeling differences in the FP are motivated by the different approaches used to solve the IP.

β) Inverse Problem

The inverse problem estimates $\boldsymbol{s}$ given a specific set of EEG measurements and additional constraints ensuring unicity. Spatial filtering and/or machine learning techniques can then be applied on the reconstructed source activity $\boldsymbol{s}$. The time dependency of the EEG signal is also often taken into account by considering a set of solutions for different time samples; $\boldsymbol{v}$ and $\boldsymbol{s}$ then become matrices.

The dimensions of $\boldsymbol{G}$ clearly indicate that the problem is ill-posed and admits more than one solution. To overcome this issue several techniques have been developed. In particular regularization methods have been widely used. Given a noisy EEG measurement vector $\tilde{\boldsymbol{v}}$, a regularization term composed of a scalar α and a function L, these methods aim at minimizing the function

$$F_\alpha(\boldsymbol{s}) = \|\boldsymbol{G}\boldsymbol{s} - \tilde{\boldsymbol{v}}\|^2 + \alpha L(\boldsymbol{s})\,. \tag{6.4}$$

If $L = \|\cdot\|^2$ the problem becomes a Tikhonov regularization and its solution is [Gre+08]

$$\tilde{\boldsymbol{s}}_\alpha = \left(\boldsymbol{G}^{\mathrm{T}}\boldsymbol{G} + \alpha\mathbf{I}\right)^{-1}\boldsymbol{G}^{\mathrm{T}}\tilde{\boldsymbol{v}}\,. \tag{6.5}$$

The appropriate choice of α is critical to obtaining a proper estimation of the solution, and several techniques are available [Gre+08]. In the literature the technique behind eq. (6.5) is often referred to as the minimum norm estimate (MNE), and is know to yield poor results [Pas99] – in particular for deep sources. The weighted minimum norm estimate (WMNE) has been introduced to correct the depth bias of MNE by introducing of a weight matrix $\boldsymbol{W}$ in the definition of the regularization function $L(\boldsymbol{s}) = \|\boldsymbol{W}\boldsymbol{s}\|^2$, leading to a different solution

$$\tilde{\boldsymbol{s}}_\alpha = \left(\boldsymbol{G}^{\mathrm{T}}\boldsymbol{G} + \alpha\boldsymbol{W}^{\mathrm{T}}\boldsymbol{W}\right)^{-1}\boldsymbol{G}^{\mathrm{T}}\tilde{\boldsymbol{v}}\,. \tag{6.6}$$

The matrix $\boldsymbol{W}$ has several definitions but usually reflects the norm of the columns of the leadfield matrix. The standardized low resolution brain electromagnetic tomography (sLORETA) is another closely related technique that normalizes the results of MNE by the diagonal of the matrix

$$\boldsymbol{S} = \boldsymbol{G}^{\mathrm{T}}\left(\boldsymbol{G}\boldsymbol{G}^{\mathrm{T}} + \alpha\mathbf{I}\right)^{-1}\boldsymbol{G}\,. \tag{6.7}$$

Thanks to its high accuracy [Pas02; Dal+00] sLORETA has been extensively used in the context of BCI [HVG18]. A final mention should be made for the low resolution brain electromagnetic tomography (LORETA) technique that uses a weighted Laplacian operator $L(\boldsymbol{s}) = \|\Delta\boldsymbol{W}_L\boldsymbol{s}\|^2$ to obtain the smoothest solution while avoiding artificial dampening of deep sources. To that end $\boldsymbol{W}_L$ is the column normalization of the leadfield matrix.

The *localized* – or *parametric* – algorithms form another family of techniques for solving the inverse problem. Instead of placing a large number of dipoles on a predefined grid and computing a single leadfield matrix, N_d dipoles (typically up to ten) are placed in the source space and their positions, moments and amplitudes are optimized to find the configuration that will yield scalp tensions as close to the actual measurement as possible. This can be achieved by minimizing the L_2 residual norm

$$\|\boldsymbol{v} - \boldsymbol{G}\big(\{\boldsymbol{d}_i\}\big)\boldsymbol{s}\big(\{\boldsymbol{d}_i\}\big)\|, \tag{6.8}$$

where $\{\boldsymbol{d}_i\}$ is a set of N_d dipoles represented by their positions and moments. Traditional optimization methods such as gradient descent or genetic algorithms [UHS98; Cuf95; FGG03; MKD02; KLH05] can be used to solve this problem and find the optimal configurations of dipole positions $\{\boldsymbol{d}_i\}$ and activations $s\big(\{\boldsymbol{d}_i\}\big)$. Since it requires re-computation of the leadfield $\boldsymbol{G}\big(\{\boldsymbol{d}_i\}\big)$ at every step of the optimization procedure this method is computationally demanding and does not seem to have found widespread adoption in the ESI-augmented BCI community.

γ) Inverse-Based BCI

Leveraging on the ESI techniques introduced above it is possible to add a spatial filtering phase to the standard BCI. One way of using these algorithms is to project the EEG signal, after filtering, to the source space, in which anatomical knowledge can be used to select a subset of dipoles that are relevant to the BCI task (Figure 6.2) [Cin+08]. This has the advantage of reducing the number of features passed down the pipeline and hence should reduced the experimental training time [HVG18]. However, anatomical ROI selection supposes that a subject-specific head model has been used, or active dipoles could be excluded from the selected dipoles. If no anatomical model is available, data-driven approaches can be used for ROI selection [HVG18]. It may seem that the benefit of ESI is lost altogether, however this approach still has numerous benefits: (i) the selected ROI is still in the source space and can be easily checked, giving insight into how the algorithms behave; (ii) statistical significance of the features has been reported to be better in the source space [Cin+08]; (iii) the deblurring effect of the IP allows for more specific spatial filtering and facilitates artifact removal; (iv) inverse-based pipelines also increase the discriminability of nearby sources [EBH16] which is required by more complex BCI tasks such as 4 classes wrist movement.

Hybrid schemes have also been introduced, for instance the scheme presented by Edelman et al. first decomposes the EEG signal into independent components using independent component analysis (ICA) before projecting the relevant components

Fig. 6.2.: Illustration of a ESI-augmented BCI pipeline. The blue color indicates components that need to be trained while the vertical arrows indicate that external information (prior) is provided to the system.

to the source space where additional feature extraction is performed [EBH16].

d) The *simBCI* Framework for Simulated BCI

Human experiments are challenging to work with, because individual results are extremely sensible to the user's own training, to its mental state between and even within runs and to a myriad of other factors (devices, electrode dryness, electrode positions, etc). Combined to the lack of absolute certainty that the user was actually performing the mental task at hand at every epoch of the trial, this makes experimental data unreliable for the first phases of theoretical developments. In the literature this challenge is often mitigated by recruiting a large number of users to perform the same simulations. In addition to being very time consuming this approach as numerous challenges. Some research teams are using a reference recording the quality of which is assumed to be reasonable [Tan+12]. Still, when trying to understand the underlying causes of any improvement or degradation in performance of a specific BCI paradigm, this kind of data makes asserting any claim very difficult.

In order to address this situation, simulated data can be of great value. Hence, a consequent part of this thesis has been dedicated to the development and validation of the first (to the best of our knowledge) framework for simulation of BCI data. A formal introduction of the *simBCI* framework has been published in [Lin+18a; Lin+18b].

The relevance of this work and the crucial need for fully controlled simulated BCI data is further illustrated by the almost concurrent development of another simulation framework [Kro+18] by an independent group.

α) Data Generation

Because the objective behind the development of simBCI was to be able to precisely describe every component of an EEG recording, the signal generation starts directly

within the brain (and not e.g. on the electrode space). Algebraically the EEG signal is generated as

$$\boldsymbol{V} = \boldsymbol{G}(\boldsymbol{S} + \boldsymbol{N}_v) + \boldsymbol{N}_s\,, \tag{6.9}$$

where $\boldsymbol{G}$ is the leadfield matrix of the simulated setup, $\boldsymbol{V} \in \mathbb{R}^{N_e \times N_s}$ contains the voltages measured at each of the N_e electrodes over the N_s samples, $\boldsymbol{S} \in \mathbb{R}^{N_d \times N_s}$ are the corresponding activations of the N_d dipoles in the brain and $\boldsymbol{N}_v$ and $\boldsymbol{N}_s$ describe additive noise originating from the brain volume and the measurement surface, respectively. The forward model behind the provided leadfield is mostly orthogonal to simBCI core functionalities, except regarding whether the dipoles moments have constrained orientation (typically orthogonal to the cortical surface) or if they are freely oriented (i.e. composed of three coordinates per dipole). This description implies that the signal is characterized by both spatial and temporal characteristics. Indeed, in order accurately simulate real EEG recording *simBCI* has to be able to express correlations between events in both time and space. In particular, the events generating the signals are placed on a *timeline* at the beginning of the simulation in order generate time sample that are not simply uncorrelated measurements of different events. The events simulating the BCI tasks are characterized by three main descriptor:

When refers to the timeline generator which are in charge of distributing the events over the different time samples of the simulation. They are also used to associate event descriptions with the timeline labels. The events either be placed randomly on the timeline (e.g. eyeblinks) or associated with trials of the actual BCI task (Figure 6.3).

Where describes the location where the event occurs; for instance, in the case of left and right MI [PN01] the activity is located in the corresponding motor cortices, while in the case of steady-state visually evoked potentials (SSVEP) [Via+10] it is located in the occipital lobe. The locations are either heuristically deduced by *simBCI* itself (e.g. eyes, left motor cortex, etc.) or, if the user has enough information about the physiological model, by the indices of specific leadfield rows. It is also possible to have more distributed effects, such as background volumetric noise, applied to the whole domain.

What is the actual description of the physiological effect associated with the BCI task, or other event such as eyeblinks or background noise. In the case of MI the main event is event-related desynchronisation (ERD) while in the case of SSVEP it is a spectral peak at the frequency of the observed stimulus. Generating this kind of realistic events is more challenging than trivial power spikes, and has required in depth review of the literature.

Listing 1 Code used for generating a BCI competition IV type of BCI signal. The code snippet was retrieved from one of the examples of the official repository.

```
% These events mark starts of trials that are to be classified
classEvents = {'left','right'};
% Parameters controlling experiment timeline generation: when events happen
timelineParams = { 'samplingFreq', 200, 'eventList', { ...
      {'when', {@when_trials, 'events',classEvents, ...
                'numTrials',10, ...
                'trialLengthMs',4000, 'restLengthMs', 2000, ...
                'trialOrder', 'random', 'includeRest', true}}, ...
      {'when', {@when_random, 'events',{'eyeblink'},'eventFreq',0.1}}, ...
      {'when', {@when_random, 'events',{'eyemove'},'eventFreq',0.2,...
                              'randomMaxDurationMs',2000}}, ...
      {'when', {@when_always, 'events',{'noise'}}} ...
   } ...
};
% List reactions to the events on the timeline
effectParams = { ...
   {'SNR', 1.0, 'name', 'signalLeft', 'triggeredBy', 'left', ...
      'what',  {@gen_desync, 'centerHz',12,'widthHz',1,'reduction',0.5}, ...
      'where', {@where_heuristic, 'position','rightMC'} }, ...
   {'SNR', 1.0, 'name', 'signalRight', 'triggeredBy', 'right', ...
      'what',  {@gen_desync, 'centerHz',12,'widthHz',1,'reduction',0.5}, ...
      'where', {@where_heuristic, 'position','leftMC'}}, ...
   {'SNR', 0.1, 'name', 'blinks', 'triggeredBy', 'eyeblink', ...
      'what',  @noise_eyeblinks, ...
      'where', {@where_heuristic, 'position','eyes'}}, ...
   {'SNR', 0.1, 'name', 'eyemove', 'triggeredBy', 'eyemove', ...
      'what',  @noise_eyemovement, ...
      'where', {@where_heuristic, 'position','eyes'}}, ...
   {'SNR', 0.005, 'name', 'noise', 'triggeredBy', 'noise', ...
      'what',  {@noise_spectrally_colored, 'subType','distance'}, ...
      'where', {@where_whole_surface}} ...
};
```

The modularity of this architecture and of the whole simBCI framework guarantees that, in case the provided primitives are not enough, the user will be able to develop and integrate its own.

In order to make sure that simBCI was capable of handling realistic simulations, the dataset generation procedure behind the BCI competition IV [Tan+12] has been re-implemented. Incidentally, it appears to be the first openly accessible re-implementation of the protocol to date. The specifications used to generate this signal are provided in Listing 1 for better illustrating the above discussion. The modular architecture makes it possible to specify all the parameters explicitly in a single master file and avoid lack of reproducibility caused by parameter scattering.

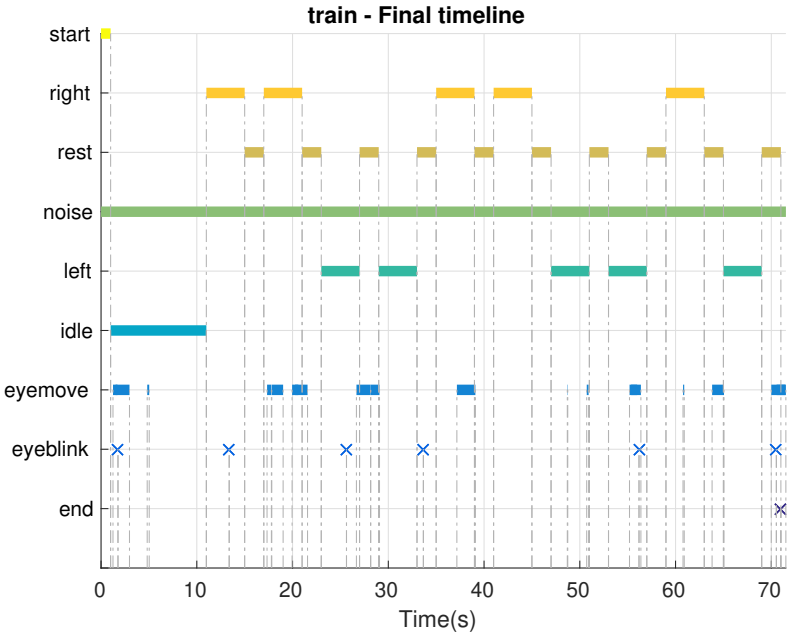

Fig. 6.3.: Timeline generated by *simBCI* for a left-right MI experiment. This timeline illustrates most of the simulation capabilities of the framework as it includes: the bci tasks, rest periods, noise and artifacts (eye movements and eye blinks).

β) BCI Processing Pipelines

The processing of the generated data is delegated to the *pipelines* which are a succession of elementary *processors* whose individual output will be consumed by the following processor. Processors can include machine learning components such as CSP, support vector machine (SVM), LDA but also inverse algorithms. For BCI experiments the content of the pipeline is completely to the user's discretion, but the final processor must be a classifier and return a vectors containing, for each trial, the probabilities that it belongs to specific classes.

To reproduce a real BCI setting, the processing is composed of a training phase and a pseudo *online* phase. During the processing phase the processors that require training can adapt their parameters, while those who do not remain unmodified. In the training phase the different processors do have access to the actual labels of the timeline. During the online phase a new timeline and dataset is generated and fed to the trained pipeline, the labels however are no longer accessible to the processors.

This architecture can support the simplest processing chains, such as a CSP-LDA combination as well as some the most advanced one. In particular pipelines following these presented by Cincotti et al. [Cin+08], Edelman et al. [EBH16], Lotte et al. [LLA09] and Besserve et al. [BMG11] have been reimplemented in *simBCI*. The reimplementation of the first two appear to be the first openly available. One of the reasons behind these re-implementations is to be compare them in a consistent and, hopefully, fair setting in order to determine their respective strength and weaknesses.

e) Experimental Protocol

α) Expected Outcomes

The development of the simBCI was motivated by the objective of improving the state-of-the-art BCI performances via improvements in (i) the forward modeling of the brain using novel computational techniques (ii) improving the speed of the overall process to ensure that the technology remains compatible with real-time applications and (iii) possibly improve upon the state-of-the-art pipelines.

β) State of the Art Implementation

As stated previously, state-of-the-art BCI processing pipelines have been reimplemented in order to study the effects of several parameters on their accuracy. A

quick overview of their behaviours is provided in the following.

The pipeline introduced by Cincotti et al. [Cin+08] is deigned for a two-class BCI system in which the user can move a cursor up and down. The authors use WMNE in order to reconstruct the cortical current density (CCD) which is then spatially filtered using anatomical knowledge of the ROIs related to the task. The spectral power of 30 frequency bands of each remaining channel are then estimated, yielding a relatively large number of features. Feature selection is then performed using r^2 analysis; three of the features most correlated to the variation in labels were selected – two in the motor cortex and one in the mesial region. The authors report an improved accuracy when using ESI in this two-classes case, and have even attempted a height classes experiments where ESI significantly improved BCI performance.

The techniques involved of the work introduced by Edelman et al. [EBH16] are significantly more complex but have the advantage of not requiring explicit selection of the ROI. The authors consider a BCI involving four different classes of movement of the right hand. The ROI is selected by performing an ICA in the electrode space. The most relevant independent component was selected by performing a time frequency analysis of the channels based on Morlet wavelets

$$\Psi_f(t) = \left(\sigma\sqrt{\pi}\right)^{-1/2} \mathrm{e}^{t^2/2\sigma^2} \mathrm{e}^{\mathrm{j}2\pi f_c t}, \tag{6.10}$$

with

$$\sigma = \frac{w_{f_c} f_c}{f\sqrt{8\ln 2}}, \tag{6.11}$$

where f_c is the central frequency of the wavelet, w_{f_c} its temporal resolution and f the frequency under consideration. These wavelets are particularity useful for evaluating the evolution of the spectrum of the signal over time. The wavelets were used to split each trial into time-localized frequency bands that were used as features. The most relevant features were determined using a search algorithm and Mahalanobis distance (MD) which characterizes the similarity of random distribution. The search algorithm was used to iteratively add to the set of selected features the feature that would maximize the distance to the rest of the features; one such set was built for each BCI class. This signal was then projected on the cortical surface using WMNE and only the dipoles with the highest amplitude were kept. In the classification the MD was used to determine which class-dependant feature set was the closest to the trial data.

γ) Experimental Protocol

To verify the hypotheses that motivated the investigation into ESI-augmented BCI an experimental protocol was put in place based on the following considerations:

Validation In order to make sure that the re-implemented state-of-the-art pipelines were behaving as intended by their original authors, simulations similar to the experiments described in their presentation papers were run. Given that the settings were identical – except for the fact that the data was simulated –, classification accuracies were also expected to closely resemble the ones given in the literature. Because of missing parameters or inaccuracies in the original pipelines descriptions the re-implementation phase turned out to be more challenging that expected. This lack of reproducibility further underlines the need for results from simulated BCI as the authors of new investigations could provide the actual configuration files of the simulator to the community for closer inspection.

Genrality Every hypotheses on the effect of a parameter on classification accuracy (e.g. increased forward model resolution) are verified against all available pipelines, in order to make sure if the improvement is anecdotal, general or restricted to specific techniques (e.g. specific inverse algorithms). However, because the pipelines are very different there is a risk that under-performance of one of them could be due to an inadequate configuration for the testing setting. For instance the number of ICA components in the pipeline presented in [EBH16] needs to be adapted to the number of classes of the BCI task. To address this issue, the hyper-parameters of the pipelines are optimized, for every new test, using machine learning and/or big data approaches. This is expected to improve the fairness of the overall testing procedure.

Significance Because of the very high dimensionality of the simulation parameters (SNR, size of the ROI, etc.), one should carefully check that any observed improvement or regression in classification accuracy is not due to a specific configuration. Thus all simulations are performed on a multi-parameter space where at least three parameter dimensions are explored at the same time. Given the curse of high dimensionality the simulation must be evaluated on very large dataset in order to obtain statistically significant results. This is, once again, possible to perform the same level of inspection with actual user recordings because of the few number of samples available to the researchers.

One of the first investigation direction coming to mind is the study of the effect of specific inverse algorithms on the accuracy of the pipelines. Investigating

which type of inverse performs best in different classes is critical to determine if improvements are possible in this area or if algorithms originating from different communities can be transplanted in BCI. For instance the epilepsy localization community has been developing several ESI algorithms [Bec+15], however it is not clear if their most performing algorithms would be equally performing in a BCI setting. The algorithms designed for epilepsy are optimized for finding high power in very localized areas. It is possible that this family of inverse algorithms translates to BCI settings such as SSVEP for which the neural activity can be expected to have higher intensity in the occipital lobe, however it is much less clear whether or not this also applies to MI where the main effect is ERD. Consequently part of the experimental protocol is dedicated to studying the raw localization accuracy of the inverse algorithms that have been re-implemented in simBCI and determine if they are potential candidates for ESI-augmented BCI. Because of the blurring effect of the FP and of the ill-posedness of the IP perfect reconstruction of the cortical activity is not to be expected. Hence inversion accuracy should rely on more sophisticated metrics than the relative error between the original and reconstructed data. When considering focal activity in the brain a large number of metrics have been introduced to characterize the accuracy of the reconstruction:

- relative error between the amplitudes of the signals;
- average distance between the original and reconstructed amplitude maxima [Mic+04; Gre+08];
- distance from the center of the brain of the original and reconstructed maximum amplitude source [Yve+96]. While simple this metric permits identification of depth-biased algorithms such as MNE;
- percentage of intersection of the original dipoles with the strongest 5% of reconstructed dipoles [BG97];
- noise reliance is also considered using the previous metric and correlate the accuracy with the SNR [Sch+99].

While some of these metrics are used in the current protocol, the one described in [Bra+16] is more adequate. The metric makes the distinction between the *precision* which is characterized by the number of original sources that have effectively been reconstructed and the *recall* which fraction of the original sources were identified by the ESI algorithm. Taken together these two measures are able to give a more robust indication of the quality of the algorithm, in particular if several sources are active at the same time (which many of the other metrics fail to characterize).

Numerous inverses that are either widely used or thought to exhibit properties worth investigating have been implemented into *simBCI*; they include

- Minimum norm estimate (MNE);
- Weighted minimum norm estimate (WMNE);
- Minimum current estimates (MCE) [UHS99];
- Low resolution brain electromagnetic tomography (LORETA) [PML94];
- Cortical low resolution brain electromagnetic tomography (cLORETA) [Wag+96];
- Standardized low resolution brain electromagnetic tomography (sLORETA) [NN12];
- Champagne [Wip+10];
- Standardized shrinking LORETA-FOCUSS (SSLOFO) [Liu+05];
- Multiple signal classification (MUSIC) [Alb+08];
- Extended source multiple signal classification (ExSoMUSIC) [Bir+11].

Other inverses are scheduled to be implemented in order to perform a thorough assessment of the compatibility of the most well know inverse algorithms with BCI. This kind of evaluation has already been performed in the context of epilepsy but not in the context of BCI and especially not in the context of more complicated schemes such as multi-task MI.

In addition to the distributed inverses described above, localized algorithms are being implemented in the framework in order to determine why they seem to have fallen out use. Indeed, one of the last contributions on the topic dates back to 2005 [KLH05]. It is not clear if this is due to the computational cost of repetitively recomputing leadfield matrices, because of a low convergence rate of the optimization procedure or an overall lack of accuracy in the BCI context.

Using the tools and concepts introduced previously the influence of different parameters can be studied on both inverses only and within an ESI-based BCI. As of this writing the following parameters are to be investigated:

Resolution The resolution of the forward model could influence the number of discriminable dipoles, which in turn could improve BCI accuracy, especially in multi-class setting such as the ones presented in [EBH16; Cin+08]. In the

current literature the number of dipoles is usually around 10 000 [BMG11] and it should be verified if more dipoles could lead to better BCI performance.

Anisotropy The tissue anisotropies of the skull and the white matter have been shown to significantly influence ESI [Wol+06]. It is worth investigating whether or not it has an effect on BCI; if the ROI is selected by a data-driven process it is not clear if any gain will be noticed, however if it is chosen *a priori* by a physician the greater the accuracy of the model the better.

Training length The time required for training the BCI system during human experiments is critical in practical BCI applications because it tires the user before any active usage of the system and is required at the beginning of every sessions. It has already been shown that the reduction in number of features that ESI can provide thanks to spatial filtering should allow for a reduced training time [HVG18].

User specific model The importance of having a user-specific model can be thoroughly checked thanks to the fully controlled environment of *simBCI*. Time, cost and technical constraints often prevent obtention of MRI models for every user and several studies have been reported to use standard templates such as [HPH16] for constructing the leadfield [Mic+04; HVG18]. The potential loss in BCI accuracy needs to be verified in a fully controlled environment.

Noise/Artefact resilience Spatial filtering in the head volume is expected to yield increase resilience of the pipeline to artifacts such as eye blinks and noise. Early results presented in [Lin+18b] seem to indicate that this is the case.

In general, the ESI literature shows a tendency to compare very complex inverse pipelines with relatively simple pure machine learning ones [Lin18] making it difficult to question the merits of ESI-augmented and purely data-driven BCIs. To provide an unbiased comparison, state-of-the-art machine learning pipelines are being implemented into simBCI. One of the main axis of research are the Riemannian manifold approaches described in [Lot+18].

f) Future Work

After the experimental protocol described in above is completed, more complex questions will be addressed, e.g. regarding the influence of ESI on the stability of transfer learning [WLL15; HVG18] or real-time applicability of the techniques [Din+15]. Some early results produced so far are detailed in [Lin+18b] and will not be recalled here because they focus mostly on data-driven approaches.

g) Conclusion

While investigating the influence of better modeling of the brain anisotropies [Rah+17] on BCI, it became clear that making scientifically sound claims would require an enormous investment in both time and money if human trials were to be used. This realization has motivated the development of the apparently first fully simulated BCI development framework. After making sure that the *simBCI* framework was providing realistic data, it was published in a domain-specific journal. This has laid the ground work for a thorough investigation into possible improvements to the state-of-the-art BCI systems, which has already started by the development of a preliminary experimental protocol and will be acted upon in the near future. The work behind the development of *simBCI* has also been the opportunity to provide the first publicly available reimplementation of several works, which is expected to positively affect the community.

Chapter 7

Conclusions and Future Work

In this thesis a series of techniques aiming to stabilize integral equations have been presented in order to obtain highly accurate and versatile formulations capable of handling low and high frequency scenarios alike. The novel scientific contributions include the extension of the qH projectors to higher order modeling, thus enabling the development of formulations that exhibit both low frequency stability and higher order convergence rates. These projectors were then applied to the wire EFIE in order to address the limitations it shares with its surface counterpart. However, while Calderón schemes are usually employed to stabilize the dense discretization behaviour of the surface formulation, b-spline wavelets were employed in the one-dimensional case. The projectors were finally leveraged upon to stabilize the numerical properties of the MFIE, which could then be combined with an already stabilized surface EFIE thus forming an highly accurate CFIE capable of handling low and high frequency applications without loss of precision nor spurious resonances, making it highly potent formulation for closed structures.

Because the above-mentioned work performed for improving forward EM modeling was completed in advance with regards to this thesis' original plan, a new line of investigations on inverse EM modeling was pursued. Due to the existing expertise of the laboratory in brain modeling, these investigations naturally focussed on the challenging domain of BCI. While the work is still in its early stages, a full assessment of the state-of-the-art has been performed and has led to the development and publication of what is probably the first fully simulated experimental BCI environment. As a side effect, this framework has made possible the distribution of the first publicly available implementation of some key contributions of the BCI community.

To complement the results reported in this thesis, several lines of research are still to be investigated:

- the high order extension of the qH still requires the development of a fast algorithm to match the high efficiency of their low order counterpart and

take full advantage of high order modeling;

- the implementation of the experimental protocol described for the BCI line of investigation is to be completed and run;
- investigations on real time inversion for BCI are required, to ensure the practicality of the most complex schemes;
- the high order techniques presented in this Chapter 3 could be applied to both the new CFIE and wire EFIE equations.

Most of these tasks and research axes are being worked on as of this writing and most of them are expected to yield publishable results in relatively short term.

Nomenclature

List of Variables and Other Mathematical Symbols

The following list summarizes frequently used variables and mathematical symbols.

Symbol	Description
Accents and Operations	
$\hat{}$	The standard hat denotes a unit vector
$\tilde{}$	The wide tilde denotes the involvement of dual basis functions
$\boldsymbol{A}^{-1}$	Inverse of the matrix $\boldsymbol{A}$ (if it exists)
$\boldsymbol{A}^{+}$	Moore-Penrose pseudo-inverse of the matrix $\boldsymbol{A}$
$\boldsymbol{A}^{\mathrm{T}}$	Transpose of the matrix $\boldsymbol{A}$
$\boldsymbol{A}^{\dagger}$	$\left(\overline{\boldsymbol{A}}\right)^{\mathrm{T}}$
$\boldsymbol{A}^{-\mathrm{T}}$	$\left(\boldsymbol{A}^{-1}\right)^{\mathrm{T}}$
$\boldsymbol{A} \otimes \boldsymbol{B}$	Kronecker product of matrices $\boldsymbol{A}$ and $\boldsymbol{B}$
Physical Quantities	
$\boldsymbol{r}, \boldsymbol{r}'$	Position vectors
$\hat{\boldsymbol{n}}$	Surface normal unit vector directed to the exterior
ε	Permittivity
μ	Permeability
ε_0	Permittivity of vacuum
μ_0	Permeability of vacuum
k	Wavenumber
f	Frequency
η	Wave impedance
ω	Angulary frequency
$\boldsymbol{j}$	Electric current density
$\boldsymbol{m}$	Magnetic current density
$\boldsymbol{e}$	Electric field
$\boldsymbol{h}$	Magnetic field
$\boldsymbol{d}$	Electric flux density

$\boldsymbol{b}$	Magnetic flux density
$G(\boldsymbol{r}, \boldsymbol{r}')$	3D Green's function

Vector Spaces and Sets

Ω	Denotes a domain in $\mathbb{R}^3$
Γ	Boundary of Ω

Abbreviations

BC Buffa-Christiansen

BCI Brain Computer Interface

BEM boundary element method

CCD cortical current density

CFIE combined field integral equation

CFIE équation intégrale du champ combiné

cLORETA cortical low resolution brain electromagnetic tomography

CSP common spatial pattern

EEG electroencephalogram

EFIE electric field integral equation

EFIE équation intégrale du champ électrique

EFIO electric field integral operator

EFIO opérateur intégral du champ électrique

EM electromagnetic

ERD event-related desynchronisation

ESI EEG source imaging

ExSoMUSIC extended source multiple signal classification

FEM finite element method

FP forward problem

GMRES generalized minimal residual method

GWP Graglia-Wilton-Peterson

ICA independent component analysis

ICM interface cerveau-machine

IP inverse problem

LDA linear discriminant analysis

LORETA low resolution brain electromagnetic tomography

LS Loop-Star

LS-EFIE Loop-Star electric field integral equation

MCE minimum current estimates

MD Mahalanobis distance

MEG magnetoencephalogram

MFIE magnetic field integral equation

MFIE équation intégrale du champ magnétique

MI motor imagery

MLFMM Multilevel Fast Multipole Method

MNE minimum norm estimate

MoM method of moments

MRI magnetic resonance imaging

MUSIC multiple signal classification

PEC perfectly electrically conducting

qH quasi-Helmholʒ

qH quasi-Helmholʒ

qH-EFIE quasi-Helmholʒ projected electric field integral equation

RCS radar cross-section

RHS right hand side

ROI region of interest

RWG Rao-Wilton-Glisson

SABRE Seizing Advances in Bci from high Resolution Eeg imaging in runtime

sLORETA standardized low resolution brain electromagnetic tomography

SNR signal-to-noise ratio

s.p.d symmetric positive definite

SSLOFO standardized shrinking LORETA-FOCUSS

SSVEP steady-state visually evoked potentials

SVD singular value decomposition

SVM support vector machine

wire EFIE thin-wire electric field integral equation

WMNE weighted minimum norm estimate

Bibliography

[Ada04] R. Adams. “Physical and Analytical Properties of a Stabilized Electric Field Integral Equation”. In: *IEEE Transactions on Antennas and Propagation* 52.2 (Feb. 2004), pp. 362–372 (cit. on pp. 88, 99).

[Alb+08] L. Albera, A. Ferreol, D. Cosandier-Rimele, I. Merlet, and F. Wendling. “Brain Source Localization Using a Fourth-Order Deflation Scheme”. In: *IEEE Transactions on Biomedical Engineering* 55.2 (Feb. 2008), pp. 490–501 (cit. on p. 128).

[And+08] F. P. Andriulli, K. Cools, H. Bagci, F. Olyslager, A. Buffa, S. Christiansen, and E. Michielssen. “A Multiplicative Calderon Preconditioner for the Electric Field Integral Equation”. In: *IEEE Transactions on Antennas and Propagation* 56.8 (Aug. 2008), pp. 2398–2412 (cit. on pp. 88, 90).

[And+13a] F. P. Andriulli, I. Bogaert, K. Cools, and E. Michielssen. “A Well-Conditioned Combined Field Integral Equation Based on Quasi-Helmholʒ Projectors”. In: *2013 International Conference on Electromagnetics in Advanced Applications (ICEAA)*. 2013 International Conference on Electromagnetics in Advanced Applications (ICEAA). Sept. 2013, pp. 644–647 (cit. on p. 89).

[And+13b] F. P. Andriulli, K. Cools, I. Bogaert, and E. Michielssen. “On a Well-Conditioned Electric Field Integral Operator for Multiply Connected Geometries”. In: *IEEE Transactions on Antennas and Propagation* 61.4 (Apr. 2013), pp. 2077–2087 (cit. on pp. 32, 33, 66, 88–90, 92–94, 99, 101).

[And+14] F. P. Andriulli, I. Bogaert, K. Cools, and E. Michielssen. “A Magnetic Type Integral Operator Which Is Stable till Extremely Low Frequencies”. In: *2014 XXXIth URSI General Assembly and Scientific Symposium (URSI GASS)*. 2014 XXXIth URSI General Assembly and Scientific Symposium (URSI GASS). Aug. 2014, pp. 1–4 (cit. on pp. 89, 93).

[And12] F. P. Andriulli. “Loop-Star and Loop-Tree Decompositions: Analysis and Efficient Algorithms”. In: *IEEE Transactions on Antennas and Propagation* 60.5 (May 2012), pp. 2347–2356 (cit. on pp. 33, 47, 50, 88).

[ATV10] F. P. Andriulli, A. Tabacco, and G. Vecchi. “Solving the EFIE at Low Frequencies With a Conditioning That Grows Only Logarithmically With the Number of Unknowns”. In: *IEEE Transactions on Antennas and Propagation* 58.5 (May 2010), pp. 1614–1624 (cit. on pp. 31, 88).

[AVV08] F. P. Andriulli, F. Vipiana, and G. Vecchi. “Hierarchical Bases for Non-hierarchic 3-D Triangular Meshes”. In: *IEEE Transactions on Antennas and Propagation* 56.8 (Aug. 2008), pp. 2288–2297 (cit. on p. 88).

[Bal12] C. A. Balanis. *Advanced Engineering Electromagnetics*. 2nd ed. Hoboken, N.J: John Wiley & Sons, 2012 (cit. on p. 18).

[BC07] A. Buffa and S. Christiansen. “A Dual Finite Element Complex on the Barycentric Refinement”. In: *Mathematics of Computation* 76.260 (2007), pp. 1743–1769 (cit. on pp. 24, 90).

[BCA15a] Y. Beghein, K. Cools, and F. P. Andriulli. “A DC Stable and Large-Time Step Well-Balanced TD-EFIE Based on Quasi-Helmholtz Projectors”. In: *IEEE Transactions on Antennas and Propagation* 63.7 (July 2015), pp. 3087–3097 (cit. on p. 89).

[BCA15b] Y. Beghein, K. Cools, and F. P. Andriulli. “A DC-Stable, Well-Balanced, Calderón Preconditioned Time Domain Electric Field Integral Equation”. In: *IEEE Transactions on Antennas and Propagation* 63.12 (Dec. 2015), pp. 5650–5660 (cit. on p. 89).

[BCA15c] Y. Beghein, K. Cools, and F. P. Andriulli. “A Robust and Low Frequency Stable Time Domain PMCHWT Equation”. In: *2015 International Conference on Electromagnetics in Advanced Applications (ICEAA)*. 2015 International Conference on Electromagnetics in Advanced Applications (ICEAA). Sept. 2015, pp. 954–957 (cit. on p. 89).

[Bec+15] H. Becker, L. Albera, P. Comon, R. Gribonval, F. Wendling, and I. Merlet. “Brain-Source Imaging: From Sparse to Tensor Models”. In: *IEEE Signal Processing Magazine* 32.6 (Nov. 2015), pp. 100–112 (cit. on p. 127).

[Beg+15] Y. Beghein, R. Mitharwal, K. Cools, and F. P. Andriulli. "Handling the Low-Frequency Breakdown of the PMCHWT Integral Equation with the Quasi-Helmholtz Projectors". In: *2015 International Conference on Electromagnetics in Advanced Applications (ICEAA)*. Sept. 2015, pp. 1534–1537 (cit. on p. 89).

[BG97] S. Baillet and L. Garnero. "A Bayesian Approach to Introducing Anatomo-Functional Priors in the EEG/MEG Inverse Problem". In: *IEEE Transactions on Biomedical Engineering* 44.5 (May 1997), pp. 374–385 (cit. on p. 127).

[BH07] O. Bruno and M. Haslam. "Regularity Theory and Superalgebraic Solvers for Wire Antenna Problems". In: *SIAM Journal on Scientific Computing* 29.4 (Jan. 1, 2007), pp. 1375–1402 (cit. on p. 65).

[Bir+11] G. Birot, L. Albera, F. Wendling, and I. Merlet. "Localization of Extended Brain Sources from EEG/MEG: The ExSo-MUSIC Approach". In: *NeuroImage* 56.1 (May 1, 2011), pp. 102–113 (cit. on p. 128).

[Bir06] N. Birbaumer. "Breaking the Silence: Brain–Computer Interfaces (BCI) for Communication and Motor Control". In: *Psychophysiology* 43.6 (Nov. 1, 2006), pp. 517–532 (cit. on p. 114).

[BMG11] M. Besserve, J. Martinerie, and L. Garnero. "Improving Quantification of Functional Networks with EEG Inverse Problem: Evidence from a Decoding Point of View". In: *NeuroImage* 55.4 (Apr. 15, 2011), pp. 1536–1547 (cit. on pp. 124, 129).

[BML01] S. Baillet, J. Mosher, and R. Leahy. "Electromagnetic Brain Mapping". In: *IEEE Signal Processing Magazine* 18.6 (2001), pp. 14–30 (cit. on pp. 27, 29).

[Bog+11a] I. Bogaert, K. Cools, F. P. Andriulli, and D. De Zutter. "Low Frequency Scaling of the Mixed MFIE for Scatterers with a Non-Simply Connected Surface". In: *Electromagnetics in Advanced Applications (ICEAA), 2011 International Conference On*. IEEE, 2011, pp. 951–954 (cit. on pp. 31, 93, 95).

[Bog+11b] I. Bogaert, K. Cools, F. P. Andriulli, J. Peeters, and D. De Zutter. "Low Frequency Stability of the Mixed Discretization of the MFIE". In: *Antennas and Propagation (EUCAP), Proceedings of the 5th European Conference On*. IEEE, 2011, pp. 2463–2465 (cit. on pp. 31, 93).

[Bog+14] I. Bogaert, K. Cools, F. P. Andriulli, and H. Bagci. “Low-Frequency Scaling of the Standard and Mixed Magnetic Field and Müller Integral Equations”. In: *IEEE Transactions on Antennas and Propagation* 62.2 (Feb. 2014), pp. 822–831 (cit. on pp. 88, 93).

[Bra+16] A. Bradley, J. Yao, J. Dewald, and C.-P. Richter. “Evaluation of Electroencephalography Source Localization Algorithms with Multiple Cortical Sources”. In: *PLOS ONE* 11.1 (Jan. 25, 2016), e0147266 (cit. on p. 127).

[Bru+09] O. Bruno, T. Elling, R. Paffenroth, and C. Turc. “Electromagnetic Integral Equations Requiring Small Numbers of Krylov-Subspace Iterations”. In: *Journal of Computational Physics* 228.17 (Sept. 2009), pp. 6169–6183 (cit. on p. 101).

[BT07] M. C. van Beurden and A. G. Tijhuis. “Analysis and Regularization of the Thin-Wire Integral Equation With Reduced Kernel”. In: *IEEE Transactions on Antennas and Propagation* 55.1 (Jan. 2007), pp. 120–129 (cit. on pp. 66, 69).

[BvE12] D. J. Bekers and S. J. L. van Eijndhoven. “Spectral Analysis of Integro-Differential Operators Applied in Linear Antenna Modelling”. In: *Proceedings of the Edinburgh Mathematical Society* 55.02 (June 2012), pp. 333–354 (cit. on p. 70).

[BW75] C. Butler and D. Wilton. “Analysis of Various Numerical Techniques Applied to Thin-Wire Scatterers”. In: *IEEE Transactions on Antennas and Propagation* 23.4 (July 1975), pp. 534–540 (cit. on p. 67).

[CC02] T. J. Cui and W. C. Chew. “Accurate Analysis of Wire Structures from Very-Low Frequency to Microwave Frequency”. In: *IEEE Transactions on Antennas and Propagation* 50.3 (Mar. 2002), pp. 301–307 (cit. on p. 66).

[Che+01] W. C. Chew, J.-M. Jin, E. Michielssen, and J. M. Song, eds. *Fast and Efficient Algorithms in Computational Electromagnetics*. Artech House, 2001 (cit. on p. 32).

[Che+09] R. Chen, J. Ding, D. Z. Ding, Z. H. Fan, and D. Wang. “A Multiresolution Curvilinear Rao–Wilton–Glisson Basis Function for Fast Analysis of Electromagnetic Scattering”. In: *IEEE Transactions on Antennas and Propagation* 57.10 (Oct. 2009), pp. 3179–3188 (cit. on p. 88).

[Che+15] J. Cheng, R. J. Adams, J. C. Young, and M. A. Khayat. "Augmented EFIE With Normally Constrained Magnetic Field and Static Charge Extraction". In: *IEEE Transactions on Antennas and Propagation* 63.11 (Nov. 2015), pp. 4952–4963 (cit. on p. 88).

[Cin+08] F. Cincotti et al. "High-Resolution EEG Techniques for Brain–Computer Interface Applications". In: *Journal of Neuroscience Methods*. Brain-Computer Interfaces (BCIs) 167.1 (Jan. 15, 2008), pp. 31–42 (cit. on pp. 115, 117, 119, 124, 125, 128).

[CMT17] S. Castaño-Candamil, A. Meinel, and M. Tangermann. "Post-Hoc Labeling of Arbitrary EEG Recordings for Data-Efficient Evaluation of Neural Decoding Methods". In: (Nov. 22, 2017). arXiv: 1711.08208 [cs, stat] (cit. on p. 115).

[CN02] S. H. Christiansen and J.-C. Nedelec. "A Preconditioner for the Electric Field Integral Equation Based on Calderon Formulas". In: *SIAM Journal on Numerical Analysis* 40.3 (Jan. 2002), pp. 1100–1135 (cit. on p. 88).

[Con+02] H. Contopanagos, B. Dembart, M. Epton, J. Ottusch, V. Rokhlin, J. Visher, and S. Wandzura. "Well-Conditioned Boundary Integral Equations for Three-Dimensional Electromagnetic Scattering". In: *IEEE Transactions on Antennas and Propagation* 50.12 (Dec. 2002), pp. 1824–1830 (cit. on pp. 88, 99).

[Coo+09a] K. Cools, F. P. Andriulli, F. Olyslager, and E. Michielssen. "Improving the MFIE's Accuracy by Using a Mixed Discretization". In: *2009 IEEE Antennas and Propagation Society International Symposium*. 2009 IEEE Antennas and Propagation Society International Symposium. June 2009, pp. 1–4 (cit. on p. 93).

[Coo+09b] K. Cools, F. Andriulli, F. Olyslager, and E. Michielssen. "Nullspaces of MFIE and Calderon Preconditioned EFIE Operators Applied to Toroidal Surfaces". In: *IEEE Transactions on Antennas and Propagation* 57.10 (Oct. 2009), pp. 3205–3215 (cit. on pp. 91–93, 96).

[Coo+11] K. Cools, F. P. Andriulli, D. De Zutter, and E. Michielssen. "Accurate and Conforming Mixed Discretization of the MFIE". In: *IEEE Antennas and Wireless Propagation Letters* 10 (2011), pp. 528–531 (cit. on pp. 24, 87, 93).

[Coy+13] D. Coyle, J. Principe, F. Lotte, and A. Nijholt. "Guest Editorial: Brain/Neuronal - Computer Game Interfaces and Interaction". In: *IEEE Transactions on Computational Intelligence and AI in Games* 5.2 (June 2013), pp. 77–81 (cit. on p. 114).

[CS07] W. C. Chew and J. M. Song. "Gedanken Experiments to Understand the Internal Resonance Problems of Electromagnetic Scattering". In: *Electromagnetics* 27.8 (Nov. 2007), pp. 457–471 (cit. on p. 89).

[CT99] C. Canuto and A. Tabacco. *Ondine Biortogonali: Teoria e Applicazioni*. Vol. 46. Pitagora, 1999 (cit. on p. 78).

[CTH08] W. C. Chew, M. S. Tong, and B. Hu. *Integral Equation Methods for Electromagnetic and Elastic Waves*. Vol. 3. Jan. 2008 (cit. on pp. 31, 88, 93).

[Cuf95] B. N. Cuffin. "A Method for Localizing EEG Sources in Realistic Head Models". In: *IEEE Transactions on Biomedical Engineering* 42.1 (Jan. 1995), pp. 68–71 (cit. on p. 119).

[CW90] Q. Chen and D. Wilton. "Electromagnetic Scattering by Three-Dimensional Arbitrary Complex Material/Conducting Bodies". In: *Antennas and Propagation Society International Symposium, 1990. AP-S. Merging Technologies for the 90's. Digest.* May 1990, 590–593 vol.2 (cit. on p. 93).

[CWR06] N. J. Champagne, D. R. Wilton, and J. D. Rockway. "The Analysis of Thin Wires Using Higher Order Elements and Basis Functions". In: *IEEE Transactions on Antennas and Propagation* 54.12 (Dec. 2006), pp. 3815–3821 (cit. on p. 65).

[Dah03] W. Dahmen. "Multiscale and Wavelet Methods for Operator Equations". In: *Multiscale Problems and Methods in Numerical Simulations*. Springer, 2003, pp. 31–96 (cit. on p. 78).

[Dal+00] A. M. Dale, A. K. Liu, B. R. Fischl, R. L. Buckner, J. W. Belliveau, J. D. Lewine, and E. Halgren. "Dynamic Statistical Parametric Mapping: Combining fMRI and MEG for High-Resolution Imaging of Cortical Activity". In: *Neuron* 26.1 (Apr. 1, 2000), pp. 55–67 (cit. on p. 118).

[Dar06] M. Darbas. "Generalized Combined Field Integral Equations for the Iterative Solution of the Three-Dimensional Maxwell Equations". In: *Applied Mathematics Letters* 19.8 (Aug. 2006), pp. 834–839 (cit. on p. 88).

[DDF01] P. J. Davies, D. B. Duncan, and S. A. Funken. “Accurate and Efficient Algorithms for Frequency Domain Scattering from a Thin Wire”. In: *Journal of Computational Physics* 168.1 (Mar. 20, 2001), pp. 155–183 (cit. on pp. 65, 69).

[DG16] A. Das and D. Gope. “Modified Separated Potential Integral Equation for Low-Frequency EFIE Conditioning”. In: *IEEE Transactions on Antennas and Propagation* 64.4 (Apr. 2016), pp. 1394–1403 (cit. on p. 88).

[Din+15] C. Dinh, D. Strohmeier, M. Luessi, D. Güllmar, D. Baumgarten, J. Haueisen, and M. S. Hämäläinen. “Real-Time MEG Source Localization Using Regional Clustering”. In: *Brain Topography* 28.6 (Nov. 1, 2015), pp. 771–784 (cit. on p. 129).

[DK92] W. Dahmen and A. Kunoth. “Multilevel Preconditioning”. In: *Numerische Mathematik* 63.1 (Dec. 1992), pp. 315–344 (cit. on p. 78).

[dMvDS88] J. C. de Munck, B. W. van Dijk, and H. Spekreijse. “Mathematical Dipoles Are Adequate to Describe Realistic Generators of Human Brain Activity”. In: *IEEE transactions on bio-medical engineering* 35.11 (Nov. 1988), pp. 960–966. pmid: 3198141 (cit. on pp. 27, 114).

[DN03] M. Djordjević and B. M. Notaroš. “Higher-Order Hierarchical Basis Functions with Improved Orthogonality Properties for Moment-Method Modeling of Metallic and Dielectric Microwave Structures”. In: *Microwave and Optical Technology Letters* 37.2 (2003), pp. 83–88 (cit. on p. 32).

[Don+01] K. C. Donepudi, J.-M. Jin, S. Velamparambil, J. Song, and W. C. Chew. “A Higher Order Parallelized Multilevel Fast Multipole Algorithm for 3-D Scattering”. In: *IEEE Transactions on Antennas and Propagation* 49.7 (July 2001), pp. 1069–1078 (cit. on p. 32).

[EBH16] B. J. Edelman, B. Baxter, and B. He. “EEG Source Imaging Enhances the Decoding of Complex Right-Hand Motor Imagery Tasks”. In: *IEEE Transactions on Biomedical Engineering* 63.1 (Jan. 2016), pp. 4–14 (cit. on pp. 115, 119, 120, 124–126, 128).

[EG10] C. L. Epstein and L. Greengard. “Debye Sources and the Numerical Solution of the Time Harmonic Maxwell Equations”. In: *Communications on Pure and Applied Mathematics* 63.4 (2010), pp. 413–463 (cit. on p. 88).

[Eib04] T. F. Eibert. "Iterative-Solver Convergence for Loop-Star and Loop-Tree Decompositions in Method-of-Moments Solutions of the Electric-Field Integral Equation". In: *Antennas and Propagation Magazine, IEEE* 46.3 (2004), pp. 80–85 (cit. on pp. 33, 88).

[FGG03] S. Finke, R. M. Gulrajani, and J. Gotman. "Conventional and Reciprocal Approaches to the Inverse Dipole Localization Problem of Electroencephalography". In: *IEEE Transactions on Biomedical Engineering* 50.6 (June 2003), pp. 657–666 (cit. on p. 119).

[Fik+11] G. Fikioris, P. J. Papakanellos, T. K. Mavrogordatos, N. Lafkas, and D. Koulikas. "Eliminating Unphysical Oscillations Arising in Galerkin Solutions to Classical Integral Equations of Antenna Theory: An Asymptotic Study". In: *SIAM Journal on Applied Mathematics* 71.2 (Jan. 2011), pp. 559–585 (cit. on pp. 66, 69).

[Fik01] G. Fikioris. "The Approximate Integral Equation for a Cylindrical Scatterer Has No Solution". In: *Journal of Electromagnetic Waves and Applications* 15.9 (Jan. 2001), pp. 1153–1159 (cit. on p. 66).

[FPA08] G. Fikioris, P. J. Papakanellos, and H. T. Anastassiu. "On the Use of Nonsingular Kernels in Certain Integral Equations for Thin-Wire Circular-Loop Antennas". In: *IEEE Transactions on Antennas and Propagation* 56.1 (Jan. 2008), pp. 151–157 (cit. on p. 66).

[FW01] G. Fikioris and T. T. Wu. "On the Application of Numerical Methods to Hallen's Equation". In: *IEEE Transactions on Antennas and Propagation* 49.3 (Mar. 2001), pp. 383–392 (cit. on pp. 65, 70).

[Ged03] S. D. Gedney. "On Deriving a Locally Corrected Nystrom Scheme from a Quadrature Sampled Moment Method". In: *IEEE Transactions on Antennas and Propagation* 51.9 (Sept. 2003), pp. 2402–2412 (cit. on p. 22).

[GMS06] A. Geranmayeh, R. Moini, and S. H. H. Sadeghi. "Numerical Simulation of Electromagnetic Fields Radiated by Lightning Return Stroke Channels: A Wavelet-Based Approach". In: *IEEE Transactions on Electromagnetic Compatibility* 48.1 (Feb. 2006), pp. 225–233 (cit. on p. 66).

[GP15] R. D. Graglia and A. F. Peterson. *Higher-Order Techniques in Computational Electromagnetics*. Mario Boella series on electromagnetism in information & communication. Edison, NJ: SciTech Publishing, 2015. 392 pp. (cit. on p. 34).

[GP97] R. D. Graglia and A. F. Peterson. "Higher Order Interpolatory Vector Bases for Computational Electromagnetics". In: *IEEE TRANSACTIONS ON ANTENNAS AND PROPAGATION* 45.3 (1997), p. 14 (cit. on pp. 32, 34, 36).

[Gre+08] R. Grech, T. Cassar, J. Muscat, K. P. Camilleri, S. G. Fabri, M. Zervakis, P. Xanthopoulos, V. Sakkalis, and B. Vanrumste. "Review on Solving the Inverse Problem in EEG Source Analysis". In: *Journal of Neuro-Engineering and Rehabilitation* 5.1 (Nov. 7, 2008), p. 25 (cit. on pp. 115, 118, 127).

[Gue+15] S. Guelton, P. Brunet, M. Amini, A. Merlini, X. Corbillon, and A. Raynaud. "Pythran: Enabling Static Optimization of Scientific Python Programs". In: *Computational Science & Discovery* 8.1 (Mar. 16, 2015), p. 014001.

[Hal+07] H. Hallez et al. "Review on Solving the Forward Problem in EEG Source Analysis". In: *Journal of NeuroEngineering and Rehabilitation* 4.1 (2007), p. 46 (cit. on p. 114).

[Hed+17] T. Hedrich, G. Pellegrino, E. Kobayashi, J. Lina, and C. Grova. "Comparison of the Spatial Resolution of Source Imaging Techniques in High-Density EEG and MEG". In: *NeuroImage* 157 (Aug. 2017), pp. 531–544 (cit. on p. 114).

[HPH16] Y. Huang, L. C. Parra, and S. Haufe. "The New York Head—A Precise Standardized Volume Conductor Model for EEG Source Localization and tES Targeting". In: *NeuroImage*. Transcranial electric stimulation (tES) and Neuroimaging 140 (Oct. 15, 2016), pp. 150–162 (cit. on p. 129).

[HS81] H. V. Henderson and S. R. Searle. "On Deriving the Inverse of a Sum of Matrices". In: *SIAM Review* 23.1 (Jan. 1981), pp. 53–60 (cit. on p. 43).

[HVG18] V. S. Handiru, A. P. Vinod, and C. Guan. "EEG Source Imaging of Movement Decoding: The State of the Art and Future Directions". In: *IEEE Systems, Man, and Cybernetics Magazine* 4.2 (Apr. 2018), pp. 14–23 (cit. on pp. 114, 115, 118, 119, 129).

[Jin15] J.-M. Jin. *Theory and Computation of Electromagnetic Fields*. Second edition. Hoboken, New Jersey: John Wiley & Sons, Inc, 2015. 715 pp. (cit. on pp. 17, 21, 69).

[Jon81] D. S. Jones. "Note on the Integral Equation for a Straight Wire Antenna". In: *IEE Proceedings H - Microwaves, Optics and Antennas* 128.2 (Apr. 1981), pp. 114–116 (cit. on p. 66).

[JTY06] S. Jarvenpaa, M. Taskinen, and P. Yla-Oijala. "Singularity Subtraction Technique for High-Order Polynomial Vector Basis Functions on Planar Triangles". In: *IEEE Transactions on Antennas and Propagation* 54.1 (Jan. 2006), pp. 42–49 (cit. on p. 32).

[KLH05] B. Kamousi, Z. Liu, and B. He. "Classification of Motor Imagery Tasks for Brain-Computer Interface Applications by Means of Two Equivalent Dipoles Analysis". In: *IEEE Transactions on Neural Systems and Rehabilitation Engineering* 13.2 (June 2005), pp. 166–171 (cit. on pp. 119, 128).

[Kol99] B. M. Kolundzija. "Electromagnetic Modeling of Composite Metallic and Dielectric Structures". In: *IEEE Transactions on Microwave Theory and Techniques* 47.7 (July 1999), pp. 1021–1032 (cit. on p. 32).

[Kro+18] L. R. Krol, J. Pawlitzki, F. Lotte, K. Gramann, and T. O. Zander. "SEREEGA: Simulating Event-Related EEG Activity". In: *Journal of Neuroscience Methods* 309 (Nov. 2018), pp. 13–24 (cit. on p. 120).

[Kyb+05] J. Kybic, M. Clerc, T. Abboud, O. Faugeras, R. Keriven, and T. Papadopoulo. "A Common Formalism for the Integral Formulations of the Forward EEG Problem". In: *IEEE Transactions on Medical Imaging* 24.1 (Jan. 2005), pp. 12–28 (cit. on p. 28).

[LB12] O. Livne and A. Brandt. "Lean Algebraic Multigrid (LAMG): Fast Graph Laplacian Linear Solver". In: *SIAM Journal on Scientific Computing* 34.4 (Jan. 2012), B499–B522 (cit. on pp. 50, 59).

[Lib+17] E. Libessart, A. Merlini, M. Arzel, C. Lahuec, and F. Andriulli. "Accélération Matérielle Pour l'imagerie Cérébrale Par EEG". June 2017.

[Lin+18a] J. T. Lindgren, A. Merlini, A. Lecuyer, and F. P. Andriulli. "SimBCI - Tool to Simulate EEG and BCI". In: 2018 (cit. on p. 120).

[Lin+18b] J. T. Lindgren, A. Merlini, A. Lecuyer, and F. P. Andriulli. "simBCI—A Framework for Studying BCI Methods by Simulated EEG". In: *IEEE Transactions on Neural Systems and Rehabilitation Engineering* 26.11 (Nov. 2018), pp. 2096–2105 (cit. on pp. 115, 116, 120, 129).

[Lin18] J. T. Lindgren. "As above, so below? Towards Understanding Inverse Models in BCI". In: *Journal of Neural Engineering* 15.1 (2018), p. 012001 (cit. on p. 129).

[Liu+05] H. Liu, P. H. Schimpf, G. Dong, X. Gao, F. Yang, and S. Gao. "Standardized Shrinking LORETA-FOCUSS (SSLOFO): A New Algorithm for Spatio-Temporal EEG Source Reconstruction". In: *IEEE Transactions on Biomedical Engineering* 52.10 (Oct. 2005), pp. 1681–1691 (cit. on p. 128).

[LL98] Y. H. Lee and Y. Lu. "Accelerating Numerical Electromagnetic Code Computation by Using the Wavelet Transform". In: *IEEE Transactions on Magnetics* 34.5 (Sept. 1998), pp. 3399–3402 (cit. on p. 66).

[LLA09] F. Lotte, A. Lecuyer, and B. Arnaldi. "FuRIA: An Inverse Solution Based Feature Extraction Algorithm Using Fuzzy Set Theory for Brain–Computer Interfaces". In: *IEEE Transactions on Signal Processing* 57.8 (Aug. 2009), pp. 3253–3263 (cit. on p. 124).

[LLB03] J.-F. Lee, R. Lee, and R. Burkholder. "Loop Star Basis Functions and a Robust Preconditioner for EFIE Scattering Problems". In: *IEEE Transactions on Antennas and Propagation* 51.8 (Aug. 2003), pp. 1855–1863 (cit. on pp. 33, 88).

[Lot+07] F. Lotte, M. Congedo, A. Lécuyer, F. Lamarche, and B. Arnaldi. "A Review of Classification Algorithms for EEG-Based Brain–Computer Interfaces". In: *Journal of Neural Engineering* 4.2 (2007), R1 (cit. on p. 114).

[Lot+18] F. Lotte, L. Bougrain, A. Cichocki, M. Clerc, M. Congedo, A. Rakotomamonjy, and F. Yger. "A Review of Classification Algorithms for EEG-Based Brain–Computer Interfaces: A 10 Year Update". In: *Journal of Neural Engineering* 15.3 (June 1, 2018), p. 031005 (cit. on pp. 114, 116, 129).

[Lot11] F. Lotte. "Generating Artificial EEG Signals To Reduce BCI Calibration Time". In: 5th International Brain-Computer Interface Workshop. Sept. 2011, pp. 176–179 (cit. on p. 115).

[Mer+17] A. Merlini, A. Pillain, K. Cools, and F. P. Andriulli. "On the Low-Frequency and Refinement Regularization of the Reduced Kernel Wire EFIE". In: *2017 IEEE International Symposium on Antennas and Propagation & USNC/URSI National Radio Science Meeting*. 2017 IEEE International Symposium on Antennas and Propagation & USNC/URSI National Radio Science Meeting. San Diego, CA, USA: IEEE, July 2017, pp. 725–726.

[Mer+18a] A. Merlini, Y. Beghein, K. Cools, E. Michielssen, and F. P. Andriulli. "Magnetic and Combined Field Integral Equations Based on the Quasi-Helmholtz Projectors". 2018 (cit. on p. 87).

[Mer+18b] A. Merlini, A. Dély, K. Cools, and F. P. Andriulli. "Electromagnetic Modelling till Arbitrarily Low Frequency via the Quasi-Helmholtz Projectors". In: *Advances in Mathematical Methods for Electromagnetics*. Ed. by K. Kobayashi and P. Smith. Institution of Engineering and Technology (IET), 2018.

[Mer+18c] A. Merlini, A. Pillain, K. Cools, and F. P. Andriulli. "Low Frequency and Refinement Regularization for the Thin-Wire EFIE". 2018.

[Mic+04] C. M. Michel, M. M. Murray, G. Lantz, S. Gonzalez, L. Spinelli, and R. Grave de Peralta. "EEG Source Imaging". In: *Clinical Neurophysiology* 115.10 (Oct. 1, 2004), pp. 2195–2222 (cit. on pp. 127, 129).

[MKD02] M. I. Miga, T. E. Kerner, and T. M. Darcey. "Source Localization Using a Current-Density Minimization Approach". In: *IEEE Transactions on Biomedical Engineering* 49.7 (July 2002), pp. 743–745 (cit. on p. 119).

[MW06] A. Mohan and D. S. Weile. "Accurate Modeling of the Cylindrical Wire Kernel". In: *Microwave and Optical Technology Letters* 48.4 (Apr. 2006), pp. 740–744 (cit. on p. 65).

[NGT97] R. D. Nevels, J. C. Goswami, and H. Tehrani. "Semi-Orthogonal versus Orthogonal Wavelet Basis Sets for Solving Integral Equations". In: *IEEE Transactions on Antennas and Propagation* 45.9 (Sept. 1997), pp. 1332–1339 (cit. on p. 66).

[NN12] A. Napov and Y. Notay. "An Algebraic Multigrid Method with Guaranteed Convergence Rate". In: *SIAM Journal on Scientific Computing* 34.2 (Jan. 1, 2012), A1079–A1109 (cit. on pp. 50, 59, 76, 93, 128).

[Not] Y. Notay. *AGMG Software and Documentation* (cit. on p. 59).

[Not+01] B. M. Notaros, B. D. Popovic, J. P. Weem, R. A. Brown, and Z. Popovic. "Efficient Large-Domain MoM Solutions to Electrically Large Practical EM Problems". In: *IEEE Transactions on Microwave Theory and Techniques* 49.1 (Jan. 2001), pp. 151–159 (cit. on p. 32).

[Not08] B. M. Notaros. "Higher Order Frequency-Domain Computational Electromagnetics". In: *IEEE Transactions on Antennas and Propagation* 56.8 (Aug. 2008), pp. 2251–2276 (cit. on p. 32).

[ON10] F. W. J. Olver and National Institute of Standards and Technology, eds. *NIST Handbook of Mathematical Functions*. Cambridge: Cambridge Univ. Press [u.a.], 2010 (cit. on p. 73).

[OPC11] E. Olivi, T. Papadopoulo, and M. Clerc. "Handling White-Matter Anisotropy in BEM for the EEG Forward Problem". In: *Biomedical Imaging: From Nano to Macro, 2011 IEEE International Symposium On*. IEEE, 2011, pp. 799–802 (cit. on p. 114).

[OS18] L. N. Olson and J. B. Schroder. *PyAMG: Algebraic Multigrid Solvers in Python v4.0*. 2018 (cit. on p. 59).

[Pas02] R. D. Pascual-Marqui. "Standardized Low Resolution Brain Electromagnetic". In: *Clinical Pharmacology* (2002), p. 16 (cit. on p. 118).

[Pas99] R. D. Pascual-Marqui. "Review of Methods for Solving the EEG Inverse Problem". In: 1.1 (1999), p. 13 (cit. on p. 118).

[Pat69] K. Paton. "An Algorithm for Finding a Fundamental Set of Cycles of a Graph". In: *Communications of the ACM* 12.9 (Sept. 1, 1969), pp. 514–518 (cit. on p. 76).

[Pea75] L. Pearson. "A Separation of the Logarithmic Singularity in the Exact Kernel of the Cylindrical Antenna Integral Equation". In: *IEEE Transactions on Antennas and Propagation* 23.2 (Mar. 1975), pp. 256–258 (cit. on p. 65).

[Pet05] A. F. Peterson. *Mapped Vector Basis Functions for Electromagnetic Integral Equations*. [San Rafael, Calif.]: Morgan & Claypool Publishers, 2005 (cit. on p. 34).

[PFM10] P. J. Papakanellos, G. Fikioris, and A. Michalopoulou. "On the Oscillations Appearing in Numerical Solutions of Solvable and Nonsolvable Integral Equations for Thin-Wire Antennas". In: *IEEE Transactions on Antennas and Propagation* 58.5 (May 2010), pp. 1635–1644 (cit. on pp. 66, 69).

[PML94] R. D. Pascual-Marqui, C. M. Michel, and D. Lehmann. "Low Resolution Electromagnetic Tomography: A New Method for Localizing Electrical Activity in the Brain". In: *International Journal of Psychophysiology* 18.1 (Oct. 1, 1994), pp. 49–65 (cit. on p. 128).

[PN01] G. Pfurtscheller and C. Neuper. "Motor Imagery and Direct Brain-Computer Communication". In: *Proceedings of the IEEE* 89.7 (July 2001), pp. 1123–1134 (cit. on p. 121).

[PRA16] A. Pillain, L. Rahmouni, and F. P. Andriulli. “On the Handling of Brain Tissue Anisotropy in the Forward EEG Problem with a Conformingly Discretized Surface Integral Method”. In: *2016 IEEE 13th International Symposium on Biomedical Imaging (ISBI)*. 2016 IEEE 13th International Symposium on Biomedical Imaging (ISBI). Apr. 2016, pp. 233–236 (cit. on p. 114).

[QC08a] Z. G. Qian and W. C. Chew. “A Quantitative Study on the Low Frequency Breakdown of EFIE”. In: *Microwave and Optical Technology Letters* 50.5 (May 2008), pp. 1159–1162 (cit. on p. 88).

[QC08b] Z. G. Qian and W. C. Chew. “An Augmented Electric Field Integral Equation for High-Speed Interconnect Analysis”. In: *Microwave and Optical Technology Letters* 50.10 (Oct. 1, 2008), pp. 2658–2662 (cit. on pp. 33, 88).

[QC10] Z.-G. Qian and W. C. Chew. “Enhanced A-EFIE With Perturbation Method”. In: *IEEE Transactions on Antennas and Propagation* 58.10 (Oct. 2010), pp. 3256–3264 (cit. on pp. 31, 43, 88, 93, 98).

[Rah+17] L. Rahmouni, A. Pillain, A. Merlini, and F. P. Andriulli. “Integral Equation Modelling of Brain Fibers for Handling White Matter Anisotropies in the EEG Forward Problem”. In: *2017 International Conference on Electromagnetics in Advanced Applications (ICEAA)*. 2017 International Conference on Electromagnetics in Advanced Applications (ICEAA). Verona, Italy: IEEE, Sept. 2017, pp. 1809–1812 (cit. on pp. 28, 130).

[Rah+18] L. Rahmouni, A. Pillain, A. Merlini, and F. P. Andriulli. “Wire-Surface BEM Formulations”. 2018.

[RBK15] T. Rouibah, A. Bayadi, and K. Kerroum. “Accelerating the Frequency-Domain Response Calculation of Complex Grounding System Using Wavelet Based MBPE Technique”. In: *Electric Power Systems Research* 121 (Apr. 1, 2015), pp. 287–294 (cit. on p. 66).

[RWG82] S. Rao, D. Wilton, and A. Glisson. “Electromagnetic Scattering by Surfaces of Arbitrary Shape”. In: *IEEE Transactions on Antennas and Propagation* 30.3 (May 1982), pp. 409–418 (cit. on pp. 22, 32, 87, 90).

[Ryn00] B. P. Rynne. “Convergence of Galerkin Method Solutions of the Integral Equation for Thin Wire Antennas”. In: *Advances in Computational Mathematics* 12.2 (Feb. 1, 2000), pp. 251–259 (cit. on p. 65).

[Ryn92] B. P. Rynne. "The Well-Posedness of the Integral Equations for Thin Wire Antennas". In: *IMA Journal of Applied Mathematics* 49.1 (1992), pp. 35–44 (cit. on p. 65).

[Sch+99] D. Schwartz, J. Badier, P. Bihoué, and A. Bouliou. "Evaluation of a New MEG-EEG Spatio-Temporal Localization Approach Using a Realistic Source Model". In: *Brain Topography* 11.4 (June 1, 1999), pp. 279–289 (cit. on p. 127).

[SF96] P. P. Silvester and R. L. Ferrari. *Finite Elements for Electrical Engineers*. 3rd ed. Cambridge university press, 1996 (cit. on p. 35).

[Sha+09] B. Shanker, M. Lu, J. Yuan, and E. Michielssen. "Time Domain Integral Equation Analysis of Scattering From Composite Bodies via Exact Evaluation of Radiation Fields". In: *IEEE Transactions on Antennas and Propagation* 57.5 (May 2009), pp. 1506–1520 (cit. on p. 33).

[SJZ10] Su Yan, Jian-Ming Jin, and Zaiping Nie. "EFIE Analysis of Low-Frequency Problems With Loop-Star Decomposition and Calderón Multiplicative Preconditioner". In: *IEEE Transactions on Antennas and Propagation* 58.3 (Mar. 2010), pp. 857–867 (cit. on p. 88).

[SL09] M. B. Stephanson and J.-F. Lee. "Preconditioned Electric Field Integral Equation Using Calderon Identities and Dual Loop/Star Basis Functions". In: *IEEE Transactions on Antennas and Propagation* 57.4 (Apr. 2009), pp. 1274–1279 (cit. on p. 88).

[Son+15] J. Song, C. Davey, C. Poulsen, P. Luu, S. Turovets, E. Anderson, K. Li, and D. Tucker. "EEG Source Localization: Sensor Density and Head Surface Coverage". In: *Journal of Neuroscience Methods* 256 (Dec. 30, 2015), pp. 9–21 (cit. on p. 115).

[SS11] S. A. Sauter and C. Schwab. *Boundary Element Methods*. Vol. 39. Springer Series in Computational Mathematics. Berlin, Heidelberg: Springer Berlin Heidelberg, 2011 (cit. on p. 22).

[Sun+13] S. Sun, Y. G. Liu, W. C. Chew, and Z. Ma. "Calderón Multiplicative Preconditioned EFIE With Perturbation Method". In: *IEEE Transactions on Antennas and Propagation* 61.1 (Jan. 2013), pp. 247–255 (cit. on p. 88).

[Tan+12] M. Tangermann et al. "Review of the BCI Competition IV". In: *Frontiers in Neuroscience* 6 (2012) (cit. on pp. 115, 120, 122).

[UHS98] K. Uutela, M. Hamalainen, and R. Salmelin. “Global Optimization in the Localization of Neuromagnetic Sources”. In: *IEEE Transactions on Biomedical Engineering* 45.6 (June 1998), pp. 716–723 (cit. on pp. 115, 119).

[UHS99] K. Uutela, M. Hämäläinen, and E. Somersalo. “Visualization of Magnetoencephalographic Data Using Minimum Current Estimates”. In: *NeuroImage* 10.2 (Aug. 1, 1999), pp. 173–180 (cit. on p. 128).

[Van07] J. G. Van Bladel. *Electromagnetic Fields*. 2. ed. IEEE Press series on electromagnetic wave theory. Piscataway, NJ: IEEE Press, 2007 (cit. on p. 87).

[Vec99] G. Vecchi. “Loop-Star Decomposition of Basis Functions in the Discretization of the EFIE”. In: *Antennas and Propagation, IEEE Transactions on* 47.2 (1999), pp. 339–346 (cit. on pp. 33, 54, 88).

[Via+10] F.-B. Vialatte, M. Maurice, J. Dauwels, and A. Cichocki. “Steady-State Visually Evoked Potentials: Focus on Essential Paradigms and Future Perspectives”. In: *Progress in Neurobiology* 90.4 (Apr. 1, 2010), pp. 418–438 (cit. on p. 121).

[Vic+16] F. Vico, M. Ferrando, L. Greengard, and Z. Gimbutas. “The Decoupled Potential Integral Equation for Time-Harmonic Electromagnetic Scattering”. In: *Communications on Pure and Applied Mathematics* 69.4 (Apr. 1, 2016), pp. 771–812 (cit. on p. 88).

[VVP07] F. Vipiana, G. Vecchi, and P. Pirinoli. “A Multiresolution System of Rao–Wilton–Glisson Functions”. In: *IEEE Transactions on Antennas and Propagation* 55.3 (Mar. 2007), pp. 924–930 (cit. on p. 88).

[VVW09] F. Vipiana, G. Vecchi, and D. R. Wilton. “Automatic Loop-Tree Scheme for Arbitrary Conducting Wire-Surface Structures”. In: *IEEE Transactions on Antennas and Propagation* 57.11 (Nov. 2009), pp. 3564–3574 (cit. on p. 66).

[VW11] F. Vipiana and D. R. Wilton. “Optimized Numerical Evaluation of Singular and Near-Singular Potential Integrals Involving Junction Basis Functions”. In: *IEEE Transactions on Antennas and Propagation* 59.1 (Jan. 2011), pp. 162–171 (cit. on p. 65).

[Wag+96] M. Wagner, M. Fuchs, H.-A. Wischmann, R. Drenckhahn, and T. Köhler. “Smooth Reconstruction of Cortical Sources from EEG or MEG Recordings”. In: *NeuroImage* 3.3 (June 1996), S168 (cit. on p. 128).

[WB76] D. Wilton and C. Butler. “Efficient Numerical Techniques for Solving Pocklington’s Equation and Their Relationships to Other Methods”. In: *IEEE Transactions on Antennas and Propagation* 24.1 (Jan. 1976), pp. 83–86 (cit. on p. 65).

[WC06] D. Wilton and N. Champagne. “Evaluation and Integration of the Thin Wire Kernel”. In: *IEEE Transactions on Antennas and Propagation* 54.4 (Apr. 2006), pp. 1200–1206 (cit. on p. 65).

[WG81a] D. Wilton and A. Glisson. “On Improving the Electric Field Integral Equation at Low Frequencies”. In: *Proc. URSI Radio Sci. Meet. Dig* 24 (1981) (cit. on pp. 33, 88).

[WG81b] D. Wilton and A. Glisson. “On Improving the Stability of the Electric Field Integral Equation at Low Frequency”. In: *Proc. IEEE Antennas and Propagation Soc. National Symp.* 1981, pp. 124–133 (cit. on pp. 88, 91, 92).

[WGK95] W.-L. Wu, A. W. Glisson, and D. Kajfez. “A Study of Two Numerical Solution Procedures for the Electric Field Integral Equation at Low Frequency”. In: *Applied Computational Electromagnetics Society Journal* 10.3 (1995), pp. 69–80 (cit. on p. 37).

[WHW94] D. Werner, J. Huffman, and P. Werner. “Techniques for Evaluating the Uniform Current Vector Potential at the Isolated Singularity of the Cylindrical Wire Kernel”. In: *IEEE Transactions on Antennas and Propagation* 42.11 (1994), pp. 1549–1553 (cit. on p. 65).

[Wil83] D. R. Wilton. “Topological Consideration in Surface Patch and Volume Cell Modeling of Electromagnetic Scatterers”. In: *Proc. URSI Int. Symp. Electromagn. Theory*. 1983, pp. 65–68 (cit. on pp. 39, 92).

[Wip+10] D. P. Wipf, J. P. Owen, H. T. Attias, K. Sekihara, and S. S. Nagarajan. “Robust Bayesian Estimation of the Location, Orientation, and Time Course of Multiple Correlated Neural Sources Using MEG”. In: *NeuroImage* 49.1 (Jan. 1, 2010), pp. 641–655 (cit. on p. 128).

[WLL15] M. Wronkiewicz, E. Larson, and A. K. C. Lee. “Leveraging Anatomical Information to Improve Transfer Learning in Brain–Computer Interfaces”. In: *Journal of Neural Engineering* 12.4 (2015), p. 046027 (cit. on p. 129).

[Wol+06] C. H. Wolters, A. Anwander, X. Tricoche, D. Weinstein, M. A. Koch, and R. S. MacLeod. "Influence of Tissue Conductivity Anisotropy on EEG/MEG Field and Return Current Computation in a Realistic Head Model: A Simulation and Visualization Study Using High-Resolution Finite Element Modeling". In: *NeuroImage* 30.3 (Apr. 15, 2006), pp. 813–826 (cit. on pp. 28, 114, 129).

[WW04] R. Wildman and D. Weile. "An Accurate Broad-Band Method of Moments Using Higher Order Basis Functions and Tree-Loop Decomposition". In: *IEEE Transactions on Antennas and Propagation* 52.11 (Nov. 2004), pp. 3005–3011 (cit. on pp. 33, 54).

[Yun+03] Yunhua Zhang, Tie Jun Cui, Weng Cho Chew, and Jun-Sheng Zhao. "Magnetic Field Integral Equation at Very Low Frequencies". In: *IEEE Transactions on Antennas and Propagation* 51.8 (Aug. 2003), pp. 1864–1871 (cit. on pp. 31, 88, 93).

[Yve+96] B. Yvert, O. Bertrand, J. Echallier, and J. Pernier. "Improved Dipole Localization Using Local Mesh Refinement of Realistic Head Geometries: An EEG Simulation Study". In: *Electroencephalography and Clinical Neurophysiology* 99.1 (July 1996), pp. 79–89 (cit. on p. 127).

[ZC00] J.-S. Zhao and W. C. Chew. "Integral Equation Solution of Maxwell's Equations from Zero Frequency to Microwave Frequencies". In: *Antennas and Propagation, IEEE Transactions on* 48.10 (2000), pp. 1635–1645 (cit. on pp. 33, 88).

[Zha+02] J.-S. Zhao, W. C. Chew, T. Cui, and Y. Zhang. "Cancellations of Surface Loop Basis Functions". In: *IEEE Antennas and Propagation Society International Symposium (IEEE Cat. No.02CH37313)*. IEEE Antennas and Propagation Society International Symposium (IEEE Cat. No.02CH37313). Vol. 1. June 2002, 58–61 vol.1 (cit. on p. 81).

[ZJ11] J. Zhu and D. Jiao. "A Rigorous Solution to the Low-Frequency Breakdown in Full-Wave Finite-Element-Based Analysis of General Problems Involving Inhomogeneous Lossless/Lossy Dielectrics and Nonideal Conductors". In: *IEEE Transactions on Microwave Theory and Techniques* 59.12 (Dec. 2011), pp. 3294–3306 (cit. on p. 88).

[ZK11] T. O. Zander and C. Kothe. "Towards Passive Brain–Computer Interfaces: Applying Brain–Computer Interface Technology to Human–Machine Systems in General". In: *Journal of Neural Engineering* 8.2 (2011), p. 025005 (cit. on p. 114).

Journal Publications

[Gue+15] S. Guelton, P. Brunet, M. Amini, A. Merlini, X. Corbillon, and A. Raynaud. “Pythran: Enabling Static Optimization of Scientific Python Programs”. In: *Computational Science & Discovery* 8.1 (Mar. 16, 2015), p. 014001.

[Lin+18b] J. T. Lindgren, A. Merlini, A. Lecuyer, and F. P. Andriulli. “simBCI—A Framework for Studying BCI Methods by Simulated EEG”. In: *IEEE Transactions on Neural Systems and Rehabilitation Engineering* 26.11 (Nov. 2018), pp. 2096–2105 (cit. on pp. 115, 116, 120, 129).

Conference Contributions

[Lib+17] E. Libessart, A. Merlini, M. Arzel, C. Lahuec, and F. Andriulli. “Accélération Matérielle Pour l’imagerie Cérébrale Par EEG”. June 2017.

[Lin+18a] J. T. Lindgren, A. Merlini, A. Lecuyer, and F. P. Andriulli. “SimBCI - Tool to Simulate EEG and BCI”. In: 2018 (cit. on p. 120).

[Mer+17] A. Merlini, A. Pillain, K. Cools, and F. P. Andriulli. “On the Low-Frequency and Refinement Regularization of the Reduced Kernel Wire EFIE”. In: *2017 IEEE International Symposium on Antennas and Propagation & USNC/URSI National Radio Science Meeting*. 2017 IEEE International Symposium on Antennas and Propagation & USNC/URSI National Radio Science Meeting. San Diego, CA, USA: IEEE, July 2017, pp. 725–726.

[Rah+17] L. Rahmouni, A. Pillain, A. Merlini, and F. P. Andriulli. “Integral Equation Modelling of Brain Fibers for Handling White Matter Anisotropies in the EEG Forward Problem”. In: *2017 International Conference on Electromagnetics in Advanced Applications (ICEAA)*. 2017 International Conference on Electromagnetics in Advanced Applications (ICEAA). Verona, Italy: IEEE, Sept. 2017, pp. 1809–1812 (cit. on pp. 28, 130).

Submitted Publications

[Mer+18a] A. Merlini, Y. Beghein, K. Cools, E. Michielssen, and F. P. Andriulli. “Magnetic and Combined Field Integral Equations Based on the Quasi-Helmholtz Projectors”. 2018 (cit. on p. 87).

[Mer+18b] A. Merlini, A. Dély, K. Cools, and F. P. Andriulli. “Electromagnetic Modelling till Arbitrarily Low Frequency via the Quasi-Helmholʒ Projectors”. In: *Advances in Mathematical Methods for Electromagnetics*. Ed. by K. Kobayashi and P. Smith. Institution of Engineering and Technology (IET), 2018.

Publications in Preparation

[Mer+18c] A. Merlini, A. Pillain, K. Cools, and F. P. Andriulli. “Low Frequency and Refinement Regularization for the Thin-Wire EFIE”. 2018.

[Rah+18] L. Rahmouni, A. Pillain, A. Merlini, and F. P. Andriulli. “Wire-Surface BEM Formulations”. 2018.

UNIVERSITE BRETAGNE LOIRE / MATHSTIC

IMT Atlantique
Bretagne-Pays de la Loire
École Mines-Télécom

Titre : Systèmes Computationnel unifiés pour Simulations de Basse à Haute Fréquence : Modélisations Rapides et Haute-Fidélité pour des Applications du Cerveau aux Radiofréquences

Mots clés : Electromagnétique computationnelle, Basses-Fréquences, Hautes-Fréquences, préconditionnement

Résumé : Dans le domaine de l'électromagnétisme computationnel, les équations intégrales de frontière sont très largement utilisées pour résoudre certains des plus grands problèmes directs, grâce à leur grande efficacité. Cependant les équations intégrales du champ électrique et du champ combiné (EFIE et CFIE), deux des formulations les plus employées, souffrent d'instabilités à basse fréquence et à haute discrétisation, ce qui limite leur versatilité. Dans cette thèse différentes approches sont présentées pour obtenir des algorithmes applicables aussi bien à des problèmes de compatibilité électromagnétique qu'à des applications radar. Les solutions présentées incluent (i) l'extension des projecteurs dit quasi-Helmholtz (qH) aux modélisations d'ordre supérieur ; (ii) l'utilisation de ces projecteurs pour stabiliser l'équation intégrale du champ magnétique et former une CFIE extrêmement précise, augmentée par des techniques de type Calderón, qui ne souffre de problèmes ni à basse fréquence ni à haute discrétisation et qui n'est pas sujette aux résonances artificielles ; (iii) le développement d'une EFIE filaire, basée sur des B-splines linéaires et les projecteurs qH, stable aux deux extrémités du spectre. Ces travaux ont été suivis de l'ouverture d'un nouvel axe de recherche visant l'amélioration des techniques de résolution des problèmes inverses en électromagnétique, avec pour objectif principal l'augmentation des performances des interfaces cerveau machine (BCIs). Les premiers résultats obtenus incluent le développement de l'un des premiers systèmes libres de simulation de bout en bout de session de BCI ayant été publié après revue par les pairs.

Title : Unified Computational Frameworks Bridging Low to High Frequency Simulations : Fast and High Fidelity Modelling from Brain to Radio-Frequency Scenarios

Keywords : Computational Electromagnetics, Low-Frequency, High-Frequency, Preconditioning

Abstract : In computational electromagnetics, boundary integral equations are the scheme of choice for solving extremely large forward electromagnetic problems due to their high efficiency. However, two of the most used of these formulations, the electric and combined field integral equations (EFIE and CFIE), suffer from stability issues at low frequency and dense discretization, limiting their applicability at both ends of the spectrum. This thesis focusses on remedying these issues to obtain full-wave solvers stable from low to high frequencies, capable of handling scenarios ranging from electromagnetic compatibility to radar applications. The solutions presented include (i) extending the quasi-Helmholtz (qH) projectors to higher order modeling thus combining stability with high order convergence rates; (ii) leveraging on the qH projectors to numerically stabilize the magnetic field integral equation and obtain a highly accurate and provably resonance-free Calderón-augmented CFIE immune to both of the aforementioned problems; and (iii) introducing a new low frequency and dense discretization stable wire EFIE based on projectors and linear B-splines. In addition, a research axis focused on enhancing Brain Computer Interface (BCIs) with high resolution electromagnetic modeling of the brain has been opened; a particular attention is dedicated to the inverse problem of electromagnetics and the associated integral equation-based forward problem. The first results of this new line of investigations include the development of one of the first peer-reviewed, freely available framework for end-to-end simulation of BCI experiments.